

**Transition delay
in boundary-layer flows
via reactive control**

by

Nicolò Fabbiane

May 2016
Technical Reports
Royal Institute of Technology
Department of Mechanics
SE-100 44 Stockholm, Sweden

Akademisk avhandling som med tillstånd av Kungliga Tekniska Högskolan i Stockholm framlägges till offentlig granskning för avläggande av teknologie doktorsexamen måndagen den 13 juni 2016 kl 10:30 i sal Kollegiesalen, Kungliga Tekniska Högskolan, Brinellvägen 8, Stockholm.

TRITA-MEK Technical report 2016:10

ISSN 0348-467X

ISRN KTH/MEK/TR-16/10-SE

ISBN 978-91-7729-030-8

Cover: uncontrolled (top) and controlled (bottom) transition to turbulence. The color-scale reports the fluctuation of streamwise wall-shear stress with respect to the laminar solution; the saturated white areas indicate the turbulent regime. Red circles and blue squares show the position of sensors and actuators, respectively. The flow is directed from right to left.

©Nicolò Fabbiane 2016

Universitetsservice US-AB, Stockholm 2016

“It. Could. Work!”

Dr. Frederick Frankenstein, *Young Frankenstein* (1974)

Transition delay in boundary-layer flows via reactive control

Nicolò Fabbiane

Linné FLOW Centre, KTH Mechanics, Royal Institute of Technology
SE-100 44 Stockholm, Sweden

Abstract

Transition delay in boundary-layer flows is achieved via reactive control of flow instabilities, i.e. Tollmien-Schlichting (TS) waves. Adaptive and model-based control techniques are investigated by means of direct numerical simulations (DNS) and experiments. The action of actuators localised in the wall region is prescribed based on localised measurement of the disturbance field; in particular, plasma actuators and surface hot-wire sensors are considered.

Performances and limitations of this control approach are evaluated both for two-dimensional (2D) and three-dimensional (3D) disturbance scenarios. The focus is on the robustness properties of the investigated control techniques; it is highlighted that static model-based control, such as the linear-quadratic-Gaussian (LQG) regulator, is very sensitive to model-inaccuracies. The reason for this behaviour is found in the feed-forward nature of the adopted sensor/actuator scheme; hence, a second, downstream sensor is introduced and actively used to recover robustness via an adaptive filtered-x least-mean-squares (fxLMS) algorithm.

Furthermore, the model of the flow required by the control algorithm is reduced to a time delay. This technique, called delayed-x least-mean-squares (dxLMS) algorithm, allows taking a step towards a self-tuning controller; by introducing a third sensor it is possible to compute on-line the suitable time-delay model with no previous knowledge of the controlled system. This self-tuning approach is successfully tested by in-flight experiments on a motor-glider.

Lastly, the transition delay capabilities of the investigated control configuration are confirmed in a complex disturbance environment. The flow is perturbed with random localised disturbances inside the boundary layer and the laminar-to-turbulence transition is delayed via a multi-input-multi-output (MIMO) version of the fxLMS algorithm. A positive theoretical net-energy-saving is observed for disturbance amplitudes up to 2% of the free-stream velocity at the actuation location, reaching values around 1000 times the input power for the lower disturbance amplitudes that have been investigated.

Key words: flow control, drag reduction, net energy saving, adaptive control, model-based control, optimal control, flat-plate boundary layer, laminar-to-turbulent transition, plasma actuator, direct numerical simulation, in-flight experiments.

Fördröjning av laminärt-turbulent omslag i gränsskiktströmning genom reaktiv kontroll

Nicolò Fabbiane

Linné FLOW Centre, KTH Mekanik, Kungliga Tekniska Högskolan
SE-100 44 Stockholm, Sverige

Sammanfattning

I den här avhandlingen har reglertekniska metoder tillämpats för att försena omslaget från ett laminärt till ett turbulent gränsskikt genom att dämpa tillväxten av små instabiliteter, så kallade Tollmien-Schlichting vågor. Adaptiva och modellbaserade metoder för reglering av strömning har undersökts med hjälp av numeriska beräkningar av Navier-Stokes ekvationer, vindtunnelexperiment och även genom direkt tillämpning på flygplan. Plasmaaktuatorer och varmtrådgivare vidhäftade på ytan av plattan eller vingen har använts i experimenten och modellerats i beräkningarna.

Prestanda och begränsningar av den valda kontrollstrategin har utvärderats för både tvådimensionella och tredimensionella gränsskiktinstabiliteter. Fokus har varit på metodernas robusthet, där vi visar att statiska metoder som linjär-kvadratiske regulatorer (LQG) är mycket känsliga för avvikelser från den nominella modellen. Detta beror främst på att regulatorer agerar i förkompenseringsläge ("feed-forward") på grund av strömningens karaktär och placeringen av givare och aktuatorer. För att minska känsligheten mot avvikelser och därmed öka robustheten har en givare införts nedströms och en adaptiv $fxLMS$ algoritm (filtered-x least-mean-squares) har tillämpats.

Vidare har modelleringen av $fxLMS$ -algoritmen förenklats genom att ersätta överföringsfunktionen mellan aktuatorer och givare med en lämplig tidsfördröjning. Denna metod som kallas för $dxLMS$ (delayed-x least-mean-squares) kräver att ytterligare en givare införs långt uppströms för att kunna uppskatta hastigheten på de propagerande instabilitetsvågorna. Denna teknik har tillämpats framgångsrikt för reglering av gränsskiktet på vingen av ett segelflygplan.

Slutligen har de reglertekniska metoderna testas för komplexa slumpmässiga tredimensionella störningar som genererats uppströms lokalt i gränsskiktet. Vi visar att en signifikant försening av laminärt-turbulentomslag äger rum med hjälp av en $fxLMS$ algoritm. En analys av energibudgeten visar att för ideala aktuatorer och givare kan den sparade energiåtgången på grund av minskad väggfriktion vara upp till 1000 gånger större än den energi som använts för reglering.

Nyckelord: strömningsstyrning, friktionsreduktion, netto energibesparing, adaptiv styrning, modellbaserad styrning, optimal kontroll, gränsskikt öve en plan platta, laminärt till turbulent omslag, plasma aktuator, DNS, flyg prov.

Preface

This thesis deals with transition delay in boundary-layer flows by reactive-control techniques. A brief introduction on the basic concepts and methods is presented in the first part. The second part contains five articles. The papers are adjusted to comply with the present thesis format for consistency, but their contents have not been altered as compared with their original counterparts.

Paper 1. N. FABBIANE, O. SEMERARO, S. BAGHERI & D.S. HENNINGSON, 2014. *Adaptive and model-based control theory applied to convectively-unstable flows*. Appl. Mech. Rev. **66** (6), 060801.

Paper 2. N. FABBIANE, B. SIMON, F. FISCHER, S. GRUNDMANN, S. BAGHERI & D.S. HENNINGSON, 2015. *On the role of adaptivity for robust laminar-flow control*. J. Fluid Mech. **767**, R1.

Paper 3. B. SIMON, N. FABBIANE, T. NEMITZ, S. BAGHERI, D.S. HENNINGSON & S. GRUNDMANN. *In-flight active-wave-cancelation via delayed-x-LMS control algorithm in a laminar boundary layer*. Under review for publication in Exp. Fluids.

Paper 4. R. DADFAR, N. FABBIANE, S. BAGHERI & D.S. HENNINGSON, 2014. *Centralised versus decentralised active control of boundary layer instabilities*. Flow Turb. Comb. **93** (4), 537–553.

Paper 5. N. FABBIANE, S. BAGHERI & D.S. HENNINGSON. *Energy efficiency and performance limitations of linear adaptive control for transition delay*. Submitted to J. Fluid Mech.

May 2016, Stockholm
Nicolò Fabbiane

Division of work between authors

The main advisor for the project is Prof. Dan S. Henningson (DH). Dr. Shervin Bagheri (SB) acts as co-advisor.

Paper 1. The code has been developed by Nicolò Fabbiane (NF). The paper has been written by NF and Onofrio Semeraro with feedback from SB and DH.

Paper 2. The experimental set-up has been designed by Bernhard Simon (BS). The model-based control has been implemented by NF, while the adaptive control by Felix Fischer. The simulations have been performed by NF using the control-code developed by NF. The paper has been written by NF and BS with feedback from Sven Grundmann (SG), SB and DH.

Paper 3. The experimental set-up has been designed by BS. The experiment has been set-up by BS and Timotheus Nemitz (TN). In-flight experiments were performed by BS, TN and NF. The simulations have been performed by NF using the control-code developed by NF. The paper has been written by BS and NF with feedback from SG, SB and DH.

Paper 4. The simulations have been performed by Reza Dadfar (RD) using the control-code developed by NF. The paper has been written by RD with feedback from NF, SB and DH.

Paper 5. Simulations and post-processing have been conducted by NF using the control-code developed by NF. The paper has been written by NF with feedback from SB and DH.

Other publications

The following paper, although related, is not included in this thesis.

N. FABBIANE, S. BAGHERI & D.S. HENNINGSON, 2015. *Adaptive control of finite-amplitude 3D disturbances in 2D boundary-layer flows*. Proceedings of TSFP-9. Melbourne, Australia.

Conferences

Part of the work in this thesis has been presented or accepted to be presented at the following international conferences. The presenting author is underlined.

N. FABBIANE, B. SIMON, F. FISCHER, S. GRUNDMANN, S. BAGHERI & D.S. HENNINGSON. *Model-based and adaptive laminar-flow control via DBD plasma actuators: an experimental comparison*. 67th Annual Meeting of APS Division of Fluid Dynamics. San Francisco, California, November 2014.

N. FABBIANE, B. SIMON, F. FISCHER, S. GRUNDMANN, S. BAGHERI & D.S. HENNINGSON. *On the role of adaptivity for robust laminar flow control*. ERCOFTAC SIG33 Workshop. Jersey, April 2015.

N. FABBIANE, S. BAGHERI & D.S. HENNINGSON. *Adaptive control of finite-amplitude 3D disturbances in 2D boundary-layer flows*. TSFP-9. Melbourne, Australia, July 2015.

N. FABBIANE, S. BAGHERI & D.S. HENNINGSON. *Closed-loop control of instabilities in boundary layers*. FOR 1779 Symposium: Active Drag Reduction. Aachen, Germany, November 2015.

N. FABBIANE, S. BAGHERI & D.S. HENNINGSON. *Limitations and efficiency of linear adaptive control for transition delay*. EFMC11. Seville, Spain, September 2016.

Contents

Abstract	v
Sammanfattning	vi
Preface	vii
Part I - Overview and summary	
Chapter 1. Introduction	1
1.1. A route to turbulence	1
1.2. The control problem	4
Chapter 2. Control of boundary-layer instabilities	6
2.1. A linear model of the flow	7
2.2. Model based control	11
2.3. Adaptive control	13
2.4. Controlled system	14
2.5. A self-tuning compensator	16
Chapter 3. Transition delay	21
3.1. A 3D compensator	22
3.2. Performance and limitations	24
3.3. Energy budget	27
Chapter 4. Conclusions and outlook	29
Acknowledgements	33
Bibliography	35

Part II - Papers

Summary of the papers	41
Paper 1. Adaptive and model-based control theory applied to convectively-unstable flows	P1
Paper 2. On the role of adaptivity for robust laminar-flow control	P2
Paper 3. In-flight active-wave-cancelation via delayed-x-LMS control algorithm in a laminar boundary layer	P3
Paper 4. Centralised versus decentralised active control of boundary layer instabilities	P4
Paper 5. Energy efficiency and performance limitations of linear adaptive control for transition delay	P5

Part I

Overview and summary

Introduction

One of the main goals pursued by fluid dynamics in the last century is the reduction of aerodynamic drag. This became a pressing objective with the advent of the aeroplane and air transportation: the need to fly faster, cheaper and, in recent times, greener motivated – and still motivates – the research on this topic for many years. The problem has been approached from very different directions: from a better wing design to reduce the drag induced by the lift¹, to a better airfoil design to keep the boundary-layer laminar as long as possible.

When a body moves through a fluid, the relative velocity between body and fluid is zero at the body surface, while far from the surface – in the *free-stream* – the velocity is dictated by the body geometry and motion. The link between these two regions is called *boundary-layer*. If the body moves with *low* speed in still air, and its motion is regular, the boundary layer that is generated is regular as well; this condition is called *laminar* flow. Since the equations that govern the flow are non-linear and very sensitive to perturbations, the flow may abruptly switch to a chaotic behaviour – the *turbulent* regime – even when small disturbances occur. The turbulent regime of the boundary layer shows a higher friction drag with respect to the laminar state, hence the effort to keep the boundary-layer laminar as long as possible.

The present work moves in the reactive control framework: the laminar-to-turbulence transition is prevented by removing those disturbances from the flow that would eventually lead to transition. The disturbances are cancelled by actuators that base their action on measurements of the disturbance in the flow.

1.1. A route to turbulence

There are several paths that lead to the turbulent regime in boundary layer flows, depending on the disturbance level in the free-stream (Saric *et al.* 2002). Weak disturbances follow a path that can be initially described by linearised equation of the flow, the Orr-Sommerfeld-Squire (OSS) equations. Linear flow instabilities – Tollmien-Schlichting (TS) waves – are triggered by free-stream disturbances; their initial growth, even if exponential, is weak. However, as the perturbation

¹The lift is the component of the aerodynamic force perpendicular to the aeroplane velocity that usually balances the weight of the aircraft.

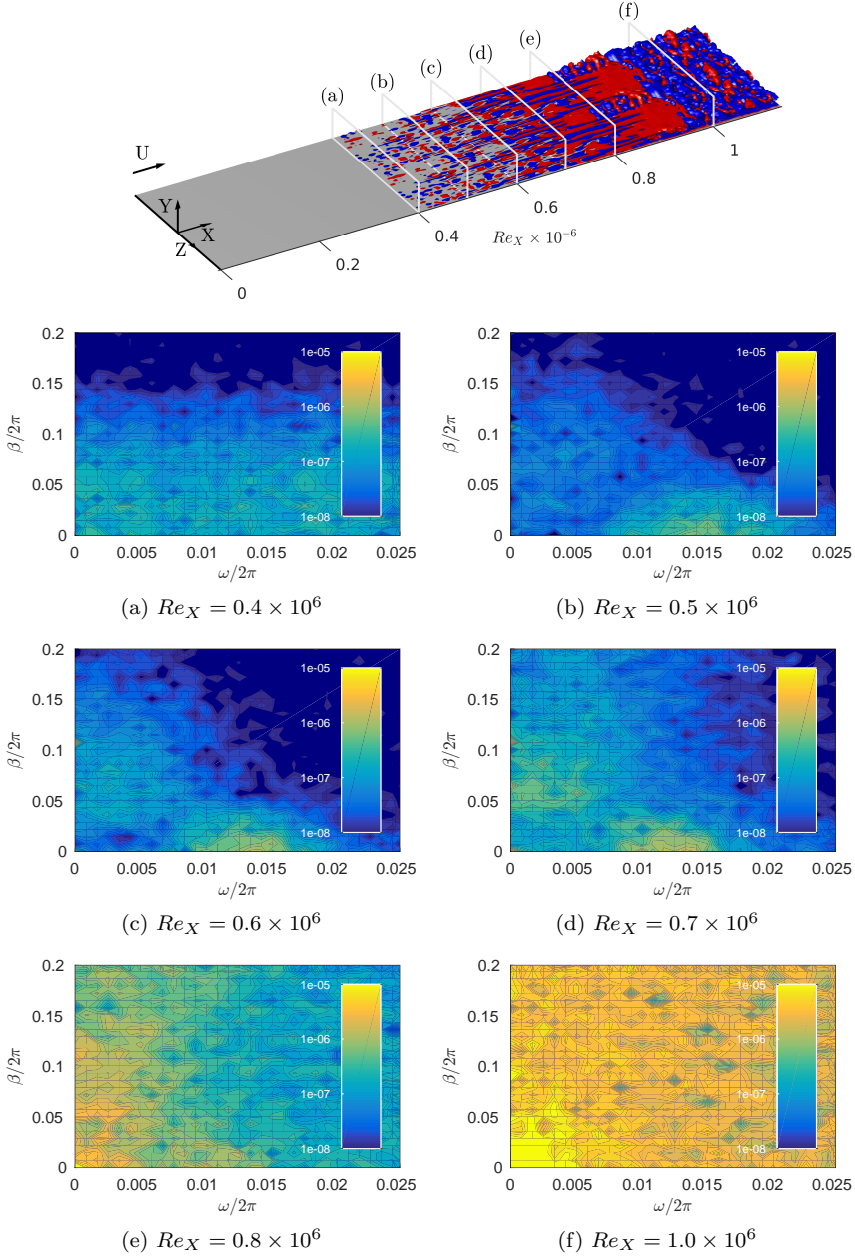


Figure 1.1: TS-wave driven transition. The skin-friction spectra are reported for different streamwise locations; β and ω are the spanwise wave-number and the temporal angular frequency, respectively. The flow is seeded close to the wall at $Re_X \approx 0.4 \times 10^6$ with uniform noise. Red and blue isosurfaces indicate positive and negative values of $u' = \pm 4 \times 10^{-3} U$, i.e. the streamwise perturbation velocity with respect to the laminar solution.

amplitude crosses a critical level, non-linear interactions arise. At this point, the disturbances rapidly grow and transition to turbulence occurs (Kachanov 1994). By increasing the disturbance amplitude, the linear asymptotic behaviour of the perturbation is not able to describe the process any more and the short-time behaviour becomes more and more important. In fact, when a perturbation is introduced in the flow, it can experience a large *transient growth*, even if the flow is stable, i.e. no linear instability occurs. This is possible because OSS-modes are not mutually orthogonal and their combination may result in an amplification of the disturbance (Henningson *et al.* 1993). For strong free-stream disturbances the linear mechanism may be by-passed. In this case, the transition to turbulence can not be predicted via the linear theory. Non-linear dynamics theory has recently helped to have a better insight into the transition process in the presence of large amplitude disturbances (Duguet *et al.* 2012); the transition to turbulence appears to occur via specific structures that cluster in limited regions of the phase space, called *edge states*. The recent work by Kreilos *et al.* (2015) is an example of how transition can be predicted by dynamical-system analysis applied to boundary layers.

This work focuses on the weak disturbance scenario, where the perturbation can be initially described by the linearised Navier-Stokes (LNS) equations. A canonical boundary layer case is investigated (Blasius 1908). Consider a uniform and constant flow with velocity U that encounters a semi-infinite flat plate aligned with the flow: since the free-stream flow is constant in time, a two-dimensional (2D), steady, laminar boundary-layer develops starting from the tip of the plate – the *leading-edge* – and extends all along the plate if the flow is not perturbed. The flow is linearly stable up to $Re_{X,c} = UX/\nu \approx 91190$, where X is the streamwise distance from the leading-edge and ν is the kinematic viscosity (Schmid & Henningson 2001); downstream of this position, unstable solutions to the OS-equations always occur. This means that if the flow is perturbed at $Re_X < Re_{X,c}$ a small perturbation will decay while being convected and it will be amplified by the flow only when it reaches the critical position $Re_{X,c}$; only then, the perturbation will start to grow exponentially and eventually evolve into turbulence.

Figure 1.1 illustrates the transition scenario described in the previous paragraph. The *receptivity* process of the free-stream disturbances is by-passed and the flow is directly perturbed inside the boundary layer region. The flow is seeded with uniform white-noise at $Re_X \approx 400\,000$, see Figure 1.1a. Immediately downstream this point (Figure 1.1b), most of the seeded spatial and temporal frequencies decay and only few of them are amplified by the flow. The latter are organised in a very specific part of the spectrum: close to the zero spanwise wave-number and frequency $f = \omega/2\pi = 0.015 U/\delta_s^*$, where δ_s^* is the displacement thickness at the seeding point. The non-linear interaction between wave-packets generates the the second peak close to the zero-frequency axis in Figure 1.1c. Farther downstream these structures reach the same magnitude as the TS-wave that generated them (Figure 1.1d). They are responsible for

the streaky structures visible in the physical flow. These structures interact with the TS-waves (Figure 1.1e), break down, and eventually lead to a fully turbulent flow (Figure 1.1f).

1.2. The control problem

By preventing or obstructing the transition process described in the previous section, transition-delay and, thus, drag-reduction can be achieved. TS-waves are present in a limited frequency band in space and time, unlike the structures that define the turbulent boundary-layer. It is hence more convenient to act on TS-waves. This approach has two main advantages: (i) the temporal frequencies that describe the perturbation behaviour are low and bounded and (ii) the energy requirement to cancel the disturbance is low because of the small amplitude of the perturbation. In view of a small power consumption to perform the control action, a large benefit is achieved in terms of transition delay and consequent drag reduction; in some sense, the non-linear breakdown to turbulence is used to design a highly energy-efficient control scheme.

Wall-mounted sensors are used to detect the upcoming disturbances. Once detected, the perturbation is cancelled via a localised forcing provided by an actuator. The choice and position of these devices is the zeroth-step in the control design process, as it determines how the control algorithm will interact with the system and deeply influences the design of the control itself (Belson *et al.* 2013). In this work, the reference sensor y – i.e. the sensor responsible for detecting the disturbance – is positioned upstream of the actuator u that performs the control action, Figure 1.2. The perturbation is introduced in the flow by the disturbance source d . The interaction between the perturbation and the wave generated by the actuator leads to an attenuation of the disturbance amplitude, which is detected by the error sensor z .

The compensator is the core of the control action, as it is the system responsible for computing the actuator forcing, based on the measurement signals. It can be designed via very different strategies; a unique classification is always limiting and for sure challenging. In this work, the classification is approached according to Wiener (1961), recently reprised and extended by the insightful review by Brunton & Noack (2015). Every control strategy is based on a model of the system that it aims to control. The model can be given a-priori based on the Navier-Stokes (NS) equations; this approach is classified as *white-box*. In fluid-dynamics, this is usually coupled with optimal control theory (Bewley & Liu 1998). The similarities with the canonical stability theory enabled these techniques to rapidly spread in the numerical community (e.g. Barbagallo *et al.* 2009; Bagheri & Henningson 2011; Sharma *et al.* 2011; Semeraro *et al.* 2013b). A different example of white-box control can be found in the numerical and experimental work by Li & Gaster (2006), where opposition control is performed based on LNS equations. White-box modelling compares with the *black-box* approach, where the model is identified starting from experimental

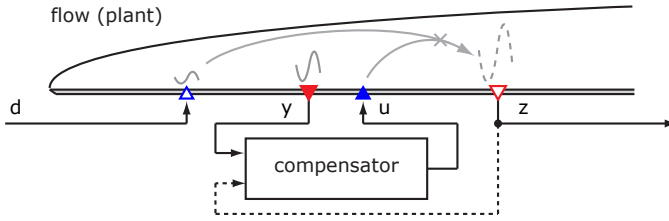


Figure 1.2: Control scheme. A 2D zero-pressure-gradient boundary layer flow is considered. The disturbance source d generates the perturbation that is attenuated downstream by the actuator u . The actuator action is based on on-line measurements by the reference sensor y and, for adaptive-control strategies, the error sensor z .

data. An example can be found in the work by Juillet *et al.* (2014), where model-identification and optimal control are used to control natural perturbations in a channel flow.

This classification holds also for the control technique. Most of the investigations along the black-box control approach are led by the experimental community; adaptive control has been largely investigated via experiments starting from Sturzebecher & Nitsche (2003) and later by many others (e.g. Kurz *et al.* 2013; Kotsonis *et al.* 2015). Between the two extremes, several intermediate *grey-box* approaches are possible, as discussed later in the outlook section of the thesis (§4).

Thesis structure. This work focuses on the comparison between the white-box and the black-box approaches. The two design philosophies are analysed and compared; in particular, the model-based linear-quadratic-Gaussian (LQG) regulator (§2.2) and the adaptive filtered-x least-mean-squares (fxLMS) algorithm (§2.3) are investigated. Their performance and limitations in attenuating 2D TS wave-packets are investigated in §2.4; the robustness properties of the adaptive approach are used to design a self-tuning compensator (§2.5), where no previous knowledge of the flow is needed to perform the control action. Lastly, a 3D disturbance and control scenario is introduced (§3.1) and the transition-delay performance is investigated. An energy budget is performed: the energy saved by the drag-reduction due to transition-delay is compared to the energy required to perform the control action (§3.3).

Control of boundary-layer instabilities

In this chapter model-based and adaptive control are presented and tested for two-dimensional (2D) disturbances in a laminar zero-pressure-gradient boundary layer flow. Performance and robustness of the two design approaches are investigated. Moreover, a self-tuning compensator is introduced in the last section of the current chapter.

The *plant* is the system that we aim to control. In this chapter, we focus on a 2D zero-pressure-gradient boundary layer flow. In the first instance, 2D disturbances are considered. This permits us to reduce the number of sensors in the flow and to introduce the control techniques that are discussed in this work in a simpler way. A three-dimensional (3D) disturbance scenario will be discussed later in §3, where the transition-delay capabilities of the proposed control set-up are discussed.

A model that describes the plant is needed. The incompressible Navier-Stokes equations govern this type of flow:

$$\frac{\partial \mathbf{u}}{\partial t} + (\mathbf{u} \cdot \nabla) \mathbf{u} = -\nabla p + \frac{1}{Re} \nabla^2 \mathbf{u} + \lambda \mathbf{u}, \quad (2.1)$$

$$\nabla \cdot \mathbf{u} = 0, \quad (2.2)$$

$$\mathbf{u}(\mathbf{x}, t)|_{\partial\Omega} = \mathbf{u}_b(\mathbf{x}), \quad (2.3)$$

$$\mathbf{u}(\mathbf{x}, 0) = \mathbf{u}_0(\mathbf{x}). \quad (2.4)$$

Velocity and pressure at position $\mathbf{x} = (X, Y)$ and time t are represented by $\mathbf{u}(\mathbf{x}, t)$ and $p(\mathbf{x}, t)$ respectively. The Reynolds number is defined as $Re = U_\infty \delta_0^* / \nu$, where U_∞ is the free-stream velocity, ν the viscosity and δ_0^* the displacement thickness in the beginning of the domain. On the boundaries $\partial\Omega$ of the computational domain Ω (see Figure 2.1), the following conditions are imposed (2.3): no-slip condition at the wall and asymptotic velocity in the upper boundary. A fringe technique is used to simulate inflow and outflow condition in the beginning and at the end of the domain (Nordström *et al.* 1999). The flow is considered periodic along the streamwise direction and a volume forcing $\lambda(\mathbf{x})\mathbf{u}(\mathbf{x}, t)$ in the last part of the domain enforces periodicity (grey region in Figure 2.1). More details can be found in Chevalier *et al.* (2007), where the pseudo-spectral DNS code used in this work is described.

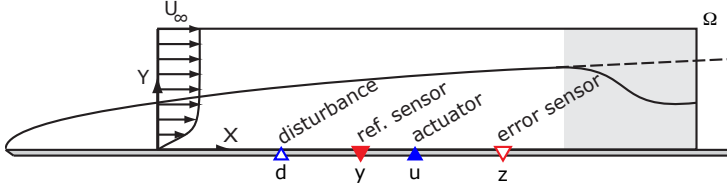


Figure 2.1: Computational domain Ω . The gray area depicts the region of the fringe forcing used to enforce the artificial periodicity in the streamwise direction.

2.1. A linear model of the flow

As we are interested in the dynamics of small disturbances, the following decomposition is introduced:

$$\mathbf{u}(\mathbf{x}, t) = \mathbf{U}(\mathbf{x}) + \epsilon \mathbf{u}'(\mathbf{x}, t), \quad (2.5)$$

$$p(\mathbf{x}, t) = P(\mathbf{x}) + \epsilon p'(\mathbf{x}, t). \quad (2.6)$$

where $\epsilon \ll 1$, $\{\mathbf{U}(\mathbf{x}), P(\mathbf{x})\}$ is the steady solution of the Navier-Stokes equations and $\{\mathbf{u}'(\mathbf{x}), p'(\mathbf{x})\}$ the perturbation. Applying this decomposition into (2.1–2.4) and neglecting the terms of order ϵ^2 and higher, the following set of linear equation is obtained:

$$\frac{\partial \mathbf{u}'}{\partial t} = -(\mathbf{U} \cdot \nabla) \mathbf{u}' - (\mathbf{u}' \cdot \nabla) \mathbf{U} - \nabla p' + \frac{1}{Re} \nabla^2 \mathbf{u}' + \lambda \mathbf{u}' + \mathbf{f}, \quad (2.7)$$

$$0 = \nabla \cdot \mathbf{u}', \quad (2.8)$$

$$\mathbf{u}'|_{\partial\Omega} = \mathbf{0}, \quad (2.9)$$

$$\mathbf{u}'(0) = \mathbf{0}. \quad (2.10)$$

The term $\mathbf{f}(\mathbf{x}, t)$ is used to model the forcing on the flow; spatial and time dependencies are decoupled as follows:

$$\mathbf{f}(\mathbf{x}, t) = \mathbf{b}_d(\mathbf{x}) d(t) + \mathbf{b}_u(\mathbf{x}) u(t). \quad (2.11)$$

Sensors are placed in the flow in order to measure the perturbation field. The measures $y(t)$ and $z(t)$ are defined by:

$$y(t) = \int_{\Omega} \mathbf{c}_y(\mathbf{x}) \cdot \mathbf{u}'(\mathbf{x}, t) \, d\Omega + n(t), \quad (2.12)$$

$$z(t) = \int_{\Omega} \mathbf{c}_z(\mathbf{x}) \cdot \mathbf{u}'(\mathbf{x}, t) \, d\Omega, \quad (2.13)$$

where the kernels $\mathbf{c}_y(\mathbf{x})$ and $\mathbf{c}_z(\mathbf{x})$ define the sensors.

In this study, a Fourier-Chebichev expansion over $N_X \times N_Y = 768 \times 101$ terms is considered. The computational domain extends over $30\delta_0^*$ in the wall normal direction and $1000\delta_0^*$ in the streamwise direction. The fringe region occupies the last $200\delta_0^*$ of the domain along the streamwise direction. The displacement thickness based Reynolds number is set to $Re = 1000$ at

the beginning of the domain and a time step $\Delta t = 0.4$ is used for the time integration. The disturbance sources are modelled as synthetic vortices (Bagheri *et al.* 2009), while the actuators are modelled as plasma actuators according to the experimental results by Kriegseis *et al.* (2013). The actuator is positioned at $X_u = 400$. The sensors mimics surface hot-wires by measuring the fluctuation in the shear stress given by the disturbance; the reference sensor y is placed at $X_y = 300$ and the error sensor z at $X_z = 500$.

Via a Galerkin projection, it is possible to transform the partial differential equation (PDE) (2.7) into an ordinary differential equation (ODE) in time (Quarteroni 2009). The Linear Time-Invariant (LTI) system that results reads:

$$\dot{\mathbf{q}}(t) = \mathbf{A} \mathbf{q}(t) + \mathbf{B}_d d(t) + \mathbf{B}_u u(t), \quad (2.14)$$

$$y(t) = \mathbf{C}_y \mathbf{q}(t) + n(t), \quad (2.15)$$

$$z(t) = \mathbf{C}_z \mathbf{q}(t), \quad (2.16)$$

where $\mathbf{q} \in \mathbb{C}^{N \times 1}$ is the state vector, $\mathbf{A} \in \mathbb{C}^{N \times N}$ is the linearised Navier-Stokes operator and $N = N_X N_Y$ is the number of degrees of freedom. The matrices $\mathbf{B}_d, \mathbf{B}_u \in \mathbb{C}^{N \times 1}$ allow the two inputs $d(t)$ and $u(t)$ to force the system. The output matrices $\mathbf{C}_y, \mathbf{C}_z \in \mathbb{C}^{1 \times N}$ filter the state $\mathbf{q}(t)$ in order to provide the output signals $y(t)$ and $z(t)$. The stochastic signal $n(t)$ represents the measurement noise that affects the output and it is usually modelled by white-noise.

Figure 2.2 reports the impulse responses for the flow case being described. The left column depicts the response of the flow to an impulse of the disturbance source: a wave packet is generated and travels downstream while growing (Figure 2.2a). The friction trace of the wave-packet is recorded by the reference sensor y (Figure 2.2c) and later by the error sensor z (Figure 2.2e). This behaviour is typical of convectively unstable flows, also known as *noise amplifiers*. This system is asymptotically stable from an input/output point of view but the perturbation grows exponentially while travelling downstream.

The convective nature of the system also leads to an important consideration about the control setup. Figure 2.2b reports the impulse response for the control input u : the wave-packet travels downstream of the actuator without being detected by the reference sensor (Figure 2.2d). Therefore, when the reference sensor y is positioned upstream the actuator, the setup results in a feed-forward control scheme, as in the current setup. Different relative positions of the actuator have been investigated by Belson *et al.* (2013); the feedback configuration – i.e. reference sensor downstream of the actuator – shows better robustness but lower performance with respect to the current feed-forward configuration. However, the feedback configuration requires the reference sensor to be very close to the actuator. Since plasma actuators are considered, this configuration is unrealistic, because of the eventual electrical interference between the sensor and the actuator.

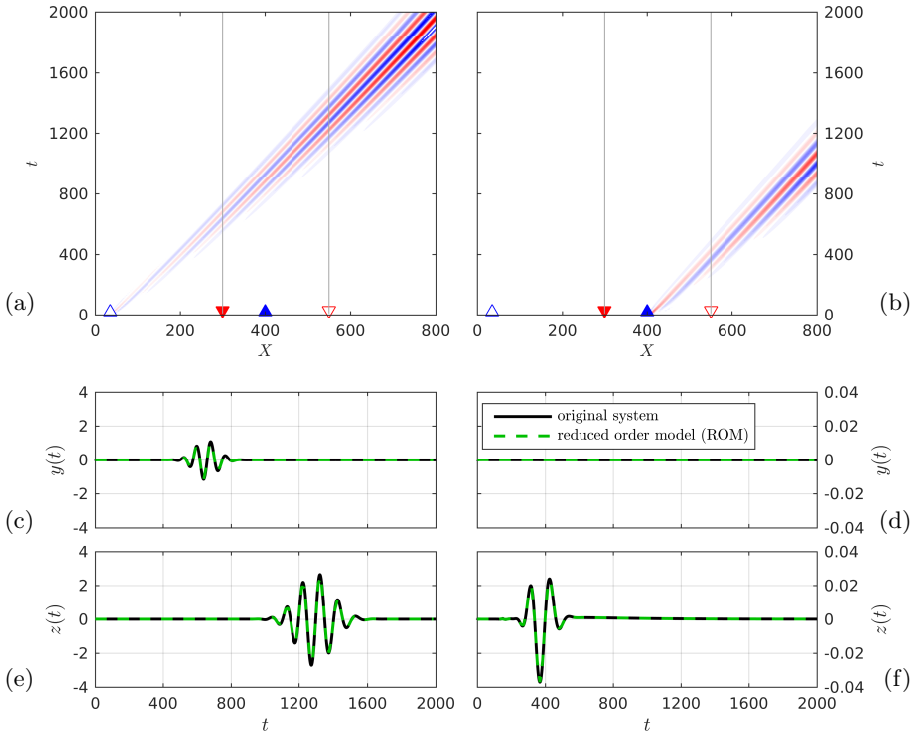


Figure 2.2: The colored areas report the friction footprint of the wavepacket generated by the disturbance source (a) and the plasma-actuator (b); red indicates positive fluctuations, while blue negative. The black lines in (c-f) report the impulse response from each input to each output for the considered flow-case. The green dashed lines report the impulse response of the reduced order model.

2.1.1. Finite Impulse Response (FIR) representation

Some control techniques relax the knowledge of the plant to its input/output (I/O) relations only. The forced response of an LTI system to a generic input signal $u(t)$ can be written as:

$$z(t) = \mathbf{C}_z e^{\mathbf{A}t} \mathbf{q}_0 + \int_0^t \mathbf{C}_z e^{\mathbf{A}\tau} \mathbf{B}_u u(t - \tau) d\tau. \quad (2.17)$$

If the system is stable, for large enough t , the first term goes to zero and the system response depends only on the forcing $u(t)$:

$$z(t) = \int_0^t \mathbf{C}_z e^{\mathbf{A}\tau} \mathbf{B}_u u(t - \tau) d\tau = \int_0^t P_{zu}(\tau) u(t - \tau) d\tau \quad (2.18)$$

where P_{zu} is the convolution kernel. The kernel is able to describe completely the I/O relation between the input $u(t)$ and the output $z(t)$.

The time-discrete counterpart of (2.18) is of particular interest when it comes to control techniques. The time-discrete output signal $z(n) = z(n\Delta t)$ is computed as a linear combination of the time-discrete history of the input signal $u(n) = u(n\Delta t)$:

$$z(n) = \sum_{j=0}^n P_{zu}(j) u(n-j). \quad (2.19)$$

Since the system is stable, the convolution kernel goes to zero as the shifting index i grows: this allows us to truncate the sum at an appropriate time $N_{zu}\Delta t$. Hence, the signal $z(n)$ can be obtained by the finite sum:

$$z(n) \approx \sum_{j=0}^{N_{zu}} P_{zu}(j) u(n-j). \quad (2.20)$$

The expression (2.20) is called Finite Impulse Response (FIR) filter.

The I/O relation $u \rightarrow z$ can thus be described by a finite number of coefficients $P_{zu}(i)$. These coefficients can be computed starting from a linear model of the flow, as the one provided by (2.14–2.16), or identified based on experimental data by dedicated algorithms, e.g. least-mean-squares (LMS). For more information, we refer to Paper 1.

2.1.2. Reduced Order Model (ROM)

Other control techniques require the direct knowledge of the system matrices \mathbf{A} , \mathbf{B} and \mathbf{C} . An example is the linear quadratic Gaussian (LQG) regulator that will be introduced in §2.2.1: this control technique requires the solution of a Riccati equation, whose computational cost is proportional to N^3 , where $N = N_X N_Y$ is the number of degrees of freedom of the system describing the plant (2.14). Due to the high computational cost, handling large systems may lead to a very expensive design process and, eventually, to the impossibility of computing the control gains. Hence, system-reduction techniques applied to the Navier-Stokes linear operator are widely used to obtain smaller – and more manageable – systems that can reproduce the I/O behaviour of the flow (Rowley 2005; Kim & Bewley 2007; Bagheri *et al.* 2009c; Ilak *et al.* 2010). The reduced order system reads:

$$\dot{\mathbf{q}}_r(t) = \mathbf{A}_r \mathbf{q}_r(t) + \mathbf{B}_{r,d} d(t) + \mathbf{B}_{r,u} u(t), \quad (2.21)$$

$$y(t) = \mathbf{C}_{r,y} \mathbf{q}_r(t) + n(t), \quad (2.22)$$

$$z(t) = \mathbf{C}_{r,z} \mathbf{q}_r(t), \quad (2.23)$$

where $\mathbf{A}_r \in \mathbb{R}^{N_r \times N_r}$ is the ROM state matrix, $\mathbf{q}_r(t) \in \mathbb{R}^{N_r \times 1}$ is the state vector, $\mathbf{B}_{r,d}, \mathbf{B}_{r,u}, \mathbf{C}_{r,y}^T, \mathbf{C}_{r,z}^T \in \mathbb{R}^{N_r \times 1}$ are the I/O matrices and $N_r \ll N$.

In this study, the Eigensystem Realization Algorithm (ERA) is used to provide a reduced-order model (ROM) (Juang & Pappa 1985). This algorithm

builds a realisation of an LTI system that mimics the I/O behaviour of the original system starting from its impulse responses from each input to each output, see Figure 2.2. This method is equivalent to a projection of the full system $\{\mathbf{A}, \mathbf{B}, \mathbf{C}\}$ on the set of its N_r most energetic balanced proper-orthogonal-decomposition (BPOD) modes (Moore 1981; Bagheri *et al.* 2009). Note that also in this approach only the I/O behaviour of the system is known. Since the transformation between the original system and the reduced order one remains unknown, the original state \mathbf{q} can not be reconstructed starting from the reduced state \mathbf{q}_r . From a control point of view this is not necessary: the control algorithm needs only a limited knowledge of the system and, in particular, only a reliable model of the transfer functions between its inputs and outputs.

The model-reduction procedure implies information loss, that eventually leads to an error: this error can be estimated *a priori* and related to the size of the ROM (Moore 1981). This estimation can be used to choose the ROM size in order to bound the error by a given tolerance: for the current problem, the ROM size $N_r = 112 \ll N$ is chosen in order to limit the relative model-reduction error below 10^{-7} .

2.2. Model based control

The compensator is the system that interacts with the plant via its control inputs and outputs in order to pilot it at the desired state. In this brief review, we will focus on a linear compensator, i.e. a compensator that can be represented by a linear dynamical system. If the system that describes the compensator is time-invariant, the compensator is called static: the compensator is designed a-priori, usually based on a model of the system, and then it is connected to the plant. If the response of the compensator, instead, can be modified on-line, the compensator is called adaptive.

This section investigates compensators that are based on a model of the plant; the model can be either numerical (Bewley & Liu 1998; Bagheri & Henningson 2011; Semeraro *et al.* 2013, e.g.) or experimentally identified (Juillet *et al.* 2014) and it is used to compute the response of the actuator. Typical examples are Model Predictive Control (MPC) and the linear Quadratic Gaussian (LQG) regulator, discussed hereafter.

2.2.1. Linear Quadratic Gaussian (LQG) regulator

The LQG regulator design is based on a complete model of the plant, Figure 2.3. It results in an LTI system that mimics the plant in order to compute the control signal $u(t)$, given the measurement signal $y(t)$ as an input. The compensator reads:

$$\dot{\hat{\mathbf{q}}}_r(t) = (\mathbf{A}_r + \mathbf{L}\mathbf{C}_{r,y}) \hat{\mathbf{q}}_r(t) + \mathbf{B}_{r,u} u(t) - \mathbf{L}y(t), \quad (2.24)$$

$$u(t) = \mathbf{K} \hat{\mathbf{q}}_r(t), \quad (2.25)$$

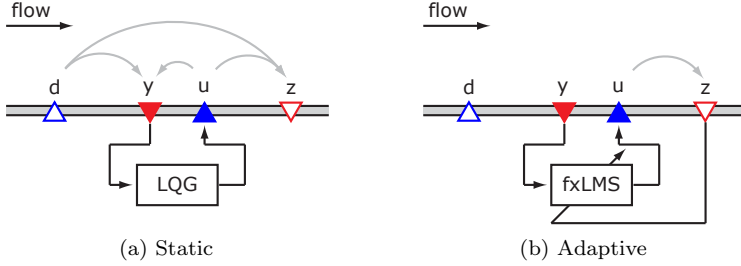


Figure 2.3: Compensator schemes for static (LQG) and adaptive (fxLMS) strategies. An adaptive scheme may also use the error signal $z(t)$ to adapt to the current flow conditions. The grey lines indicate the I/O relations required to be modelled by each strategy.

where $\hat{\mathbf{q}}_r(t) \in \mathbb{R}^{N_r \times 1}$ is the compensator state vector. The subscript r refers to the Reduced Order Model (ROM) of the flow discussed in §2.1.2. The compensator is composed of two parts: the observer (2.24) and the controller (2.25). The former filters the measurement signal $y(t)$ by the estimation gain matrix $\mathbf{L} \in \mathbb{R}^{N_r \times 1}$ and reconstructs an estimation $\hat{\mathbf{q}}_r(t)$ of the state of the controlled system $\mathbf{q}_r(t)$. The latter computes the control signal filtering the estimated state $\hat{\mathbf{q}}_r(t)$ and the control-gain matrix $\mathbf{K} \in \mathbb{R}^{1 \times N_r}$.

2.2.1.1. Observer: Kalman filter

The observer is designed to minimise the covariance of the difference between the plant state \mathbf{q}_r and the estimated state $\hat{\mathbf{q}}$ when the system is excited by an unknown white-noise signal $d(t)$. To do this, the observer uses the measurement $y(t)$ affected by an error $n(t)$, also modelled as white noise, and the control signal $u(t)$. The minimization procedure leads to:

$$\mathbf{L} = -\mathbf{Y}\mathbf{C}_{r,y}^H R_n^{-1}, \quad (2.26)$$

where $\mathbf{Y} \in \mathbb{R}^{N_r \times N_r}$ is the solution of the following Riccati equation:

$$\mathbf{A}_r \mathbf{Y} + \mathbf{Y} \mathbf{A}_r^H - \mathbf{Y} \mathbf{C}_{r,y}^H R_n^{-1} \mathbf{C}_{r,y} \mathbf{Y} + \mathbf{B}_{r,d} R_d \mathbf{B}_{r,d}^H = \mathbf{0}. \quad (2.27)$$

The parameters R_d and R_n are the expected variances of the disturbance signal $d(t)$ and measurement noise signal $n(t)$.

2.2.1.2. Controller: Linear Quadratic Regulator (LQR)

LQR design relies on the knowledge of the state \mathbf{q}_r , or its estimation $\hat{\mathbf{q}}_r$. The procedure is based on the minimization of a quadratic cost-function \mathcal{N} based on the error-sensor measurements $z(t)$ and on the control signal $u(t)$:

$$\mathcal{N} = \int_0^\infty z(t) w_z z(t) + u(t) w_u u(t) dt. \quad (2.28)$$

The ratio between the control-strength parameter w_u and the performance parameter w_z allows the design of a controller capable of attenuating the disturbances in the system, while limiting the control effort. The minimisation procedure leads to the control law in (2.25) where the control-gain matrix is defined as:

$$\mathbf{K} = -w_u^{-1} \mathbf{B}_{r,u}^H \mathbf{X}. \quad (2.29)$$

The matrix $\mathbf{X} \in \mathbb{R}^{N_r \times N_r}$ is the solution of the Riccati equation:

$$\mathbf{A}_r^H \mathbf{X} + \mathbf{X} \mathbf{A}_r - \mathbf{X} \mathbf{B}_{r,u} w_u^{-1} \mathbf{B}_{r,u}^H \mathbf{X} + \mathbf{C}_{r,z}^H w_z \mathbf{C}_{r,z} = \mathbf{0}. \quad (2.30)$$

Note that the controller design is completely independent of the observer design and vice-versa. This is commonly known as the *separation principle* (Glad & Ljung 2000).

2.3. Adaptive control

In an adaptive control method the compensator adjusts on-line its response in order to optimise its performance: the compensator adjustment is achieved by monitoring its performance and, based on that, the correction is computed. A typical example of this kind of compensator is the filtered-x least-mean-squares (fxLMS) algorithm, investigated by Sturzebecher & Nitsche (2003) and Kurz *et al.* (2013) to attenuate 2D disturbances in a boundary-layer flow.

2.3.1. Filtered-x Least-Mean-Squares (fxLMS) algorithm

The fxLMS algorithm relies on a minimisation procedure that is performed on-line. This allows the algorithm to use the actual measurements from the flow, giving this method the adaptive features that characterise it.

The compensator is a linear system. As seen in §2.1.1 for the plant, a linear system can be represented both in state-space form (like the LQG regulator in the previous section) or by a Finite Impulse Response (FIR) filter. This control technique uses the latter representation and the control signal is given by:

$$u(n) = \sum_{i=1}^{N_K} K(i) y(n-i) \quad (2.31)$$

where $u(n) = u(n \Delta t)$ and $y(n) = y(n \Delta t)$ are the time-discrete representations of the time-continuous signals $u(t)$ and $y(t)$ and Δt is the sampling time step. The N_K coefficients $K(i)$ constitute the kernel of the filter and they are related to the impulse response of the compensator. These coefficients are updated at each time step in order to satisfy the minimisation problem,

$$\min_{K(i)} z^2(n), \quad (2.32)$$

via a steepest-descend algorithm. The resulting updating law is:

$$K(i|n+1) = K(i|n) + \mu z(n) \sum_{j=1}^{N_{zu}} P_{zu}(j) y(n-i-j). \quad (2.33)$$

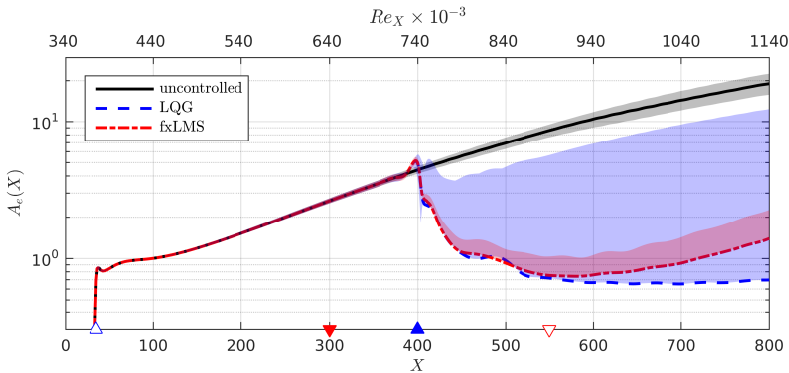


Figure 2.4: TS amplitude $A_e(X)$. The lines report the performances of the two compensators at design condition. The shaded regions indicate the performance variation when the asymptotic velocity is changed in a $\pm 5\%$ range with respect to the design condition.

Note that the knowledge of the plant is limited to the time-discrete kernel $P_{zu}(i)$ that describes the I/O relation $u \rightarrow z$. This transfer function is commonly called *secondary path* (Sturzebecher & Nitsche 2003).

2.4. Controlled system

When the disturbance source is fed with uniform white-noise, it creates a train of wave packets that travels downstream while growing in amplitude. A time-averaged measure of the disturbance amplitude A_e is defined:

$$A_e^2(X) = \int_0^{L_Y} \left\langle \left(\frac{u'}{\bar{U}} \right)^2 \right\rangle_t dY, \quad (2.34)$$

where L_Y is the wall-normal size of the computational box. The solid line in Figure 2.4 reports this quantity for the uncontrolled case; the amplitude of the perturbation grows exponentially throughout the domain and is increased by a factor of 25 at the end of the domain.

An LQG regulator is designed; the relative weight w_u/w_z for the LQR controller is set to 0.1, as the disturbance-noise ratio R_n/R_d for the Kalman filter. The dashed line in Figure 2.4 shows the disturbance amplitude for the LQG controlled case: the perturbation is attenuated downstream of the actuator and continues to decay downstream of the error sensor. Hence, the disturbance is attenuated by a factor of 35 with respect to the uncontrolled case in the end of the domain.

The adaptive fxLMS algorithm is capable of comparable performances, as shown by the dot-dashed line in Figure 2.4. The disturbance amplitude is effectively reduced downstream of the actuator but not completely cancelled as

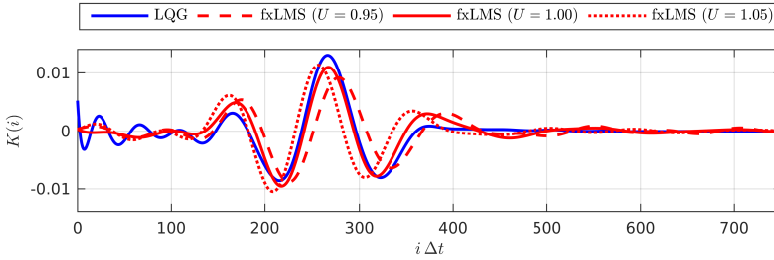


Figure 2.5: Control kernels $K(i)$. LQG and fxLMS solutions to the control problem are reported for different free-stream conditions.

in the LQG case. The wave-packets, in fact, start growing again downstream of the error sensor, resulting in a lower attenuation at the end of the domain.

The main strength of the adaptive algorithm is revealed when the external conditions are changed with respect to the design point. The coloured areas in Figure 2.4 indicate the performance variation if the free-stream velocity varies between $0.95 U$ and $1.05 U$, where U refers to the design condition. The LQG regulator loses almost all its performance, while the fxLMS performance is only marginally effected by the change in the free-stream condition. The adaptive algorithm acts on the control law in order to adjust to the changed condition and to compensate for the modified phase-shift and amplification of the perturbation. This can also be seen in the control kernels reported in Figure 2.5: the peak position and magnitude is modified for different flow condition to maintain the compensator performance. Further details about LQG and fxLMS sensitivity to changes in the free-stream condition can be found in Paper 1 and Paper 2.

2.4.1. Wind-tunnel experiments

Wind-tunnel experiments are conducted to investigate the robustness of model-based and adaptive control (Paper 2). The control of a zero-pressure-gradient boundary-layer over a flat-plate is investigated in the open-loop wind tunnel at TU Darmstadt. In the current setup, two-dimensional TS wave-packets are generated by 16 wall-mounted loudspeakers and a DBD plasma actuator is used to perform the control action. The control-sensors are flush-mounted surface hot-wires. Additionally, a boundary-layer hot-wire probe is mounted on a traverse system to measure the perturbation amplitude at different streamwise locations.

An LQG compensator is designed based on DNS simulations matching the experimental set-up and the measured performance matches the simulated behaviour of the control. Figure 2.6 reports the control performance for a 200 Hz TS-wave, i.e. a non-dimensional frequency $F = 2\pi\nu/U^2 f \approx 100$ (Schmid & Henningson 2001): the amplitude is attenuated downstream of the control region as predicted by the DNS simulation; Figure 2.6b-c shows the streamwise

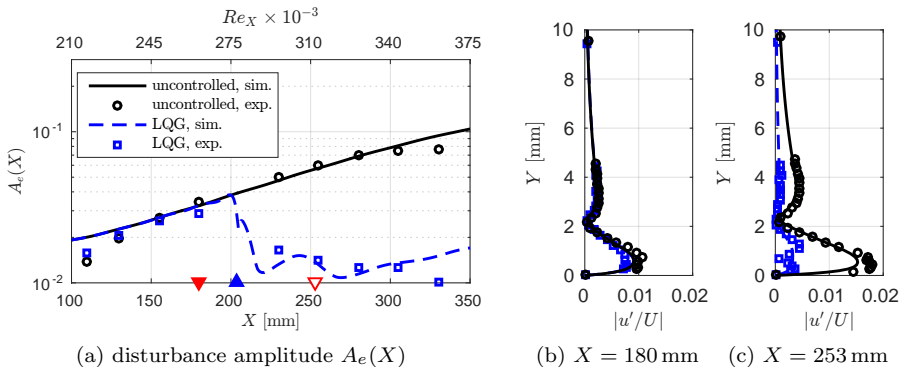


Figure 2.6: TS-wave amplitude for a disturbance frequency $f = 200$ Hz. Lines and circles depict simulated and experimental data, respectively. (a) shows the integral TS-wave amplitude A_e as a function of the streamwise position, respectively. (b) and (c) show the TS-wave shape at reference and error sensor location.

perturbation velocity as a function of the wall-normal position. The reported values are normalised by the free-stream velocity $U_\infty = 12$ m/s. The TS-wave is attenuated along all the wall-normal direction, and not only in the wall-region. This confirms the choice of the surface hot-wires sensors for estimating the performance of the actuator; in fact, a reduction of the perturbation amplitude in the wall region corresponds to an attenuation of the perturbation also farther away from the wall.

When the free-stream condition is changed, the LQG compensator shows in the experiments the same robustness issues that are highlighted by the simulation: the control rapidly loses performance as the free-stream velocity differs from the design-condition. The adaptive fxLMS algorithm is implemented to improve the robustness of the control strategy, showing the same properties observed in simulations.

2.5. A self-tuning compensator

In the previous section, it was shown how the fxLMS algorithm is able to compensate model inaccuracies and provide an effective control action. This property can be used for two different purposes: (i) enhancing the robustness of the control strategy §2.4, (ii) simplifying the model of the flow. An example of the latter is the delayed-x least-mean-squares (dxLMS) algorithm, where the secondary path P_{zu} is approximated by a time delay.

This is possible because of the convective nature of the TS-wave instability. The wave-packet, in fact, travels with a specific *group speed* c_g (Schmid & Henningson 2001). Therefore, a third sensor p is introduced upstream of the reference sensor y at $X_p = 250$ (Figure 2.7a); this sensor is used to evaluate the group speed at the beginning of the control region via the correlation R_{py}

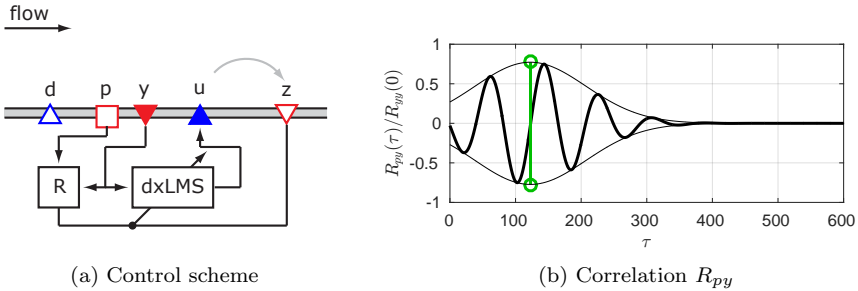


Figure 2.7: dxLMS control algorithm. A third sensor p is introduced in order to estimate the wave-packet group speed via the correlation R_{ppy} . The grey line indicates the I/O relation required to be modelled by the control strategy, i.e. the secondary path P_{zu} .

between the two measurement signals:

$$R_{py}(\tau) = \frac{1}{T} \int_{-T/2}^{+T/2} p(t - \tau) y(t) dt, \quad (2.35)$$

where T is the signal length. The maximum of the envelope of the correlation identifies the time $\bar{\tau}_{py}$ that it takes for the wave-packet to travel from the sensor p to the sensor y (Figure 2.7b). Hence, an approximation of the group-speed is computed as:

$$\bar{c}_g = \frac{X_y - X_p}{\bar{\tau}_{py}}. \quad (2.36)$$

where X_y and X_p are the streamwise position of phase and reference sensors. The time delay to be used in the secondary-path modelling is given by:

$$\bar{\tau}_{uz} = \frac{X_z - X_u}{\bar{c}_g} = \frac{X_z - X_u}{X_y - X_p} \bar{\tau}_{py}. \quad (2.37)$$

This estimation of the time-delay is based on the reasonable assumption that the group speed is constant throughout the control region (Paper 3; Li & Gaster 2006). The resulting time-delay model of the secondary path is reported in Figure 2.8a; It can be seen that the identified time-delay predictably falls in the middle of the trace of the wave-packet generated by the actuator.

Better insight into this approximation is given by the Bode diagram of the real and modelled secondary path. The two secondary paths are very different in magnitude (Figure 2.8b): the time-delay has a flat gain – i.e. amplifies each frequency by the same factor – while the real secondary path amplifies only the frequencies associated to an unstable TS-wave. The LMS algorithm, however, is not sensitive to this type of inaccuracies.

The stability limitation of the LMS algorithm is given by phase-errors only; this algorithm is, in fact, able to compensate a phase error up to $\pm\pi/2$ with

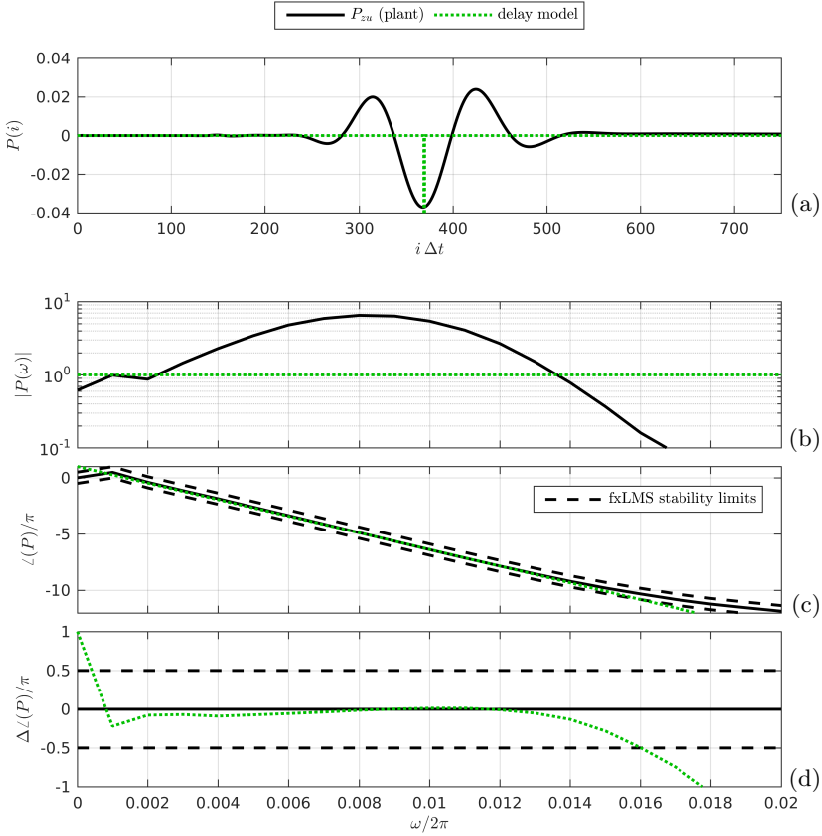


Figure 2.8: Secondary path. The solid black line in (a) depicts the real secondary path of the plant, while the dotted green line shows the time-delay approximation used by the dxLMS algorithm. Magnitude and argument of the real secondary path and the delay model are reported in (b-c). The phase error is shown in (d) for the time delay approximation with respect to the real secondary path. The dashed lines indicate the stability limit for the LMS algorithm.

respect to the real secondary path of the system (Snyder & Hansen 1994). For this reason, it is important that the phase is well approximated by the time-delay model. Figure 2.8c shows that the time delay gives a good approximation of the phase for all the frequencies that are amplified by the flow. This can be better seen in Figure 2.8d where the phase error is reported; the error stays inside the algorithm stability limits for all the amplified frequencies.

The performance given by the approximated secondary path is very close to the one given by the full model (Figure 2.9). The two techniques converge to almost the same kernel solution; the dxLMS with delay-identification has the

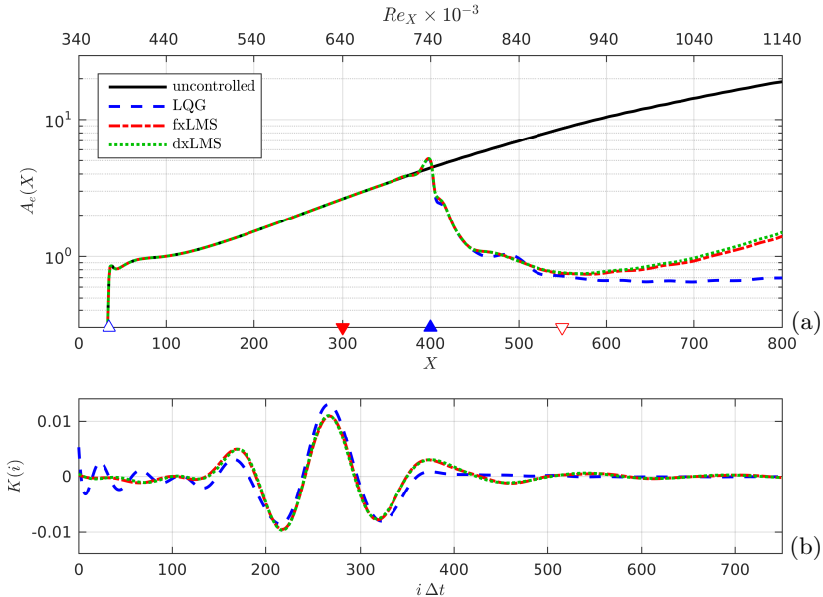


Figure 2.9: dxLMS performance. The lines in (a) report the performances of dxLMS approach compared to LQG and fxLMS. The control kernels that result from the three different compensator-design approaches are shown in (b).

so-called self-tuning property, i.e. “*under certain condition [...] the controller converges eventually to the one that could be designed if the process model was known a priori*” (Åström et al. 1977). Further information about this approach can be found in Paper 3.

2.5.1. In-flight experiments

A set-up similar to the one used in wind-tunnel experiments (§2.4.1) is used for in-flight investigations in collaboration with TU Darmstadt. A motor-glider Grub G109b is used for the experimental campaign; the right wing of the glider is equipped with a natural laminar flow (NLF) airfoil wind glove, where the experimental equipment is mounted. Sensors and actuators are installed on a flush-mounted plexiglass plate on the pressure side of the wing. The flat airfoil shape in this region creates an almost linear pressure gradient which is adjustable between moderate positive and negative values, depending on the angle of attack. The flight condition is monitored by an environmental data acquisition set-up on the left wing; flight velocity, angle of attack and side-slip angle are measured by a Prandtl tube and a wind vane mounted on a boom protruding upstream into the flow. All the measurements are collected with the engine turned off and the propeller feathered, i.e. when the aircraft is in glider-mode.

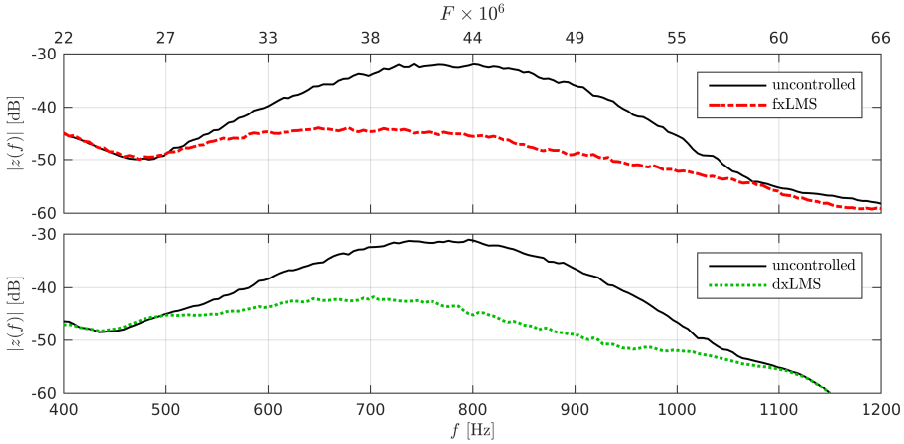


Figure 2.10: Control performance for fxLMS and dxLMS algorithm at an angle of attack $\alpha = 3^\circ$. The spectra show the signal reduction at position of the error sensor z .

The self-tuning dxLMS compensator introduced in §2.5 is tested and compared with the fxLMS algorithm. The two control approaches are equivalent, if the phase error is inside the stability region for the LMS algorithm. Figure 2.10 shows the control performance as measured by the error sensor z : the two compensators behave similarly and disturbance-attenuation is achieved in the TS-region of the signal spectrum. The difference between the two graphs is caused by the change in altitude during the different measurement runs; hence, a direct comparison is not possible since the change in density and viscosity slightly changes the flow condition and, therefore, the TS-wave amplification and phase.

Transition delay

In the previous chapter the assumption of a purely 2D flow has been made to simplify the study. This permitted to easily highlight advantages and disadvantages of the investigated control techniques. However, in real environments this assumption is far from reasonable. For this reason, it is necessary to address the control problem allowing a disturbance to develop in three dimensions.

The numerical and experimental work by Li & Gaster (2006) falls into this framework: the control of 3D disturbances via opposition control by using a linear model of the flow based on the Navier-Stokes equations. In the work by Semeraro *et al.* (2013), a LQG regulator is designed to control a single 3D wave-packet via localised sensors and actuators. All the sensors and actuators are connected to each other by the compensator. This leads to a prohibitive increase of the compensator complexity if a large spanwise portion of the flow is meant to be controlled. In the recent work presented in Paper 4, the possibility to limit the number of interconnections between sensors and actuators is investigated by dividing them in equal sets along the spanwise direction, each commanded by one compensator. This structure, called *control units*, is thus replicated along the spanwise direction in order to fill the entire domain.

The study presented in this chapter is a further development of this idea (Paper 5). However, the modularity of the control action is not based on an a-priori division in control units but rather on considerations about the control kernel. A distributed 3D disturbance field is generated using a spanwise row of independent random forcings d (Figure 3.1), generating a complex, 3D, random pattern of disturbances. The control action is performed by a row of equispaced actuators forcing the flow in the proximity of the wall. Similar to the 2D case, their action $u_l(t)$ is computed based on the measurements $y_m(t)$ by a row of sensors upstream the actuators; for this set-up the number of sensors is equal to the number of actuators and they are positioned aligned with the flow direction (Figure 3.2).

This control approach is able to delay the laminar-to-turbulence transition and, consequently, provide drag-reduction with respect to the uncontrolled case (Paper 5). Moreover, the saved power due to drag reduction is compared to the power that is needed to perform the control action (§3.3). In order to compute the latter, ideal as well as real actuator models are considered.

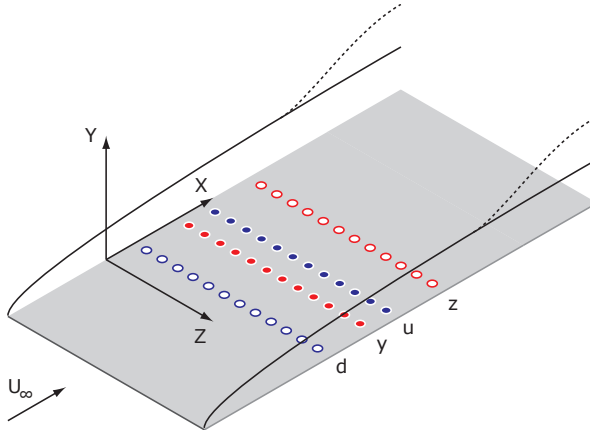


Figure 3.1: 3D control set-up. Random 3D disturbances are generated by a row of localised independent forcings d . The measurements from the sensors y and z are used to compute the actuation signal for the actuators u .

3.1. A 3D compensator

A linear control law is assumed:

$$u_l(n) = \sum_m \sum_i K_{ml}(i) y_m(n-i) \quad \forall l, \quad (3.1)$$

where $K_{ml}(i) \in \mathbb{R}^{M \times M}$ is the convolution kernel of the compensator. As a consequence, the number of transfer functions between the M sensors y_m and the M actuators u_l is M^2 . This imposes a computational constraint when M is large, which is the case when covering a large spanwise region with the controller. However, since the flow is spanwise homogeneous, the same transfer function K_m from all the sensors y_{m+l} to one arbitrary actuator u_l is replicated for each actuator u_m , as shown in Figure 3.2. This assumption reduces the number of transfer functions to be designed from M^2 to M . Hence, the Finite Impulse Response (FIR) filter representation of the control law reads:

$$u_l(n) = \sum_m \sum_i K_m(i) y_{m+l}(n-i) \quad \forall l \quad (3.2)$$

where one kernel dimension is suppressed and, as a consequence, $K_m(i) \in \mathbb{R}^{M \times 1}$.

3.1.1. Multi-input multi-output (MIMO) *fxLMS*

A multi-input multi-output (MIMO) version of the *fxLMS* algorithm introduced in §2.3.1 is used to dynamically design the compensator. The algorithm

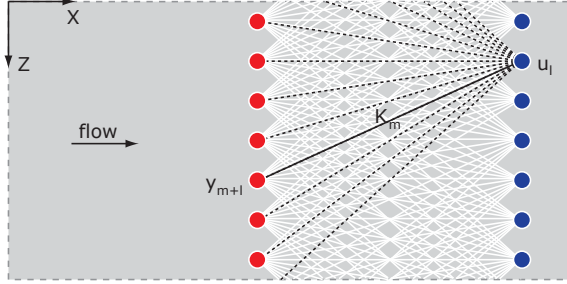


Figure 3.2: Compensator structure. The action of each actuator u_l is computed by filtering the signals from all the sensor $y_m + l$ via a linear filter K_m .

minimises the sum of the squared measurement signals $z_l(n)$:

$$\min_{K_m} \left(\sum_l z_l^2(n) \right). \quad (3.3)$$

The kernel is updated via a steepest descent algorithm at each time step:

$$K_m(i|n+1) = K_m(i|n) - \mu \lambda_m(i|n). \quad (3.4)$$

where the descend direction $\lambda_m(j|n)$ is given by:

$$\lambda_m(i|n) = \frac{\partial (\sum_l z_l^2(n))}{\partial K_m(i)} = 2 \sum_l z_l(n) \frac{\partial z_l(n)}{\partial K_m(i)}. \quad (3.5)$$

The error sensor signal is given by the superposition of the contributions given by the disturbance sources d_l and the actuators u_l :

$$\begin{aligned} z_l(n) &= \sum_r \sum_j P_{zd,r}(j) d_{r+l}(n-j) + \sum_r \sum_j P_{zu,r}(j) u_{r+l}(n-j) = \\ &= [\dots] + \sum_r \sum_j P_{zu,r}(j) \sum_m \sum_i K_m(i) y_{m+r+l}(n-j-i) = \\ &= [\dots] + \sum_m \sum_i K_m(i) \sum_r \sum_j P_{zu,r}(j) y_{r+m+l}(n-j-i) = \\ &= [\dots] + \sum_m \sum_i K_m(i) f_{m+l}(n-i), \end{aligned} \quad (3.6)$$

where the same spanwise homogeneity assumption has been made for the plant kernels $P_{zd,r}(j)$ and $P_{zu,r}(j)$ that represent the transfer functions $d_r \rightarrow z_l$ and $u_r \rightarrow z_l$ respectively. Therefore, the descend direction is given by:

$$\lambda_m(i|n) = 2 \sum_l z_l(n) \frac{\partial z_l(n)}{\partial K_m(i)} = 2 \sum_l z_l(n) f_{m+l}(n-i). \quad (3.7)$$

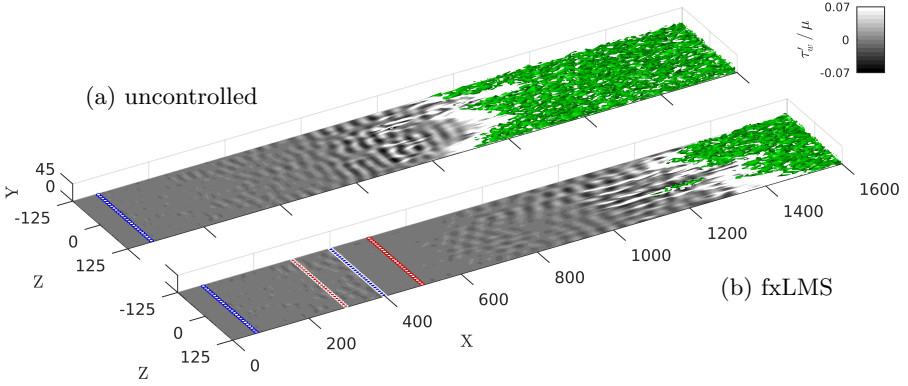


Figure 3.3: Disturbance attenuation and transition delay. The shaded gray area report the skin friction fluctuations $\tau'_w = \tau_w - \tau_{w,lam}$ with respect to the laminar solution. The green surfaces indicate the λ_2 -criterion with a threshold of -2×10^{-3} . The disturbance sources are fed with white-noise signals that range between $\pm 2 \times 10^{-3}$, resulting in a perturbation amplitude $A(100) = 0.11\%$. The fringe region is not shown.

This expression – except for the sum over the index l – is similar to the expression of $\lambda(i|n)$ in the 2D case in (2.33).

3.2. Performance and limitations

Non-linear simulations are performed in a 3D extension of the domain used in the previous section. The domain extents are $[0, 2000] \times [0, 45] \times [-125, 125]$ in the streamwise, wall-normal and spanwise directions. The fringe forcing used to enforce the streamwise periodicity takes place in the last 400 spatial units along the streamwise direction (Chevalier *et al.* 2007). The flow is approximated by 1536×384 Fourier modes along the streamwise and spanwise direction and by 151 Chebyshev polynomials in the wall-normal direction. The time step Δt is set to 0.4 as in the previous 2D study. Turbulence will appear in the end of the domain. Since the focus is on laminar-to-turbulence transition and not on turbulence itself, a deconvolution model is used for large-eddy simulations (LES) to avoid increasing the spatial resolution (Stolz *et al.* 2001).

The perturbation is introduced at $X = 65$ via the following volume forcing:

$$\mathbf{f}_d = \sum_l \mathbf{b}_{d,l}(\mathbf{x}) d_l(t). \quad (3.8)$$

The 25 forcing shapes $\mathbf{b}_{d,l}$ are equally-spaced along the spanwise direction and are modelled as synthetic vortices and each disturbance signal $d_l(t)$ is a uniformly-distributed white-noise signal that ranges between $\pm a_d$ (Fabbiane

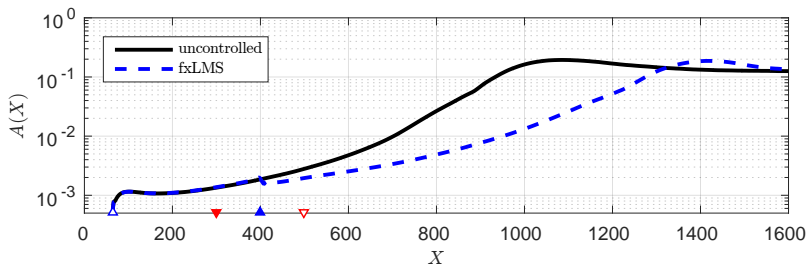


Figure 3.4: Perturbation attenuation and transition delay. The amplitude of the perturbation field as defined in (3.9) is reported as a function of the streamwise coordinate X for the controlled and uncontrolled cases in Figure 3.3.

et al. 2015a, Paper 5). Reference and error sensors y_l and z_l are positioned at $X_y = 300$ and $X_z = 500$ with the same spanwise spacing $\Delta Z = 10$ as the disturbance sources. As in the previous section, the sensors measure the shear-stress fluctuation of the perturbation field averaged, in this case, over the spanwise extension of the sensor ΔZ . The actuators are positioned at $X_u = 400$ and are spaced along Z as the sensors. They are modelled by a modulated volume forcing similar to the disturbance sources; the forcing shapes are computed in order to model a plasma actuator, based on the experimental data by (Kriegseis *et al.* 2013).

The disturbance sources are fed with white-noise signals with amplitude $a_d = 2 \times 10^{-3}$. A snapshot of the resulting flow is shown in Figure 3.3a: the grey shaded area reports the skin friction fluctuation with respect to the laminar solution, while isosurfaces of $\lambda_2 = -2 \times 10^{-3}$ are depicted in green (Jeong & Hussain 1995). The random forcing triggers a pattern of random wave-packets that travel downstream in the domain while growing in amplitude, as it can be seen by their friction footprint. At $X = 900$ the flow departs from the laminar solution and the turbulent structures identified by the λ_2 -criterion appear. This is the TS-wave driven transition to turbulence, cfr. §1.1.

Figure 3.3b reports the same disturbance scenario when the control is active. The perturbation is almost completely cancelled downstream of the actuators, as it can be seen by the friction fluctuations. The same transition scenario is present but moved downstream with respect to the uncontrolled case. The control is effective in delaying the laminar-to-turbulence transition.

A measurement of the perturbation field amplitude is introduced to quantitatively assess the control action:

$$A^2(X) = \max_Y \left\langle \left(\frac{u - U}{U} \right)^2 \right\rangle_{Z,t}, \quad (3.9)$$

where $U(X, Y, Z)$ is the streamwise component of the mean flow. Figure 3.4 reports the amplitude values for the controlled and uncontrolled cases illustrated in Figure 3.3. The two curves depart from each other directly downstream of

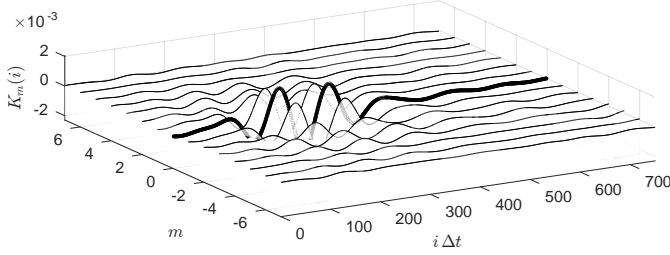


Figure 3.5: Control kernel. The thick line indicates $K_0(t)$, i.e. the connection between sensors and actuators at the same spanwise location.

the actuators; the uncontrolled case saturates first around the uncontrolled transition location, while the controlled case shows a lower disturbance amplitude up to its transition location. The perturbation field is hence attenuated by the control action.

The kernel that results from the MIMO fXLMS dynamic design is shown in Figure 3.5: the solid thick line depicts $K_0(i)$, i.e. the connection between sensors and actuators at the same spanwise position. The kernel is similar to the 2D solution in the previous chapter and it has a compact support along the spanwise direction; hence, each sensor drives a limited number of actuators, that does not depend by the distance between sensors and actuators (Fabbiane *et al.* 2015a).

In order to better evaluate the effect of the control on the friction drag, the spanwise averaged friction coefficient is introduced as:

$$c_f(X) = \frac{\langle \tau_w \rangle_Z}{\frac{1}{2} \rho U^2}, \quad (3.10)$$

where $\langle \cdot \rangle_Z$ is the spanwise average operator. The friction coefficient for the current flow case is shown in Figure 3.6a for both the controlled and uncontrolled cases. In the controlled case the transition is simply delayed without introducing any additional friction with respect to the laminar solution. Hence, the spatial delay of the transition is directly related to the drag-save resulting from applying the control (Paper 5).

The disturbance amplitude is then increased up to the point where no residual effect of the control is visible. Figure 3.6b shows the transition location as a function of the disturbance amplitude; the perturbation field amplitude at $X = 100$ is used as a measure of the amplitude of the disturbance. The transition point is identified as the point where the friction coefficient crosses the average between the laminar and the turbulent value of the friction coefficient, dot-dashed line in Figure 3.6a. The control is effective up to a seeded perturbation amplitude $A(100) = 0.40\%$, that rises up to approximately 2% at the actuator location.

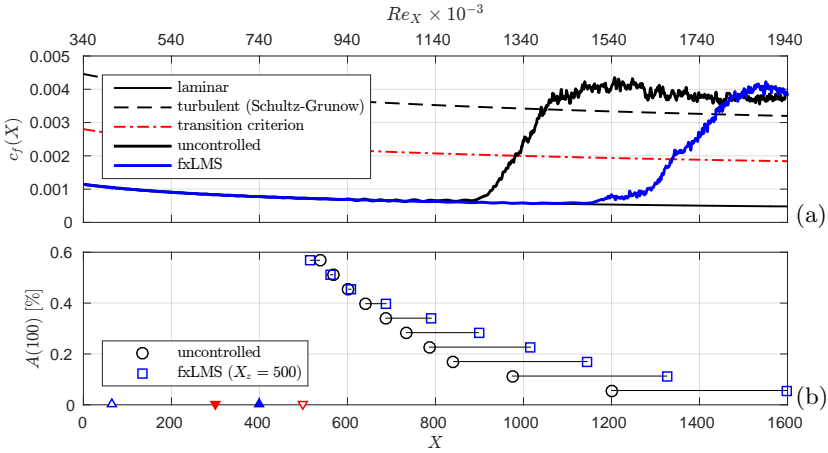


Figure 3.6: Transition delay. (a) reports the Z -averaged friction coefficient for the flow case in Figure 3.3, $A(100) \approx 0.12\%$. (b) reports the transition location for increasing disturbance amplitude $A(100)$. The transition positions are computed based on a time-averaged flow over 1200 time units.

3.3. Energy budget

A control strategy is successful when its benefit is larger than its cost. Hence, the power consumption of the control P_c is estimated via two different actuator models: the ideal actuator and the plasma actuator. The ideal actuator is based on the fluid-dynamical power that the volume forcing exchanges with the flow; this ideal actuator, however, does not take into consideration the energy spent in order to create the volume forcing given by the actuator. A model of the plasma-actuator power consumption is obtained by combining the two experimental works by Kriegseis *et al.* (2011, 2013). Two different operation modes are considered: (i) *dual* where two plasma actuators are considered, one responsible for the positive forcing and one for the negative one, and (ii) *hybrid* where an offset forcing is used in order to avoid negative forcing by the actuator. Further details about this procedure can be found in Paper 5.

The power gain is defined as:

$$\Gamma = \frac{P_s}{P_c}, \quad (3.11)$$

where $P_s = U \Delta D$ is the power saved by the drag-reduction ΔD that results from applying the control. Figure 3.7 shows Γ for the different actuator models as a function of the disturbance amplitude. In the ideal case the control strategy is capable of power gains up to 10^3 . This means that the power saved is 1000 times the power that is spent to perform the control action. For increasing amplitudes, the gain decreases until the break-even point $\Gamma = 1$ is reached for

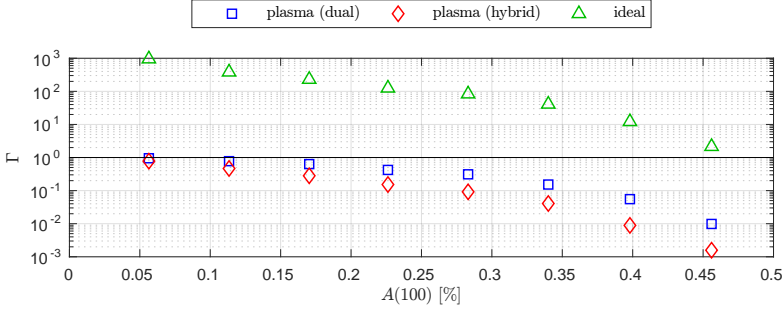


Figure 3.7: Energy budget. The reported quantities are computed based on a time-averaged flow over 1200 time units. The solid black line indicates $\Gamma = 1$, i.e. the break-even point for the control strategy.

$A(100) = 0.46\%$. At this point the control is on the limit of its effective range and it is not effective in delaying the transition any more, cfr. Figure 3.6b.

Unfortunately, the power-gain Γ barely reaches the break-even point when a plasma actuator model is considered; a reason for this can be found in the lower efficiency of the plasma actuator (Jolibois & Moreau 2009; Cattafesta & Sheplak 2010). The results by Kriegseis *et al.* (2011) are based on research studies on plasma actuators at the time and no new data on the state-of-the-art is available in the literature. These results highlight that the energy efficiency of the plasma actuator is critical to its use for this type of control. However, this is not a rejection of this type of actuator; this preliminary estimation of the energy consumption by a real actuator has to be considered as an invitation for the scientific community to improve the design of plasma actuators.

Conclusions and outlook

Linear reactive control of boundary-layer instabilities has been addressed. The model-based control – more precisely LQG regulator – is able to attenuate the perturbation amplitude by using the knowledge of the flow status close to the wall. Because of the relative position of sensors and actuators, the control law results in a feed-forward wave-cancellation. For this technique, an accurate model of the perturbation behaviour is crucial to performance; it is in fact shown that, when model inaccuracies occur, the compensator performance rapidly degrades (Paper 2).

Robustness to model inaccuracies is recovered via adaptive control (Paper 1; Paper 2). The perturbation attenuation is monitored on-line by a second sensor downstream of the actuator and the control law is modified in order to maximize the performance. This approach gives the compensator a feed-back not directly on its action but on the validity of its control law. A recovery in robustness to model inaccuracies is shown by the fxLMS adaptive algorithm.

A self-tuning approach is proposed based on this algorithm. The modelling requirement by fxLMS are reduced to a time-delay that is computed by measuring the phase speed upstream the actuator via a third sensor. The performance of the compensator is unchanged by this model approximation both in DNS and in in-flight experiments (Paper 3).

Transition delay is achieved in a low-amplitude 3D disturbance scenario (Paper 5). The consequent drag-reduction is computed and an energy budget is performed: the power saved thanks to the delay of the laminar-to-turbulence transition is three orders of magnitude larger than the ideal power spent to perform the required forcing to control the flow.

For increasing disturbance levels, non-linear interactions arise in the flow. Since the compensator assumes a linear behaviour of the perturbation field, it gradually reduces its performance because its perturbation model fails with respect to the actual flow conditions. No transition-delay and energy-saving are achieved for perturbation amplitudes greater than 2% of the free-stream velocity. If the fxLMS algorithm is used, the adaptivity nature of the algorithm is able to marginally compensate the non-linearities in the flow.

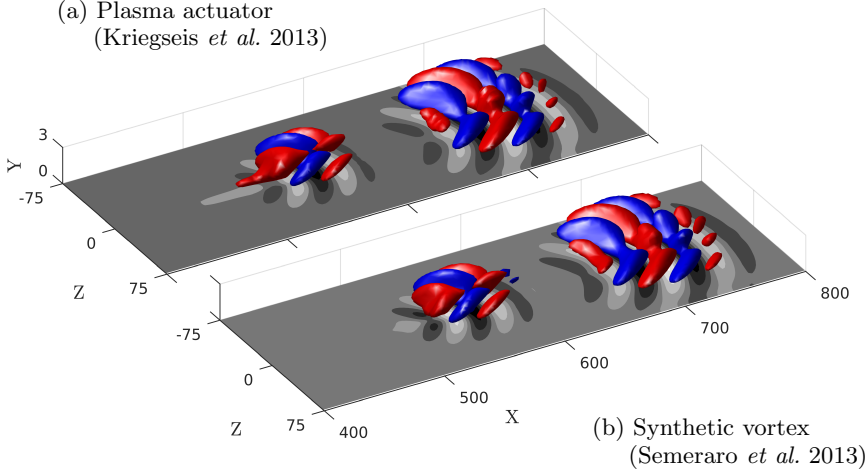


Figure 4.1: Actuator impulse response. Isosurfaces of positive and negative perturbation velocity are depicted in red and blue. The generated wave-packets are reported at $t = 400$ and $t = 800$; even if the two volume forcings are different, the resulting wave-packets are almost identical.

Actuator

The net-energy-saving of the control set-up depends on the actuator and its efficiency. The theoretical results are obtained for an ideal actuator model (Paper 5); this actuator presents a unitary efficiency, i.e. the supplied energy is transferred to the flow with no losses. Real actuators behave differently: the supplied energy is not entirely transferred to the flow and part of it is lost in the forcing process. For plasma actuators this energy loss is considerable (Jolibois & Moreau 2009) and may invalidate the control performance. This confirms the overall energy-saving based on the plasma actuator model by Kriegseis *et al.* (2011); this estimation confirms the need to improve the design of these actuators in order to improve their energy-efficiency.

It is also possible to consider different types of actuators (Cattafesta & Sheplak 2010). In this case, the control takes place by wave-packet superposition: the actuator generates a wave-packet with opposite phase to the one that is detected by the reference sensors and, therefore, the original disturbance is cancelled. In the light of this, every actuator that is able to produce a TS wave-packet is suitable for the presented control approach. Figure 4.1 shows, as an example, the impulse response for two different volume forcings used for flow control by Semeraro *et al.* (2013) and Paper 5, respectively; the final wave-packet is almost identical. This leads to two conclusions: (i) it is the effect of an actuator that is important to model, and not the actuator itself (Bagheri 2010) and (ii) many different actuators may be equally suitable for reactive control.

Disturbance

In this work, the disturbances are introduced directly inside the boundary layer (Bagheri *et al.* 2009a; Semeraro *et al.* 2011, 2013). The receptivity process of free-stream disturbances is then modelled by assuming it will result in TS wave-packets. This assumption is valid for various disturbance scenarios (Saric *et al.* 2002): free-stream disturbances interacting with surface roughness (Goldstein 1985) or sound waves interacting with the leading-edge (Giannetti & Luchini 2006; Shahriari *et al.* 2016). However, TS wave-packets are not the only perturbations that populate the boundary layer: in presence of high free-stream turbulence, streaks are induced inside the boundary layer (Matsubara & Alfredsson 2001) and structures different from TS-waves may also appear in a linear framework (Dadfar *et al.* 2014).

This suggests further investigation of the presented control approach when the disturbance is introduced outside of the boundary-layer. Since the leading-edge has a crucial role in the receptivity process, a full flat-plate/wing geometry has to be taken into consideration for these investigations, e.g. the DNS set-up in Paper 3. This may lead to computationally challenging simulations, in particular if a 3D computational box is considered in order to evaluate the transition-delay. An example of the required simulation set-up can be found in Hosseini *et al.* (2013), where boundary-layer stabilisation by roughness elements is studied under a free-stream turbulence forcing.

Control algorithm

The two design approaches presented in this work – although effective for the investigated control problem – cover only a part of the possible control techniques used in flow control. Figure 4.2 is a complete schematic of the most popular control techniques used in fluid-dynamics (Brunton & Noack 2015). The proposed model-based approach combines a linear reduced-order-model obtained via BPOD and \mathcal{H}_2 optimal control (§2.2.1), while the adaptive fxLMS algorithm can be seen both as opposition and extremum-seeking control (§2.3.1).

These two design approaches result in a linear compensator: the control signal is linearly dependent on the time history of the reference signal through the control kernel, that is computed based on a linear model of the system. The compensator uses the model to predict the control effect on the system. When non-linearities arise, the model fails, its prediction is not reliable and, therefore, the compensator fails at controlling the flow. Adaptive control can be used to partially recover the control performance; the fxLMS algorithm, for example, shows the ability to compensate for small non-linearities. However, since its adaptation path is also based on a linear model of the flow, the adaptation fails when the flow behaviour is *too* non-linear.

The performance of the control is model dependent. Enhancing the model complexity and/or robustness may result in an extension of the compensator performance-envelope: non-linear models (Noack *et al.* 2003), system identification (Hervé *et al.* 2012) and dynamic observers (Guzmán Iñigo *et al.* 2014) are

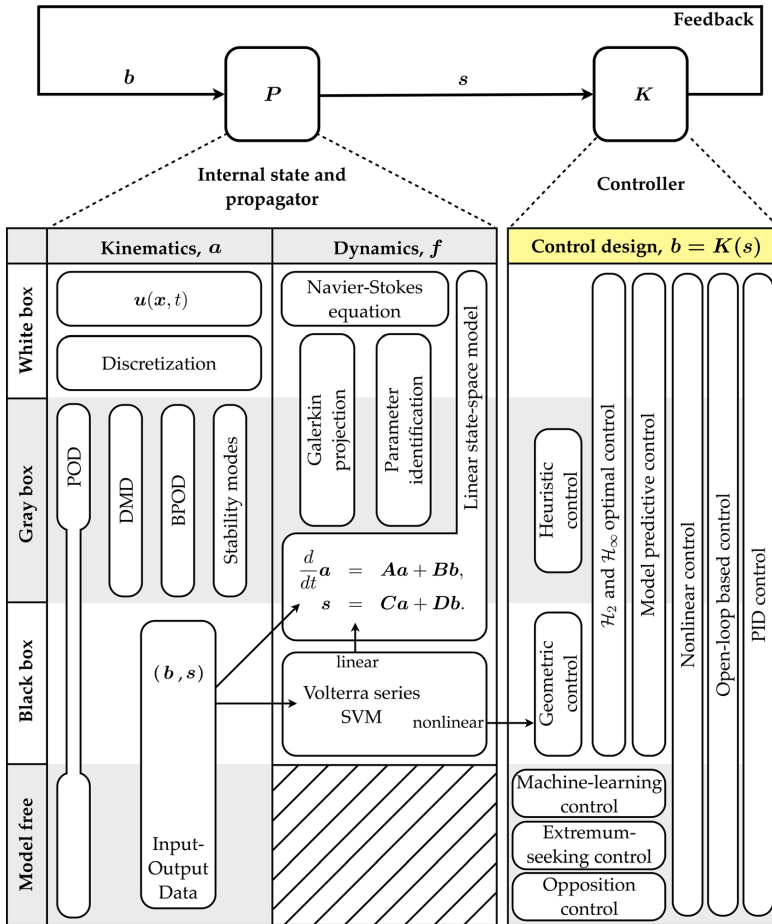


Figure 4.2: Schematic illustrating popular choices at the various levels of kinematic and dynamic descriptions of the turbulent system P and choices for designing the controller K . (Courtesy of Steven L. Brunton and Bernd R. Noack.)

an example of this. In this direction, the past decade saw a growing interest in data-driven techniques (Fleming & Purshouse 2002), in particular in model free-approaches as machine-learning control. These techniques learn about the system behaviour by observing it and build input-output maps that are used to perform the control action. They are very powerful when no reliable model of the system is available a-priori, or when it comes to turbulence control – i.e. chaotic systems – since they are able to follow the chaotic-attractor dynamics modified by the control itself. However, their validity envelope depends on the extent of their training; uncertainties of the environmental condition and/or the presence of unmodelled disturbances may still present a robustness problem.

Acknowledgements

Stockholm, 16 May 2016

Today I send my PhD thesis for print, and I turn thirty.

As every n -tieth birthday, it leads to an balance about the past and a view into the future. Considering the PhD defence coming in four weeks, I must say this is one of the most important birthdays in my life.

I remember when I understood that science would have been part of my life; I was in middle school and Mr. Ballarini – my maths teacher – was giving us a written test. For me, it was like playing and I wanted to continue that game. The years passed and, in high school, Ms. Maffezzoli explained to me that the game I loved could also be used to predict complicated physical phenomena: skidding cars, flying bullets, bouncing objects and more. The maths became more and more complicated and, because of that, more and more fun.

The decision to study engineering came naturally and my passion for aviation brought me to aeronautics. I wanted to design airplanes structures. As always, never be sure about anything in your life: the first fluid dynamics course by Dr. Quartapelle made me realize that structures are overrated and fluids are where the fun is. Hence, I took my Master in fluid dynamics. When the time came for a thesis, most of my friends were looking at industry: for me it was different, I wanted to take that last chance of discovering something new and not simply designing something discovered by someone else. I asked Maurizio¹ for a thesis topic and we wrote a DNS code.

It was still not enough and I wanted to continue doing what a very good friend of mine describes as “*sempre meglio che lavorare*”².

This took me here, to KTH. I thank Prof. Dan Henningson for giving me the opportunity to show him he was right about hiring me. I hope I succeeded. I would also like to thank Dr. Shervin Bagheri – my co-advisor – for his guidance throughout my doctoral studies and Dr. Ardeshir Hanifi for his contagious laugh and his indisputable style. A special thank goes to Onofrio, now Dr.

¹Prof. Maurizio Quadrio.

²Transl.: “[it is and will] always [be] better than working”.

Semeraro; he was – and still is – a good mentor and a great friend to me. I am very thankful for that.

Since I moved to Stockholm in the Swedish spring of 2012, I met a lot of people who accompanied me during these last few years. I first want to mention Cristina, my *sister-in-Sweden*; she listened to me complaining about everything, mostly girls I dated, girls I would have liked to date, and girls who did not want to date me. Remember I did the same for you. I thank my friends Michele, Paola, Marta, Karin and Chiara for enjoying Stockholm and its beauty with me. I also thank all my colleagues in particular Elektra³, Jacopo³, Alexandra, Mattias, Clio, Nima, Taras, Armin, Iman, Luca and Ellinor. With them I spent endless nights in photography museums without looking at a single picture, smoked pipe till late looking at the city skyline, travelled by boat to different countries, learned how to properly dance Ukrainian and Persian style. They made the office not only a nice place to work but also a nice place to be.

This project gave me the opportunity to travel around the world. In particular, I will always remember my visit at TU Darmstadt; I thank Prof. Sven Grundmann and Bernhard Simon for the fruitful collaboration and for showing me in the real world what I only dared to simulate.

My deepest gratitude goes to all my friends I left in Italy when I moved to Sweden: they never denied me their support, despite the geographical distance. Above all, I would like to thank Alberto, Agnese and their little daughter Alice for making me feel like I never left, every time I visit them.

Last, but not least, I would like to thank my grandparents, who can not read English but will nevertheless understand how grateful I am to them, and my parents: my mother for her unconstrained love and support, and my father for making me look at the stars in the sky with curiosity.

Thank you.

Nicolò

³Thank you also for proofreading this manuscript.

Bibliography

- ÅSTRÖM, K. J., BORISSON, U., LJUNG, L. & WITTENMARK, B. 1977 Theory and applications of self-tuning regulators. *Automatica* **13** (5), 457–476.
- BAGHERI, S. 2010 Analysis and control of transitional shear flows using global modes. PhD thesis, KTH, Stockholm.
- BAGHERI, S., AKERVIK, E., BRANDT, L. & HENNINGSON, D. S. 2009*a* Matrix-Free Methods for the Stability and Control of Boundary Layers. *AIAA J.* **47**, 1057–1068.
- BAGHERI, S., BRANDT, L. & HENNINGSON, D. S. 2009*b* Input–output analysis, model reduction and control of the flat-plate boundary layer. *J. Fluid Mech.* **620** (1), 263–298.
- BAGHERI, S. & HENNINGSON, D. S. 2011 Transition delay using control theory. *Philos. Trans. R. Soc.* **369**, 1365–1381.
- BAGHERI, S., HÖPFFNER, J., SCHMID, P. J. & HENNINGSON, D. S. 2009*c* Input-Output Analysis and Control Design Applied to a Linear Model of Spatially Developing Flows. *Appl. Mech. Rev.* **62**.
- BARBAGALLO, A., SIPP, D. & SCHMID, P. J. 2009 Closed-loop control of an open cavity flow using reduced order models. *J. Fluid Mech.* **641**, 1–50.
- BELSON, B. A., SEMERARO, O., ROWLEY, C. W. & HENNINGSON, D. S. 2013 Feedback control of instabilities in the two-dimensional Blasius boundary layer: The role of sensors and actuators. *Phys. Fluids* **25**.
- BEWLEY, T. R. & LIU, S. 1998 Optimal and Robust Control and Estimation of Linear Paths to Transition. *J. Fluid Mech.* **365**, 305–349.
- BLASIUS, H. 1908 Grenzschichten in Flüssigkeiten mit kleiner Reibung. *Z. Angew. Math. Phys.* **56** (1), 1–37.
- BRUNTON, S. L. & NOACK, B. R. 2015 Closed-loop turbulence control: Progress and challenges. *Applied Mechanics Reviews* **67** (5), AMR–14–1091.
- CATTAFESTA, L. N. & SHEPLAK, M. 2010 Actuators for Active Flow Control. *Ann. Rev. Fluid Mech.* **43**, 247–272.
- CHEVALIER, M., SCHLATTER, P., LUNDBLADH, A. & HENNINGSON, D. S. 2007 A pseudo-spectral solver for incompressible boundary layer flows. *Tech. Rep. TRITA-MEK 2007:07*. KTH Mechanics, Stockholm, Sweden.
- DADFAR, R., HANIFI, A. & HENNINGSON, D. S. 2014 Feedback control for laminarization of flow over wings. *Flow, Turb. and Comb.* **94** (1), 43–62.
- DUGUET, Y., SCHLATTER, P. S., HENNINGSON, D. S. & ECKHARDT, B. 2012 Self-sustained localized structures in a boundary-layer flow. *Phys. Rev. Lett.* **108**, 044501.

- FABBIANE, N., BAGHERI, S. & HENNINGSON, D. S. 2015 Adaptive control of finite-amplitude 3D disturbances in 2D boundary-layer flows. In *Proceedings of TSFP-9*. Melbourne.
- FLEMING, P. J. & PURSHOUSE, R. C. 2002 Evolutionary algorithms in control systems engineering: a survey. *Control engineering practice* **10** (11), 1223–1241.
- GIANNETTI, F. & LUCHINI, P. 2006 Leading-edge receptivity by adjoint methods. *J. Fluid Mech.* **547**, 21–53.
- GLAD, T. & LJUNG, L. 2000 *Control Theory*. London: Taylor & Francis.
- GOLDSTEIN, M. E. 1985 Scattering of acoustic waves into tollmien-schlichting waves by small streamwise variations in surface geometry. *Journal of Fluid Mechanics* **154**, 509–529.
- GUZMÁN IÑIGO, J., SIPP, D. & SCHMID, P. J. 2014 A dynamic observer to capture and control perturbation energy in noise amplifiers. *Journal of Fluid Mechanics* **758**, 728–753.
- HENNINGSON, D. S., LUNDBLADH, A. & JOHANSSON, A. V. 1993 A mechanism for bypass transition from localized disturbances in wall-bounded shear flows. *Journal of Fluid Mechanics* **250**, 169–207.
- HERVÉ, A., SIPP, D., SCHMID, P. J. & SAMUELIDES, M. 2012 A physics-based approach to flow control using system identification. *Journal of Fluid Mechanics* **702**, 26–58.
- HOSSEINI, S. M., TEMPELMANN, D., HANIFI, A. & HENNINGSON, D. S. 2013 Stabilization of a swept-wing boundary layer by distributed roughness elements. *Journal of Fluid Mechanics* **718**, R1.
- ILAK, M., BAGHERI, S., BRANDT, L., ROWLEY, C. W. & HENNINGSON, D. S. 2010 Model Reduction of the Nonlinear Complex Ginzburg-Landau Equation. *SIAM J. Appl. Dyn. Sys.* **9** (4), 1284–1302.
- JEONG, J. & HUSSAIN, F. 1995 On the identification of a vortex. *Journal of Fluid Mechanics* **285**, 69–94.
- JOLIBOIS, J. & MOREAU, E. 2009 Enhancement of the Electromechanical Performances of a Single Dielectric Barrier Discharge Actuator. *IEEE Transactions on Dielectrics and Electrical Insulation* **16** (3), 758–767.
- JUANG, J.-N. & PAPPAS, R. S. 1985 An eigensystem realization algorithm for modal parameter identification and model reduction. *J. Guid., Con. Dyn.* **8** (5), 620–627.
- JUILLET, F., MCKEON, B. J. & SCHMID, P. J. 2014 Experimental Control of Natural Perturbations in Channel Flow. *J. Fluid Mech.* **752**, 296–309.
- KACHANOV, Y. S. 1994 Physical mechanisms of laminar-boundary-layer transition. *Annual review of fluid mechanics* **26** (1), 411–482.
- KIM, J. & BEWLEY, T. R. 2007 A Linear Systems Approach to Flow Control. *Ann. Rev. Fluid Mech.* **39**, 39–383.
- KOTSONIS, M., SHUKLA, R. K. & PRÖBSTING, S. 2015 Control of Natural Tollmien-Schlichting Waves using Dielectric Barrier Discharge Plasma Actuators. *Intl J. of Flow Control* **7** (1-2), 37–54.
- KREILOS, T., KHAPKO, T., SCHLATTER, P., DUGUET, Y., HENNINGSON, D. S. & ECKHARDT, B. E. 2015 Bypass transition and spot nucleation in boundary layers. *Phys. Rev. Fluids* (under review).
- KRIEGSEIS, J., MÖLLER, B., GRUNDMANN, S. & TROPEA, C. 2011 Capacitance and

- power consumption quantification of dielectric barrier discharge (DBD) plasma actuators. *Journal of Electrostatics* **69** (4), 302–312.
- KRIEGSEIS, J., SCHWARZ, C., TROPEA, C. & GRUNDMANN, S. 2013 Velocity-Information-Based Force-Term Estimation of Dielectric-Barrier Discharge Plasma Actuators. *J. Phys. D* **46** (5), 055202.
- KURZ, A., GOLDIN, N., KING, R., TROPEA, C. D. & GRUNDMANN, S. 2013 Hybrid Transition Control Approach for Plasma Actuators. *Exp. Fluids* **54** (11), 1–4.
- LI, Y. & GASTER, M. 2006 Active Control of Boundary-Layer Instabilities. *J. Fluid Mech.* **550**, 185–205.
- MATSUBARA, M. & ALFREDSSON, P. H. 2001 Disturbance growth in boundary layers subjected to free-stream turbulence. *J. Fluid Mech.* **430**, 149–168.
- MOORE, B. 1981 Principal Component Analysis in Linear Systems: Controllability, Observability, and Model reduction. *IEEE Trans. Autom. Control* **26** (1), 17–32.
- NOACK, B. R., AFANASIEF, K., MORZYNSKI, M., TADMOR, G. & THIELE, F. 2003 A hierarchy of low-dimensional models for the transient and post-transient cylinder wake. *J. Fluid Mech.* **497**, 335–363.
- NORDSTRÖM, J., NORDIN, N. & HENNINGSON, D. S. 1999 The fringe region technique and the Fourier method used in the direct numerical simulation of spatially evolving viscous flows. *SIAM J. Sci. Comp.* **20** (4), 1365–1393.
- QUARTERONI, A. 2009 *Numerical Models for Differential Problems*. Springer.
- ROWLEY, C. W. 2005 Model reduction for fluids, using balanced proper orthogonal decomposition. *Intl J. of Bifurcation and Chaos* **15** (03), 997–1013.
- SARIC, W. S., REED, H. L. & KERSCHEN, E. J. 2002 Boundary-layer Receptivity to Freestream Disturbances. *Ann. Rev. Fluid Mech.* **34** (1), 291–319.
- SCHMID, P. J. & HENNINGSON, D. S. 2001 *Stability and Transition in Shear Flows. Applied Mathematical Sciences* v. 142. Springer-Verlag.
- SEMERARO, O., BAGHERI, S., BRANDT, L. & HENNINGSON, D. S. 2011 Feedback control of three-dimensional optimal disturbances using reduced-order models. *J. Fluid Mech.* **677**, 63–102.
- SEMERARO, O., BAGHERI, S., BRANDT, L. & HENNINGSON, D. S. 2013a Transition delay in a boundary layer flow using active control. *J. Fluid Mech.* **731** (9), 288–311.
- SEMERARO, O., PRALITS, J. O., ROWLEY, C. W. & HENNINGSON, D. S. 2013b Riccati-less approach for optimal control and estimation: an application to two-dimensional boundary layers. *J. Fluid Mech.* **731**, 394–417.
- SHAHRIARI, N., BODONY, D., HANIFI, A. & HENNINGSON, D. 2016 Acoustic receptivity simulations of flow past a flat plate with elliptic leading edge. *J. Fluid Mech.* (submitted).
- SHARMA, A. S., MORRISON, J. F., MCKEON, B. J., LIMEBEER, D. J. N., KOBERG, W. H. & SHERWIN, S. J. 2011 Relaminarisation of $Re_\tau = 100$ channel flow with globally stabilising linear feedback control. *Physics of Fluids* **23** (12).
- SNYDER, S. D. & HANSEN, C. H. 1994 The effect of transfer function estimation errors on the filtered-x LMS algorithm. *IEEE Transactions on Signal Processing* **42** (4), 950–953.
- STOLZ, S., ADAMS, N. A. & KLEISER, L. 2001 The approximate deconvolution model for large-eddy simulations of compressible flows and its application to shock-turbulent-boundary-layer interaction. *Phys. Fluids* **13**, 2985.

- STURZEBECKER, D. & NITSCHKE, W. 2003 Active cancellation of Tollmien–Schlichting instabilities on a wing using multi-channel sensor actuator systems . *Intl J. Heat and Fluid Flow* **24**, 572–583.
- WIENER, N. 1961 *Cybernetics or Control and Communication in the Animal and the Machine*. MIT press.

Part II

Papers

Summary of the papers

Paper 1

Adaptive and model-based control theory applied to convectively-unstable flows

A review of the control methodologies aimed at delaying the laminar-to-turbulent transition in convectively unstable flows is presented. A simple one-dimensional system – the Kuramoto-Sivashinsky (KS) equation – able to replicate the stability of this type of flows is introduced to illustrate the different techniques via applied-control examples.

The compensator design is investigated as a coupling of a controller and an estimator. The former is responsible for computing the control signal assuming a complete knowledge of the system state. Optimal control techniques are reviewed: Linear Quadratic Regulator (LQR) and Model Predictive Control (MPC) are examined, in particular when saturation constraints are applied to the actuator. The estimator provides to the controller an estimation of the system state based on limited measurements in the flow. The conventional Kalman filter is introduced as well as system identification techniques borrowed from signal-processing theory.

In the end, the complete compensator is analysed. The difference between static (LQG) and adaptive (fxLMS) compensators is investigated, highlighting a strong sensitivity of the static controller to inaccuracies of the model used in the design process.

Scripts to generate all the presented data and figures are available in MATLAB format at <http://www.mech.kth.se/~nicolo/ks/>.

Paper 2

On the role of adaptivity for robust laminar-flow control

The control problem is addressed in an experimental set-up in order to investigate the necessity of adaptivity in real flow applications. An fxLMS adaptive compensator is compared with a model-based LQG regulator when attenuating 2D TS-waves in a zero-pressure-gradient boundary layer flow.

The experiments are conducted in the open-circuit wind tunnel at TU Darmstadt, Germany. A 2D disturbance is generated by a disturbance source and is downstream detected by a surface-mounted hot-wire sensor. Based on

these measurements, the compensator prescribes a suitable forcing to a dielectric-barrier-discharge (DBD) plasma actuator in order to cancel the upcoming wave. A second hot-wire sensor is placed farther downstream to monitor the compensator performance. DNS of the experimental set-up are carried out and, based on these, the LQG regulator is designed.

The model-based regulator is found to be less effective than the fxLMS compensator because of unavoidable modelling inaccuracies. Moreover, the performance of the LQG regulator degrades as the flow response departs from the design model. In particular, free-stream velocity variation is investigated: the static compensator turns out not to be able to prescribe the correct phase information to the actuator. Otherwise, the adaptive compensator is able to autonomously adjust to the modified flow conditions and effectively perform the control action for a broader interval of velocity variations.

Paper 3

In-flight active-wave-cancellation via delayed-x-LMS control algorithm in a laminar boundary layer

The adaptive control techniques investigated in Paper 2 are pushed towards a black-box approach. In particular, the stability properties of the fxLMS algorithm are used to further simplify the model of the flow and design a self-tuning compensator.

The secondary path – i.e. the transfer function between actuator and error sensor – is modelled by a time-delay only. This control technique, that is known as delayed-x LMS (dxLMS) algorithm, is successfully tested in cancelling 2D TS-waves in-flight; the experiment is set on a motor-glider Grub G-109 at TU Darmstadt. The set-up is similar to that in Paper 2: the disturbance is artificially generated by a row of 12 loudspeakers and it is detected downstream by the reference sensor, a surface hot-wire. Hence, the control action is performed by a wall-mounted DBD plasma-actuator. A second surface hot-wire is mounted farther downstream, to provide the performance information needed by the adaptive algorithm.

The time-delay for the secondary path modelling is computed via a measurement of the perturbation group speed. A third sensor is positioned upstream of the reference sensor for this purpose. This allows the design of a self-tuning controller that needs no external information about the flow; the resulting “black-box” approach is to be considered a big step forward towards a real application of this control technique.

Paper 4

Centralised versus decentralised active control of boundary layer instabilities

The control of 3D disturbances in a zero-pressure-gradient boundary-layer flow is addressed via model-based optimal control. In particular, this work focuses

on the possibility to divide and replicate the control law along the homogeneous span-wise direction in order to reduce the complexity of the controller.

DNS are performed to investigate the control performance. Evenly localised objects are distributed in the spanwise direction in the wall region (18 disturbances sources, 18 actuators, 18 estimation sensors and 18 objective sensors) and span-wise subsets of these objects are identified by signal-energy based techniques. LQG compensators are designed based on these subsets and replicated along the span-wise direction to fill the computational domain. Hence, the performance loss due to the missing connections are evaluated in order to identify a “minimal” control unit, i.e. a minimal subset of sensors and actuators able to perform an effective control action.

Paper 5

Energy efficiency and performance limitations of linear adaptive control for transition delay

Transition-delay and energy-saving capabilities of reactive flow control are investigated. A MIMO fxLMS algorithm is introduced in order to control a 3D disturbance scenario in a 2D zero-pressure-gradient boundary-layer flow.

Random disturbances are introduced in the flow via localised volume forcing inside the boundary layer. The compensator performance is evaluated for increasing disturbance level; the investigated control setup results able to delay the laminar-to-turbulence transition up to the point where transition occurs in the control region.

The energy efficiency is also evaluated: ideal as well as real actuators models are considered in order to compute the power needed to perform the control action. When ideal actuators are considered, a net-energy-saving up to 1000 times the power spent for the control is recorded and the balance remains positive as long as transition delay is achieved. However, when plasma actuators are considered, the break-even point is barely reached because of their low efficiency. This result should motivate further studies on the design and optimisation of these type of actuators.

Paper 1

Adaptive and model-based control theory applied to convectively-unstable flows

Nicolò Fabbiane¹, Onofrio Semeraro²,
Shervin Bagheri¹ and Dan S. Henningson¹

¹ Linné FLOW Centre, KTH Mechanics, S-100 44 Stockholm, Sweden

² LadHyX, CNRS-École Polytechnique, 91128 Palaiseau, France

Applied Mechanics Reviews (2014), vol. **66** (6), 060801

Research on active control for the delay of laminar-turbulent transition in boundary layers has made a significant progress in the last two decades, but the employed strategies have been many and dispersed. Using one framework, we review model-based techniques, such as linear-quadratic regulators, and model-free adaptive methods, such as least-mean square filters. The former are supported by a elegant and powerful theoretical basis, whereas the latter may provide a more practical approach in the presence of complex disturbance environments, that are difficult to model. We compare the methods with a particular focus on efficiency, practicability and robustness to uncertainties. Each step is exemplified on the one-dimensional linearized Kuramoto-Sivashinsky equation, that shows many similarities with the initial linear stages of the transition process of the flow over a flat plate. Also, the source code for the examples are provided.

1. Introduction

The key motivation in research on drag reduction is to develop new technology that will result in the design of vehicles with a significantly lower fuel consumption. The field is broad, ranging from passive methods, such as coating surfaces with materials that are super-hydrophobic or non-smooth (Bushnell & Moore 1991), to active methods, such as applying wall suction or using measurement-based closed-loop control (Kim & Bewley 2007). This work positions itself in the field of active control methods for skin-friction drag. In general, the mean skin friction of a turbulent boundary layer on a flat plate is an order of magnitude larger compared to a laminar boundary layer. One strategy to reduce skin-friction drag is thus to push the laminar-turbulent transition on a flat plate downstream (Schlichting & Gersten 2000). Different transition scenarios may occur in a boundary layer flows, depending on the intensity of the external disturbances acting on the flow, (Saric *et al.* 2002). Under low levels of free-stream turbulence and sufficiently far downstream, the transition process is initiated by the linear growth of small perturbations called Tollmien-Schlichting (TS)

waves (Schlichting & Gersten 2000). Eventually, these perturbations reach finite amplitudes and breakdown to smaller scales via nonlinear mechanisms (Schmid & Henningson 2001). However, in presence of stronger free-stream disturbances, the exponential growth of TS waves are bypassed and transition may be directly triggered by the algebraic growth of stream-wise elongated structures, called streaks (Saric *et al.* 2002). One may delay transition by damping the growth of TS waves and/or streaks, and thus postpone their nonlinear breakdown. This strategy enables the use of linear theory for control design.

Fluid dynamists noticed in the early 90's, that many of the emerging concepts in hydrodynamic stability theory already existed in linear systems theory (Jovanovic & Bamieh 2005; Schmid 2007). For example, the analysis of a system forced by harmonic excitations is referred to as signalling problem by fluid dynamicists, while control theorists analyze the problem by constructing a Bode diagram, (Glad & Ljung 2000); similarly, a large transient growth of a fluid system corresponds to large norm of a transfer function and matrix with stable eigenvalues can be called either globally stable or Hurtwitz, (Schmid & Henningson 2001; Huerre & Monkewitz 1990).

However, the systems theoretical approach had taken one step further, by "closing the loop", i.e providing rigorous conditions and tools to modify the linear system at hand. It was realized by fluid dynamists that the extension of hydrodynamic stability theory to include tools and concepts from linear control theory was natural (Joshi *et al.* 1997; Bewley & Liu 1998; Cortelezzi *et al.* 1998). A long series of numerical investigations addressing the various aspects of closed-loop control of transitional (Högberg *et al.* 2003a; Chevalier *et al.* 2007a; Monokrousos *et al.* 2008) and turbulent flows (Lee *et al.* 2001; Högberg *et al.* 2003; Chevalier *et al.* 2006) followed in the wake of these initial contributions.

At the same time, research on active control for transition delay has been advanced from a more practical approach using system identification methods (Ljung 1999) and active wave-cancellation techniques (Elliott & Nelson 1993). Most work (but not all) is experimental, which due to feasibility constraints, has favoured an engineering and occasionally *ad hoc* methods. One of the first examples of this approach is the control of TS waves in the experiments by Milling (1981) using a wave-cancellation control; the propagating waves are cancelled by generating perturbations with opposite phase. This work was followed by number of successful experimental investigations (Jacobson & Reynolds 1998; Sturzebecher & Nitsche 2003; Rathnasingham & Breuer 2003; Lundell 2007) of transition delay using more sophisticated system identification techniques.

On the other hand, both numerical and experimental approaches have pushed forward flow control research, they have in a large extent evolved disconnected from each other; the systems control theoretical approach has provided very important insights into physical mechanisms and constraints that has to be addressed in order to design active control that is optimal and robust, but most work has stayed at a proof-of-concept level and have not yet been

fully implemented in practical applications. Although, there are exceptions (McKeon *et al.* 2013; Goldin *et al.* 2013), the majority of experimental active control has essentially suffered from the opposite; most controllers are developed directly in the experimental setting on a trial-and-error basis, with many tuning parameters, that have to be chosen for each particular set-up.

This review aims at presenting model-based and model-free techniques that are appropriate for the control of TS waves in a flat-plate boundary layer. We compare and link the two approaches using a linear model, that similar to the linearized Navier-Stokes equations, exhibits a large transient amplification behaviour and time delays. This presentation is unavoidably influenced by the authors background and previous work; complementary reviews on flow control can be found in Kim & Bewley (2007), Sipp *et al.* (2010) and Bagheri & Henningson (2011), where the linear approach is analyzed, and in the reviews by Bagheri *et al.* (2009c) and Sipp & Schmid (2013), focussed on the identification of reduced-order models for the linear control design. Finally, we refer to Gad-el Hak (1996), Bewley (2001) and Collis *et al.* (2004) for a broader perspective.

1.1. The control problem

Consider a steady uniform flow U_∞ over a thin flat plate of length L and infinite width. Inside the two-dimensional (2D) (Blasius) boundary layer that develops over the plate, we place a small localized disturbance (denoted by d in Figure 1) of simple Gaussian shape; the set-up is the same as in Bagheri *et al.* (2009) and the simulation is performed using a spectral code (Chevalier *et al.* 2007). Figure 2 summarizes the spatio-temporal evolution of the disturbance. It shows a contour plot of the stream-wise component of the perturbation velocity at a wall normal position $Y = \delta^*(0)$, where $\delta^*(X)$ is the displacement thickness of the boundary layer. The temporal growth of this disturbance is determined by classical linear stability theory (i.e. eigenvalue analysis of the linearized Navier-Stokes equations). Such an analysis reveals that asymptotically a compact wave-packet emerges – a TS wave-packet – that grows in time at an exponential rate while travelling downstream at group velocity of approximately $U_\infty/3$. This disturbance behaviour is observed as long as the amplitude is below a critical value (usually a few percent of U_∞) (Schmid & Henningson 2001). Above the critical value, nonlinear effects have to be taken into account; they eventually result in a break down of the disturbance to smaller scales and finally to transition from a laminar to a turbulent flow (Schmid & Henningson 2001). However, the key point – that enables the use of linear theory for transition control – is that the disturbance may grow several orders of magnitude before it breaks down.

Using a spatially localized forcing (denoted by u in Figure 1) downstream of the disturbance, one may modify the conditions in order to reduce the amplitude of the wave-packet and thus delay the transition to turbulence. Physically this forcing is provided by devices called *actuators*. An example of an actuator is a loudspeaker that generates short pulses through a small orifice in the plate.

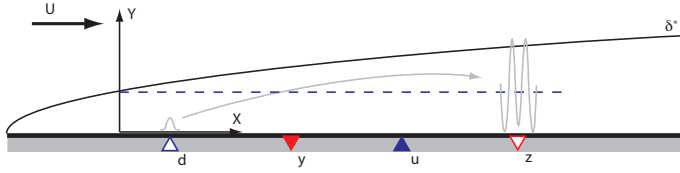


Figure 1: Scheme of a Blasius boundary-layer flow developing over a flat plate. A disturbance modelled by d grows exponentially while convected downstream. The actuator u is used to attenuate the disturbance before it triggers transition to turbulence; the actuation signal is computed based on the measurements provided by the sensor y . The output z , located downstream of the actuator, estimates the efficiency of the control action.

The volume of the loudspeaker and the shape of the orifice determines the type of actuation. Another example is plasma actuators, where a plasma arch is used to induce a forcing on the flow (Grundmann & Tropea 2008).

In closed-loop control, a sensor (denoted by y in Figure 1) is used to measure the disturbance that is meant to be cancelled by the actuator (u): based on these measurements one computes the actuator action in order to effectively reduce the amplitude of the perturbation. Examples of sensors include pressure measurements using a small microphone membrane mounted flush to the wall, velocity measurements using hot-wire anemometry near the wall or shear-stress measurements using thermal sensors (wall wires). Finally, we place a second sensor (denoted by z in Figure 1) downstream of the actuator to measure the amplitude of the perturbation after the actuator action. The minimization of this output signal may serve as an objective of our control design, but the measurements also provide a means to assess the performance of the controller.

Having introduced the inputs and outputs, the control problem can be formulated as the following: given the measurement $y(t)$, compute the modulation signal $u(t)$ in order to minimize a cost function based on $z(t)$. The system that when given the measurement $y(t)$, provides the control signal $u(t)$ is referred to as the *compensator*. The design of the compensator has to take into account competing aspects such as robustness, performance and practical feasibility.

The objective of this review is to guide the reader through the steps of compensator design process. We will exemplify the theory and the associated methods on a one-dimensional (1D) model based on the linearized Kuramoto-Sivashinsky (KS) equation (presented in §2). The model reproduces the most important stability properties of the flat-plate boundary layer, but it avoids the problem of high-dimensionality and thus the high numerical costs. In §3 full-information control problem is addressed via optimal control theory; linear quadratic regulator (LQR) and model-predictive controller (MPC) strategies

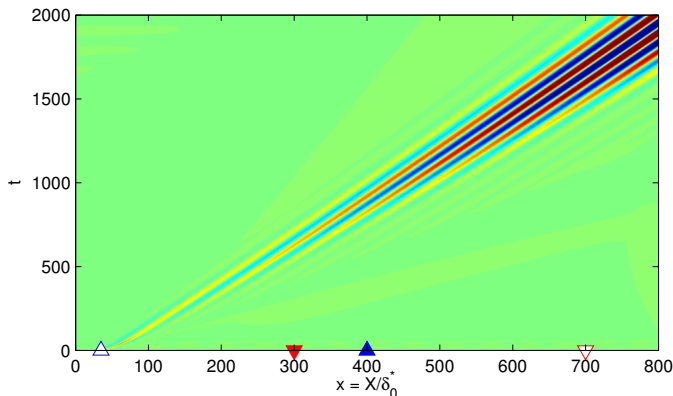


Figure 2: Response to a small, localized initial condition in a Blasius boundary-layer flow. A Tollmien-Schlichting wave-packet emerges and grows exponentially while propagating downstream. Contours of the streamwise component of the velocity are shown as a function of the streamwise direction (x) and time (t). The location along the normal-direction y is chosen in the vicinity of the wall.

are derived and compared. The disturbance estimation problem is addressed in §4, where classical Kalman estimation theory and least-mean-square techniques will be introduced and compared. The techniques of sections §3 and §4, will be combined in order to design the compensator in §5. This section also contains adaptive algorithms that enhance the robustness of the compensator. The review finalizes with a discussion §6 about some important features characterizing the control problem when applied to three-dimensional (3D) fluid flows and conclusions §7.

2. Framework

We first introduce our choice of model KS equation, inputs (actuators/disturbances) and sensors. This is followed by a presentation of concepts pertinent to our work, namely the state-space formulation (§2.4), transfer functions and finite-impulse response (§2.5), controllability and observability (§2.6), closed-loop system (§2.7) and robustness (§2.8). This chapter contains the mathematical ingredients that will be used in the following sections.

2.1. Kuramoto-Sivashinsky model

In this paper, we focus our attention on flows dominated by convection/advection, where disturbances have negligible upstream influence and are quickly swept downstream with the flow. We make use of a particular variant of the KS equation to model a linear and convection-dominated flow. Originally, the KS equation was developed to describe the flame front flutter in laminar flames (Kuramoto & Tsuzuki 1976; Sivashinsky 1977). This model exhibits in its

space-periodic form a spatio-temporal chaotic behaviour, with some similarities to turbulence (Manneville 1995). The standard KS equation reads

$$\frac{\partial \tilde{v}}{\partial \tilde{t}} + \tilde{v} \frac{\partial \tilde{v}}{\partial \tilde{x}} = -\eta \frac{\partial^2 \tilde{v}}{\partial \tilde{x}^2} - \mu \frac{\partial^4 \tilde{v}}{\partial \tilde{x}^4}, \quad (1)$$

where \tilde{t} is the time, $\tilde{x} \in [0, \tilde{L})$ the spatial coordinate and $\tilde{v} = \tilde{v}(\tilde{x}, \tilde{t})$ the velocity. The boundary conditions accompanying (1) are periodic in \tilde{x} . The second term on the left side in (1) is the nonlinear convection term, while on the right side two viscosity terms appear. The two latter terms may be associated to the production and dissipation of energy at different spatial scales. In particular, the second-order derivative term is related to the production of the energy via the variable η , called *anti-viscosity*, while the dissipation of the energy is connected to the fourth-order derivative term, multiplied by the *hyper-viscosity* μ (Cvitanović *et al.* 2012).

Equation (1) can be rewritten such that it is parametrized by a Reynolds-number-like coefficient. Introducing a reference length \tilde{l} and a reference velocity \tilde{V} , define the non-dimensional position x , velocity v and time t by

$$x = \frac{\tilde{x}}{\tilde{l}}, \quad v = \frac{\tilde{v}}{\tilde{V}}, \quad t = \frac{\tilde{V}}{\tilde{l}} \tilde{t}. \quad (2)$$

Applying the transformation to (1), the KS equation in dimensionless form becomes

$$\frac{\partial v}{\partial t} + v \frac{\partial v}{\partial x} = -\frac{1}{\mathcal{R}} \left(\mathcal{P} \frac{\partial^2 v}{\partial x^2} + \frac{\partial^4 v}{\partial x^4} \right), \quad (3)$$

where $x \in [0, L)$. The parameters \mathcal{R} and \mathcal{P} are defined as

$$\mathcal{R} = \frac{\tilde{V} \tilde{l}^3}{\mu}, \quad \mathcal{P} = \frac{\eta}{\mu} \tilde{l}^2, \quad (4)$$

where \mathcal{R} takes the role of the Reynolds number Re_{δ^*} , and \mathcal{P} regulates the balance between energy production and dissipation.

We assume that the system is sufficiently close to a steady solution $V(x) = V$. Then, it is possible to describe the dynamics of perturbations using the linearized KS equation. For the chosen parameters, the steady solution is stable, but an external perturbation may be amplified by an order-of-magnitude before it dies out (this requires non-periodic boundary conditions in the streamwise direction as we impose below). Introduce the perturbation $v'(x, t)$

$$v(x, t) = V + \epsilon v'(x, t), \quad (5)$$

where $\epsilon \ll 1$. By inserting this decomposition into (3) and neglecting the terms of order ϵ^2 and higher, the linearized KS equation is obtained

$$\frac{\partial v'}{\partial t} = -V \frac{\partial v'}{\partial x} - \frac{1}{\mathcal{R}} \left(\mathcal{P} \frac{\partial^2 v'}{\partial x^2} + \frac{\partial^4 v'}{\partial x^4} \right). \quad (6)$$

It is the convective and amplifying properties of this non-normal system that makes it a good model of the 2D Blasius boundary layer flow. Following

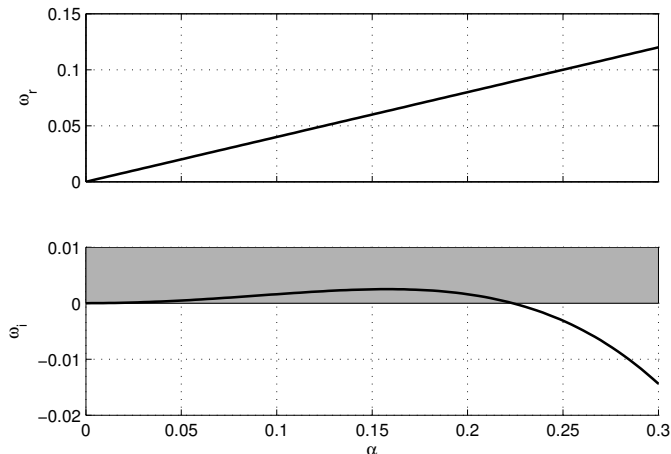


Figure 3: The real frequency ω_r and its imaginary part ω_i are shown as a function of the spatial frequency α , in (a) and (b), respectively. The relation among the spatial and temporal frequencies is given by the dispersion relation (8). Positive values of ω_i characterize unstable waves (grey region).

Charru (2011), we analyze the stability properties of (6), by assuming travelling wave-like solutions:

$$v' = \hat{v} e^{i(\alpha x - \omega t)}, \quad (7)$$

where $\alpha \in \mathbb{R}$ and $\omega = \omega_r + i\omega_i \in \mathbb{C}$. Substituting (7) in (6), a dispersion relation between the spatial wave-number α and the temporal frequency ω is obtained

$$\omega = V\alpha + i \left(\frac{\mathcal{P}}{\mathcal{R}} \alpha^2 - \frac{1}{\mathcal{R}} \alpha^4 \right). \quad (8)$$

This relation is shown in Figure 3 for $\mathcal{R} = 0.25$, $\mathcal{P} = 0.05$ and $V = 0.4$. The parameters are chosen to closely model the Blasius boundary layer at $Re_{\delta^*} = 1000$. The imaginary part of the frequency ω_i is the exponential temporal growth rate of a wave with wave-number α . In (8) it can be observed that the term in α^2 (associated to the production parameter \mathcal{P}), is providing a positive contribution to ω_i , while the α^4 term (related to the dissipation parameter \mathcal{R}), has a stabilizing effect. The competition between these two terms determines stability of the considered wave. From Figure 3, it can be observed that for an interval of wave-numbers α , $\omega_i > 0$, i.e. the wave is unstable. The real part ω_r determines the phase speed of the wave in the x direction,

$$c \triangleq \frac{\omega_r}{\alpha} = V. \quad (9)$$

Note that the phase speed c is independent of α , in contrast to the boundary-layer flow, which is dispersive (Schmid & Henningson 2001).

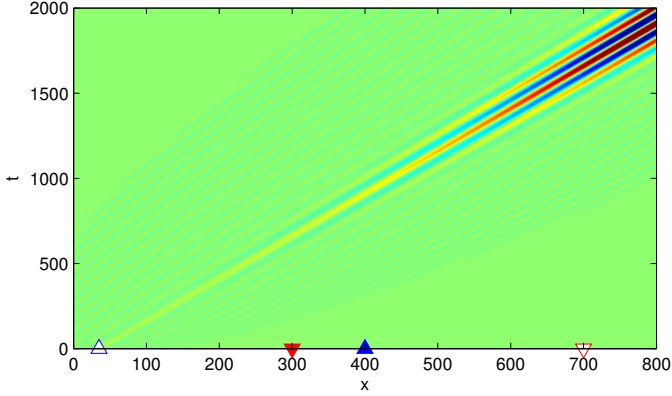


Figure 4: Response to a small, localized initial condition in a 1D KS flow (6) with $\mathcal{R} = 0.25$, $\mathcal{P} = 0.05$ and $V = 0.4$. The contours are shown as a function of the streamwise direction (x) and the time (t). The initial condition triggers a growing and travelling wave-packet, similar to the 2D boundary-layer flow shown in Figure 2. [script00.m].

2.2. Outflow boundary condition

So far in our analysis we have assumed periodic boundary conditions for the KS equation. As we are interested in modelling the amplification of a propagating wave-packet near a stable steady solution (as observed in the case of boundary-layer flow), it is appropriate to change the boundary conditions to an outflow condition on the right side of the domain

$$\left. \frac{\partial^3 v'}{\partial x^3} \right|_{x=L} = 0, \quad \left. \frac{\partial v'}{\partial x} \right|_{x=L} = 0, \quad (10)$$

while on the left side of the domain, at the inlet, an unperturbed boundary condition is considered

$$v'|_{x=0} = 0, \quad \left. \frac{\partial v'}{\partial x} \right|_{x=0} = 0. \quad (11)$$

With an outflow boundary condition, a localized initial perturbation in the upstream region of the domain travels in the downstream direction while growing exponentially in amplitude until it leaves the domain. This is the signature of a convectively unstable flow. Note that this choice of boundary conditions is the main variant with respect of the original KS equation, characterized by periodic boundaries. Figure 4 shows the spatio-temporal response to a localized initial condition of KS equation with outflow boundary condition. The set of parameters \mathcal{R} , \mathcal{P} and V has been chosen to mimic the response of the 2D boundary-layer flow, shown in Figure 2. However, note that in the KS model the wave crests travel parallel to each other with the same speed of the wave-packet, whereas in the boundary layer, they travel faster than the wave-packet which

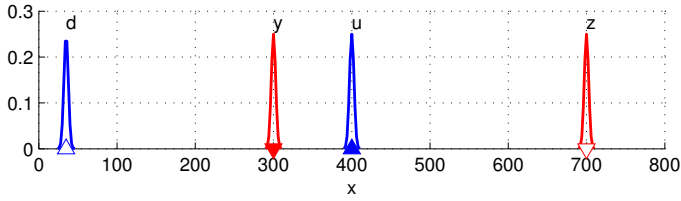


Figure 5: Spatial support of the inputs and outputs along the streamwise direction. All the elements are modelled as a Gaussian function in (14), with $\sigma_d = \sigma_u = \sigma_y = \sigma_z = 4$.

they form. Indeed the system is not dispersive, i.e. the phase speed c equals the group speed c_g as shown by (9); conversely, as already noticed, the 2D BL is dispersive.

2.3. Introducing inputs and outputs

Having presented the dynamics of the linear system, we now proceed with a more systematic analysis of the inputs (actuators/disturbances) and sensor outputs described in §1.1. Consider the linearized KS equation in (6)

$$\frac{\partial v'}{\partial t} = -V \frac{\partial v'}{\partial x} - \frac{1}{\mathcal{R}} \left(\mathcal{P} \frac{\partial^2 v'}{\partial x^2} + \frac{\partial^4 v'}{\partial x^4} \right) + f'(x, t), \quad (12)$$

where the forcing term $f'(x, t)$ now appears on the right-hand side. This term is decomposed into two parts,

$$f'(x, t) = b_d(x) d(t) + b_u(x) u(t). \quad (13)$$

The temporal signal of the incoming external disturbance and of the actuator are denoted by $d(t)$ and $u(t)$, respectively, while the corresponding spatial distribution is described by b_d and b_u . In this work, the time-independent spatial distribution of the inputs is described by the Gaussian function,

$$g(x; \hat{x}, \sigma) = \frac{1}{\sigma} \exp \left[- \left(\frac{x - \hat{x}}{\sigma} \right)^2 \right]. \quad (14)$$

The scalar parameter σ determines the width of the Gaussian distribution, whereas \hat{x} determines the centre of the Gaussian. The two forcing distributions in (13) are

$$b_d(x) = g(x; \hat{x}_d, \sigma_d), \quad b_u(x) = g(x; \hat{x}_u, \sigma_u). \quad (15)$$

The disturbance d is positioned in the beginning of the domain at $\hat{x}_d = 35$, while the actuator u in the middle of the domain at $\hat{x}_u = 400$ (see Figure 5). In the presentation above, the particular shape $b_d(x)$ of the disturbance d is part of the modelling process. However, note that the introduction of the upstream disturbance using a localized and well defined shape $b_d(x)$ is a model. In practice, due to the receptivity processes, the distribution and the appearance

of the incoming disturbance is not known *a-priori*, and thus difficult to predict using – for instance – a low-order model.

A similar issue may arise for the model of the actuator $b_u(x)$, where the forcing distribution can even be time varying. For example the spatial force that a plasma actuator induces in the flow depends on the supplied voltage, e.g. modulated by the amplitude $u(t)$ (Grundmann & Tropea 2008). As we will discuss in the following sections, one may design a controller without knowing $b_d(x)$ and $b_u(x)$, but for the sake of presentation we may assume in this section, that such models exist.

By using (14) as integration weights, we define two outputs of the system as

$$y(t) = \int_0^L c_y(x) v'(x, t) dx + n(t), \quad (16)$$

$$z(t) = \int_0^L c_z(x) v'(x, t) dx, \quad (17)$$

where L is the length of the domain defined earlier and

$$c_y(x) = g(x; \hat{x}_y, \sigma_y), \quad c_z(x) = g(x; \hat{x}_z, \sigma_z).$$

The output y provides a measurement of an observable physical quantity – for example shear-stress, a velocity component or pressure near the wall – averaged with the Gaussian weight. In realistic conditions, this measured quantity is subject to some form of noise, that may arise from calibration drifting, truncation errors and/or incomplete cable shielding, etc. This is taken into account by the forcing term $n(t)$. It is often modelled as random noise with Gaussian distribution of zero-mean and variance α , and can be regarded as an input of the system. The second output $z(t)$, located far downstream, represents the *objective* of the controller: assuming that the flow has been already modified due to the action of the controller, this *controlled* output is the quantity that we aim to keep as small as possible.

In Figure 6, we show the response of our system to a Gaussian white noise in $d(t)$ with a unit variance, where all temporal frequencies are excited. Via the dispersion relation (8), each temporal frequency ω_r is related to a spatial frequency $\alpha = V \omega_r$. The input signal $d(t)$ is thus filtered by the system, where after a short transient, only the unstable spatial wavelengths are present in the state $\mathbf{v}(t)$, Figure 6(a), and the two output signals $y(t)$ and $z(t)$, Figure 6(c-d). The variance of the output $z(t)$ is higher than the variance of $y(t)$ by a factor 10, independently by the realization; this is because the wave-packets generated by d is growing in amplitude while convected downstream. We note that each realization will generate a different time evolution of the system but with the same statistical properties (black and grey lines in Figure 6(b-d)).

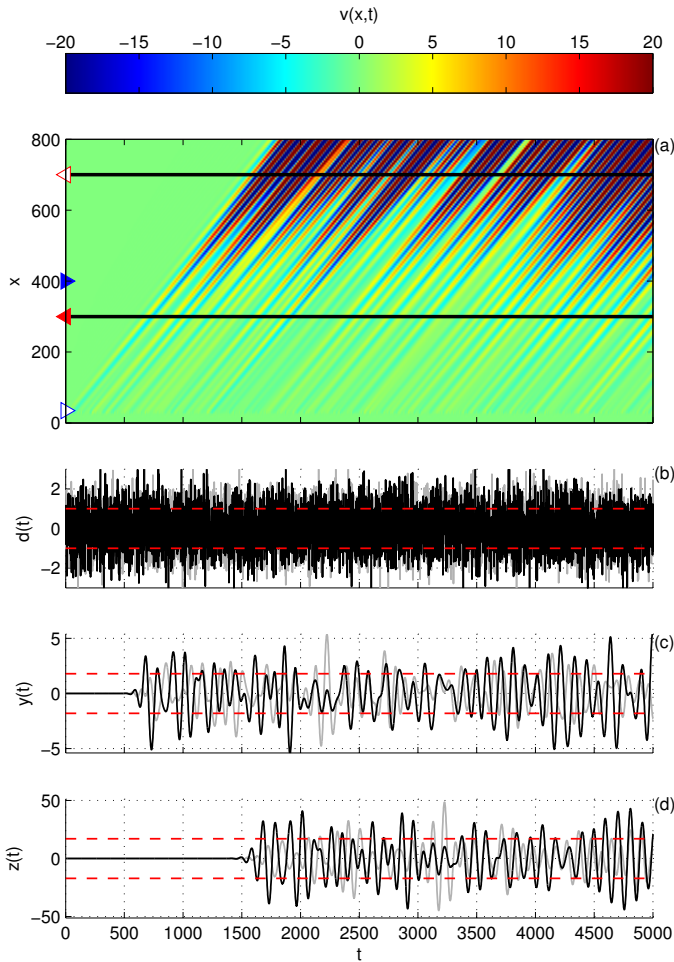


Figure 6: Top frame (a) shows the spatio-temporal response to white noise $d(t)$, (b). The velocity contours are shown as a function of the streamwise direction (x) and time (t). The signals $y(t)$ and $z(t)$ are shown for two different realizations (black and grey lines) in (c) and (d), respectively. Red dashed lines indicate the standard deviation of the signals. [`script01.m`]

2.4. State-space formulation

We discretize the spatial part of (12) by a finite-difference scheme. As further detailed in §7, the solution is approximated by

$$v'_i(t) = v'(x_i, t) \quad i = 1, 2, \dots, n_v$$

defined on the equispaced nodes $x_i = iL/n_v$, where $n_v = 400$. The spatial derivatives are approximated by a finite difference scheme based on five-points stencils. Boundary conditions in (11–10) are imposed using four ghost nodes $i = -1, 0$ and $i = n_v + 1, n_v + 2$. The resulting finite-dimensional state-space system (called *plant*) is

$$\dot{\mathbf{v}}(t) = \mathbf{A} \mathbf{v}(t) + \mathbf{B}_d d(t) + \mathbf{B}_u u(t), \quad (18)$$

$$y(t) = \mathbf{C}_y \mathbf{v}(t) + n(t), \quad (19)$$

$$z(t) = \mathbf{C}_z \mathbf{v}(t), \quad (20)$$

where $\mathbf{v} \in \mathbb{R}^{n_v}$ represents the nodal values v'_i . The output matrices \mathbf{C}_y and \mathbf{C}_z approximate the integrals in (16–17) via the trapezoidal rule, while the input matrices \mathbf{B}_d and \mathbf{B}_u are given by the evaluation of (15) at the nodes.

Some of the control algorithms that we will describe are preferably formulated in a time-discrete setting. The time-discrete variable corresponding to $a(t)$ is

$$a(k) = a(k\Delta t), \quad k = 1, 2, \dots \quad (21)$$

where Δt is the sampling time. Accordingly, the time-discrete state-space system is defined as:

$$\mathbf{v}(k+1) = \tilde{\mathbf{A}} \mathbf{v}(k) + \tilde{\mathbf{B}}_d d(k) + \tilde{\mathbf{B}}_u u(k), \quad (22)$$

$$y(k) = \tilde{\mathbf{C}}_y \mathbf{v}(k) + n(k), \quad (23)$$

$$z(k) = \tilde{\mathbf{C}}_z \mathbf{v}(k), \quad (24)$$

where $\tilde{\mathbf{A}} = \exp(\mathbf{A} \Delta t)$, $\tilde{\mathbf{B}} = \Delta t \mathbf{B}$ and $\tilde{\mathbf{C}} = \mathbf{C}$. For more details, the interested reader can refer to any control book, see e.g. (Glad & Ljung 2000).

2.5. Transfer functions and Finite-impulse responses

Given a measurement signal $y(t)$, our aim is to design an actuator signal $u(t)$. The relation between input and output signals is of primary importance. Since we are interested in the effect of the control signal $u(t)$ on the system, we assume the disturbance signal $d(t)$ to be zero. Thus, given an input signal $u(t)$ and a zero initial condition of the state, the output $z(t)$ of (18–20) may formally be written as

$$z(t) = \int_0^t \mathcal{P}_{zu}(t) u(t - \tau) d\tau, \quad (25)$$

where the kernel is defined by

$$\mathcal{P}_{zu}(t) \triangleq \mathbf{C}_z e^{\mathbf{A}t} \mathbf{B}_u, \quad t \geq 0. \quad (26)$$

Note that the description of the input-output (I/O) behaviour between $u(t)$ and $z(t)$ does not require the knowledge of the full dynamics of the state but only a representation of the impulse response between the input u and the output z , here represented by (26). A Laplace transform results in a transfer function

$$\hat{z}(s) = \hat{\mathcal{P}}_{zu}(s) \hat{u}(s) = (\mathbf{C}_z (s\mathbf{I} - \mathbf{A})^{-1} \mathbf{B}_u) \hat{u}(s)$$

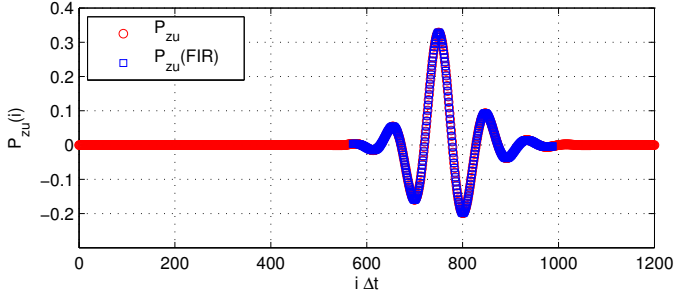


Figure 7: Time discrete impulse response (\circ) between the input u to the output z ; due to the presence of strong time-delays in the system, a lag of $t \approx 550$ is observed. The relevant part of the kernel is reconstructed via a FIR filter (\square). [script02.m]

with $s \in \mathbb{C}$. Henceforth the *hat* on the transformed quantities is omitted since related by a linear transformation to the corresponding quantities in time-domain. One may formulate a similar expression for the other input-output relations, which for our case with three inputs and two outputs, induces 6 transfer functions, i.e.

$$\begin{bmatrix} z(s) \\ y(s) \end{bmatrix} = \begin{bmatrix} \mathcal{P}_{zd}(s) & \mathcal{P}_{zu}(s) & \mathcal{P}_{zn}(s) \\ \mathcal{P}_{yd}(s) & \mathcal{P}_{yu}(s) & \mathcal{P}_{yn}(s) \end{bmatrix} \begin{bmatrix} d(s) \\ u(s) \\ n(s) \end{bmatrix}. \quad (27)$$

I/O relations similar to (25) can be found for the time-discrete system. The response $z(k)$ of the system (with $\mathbf{v}_0 = 0$) to an input $u(k)$ is

$$z(k) = \sum_{i=1}^k \tilde{\mathcal{P}}_{zu}(i) u(k-i), \quad (28)$$

where

$$\tilde{\mathcal{P}}_{zu}(k) \triangleq \tilde{\mathbf{C}}_z \tilde{\mathbf{A}}^{k-1} \tilde{\mathbf{B}}_u, \quad k = 1, 2, \dots \quad (29)$$

This procedure is usually referred to as *z-transform*; for more details, we refer to Glad & Ljung (2000) and Skogestad & Postlethwaite (2005). In the limit of $k \rightarrow \infty$, it is possible to truncate (28), since the propagating wave-packet that is generated by an impulse in u will be detected by the output z after a time-delay (this can be observed in Figure 7, where the impulse response is depicted). Thus, $\tilde{\mathcal{P}}_{zu}(i)$ is non-zero only in a short time interval and one may truncate the sum to a finite number of time steps, $N_{zu,f}$. Due to the strong time-delay, the initial part of the sum is also zero and the lower limit of the sum can start from $N_{zu,i}$. This results in a sum

$$z(k) \approx \sum_{i=N_{zu,i}}^{N_{zu,f}} \tilde{\mathcal{P}}_{zu}(i) u(k-i), \quad (30)$$

which is called the Finite Impulse Response (FIR), Aström & Wittenmark (1995). Note that the presence of time delays in the system is a limiting factor of the control performance. In general, a disturbance with a time scale smaller than the time delay that affects the system is difficult to control (Glad & Ljung 2000). In particular, while the compensator could still be able to damp those disturbances, it may lack robustness, §2.8.

2.6. Controllability and observability

The choice of sensors and actuators is particular relevant for the control design; indeed, the measurement of the sensor y enables to compute the control signal $u(t)$, that feeds the actuator. Thus, it is important to know: (i) if the system can be affected by the actuator u ; (ii) if the system can be detected by the sensor y . In other words, we aim at identify the states of the system that are *controllable* and/or *observable*. These two properties of the I/O system are referred to as *observability* and *controllability* (Glad & Ljung 2000; Bagheri *et al.* 2009c) and can be analyzed introducing the corresponding Gramians \mathbf{G}_o and \mathbf{G}_c

$$\mathbf{G}_o \triangleq \int_0^\infty e^{\mathbf{A}^H t} \mathbf{C}^H \mathbf{C} e^{\mathbf{A} t} dt, \quad (31)$$

$$\mathbf{G}_c \triangleq \int_0^\infty e^{\mathbf{A} t} \mathbf{B} \mathbf{B}^H e^{\mathbf{A}^H t} dt. \quad (32)$$

By construction, the Gramians ($\mathbf{G}_o, \mathbf{G}_c$) are positive semi-definite matrices in $\mathbb{R}^{n_v \times n_v}$ and can be computed for each or all the outputs/inputs. It can be proved that the two Gramians are solutions of the Lyapunov equations (Glad & Ljung 2000)

$$\mathbf{A}^H \mathbf{G}_o + \mathbf{G}_o \mathbf{A} + \mathbf{C}^H \mathbf{C} = \mathbf{0}, \quad (33)$$

$$\mathbf{A} \mathbf{G}_c + \mathbf{G}_c \mathbf{A}^H + \mathbf{B} \mathbf{B}^H = \mathbf{0}. \quad (34)$$

The spatial information related to the Gramians can be analyzed by diagonalizing them; the corresponding decompositions allow to identify and rank the most controllable/observable structures (Bagheri *et al.* 2009c). On the other hand, for systems characterized by a small number of degrees of freedom, it is possible to directly identify the regions where the flow is observable and/or controllable. Figure 8 shows the controllability Gramian related to the actuator u ($\mathbf{G}_{c,u}$) and the observability Gramian related to the sensor y ($\mathbf{G}_{o,y}$) for our system. The region downstream of the actuator is influenced by its action, due to the strong convection of the flow. The observability Gramian $\mathbf{G}_{o,y}$ indicates the region where a propagating perturbation can be observed by the sensor y . Note that the two regions do not overlap, thus wave-packets generated at the location u are not detected by a sensor y , when is placed upstream of the actuator. This feature has important consequences on the closed-loop analysis, as introduced in the next section.

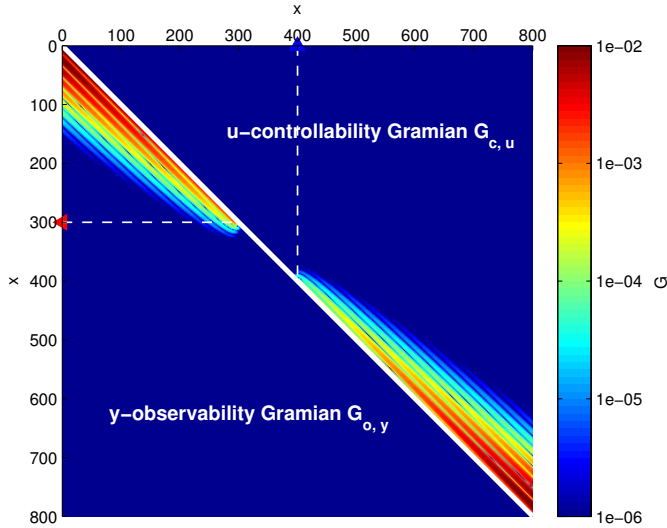


Figure 8: Controllability ($\mathbf{G}_{c,u}$) and observability ($\mathbf{G}_{o,y}$) Gramians, normalized by their trace; the absolute values are reported in logarithmic scale as a function of the streamwise direction (x). Due to the symmetry, only the upper/lower triangular part of each Gramian is shown. [script03.m]

2.7. Closed-loop system

The aim of the control design is to identify a second linear system \mathcal{K}_{uy} , called *compensator*, that provides a mapping between the measurements $y(t)$ and the control-input $u(t)$, i.e.

$$u(t) = \int_0^\infty \mathcal{K}_{uy}(\tau) y(t - \tau) d\tau$$

The chosen compensator is also called *output feedback controller* (Doyle *et al.* 1989; Zhou *et al.* 2002). This definition underlines the dependency of the control input $u(t)$ from the measurements $y(t)$. By considering the relation in frequency domain and inserting it into the plant (27), the *closed-loop* system between $d(s)$ and $z(s)$ is obtained in the form,

$$z(s) = \left[\mathcal{P}_{zd}(s) + \frac{\mathcal{P}_{zu}(s) \mathcal{K}_{uy}(s) \mathcal{P}_{yd}(s)}{1 - \mathcal{P}_{yu}(s) \mathcal{K}_{uy}(s)} \right] d(s). \quad (35)$$

By choosing an appropriate $\mathcal{K}_{uy}(s)$, we may modify the system dynamics. The graphical representation of the closed-loop system is shown in Figure 9. The transfer function $\mathcal{P}_{yu}(s)$ describes the signal dynamics from the actuator u to the sensor y . By definition, a feedback configuration is obtained when $\mathcal{P}_{yu}(s) \neq 0$, i.e. when the sensor can measure the effect of the actuation. On the other hand, if $\mathcal{P}_{yu}(s)$ is zero (or very small), the closed-loop system reduces to a disturbance

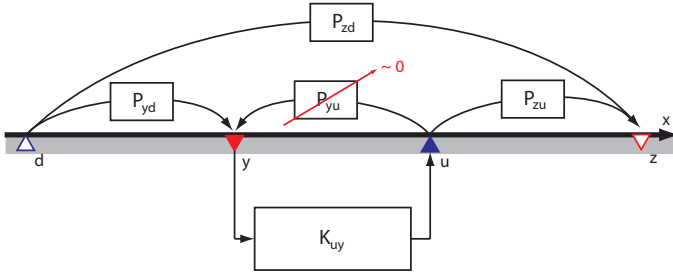


Figure 9: Schematic figure showing the 5 transfer functions defining the closed-loop system (35). The transfer functions \mathcal{P}_{yd} , \mathcal{P}_{zd} describe the input/output behaviour between the disturbance d and the outputs y and z , respectively; \mathcal{P}_{yu} and \mathcal{P}_{zu} relate the actuator u to the two outputs y and z , respectively, while \mathcal{K}_{uy} is the compensator transfer-function. Because of the convectively unstable nature of the flow, \mathcal{P}_{yu} is negligible for the chosen sensor/actuator locations; thus it does not allow any feedback.

feedforward configuration (Doyle *et al.* 1989; Zhou *et al.* 2002). In this special case, from the dynamical point of view such a system behaves as an open-loop system despite the closed-loop design (Skogestad & Postlethwaite 2005). Due to this inherent ambivalence within the framework of the output feedback control, sometimes the definition of *reactive control* is used for indicating all the cases where the control signal is computed based on measurements of the system; thus, the definition of closed-loop system more properly applies to a system where the reactive controller is characterized by feedback (Gad-el Hak 2007).

In a convection-dominated system, the sensor should be placed upstream of the actuator, in order to detect the upcoming wave-packet before it reaches the actuator (see also Figure 8); if it is placed downstream, the actuator has no possibility to influence the propagating disturbance once it has reached the sensor. Figure 10 shows the state and signal responses of the KS system to impulse in u , where it is clear that the actuator's action is not detected by the sensor y , in practice $\mathcal{P}_{yu}(s) \approx 0$. Note that no assumptions about the compensator has been made; the feedback or feedforward setting is determined by the choice of sensor and actuator placement.

2.8. Robustness

In practice, model uncertainties are unavoidable and it is important to estimate how much the error arising from the mismatch between the physical system and the model affects the stability and performance of the closed-loop system. In general, one wishes to have a controller that does not amplify un-modelled errors over a range of off-design conditions: a robustness analysis aims at identify this range. A useful quantity in this context, is the sensitivity transfer function,

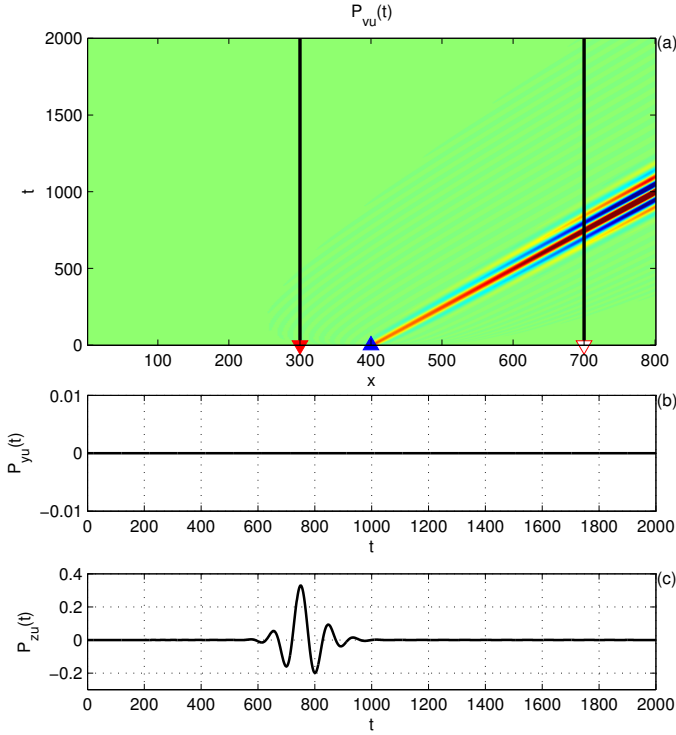


Figure 10: The disturbance generated by the impulse response of the system at the actuator location u in (a) is shown as a function of the streamwise direction (x) and time (t). The wave-packet is detected only by the output z (c); due to the convective nature of the flow, the sensor placed upstream of the actuator can not detect the propagating disturbance, and the resulting signal is practically null (b). [`script02.m`]

which is defined as the denominator in the second term on the right-hand side of (35), i.e.

$$\mathcal{S}(s) = \frac{1}{1 - \mathcal{P}_{yu}(s)\mathcal{K}_{uy}(s)}. \quad (36)$$

Robustness can be quantified as the infinity norm of $\mathcal{S}(s)$. Good stability margins are guaranteed when this norm is bounded, typically $\|\mathcal{S}\|_\infty < 2.0$, see Skogestad & Postlethwaite (2005). A second measure is the phase margin, that represents the maximum amount of allowable phase error before the instability of the closed-loop occurs. Indeed, the gain margin and the phase margin are the upper limit of amplification and phase error, respectively, that guarantee marginal stability of the closed-loop system.

Note that the internal stability functions are characterized by a proper dynamics. In the *loop-shaping* approach, the controller is designed by shaping the behaviour of the internal transfer function (Skogestad & Postlethwaite 2005). Unfortunately, this methodology is difficult to be applied in complex system. A systematic approach for the robust design is represented by the optimal, robust \mathcal{H}_∞ (see (Zhou *et al.* 2002)), where the sensitivity margins can be optimized. A more computationally demanding alternative is represented by the controllers based on numerical optimization running on-line, such as the model-predictive control (MPC) (§3.2) or adaptive controllers (§5.4).

Thus, feedback controllers may be designed to have small sensitivity. In that regard robustness is a non-issue in a pure feedforward configuration; indeed, $\mathcal{P}_{yu}(s) \approx 0$ and $\|\mathcal{S}\|_\infty \approx 1$. However, a feedforward controller is highly affected by unknown disturbances and model uncertainty, that drastically reduce the overall performance of the device. Moreover, a feedforward controller is not capable in modifying the dynamics of an unstable plant; thus, feedback controllers are required for globally unstable flows (Sipp & Schmid 2013).

The studies performed by Juillet *et al.* (2013) and Belson *et al.* (2013) show that in convectively unstable flows a feedback configuration allows the possibility of robust-control design but it does not guarantee *optimal* performances in terms of amplitude reduction. In this review, we adopt a feedforward configuration in order to achieve optimal performances. As we will show in §5.4, robustness may be addressed to some extent using adaptive control techniques.

3. Model-based control

In this section, we assume the full knowledge of the state $\mathbf{v}(t)$ for the computation of the control signal $u(t)$. This signal is fed back into the system in order to minimize the energy of the output $z(t)$. For linear systems, it is possible to identify a *feedback gain* $\mathbf{K}(t)$, relating the control signal to the state, i.e.

$$u(t) = \mathbf{K}(t)\mathbf{v}(t). \quad (37)$$

The aim of the section is to compare and link the classical LQR problem (Lewis & Syrmos 1995) to the more general MPC approach (Bewley *et al.* 2001; Kim & Bewley 2007). In the former approach, one assumes an infinite time horizon ($t \rightarrow \infty$), allowing the computation of the feedback gain by solving a Riccati equation (see §3.1.1). In the latter approach, the optimization is performed with a final time T that is receding, i.e. it slides forward in time as the system evolves. In §3.2.1, we introduce this technique for the control of a linear system with constraints on the actuator signal, while in §3.2.3 the close connection between the unconstrained MPC and the LQR is shown. Finally, note that the framework introduced in this section makes use of a system's model. Model-free methods based on adaptive strategies are introduced in §5.

3.1. Optimal control

The aim of the controller is to compute a control signal $u(t)$ in order to minimize the norm of the fictitious output

$$\mathbf{z}'(t) = \begin{bmatrix} z(t) \\ u(t) \end{bmatrix} = \begin{bmatrix} \mathbf{C}_z \\ \mathbf{0} \end{bmatrix} \mathbf{v}(t) + \begin{bmatrix} 0 \\ 1 \end{bmatrix} u(t), \quad (38)$$

where now the control signal is also included. We define a *cost function* of the system

$$\mathcal{L}(\mathbf{v}(u), u) = \frac{1}{2} \int_0^T \begin{bmatrix} z \\ u \end{bmatrix}^H \begin{bmatrix} w_z & 0 \\ 0 & w_u \end{bmatrix} \begin{bmatrix} z \\ u \end{bmatrix} dt. \quad (39)$$

This cost function is quadratic and includes the constant matrices $w_z \geq 0$ and $w_u > 0$. The matrix w_z is used to normalize the cost output, specially when multiple $z(t)$ are used, while the weight w_u determines the amount of penalty on control effort (Lewis & Syrmos 1995). Using (38), (39) is rewritten as

$$\begin{aligned} \mathcal{L}(\mathbf{v}(u), u) &= \frac{1}{2} \int_0^T (\mathbf{v}^H (\mathbf{C}_z^H w_z \mathbf{C}_z) \mathbf{v} + u^H w_u u) dt = \\ &= \frac{1}{2} \int_0^T (\mathbf{v}^H \mathbf{W}_v \mathbf{v} + u^H w_u u) dt \end{aligned} \quad (40)$$

where $\mathbf{W}_v = \mathbf{C}_z^H w_z \mathbf{C}_z$. We recall from §2.3 that the sensor \mathbf{C}_z is placed far downstream in the domain, so we are minimizing the energy in localized region. We seek a control signal $u(t)$ that minimizes the cost function $\mathcal{L}(\mathbf{v}(u), u)$ in some time interval $t \in [0, T]$ subject to the dynamic constraint

$$\dot{\mathbf{v}}(t) = \mathbf{A} \mathbf{v}(t) + \mathbf{B}_u u(t). \quad (41)$$

Note that we do not consider the disturbance $d(t)$ for the solution of the optimal control problem. In a variational approach, one defines a Lagrangian

$$\begin{aligned} \tilde{\mathcal{L}}(\mathbf{v}(u), u) &= \frac{1}{2} \int_0^T (\mathbf{v}^H \mathbf{W}_v \mathbf{v} + u^H w_u u) dt + \\ &+ \int_0^T \mathbf{p}^H (\dot{\mathbf{v}} - \mathbf{A} \mathbf{v} - \mathbf{B}_u u) dt, \end{aligned} \quad (42)$$

where the term $\mathbf{p}(t)$ acts as a Lagrangian multiplier (Gunzburger 2003), also called the adjoint state. The expression in the last term is obtained via integration by parts. Instead of minimizing \mathcal{L} with a constraint (41) one may minimize $\tilde{\mathcal{L}}$ without any constraints.

The dynamics of the adjoint state $\mathbf{p}(t)$ is obtained by requiring $\partial \tilde{\mathcal{L}} / \partial \mathbf{v} = \mathbf{0}$, which leads to

$$\begin{aligned} -\dot{\mathbf{p}}(t) &= \mathbf{A}^H \mathbf{p}(t) + \mathbf{W}_v \mathbf{v}(t), \\ \mathbf{0} &= \mathbf{p}(T). \end{aligned} \quad (43)$$

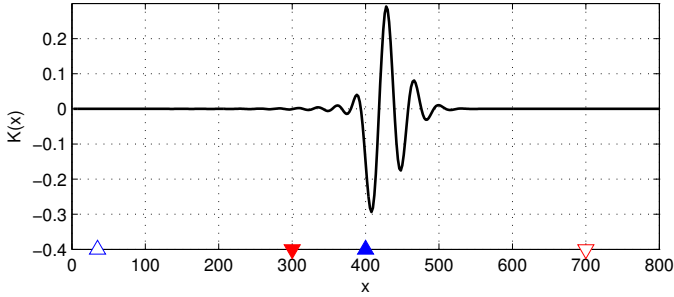


Figure 11: Control gain \mathbf{K} computed using the LQR technique for $w_z = 1$ and $w_u = 1$, (see §3.1.1). [`script04.m`]

The adjoint field $\mathbf{p}(t)$ is computed by marching backwards in time this equation, from $t = T$ to $t = 0$. The optimality condition is obtained by the gradient

$$\frac{\partial \tilde{\mathcal{L}}}{\partial u} = \mathbf{B}_u^H \mathbf{p} + w_u u. \quad (44)$$

The resulting equations' system can be solved iteratively as follows:

1. The state $\mathbf{v}(t)$ is computed by marching forward in time (41) in $t \in [0, T]$. At the first iteration step, $k = 1$, an initial guess is taken for the control signal $u(t)$.
2. The adjoint state $\mathbf{p}(t)$ is evaluated marching (43) backward in time, from $t = T$ to $t = 0$. The initial condition $\mathbf{p}(T)$ is taken to be zero.
3. Once the adjoint state $\mathbf{p}(t)$ is available, it is possible to compute the gradient via (44) and apply it for the update of the control signal using a gradient-based method; one may for example apply directly the negative gradient $\Delta u_k = -\frac{\partial \tilde{\mathcal{L}}_k}{\partial u}$, such that the update of the control signal at each iteration is given by

$$u_{k+1} = u_k + \mu_k \Delta u_k.$$

The scalar-valued parameter μ_k is the step-length for the optimization, properly chosen by applying backtracking or exact line search (Boyd & Vandenberghe 2004). An alternative choice to the steepest descent algorithm is a conjugate gradient method (Press *et al.* 2007).

The iteration stops when the difference of the cost function \mathcal{L} estimated at two successive iteration steps is below a certain tolerance or the gradient value $\partial \tilde{\mathcal{L}} / \partial u \rightarrow 0$. We refer to Gunzburger (2003) for more details and to Corbett & Bottaro (2001) for an application in flow optimization.

3.1.1.1. Linear-quadratic regulator (LQR)

The framework outlined in the previous section is rather general and it can be applied for the computation of the control signal $u(t)$ also when nonlinear

systems or receding finite-time horizons are considered. However, a drawback of the procedure is the necessity of running an optimization on-line, next to the main flow simulation/experiment. When a linear time-invariant system is considered, a classic way to proceed is to directly use the optimal condition (44) in order to identify the optimal control signal $u(t)$

$$u(t) = -w_u^{-1} \mathbf{B}_u^H \mathbf{p}(t). \quad (45)$$

The computed control signal $u(t)$ is *optimal* as it minimizes the cost function $\mathcal{L}(\mathbf{v}(u), u)$ previously defined. Assuming a linear relation between the adjoint state and the direct state, $\mathbf{p}(t) = \mathbf{X}(t)\mathbf{v}(t)$, the feedback gain is given by

$$\mathbf{K}(t) = -w_u^{-1} \mathbf{B}_u^H \mathbf{X}(t). \quad (46)$$

It can be shown that the matrix $\mathbf{X}(t)$ is the solution of a differential Riccati equation (Lewis & Syrmos 1995). When \mathbf{A} is stable, $\mathbf{X}(t)$ reaches a steady state as $T \rightarrow \infty$, which is a solution of the algebraic Riccati equation

$$\mathbf{0} = \mathbf{A}^H \mathbf{X} + \mathbf{X} \mathbf{A} - \mathbf{X} \mathbf{B}_u w_u^{-1} \mathbf{B}_u^H \mathbf{X} + \mathbf{W}_v. \quad (47)$$

The advantage of this procedure is that \mathbf{K} is a constant and needs to be computed only once. The spatial distribution of the control gain \mathbf{K} is shown in Figure 11 for the KS system analysed in §2, where the actuator is located at $x = 400$ and the objective output at $x = 700$. From Figure 11 one can see that the gain is a compact structure between the elements \mathbf{B}_u and \mathbf{C}_z . The control gain is independent on the shape of external disturbance \mathbf{B}_d .

For low-dimensional systems ($n_v < 10^3$), solvers for the Riccati equations (47) are available in standard software packages (Arnold & Laub 1984). For larger systems $n_v > 10^3$, as the ones investigated in flow control, direct methods are not computationally feasible. Indeed, the solution of (47) is a full matrix, whose storage requirement is at least of order $O(n_v^2)$. The computational complexity is of order $O(n_v^3)$ regardless the structure of the system matrix \mathbf{A} (Benner *et al.* 2008). Alternative techniques include the Chandrasekhar method (Banks & Ito 1991), Krylov subspace methods (Benner 2004), decentralized techniques based on Fourier transforms for spatially invariant system (Bamieh *et al.* 2002; Högberg & Bewley 2000; Högberg *et al.* 2003a) and finally iterative algorithms (Akhtar *et al.* 2010; Martensson & Rantzer 2011; Pralits & Luchini 2010; Semeraro *et al.* 2013b). Yet, a different approach consists of reducing n_v before the control techniques are applied. In practice, we seek a low-order surrogate system, typically of $O(n_{v,r}) \approx 10 - 10^2$, whose dynamics reproduces the main features of the original, full-order system. Once the low-order model is identified, the controller is designed and fed into the full-order system; such an approach enables the application of a controller next to real experiments, using small (and fast) real-time computations. The *model-reduction* problem is an important aspect of control design for flow control; we refer to §6 for a brief overview.

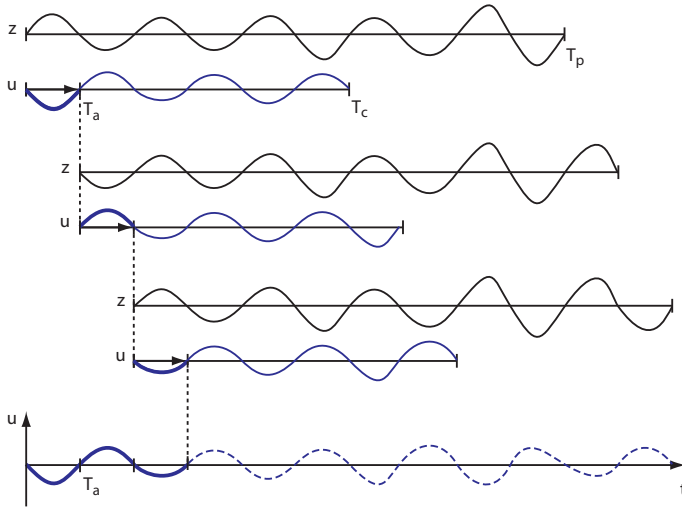


Figure 12: MPC strategy: the controller is computed over a finite time-horizon T_c , based on the a predicted time-horizon T_p . Once the solution is available, the control signal is applied on a shorter time windows T_a . In the successive step, the time-window slides forward in time and the optimization is performed again, starting from a new initial condition at $t = T_a$. The procedures is iterated while proceeding forward in time.

3.2. Model-predictive control (MPC)

MPC controllers make use of an identified model to predict the behaviour of the system over a finite-time horizon (see Garcia *et al.* (1989), Qin & Badgwell (2003) and Noack *et al.* (2011) for an overview on the technique). In contrast with the optimal controllers presented in the previous section, the iterative procedure is characterized by a receding finite horizon of optimization. This strategy is illustrated in Figure 12; at time t_0 , a control signal is computed for a short window in time $[t_0, t_0 + T_c]$ by minimising a cost function (not necessarily quadratic); T_c is the final time of optimization for the control problem. The minimization is performed on-line, based on the prediction of the future trajectories emanating from the current state at t_0 over a window of time $[t_0, t_0 + T_p]$, such that $T_p \geq T_c$. In other words, the control signal is computed over an horizon T_c in order to minimize the predicted deviations from the reference trajectory evaluated on a (generally) longer time of prediction T_p . Once the calculation is performed, only the first step T_a is actually used for controlling the system. After this step, the plant is sampled again and the procedure is repeated at time $t = t_0 + T_a$, starting from the new initial state.

The MPC approach is applicable to nonlinear models as well as all nonlinear constraints (for example an upper maximum amplitude for the actuator signals). We present an example of the latter case in the following section.

3.2.1. MPC for linear systems with constraints

Although it is possible to define MPC in continuous-time formulation (see for instance (Garcia *et al.* 1989), (Bewley *et al.* 2001)), we make use of the more convenient discrete-time formulation. Let $M = T_p/\Delta t$ and $N = T_c/\Delta t$, where the parameter Δt is the sampling time. Since $T_p \geq T_c$, we have $M \geq N$. Augmenting the expression (28) with a term representing an initial state $\mathbf{v}(k)$ at time k , we get

$$\begin{aligned} z(k+j|k) &= \tilde{\mathbf{C}}_z \tilde{\mathbf{A}}^j \mathbf{v}(k) + \sum_{i=1}^{\min(j,N)} \tilde{\mathbf{C}}_z \tilde{\mathbf{A}}^{i-1} \tilde{\mathbf{B}}_u u(k+j-i) = \\ &= \tilde{\mathcal{P}}_{z\mathbf{v}}(j) \mathbf{v}(k) + \sum_{i=1}^{\min(j,N)} \tilde{\mathcal{P}}_{zu}(i) u(k+j-i), \end{aligned} \quad (48)$$

where $j = 1, 2, \dots, M$. The state equation can be written in matrix form by recursive iteration, resulting in the matrix-relation

$$\mathbf{z}_p(k) = \mathbf{P}_{z\mathbf{v}} \mathbf{v}(k) + \mathbf{P}_{z\mathbf{u}} \mathbf{u}_p(k). \quad (49)$$

The matrix $\mathbf{P}_{z\mathbf{v}}$ appearing in (49) is the observability matrix of the discrete-time system

$$\mathbf{P}_{z\mathbf{v}} = \begin{bmatrix} \tilde{\mathcal{P}}_{z\mathbf{v}}(1) \\ \tilde{\mathcal{P}}_{z\mathbf{v}}(2) \\ \vdots \\ \tilde{\mathcal{P}}_{z\mathbf{v}}(M) \end{bmatrix} = \begin{bmatrix} \tilde{\mathbf{C}}_z \tilde{\mathbf{A}} \\ \tilde{\mathbf{C}}_z \tilde{\mathbf{A}}^2 \\ \vdots \\ \tilde{\mathbf{C}}_z \tilde{\mathbf{A}}^M \end{bmatrix}, \quad (50)$$

while the matrix $\mathbf{P}_{z\mathbf{u}}$, related to the convolution operator, reads

$$\mathbf{P}_{z\mathbf{u}} = \begin{bmatrix} \tilde{\mathcal{P}}_{zu}(1) & & & & \\ \tilde{\mathcal{P}}_{zu}(2) & \tilde{\mathcal{P}}_{zu}(1) & & & \\ \vdots & \vdots & \ddots & & \\ \tilde{\mathcal{P}}_{zu}(N) & \tilde{\mathcal{P}}_{zu}(N-1) & \cdots & \tilde{\mathcal{P}}_{zu}(1) & \\ \vdots & \vdots & & \vdots & \\ \tilde{\mathcal{P}}_{zu}(M) & \tilde{\mathcal{P}}_{zu}(M-1) & \cdots & \tilde{\mathcal{P}}_{zu}(M-N+1) & \end{bmatrix} = \begin{bmatrix} \tilde{\mathbf{C}}_z \tilde{\mathbf{B}}_u & & & & \\ \tilde{\mathbf{C}}_z \tilde{\mathbf{A}} \tilde{\mathbf{B}}_u & \tilde{\mathbf{C}}_z \tilde{\mathbf{B}}_u & & & \\ \vdots & \vdots & \ddots & & \\ \tilde{\mathbf{C}}_z \tilde{\mathbf{A}}^{N-1} \tilde{\mathbf{B}}_u & \tilde{\mathbf{C}}_z \tilde{\mathbf{A}}^{N-2} \tilde{\mathbf{B}}_u & \cdots & \tilde{\mathbf{C}}_z \tilde{\mathbf{B}}_u & \\ \vdots & \vdots & & \vdots & \\ \tilde{\mathbf{C}}_z \tilde{\mathbf{A}}^{M-1} \tilde{\mathbf{B}}_u & \tilde{\mathbf{C}}_z \tilde{\mathbf{A}}^{M-2} \tilde{\mathbf{B}}_u & \cdots & \tilde{\mathbf{C}}_z \tilde{\mathbf{A}}^{M-N} \tilde{\mathbf{B}}_u & \end{bmatrix}. \quad (51)$$

In literature, the matrix $\mathbf{P}_{\mathbf{z}\mathbf{u}}$ is also referred to as dynamic matrix, because it takes into account the current and future input changes of the system. Note that the entries of the observability matrix (50) are directly obtained from the model realization, while the entries of the dynamic matrix (51) are represented by the time-discrete impulse response between the actuator u and the sensor z . The input vector $\mathbf{z}_{\mathbf{p}}(k)$ and output vector $\mathbf{u}_{\mathbf{p}}(k)$ are defined collecting the corresponding time-signals at each discrete step

$$\mathbf{z}_{\mathbf{p}}(k) = \begin{bmatrix} z(k+1|k) \\ z(k+2|k) \\ \vdots \\ z(k+M|k) \end{bmatrix}, \quad \mathbf{u}_{\mathbf{p}}(k) = \begin{bmatrix} u(k|k) \\ u(k+1|k) \\ \vdots \\ u(k+N-1|k) \end{bmatrix}. \quad (52)$$

Thus, the matrix relation (49) provides a linear relation between the state $\mathbf{v}(k)$ and the output $\mathbf{z}_{\mathbf{p}}(k)$ when the system is forced by the control input $\mathbf{u}_{\mathbf{p}}(k)$. The evaluation of the future output vector $\mathbf{z}_{\mathbf{p}}(k)$ represents the *prediction* step of the procedure; indeed, assuming that the control signal contained in the vector $\mathbf{u}_{\mathbf{p}}(k)$ is known, we aim at computing the future output $\mathbf{z}_{\mathbf{p}}(k)$, related to the trajectory emanating from the initial condition $\mathbf{v}(k)$.

By following the same rationale already adopted in the optimal control problem, a cost function $\mathcal{L}(k)$ that minimizes the output $z(t)$ while limiting the control expense is defined,

$$\begin{aligned} \mathcal{L}(k) &= \sum_{i=1}^M z^H(k+i|k) w_z z(k+i|k) \\ &\quad + \sum_{i=0}^{N-1} u^H(k+i|k) w_u u(k+i|k) = \\ &= \mathbf{z}_{\mathbf{p}}(k)^H \mathbf{W}_{\mathbf{z}} \mathbf{z}_{\mathbf{p}}(k) + \mathbf{u}_{\mathbf{p}}(k)^H \mathbf{W}_{\mathbf{u}} \mathbf{u}_{\mathbf{p}}(k). \end{aligned} \quad (53)$$

The parameters $\mathbf{W}_{\mathbf{z}}$ and $\mathbf{W}_{\mathbf{u}}$ are represented by block diagonal matrices containing the weights w_z and w_u . One may also have non-quadratic costs functions in MPC; examples are given by Bewley *et al.* (2001) for the control of a turbulent channel. In our case, we choose a quadratic cost function in order to compare performance with the LQR controller. By combining the cost function (53) and the state equation (49), we get

$$\begin{aligned} \mathcal{L}(k) &= \mathbf{z}_{\mathbf{p}}(k)^H \mathbf{W}_{\mathbf{z}} \mathbf{z}_{\mathbf{p}}(k) + \mathbf{u}_{\mathbf{p}}(k)^H \mathbf{W}_{\mathbf{u}} \mathbf{u}_{\mathbf{p}}(k) = \\ &= [\mathbf{P}_{\mathbf{z}\mathbf{v}}\mathbf{v}(k) + \mathbf{P}_{\mathbf{z}\mathbf{u}}\mathbf{u}_{\mathbf{p}}(k)]^H \mathbf{W}_{\mathbf{z}} [\mathbf{P}_{\mathbf{z}\mathbf{v}}\mathbf{v}(k) + \mathbf{P}_{\mathbf{z}\mathbf{u}}\mathbf{u}_{\mathbf{p}}(k)] + \\ &\quad + \mathbf{u}_{\mathbf{p}}(k)^H \mathbf{W}_{\mathbf{u}} \mathbf{u}_{\mathbf{p}}(k). \end{aligned} \quad (54)$$

Note that this manipulation is analogous to the definition of Lagrangian already shown for the LQR problem (42). The minimization of $\mathcal{L}(k)$ with respect of $\mathbf{u}_{\mathbf{p}}(k)$ reads

$$\min_{\mathbf{u}_{\mathbf{p}}(k)} \left\{ \frac{1}{2} \mathbf{u}_{\mathbf{p}}^H(k) \mathbf{H} \mathbf{u}_{\mathbf{p}}(k) + \mathbf{c}(k) \mathbf{u}_{\mathbf{p}}(k) : C \mathbf{u}_{\mathbf{p}}(k) \leq D \right\} \quad (55)$$

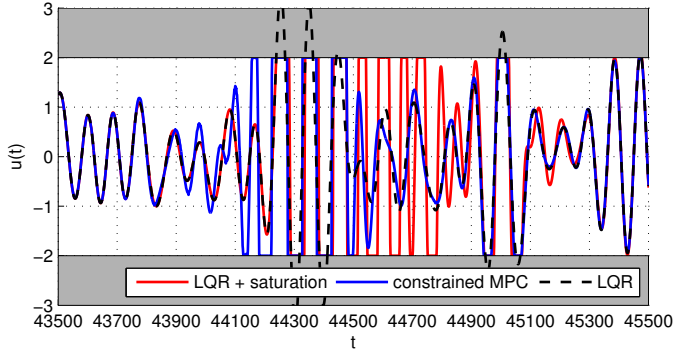


Figure 13: Control design in presence of constraints: the grey regions indicate the limits imposed to the amplitude of the control signal $u(t)$. The control $u(t)$ is designed following two different strategies: LQR with a saturation function (—) and constrained MPC (—), see §3.2.2. The LQR solution (---) is introduced as reference. The performances of the controllers are shown in terms of *rms*-velocity reduction in Figure 14.

where

$$\begin{aligned} \mathbf{H} &= 2 (\mathbf{P}_{\mathbf{z}\mathbf{u}}^H \mathbf{W}_{\mathbf{z}} \mathbf{P}_{\mathbf{z}\mathbf{u}} + \mathbf{W}_{\mathbf{u}}) \\ \mathbf{c}(k) &= 2 \mathbf{v}^H(k) \mathbf{P}_{\mathbf{z}\mathbf{v}}^H \mathbf{W}_{\mathbf{z}} \mathbf{P}_{\mathbf{z}\mathbf{u}} \end{aligned} \quad (56)$$

and $\mathbf{C}\mathbf{u}_{\mathbf{p}}(k) \leq D$ is a constraint (Bryd *et al.* 1999), which we have not specified yet. Once this minimization problem is solved, the control signal is applied for one time step, corresponding to $\Delta T = T_a$, followed by a new iteration at step $k + 1$.

3.2.2. Actuator saturation as constraint

The need of introducing constraints in the optimization process usually arises when we consider real actuators characterized by nonlinear behaviour, due for instance to saturation effects. For example, the body force generated by plasma actuators (Grundmann & Tropea 2008; Corke *et al.* 2010) – usually approximated by considering the macroscopic effects on a flow – is often modelled as a nonlinear function of the voltage (Suzen *et al.* 2005; Kriegseis 2011).

Consider now a control signal, whose amplitude is required to be bounded in the interval $-u_{\max} \leq u \leq u_{\max}$. We thus minimize

$$\min_{\mathbf{u}_{\mathbf{p}}(k)} \left\{ \frac{1}{2} \mathbf{u}_{\mathbf{p}}^H(k) \mathbf{H} \mathbf{u}_{\mathbf{p}}(k) + \mathbf{c}(k) \mathbf{u}_{\mathbf{p}}(k) : \bar{\mathbf{u}}_{\min} \leq \mathbf{u}_{\mathbf{p}}(k) \leq \bar{\mathbf{u}}_{\max} \right\}, \quad (57)$$

where \mathbf{H} and \mathbf{c} are given by (56). One may solve this constrained MPC using nonlinear programming (Boyd & Vandenberghe 2004). Since the function to be minimized is a quadratic function, we have used a reflective Newton

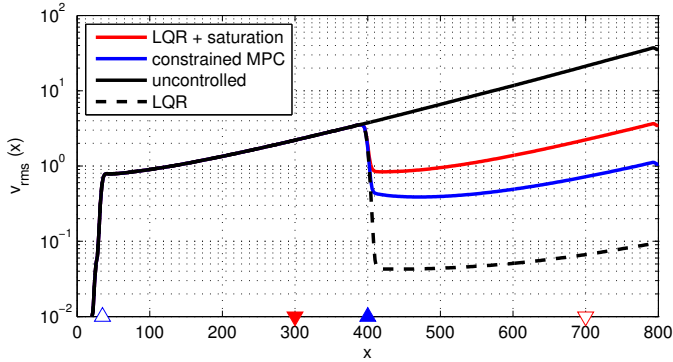


Figure 14: Control of the KS equation. The *rms* velocity as a function of the x direction is analyzed; the uncontrolled configuration (—) is compared to three different control strategies already considered in Figure 13 (same legend).

method suggested by Coleman & Li (1996); this method is implemented in the MATLAB[®] routine `quadprog.m`.

We proceed by comparing the performance of the MPC controller with the LQR solution discussed in §3.1.1. For a direct comparison, we apply an *ad hoc* saturation function to the LQR control signal, i.e.

$$u_{LQR} = \begin{cases} u_{LQR} & \text{if } \bar{u}_{min} < u_{LQR} < \bar{u}_{max} \\ \bar{u}_{min} & \text{if } \bar{u}_{min} \geq u_{LQR} \\ \bar{u}_{max} & \text{if } \bar{u}_{max} \leq u_{LQR} \end{cases}. \quad (58)$$

As shown in Figure 13, the control signal computed by the MPC (blue solid line) closely follows the LQR solution (dashed black line), except in the intervals where the value is larger or smaller than the imposed constraint. By simply applying the saturation function in (58) to the LQR signal, the controller becomes suboptimal; the resulting solution deviates from the optimal one and settles back on it after $t \approx 300$ time units. Simply cutting off the actuator signal of LQR results in a significant reduction of performance, which in terms of root-mean-square (*rms*) is almost one order of magnitude (shown in Figure 14). The main drawback of the constrained MPC is the computational time required by the on-line optimization, that can be prohibitive in experimental settings.

3.2.3. MPC for linear systems without constraints

For a linear system with the quadratic cost function (40) but without constraints, a prediction/actuation time sufficiently long allows to approximate the solution of the LQR. This is not obvious from the mere comparison of the continuous-time LQR-objective function, (40) and (42), and the discrete-time MPC-objective function, (53) and (54). For a detailed discussion, we refer to Anderson & Moore

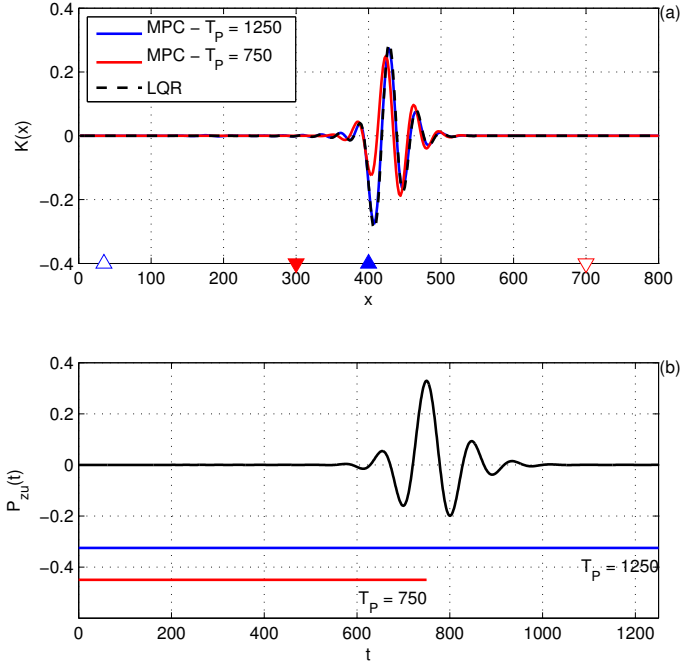


Figure 15: In (a) the LQR solution (§3.1.1) is compared to the MPC gains computed for two different times of optimization T_p without constraints, see §3.2.3. The optimization times are compared to the impulse response $\mathcal{P}_{zu}(t)$ (b). Note that for longer time T_p , covering the main dynamics of the impulse response $\mathcal{P}_{zu}(t)$, the MPC and LQR solutions are equivalent.

(1990), where the equivalence is demonstrated analytically. In the following, the equivalence is exemplified using the KS equation.

When there are not imposed constraints, the optimization problem in (55) corresponds to a Quadratic Program (Boyd & Vandenberghe 2004); by taking the derivative of $\mathcal{L}(k)$ with respect of $\mathbf{u}_p(k)$, we may obtain $\mathbf{u}_p(k)$ as solution of the following least-square problem

$$\begin{aligned}
 \mathbf{u}_p(k) &= -\mathbf{H}^\dagger \mathbf{c}^H = \\
 &= -(\mathbf{P}_{zu}^H \mathbf{W}_z \mathbf{P}_{zu} + \mathbf{W}_u)^\dagger \mathbf{P}_{zu}^H \mathbf{W}_z \mathbf{P}_{zv} \mathbf{v}(k) = \\
 &= \begin{bmatrix} \mathbf{K}_0 \\ \mathbf{K}_1 \\ \vdots \\ \mathbf{K}_{N-1} \end{bmatrix} \mathbf{v}(k), \tag{59}
 \end{aligned}$$

where $(\cdot)^\dagger$ indicates the Moore-Penrose generalized inverse matrix, (Penrose 1955). Note that this is a least square problem (in general, $M \geq N$). If we assume an actuation time-horizon $T_a = \Delta t$, at each time step the control signal $u(k)$ reads

$$u(k) = \mathbf{K}_0 \mathbf{v}(k). \quad (60)$$

In Figure 15(a), the solid dashed line corresponds to the LQR gain obtained by solving a Riccati equation, while the coloured lines correspond to the unconstrained MPC solution for different final time of prediction T_p . For a shorter time of optimization ($T_p = 750$, red solid line) only a portion of the dynamics of $\hat{\mathcal{P}}_{zu}(i)$ (see Figure 15(b)) is contained in the MPC gain. For longer times ($T_p = 1250$, blue solid line) the MPC converges to the infinite-time horizon LQR solution.

4. Estimation

In this section, we assume that the only information we can extract from the system is the measurement $y(t)$. This signal is used to provide an estimation $\hat{\mathbf{v}}(t)$ of the state such that the error given by

$$\mathbf{e}(t) = \mathbf{v}(t) - \hat{\mathbf{v}}(t), \quad (61)$$

is kept as small as possible. We first derive the classical Kalman Filter, where in addition to $y(t)$, one requires a state-space model of the physical system. Then we discuss the least-mean square (LMS) technique, which only relies on the measurement $y(t)$.

4.1. Luenberger observer and Kalman filter

The observer is a system in the following form

$$\dot{\hat{\mathbf{v}}}(t) = \mathbf{A} \hat{\mathbf{v}}(t) + \mathbf{B}_u u(t) - \mathbf{L} (y(t) - \hat{y}(t)), \quad (62)$$

$$\hat{y}(t) = \mathbf{C}_y \hat{\mathbf{v}}(t), \quad (63)$$

$$\hat{z}(t) = \mathbf{C}_z \hat{\mathbf{v}}(t). \quad (64)$$

This formulation was proposed for the first time by Luenberger in Luenberger (1979), from whom it takes the name. Comparing this system with (18), it can be noticed that it takes into account the actuator signal $u(t)$ but it ignores the unmeasurable inputs – the disturbance $d(t)$ and the measurement error $n(t)$. In order to compensate this lack of information, a correction term based on the estimation $\hat{y}(t)$ of the measurement $y(t)$ is introduced, filtered by the gain matrix \mathbf{L} .

The aim is to design \mathbf{L} in order to minimize the magnitude of the error between the real and the estimated state, i.e. expression defined in (61). Taking the difference term by term between (18) and (62), an evolution equation for the $\mathbf{e}(t)$ is obtained,

$$\dot{\mathbf{e}}(t) = (\mathbf{A} + \mathbf{L}\mathbf{C}) \mathbf{e}(t) + \mathbf{B}_d d(t) - \mathbf{L}n(t). \quad (65)$$

It can be seen that the error is forced by the disturbance $d(t)$ and the measurement error $n(t)$, i.e. precisely the unknown inputs of the system.

4.1.1. Kalman filter

In the Kalman filter approach both the disturbance $d(t)$ and the measurement error $n(t)$ are modelled by white noise, requiring a statistical description of the signals. The auto-correlation of the disturbance signal is given by

$$\mathcal{R}_d(\tau) \triangleq \int_{-\infty}^{+\infty} d(t) d^H(t - \tau) dt. \quad (66)$$

This function tells us how much a signal is correlated to itself after a shift τ in time. For a white noise signal this function is non-zero only when a zero shifting ($\tau = 0$) in time is considered and its value is the variance of the signal. Hence, the correlation functions for the considered inputs signal $d(t)$ and $n(t)$ are

$$\mathcal{R}_d(\tau) = R_d \delta(\tau) \quad \text{and} \quad \mathcal{R}_n(\tau) = R_n \delta(\tau), \quad (67)$$

where R_d and R_n are the variances of the two signals and $\delta(\tau)$ is the continuous Dirac delta function. When a system is forced by random signals, also the state becomes a random process and it has to be described via its statistical properties. Generally the calculation of these statistics requires a long time history of the response of the system to the random inputs. But for the linear system (65), it is possible to calculate the variance of the state $\mathbf{R}_e \in \mathbb{R}^{n_v \times n_v}$ by solving the following Lyapunov equation (Bagheri *et al.* 2009c)

$$(\mathbf{A} + \mathbf{L}\mathbf{C}_y)^H \mathbf{R}_e + \mathbf{R}_e (\mathbf{A} + \mathbf{L}\mathbf{C}_y) + \mathbf{B}_d R_d \mathbf{B}_d^H + \mathbf{L} R_n \mathbf{L}^H = \mathbf{0}. \quad (68)$$

The trace of \mathbf{R}_e is a measure of how much the mean value of the error $\mathbf{e}(t)$ differs from zero during its time evolution. One may thus define the following cost function for the design of \mathbf{L}

$$\mathcal{N} = \text{Tr}(\mathbf{R}_e) = \lim_{T \rightarrow \infty} \frac{1}{2T} \int_{-T}^T \mathbf{e}^H(t) \mathbf{e}(t) dt, \quad (69)$$

where $\text{Tr}(\cdot)$ indicates the trace operator.

With a similar approach as in §3.1, we define a Lagrangian:

$$\begin{aligned} \tilde{\mathcal{N}} = \text{Tr} \left\{ \mathbf{R}_e + \boldsymbol{\lambda} \left[(\mathbf{A} + \mathbf{L}\mathbf{C}_y)^H \mathbf{R}_e + \mathbf{R}_e (\mathbf{A} + \mathbf{L}\mathbf{C}_y) + \right. \right. \\ \left. \left. + \mathbf{B}_d R_d \mathbf{B}_d^H + \mathbf{L} R_n \mathbf{L}^H \right] \right\} \end{aligned} \quad (70)$$

where the Lagrangian multiplier $\boldsymbol{\lambda}$ enforces the constraint given by (68). The solution of the minimization is obtained by imposing the solution to be stationary respect the three parameters \mathbf{L} , \mathbf{R}_e and $\boldsymbol{\lambda}$. The zero-gradient condition for \mathbf{L} gives us the expression for the estimation gain,

$$\mathbf{L} = -R_n^{-1} \mathbf{C}_y \mathbf{R}_e. \quad (71)$$

The zero-gradient condition for the Lagrangian multiplier $\boldsymbol{\lambda}$ returns the Lyapunov equation in (68): combining this equation with (71), a Riccati equation is

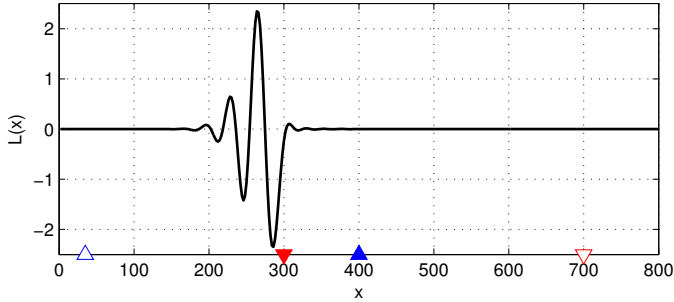


Figure 16: Kalman estimation gain \mathbf{L} computed for $R_d = 1$ and $R_n = 0.1$, (see §4.1.1). [script06.m]

obtained for \mathbf{R}_e :

$$\mathbf{A}^H \mathbf{R}_e + \mathbf{R}_e \mathbf{A} - \mathbf{R}_e \mathbf{C}_y^H R_n^{-1} \mathbf{C}_y + \mathbf{B}_d R_d \mathbf{B}_d^H = \mathbf{0}. \quad (72)$$

In Figure 16 the estimation gain \mathbf{L} is shown, where it can be observed that the spatial support is localized in the region immediately upstream of the sensor y . In this region the amplitude of the forcing term in the estimator is the largest to suppress estimation error. In Figure 17 we compare the full state (a) to the estimated state (b) when the system is forced by a noise signal $d(t)$. As a result of strong convection, we observe that an estimation is possible only after the disturbance has reached the sensor at $x = 300$, since upstream of this point there are no measurements. For control design it is important that $\mathbf{v}(t)$ is well estimated in the region where the actuators are placed; hence, the actuators have to be placed downstream of the sensors (Belson *et al.* 2013; Juillet *et al.* 2013).

4.2. Estimation based on linear filters

A significant drawback of the Kalman filter, is that it requires a model of the disturbance \mathbf{B}_d for the solution of the Riccati equation (72). One may circumvent this issue by using FIR to formulate the estimation problem. In analogue to the formulations based LQR (model based) and on MPC (FIR based), we will compare and link the Kalman filter to a system identification technique called the Least-Square-Mean filter (LMS). Many other system identification technique exists, the most common being the AutoRegressive-Moving-Average with eXogenous inputs (ARMAX) employed in the work of Hervé *et al.* (2012).

From (62–64), we observe that the estimator-input is the measurement $y(k)$, while the output is given by the estimated values of $z(k)$. The associated FIR of this system is

$$\hat{z}(k) = \sum_{i=N_{i,zy}}^{N_{f,zy}} \left(-\mathbf{C}_z \hat{\mathbf{A}}^{i-1} \Delta t \mathbf{L} \right) y(k-i) = \sum_{i=N_{i,zy}}^{N_{f,zy}} \tilde{\mathcal{E}}_{zy}(i) y(k-i) \quad (73)$$

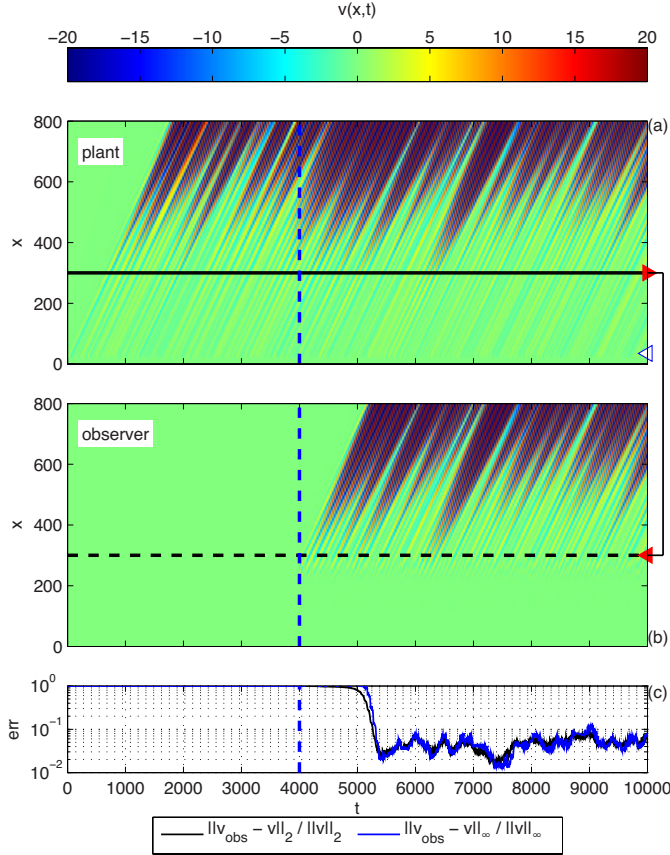


Figure 17: Spatio-temporal evolution of the response of the system to a disturbance $d(t)$ (a), compared to the estimated full-order state, using a Kalman filter (b); the contours are shown as a function of the streamwise direction (x) and time (t). The error-norm between the original state and the estimated state is shown in (c). The vertical blue, dashed line indicates when the estimator is turned on. [script06.m]

where $\hat{\mathbf{A}} = e^{(\mathbf{A} + \mathbf{L}\mathbf{C}_y)\Delta t}$ and $\tilde{\mathcal{E}}_{zy}(i)$ denotes the impulse response from the measurement $y(k)$ to the output $z(k)$. Note that, since we are considering a convectively unstable system, the sum in (73) is truncated using appropriate limits $N_{i,zy}$ and $N_{f,zy}$ (Aström & Wittenmark 1995). Next, we present a method where $\tilde{\mathcal{E}}_{zy}(i)$ is approximated directly from measurements, instead of its construction using the state-space model.

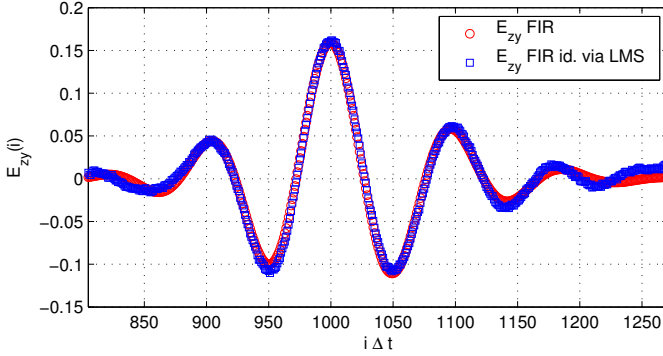


Figure 18: Impulse responses ($y \rightarrow z$) of the estimator as a function of the discrete-time. Red circles (\circ) correspond to the FIR time-discrete Kalman-filter-based kernel $\tilde{\mathcal{E}}_{zy}(i)$ and the blue squares (\square) to the one identified by the LMS algorithm. [script07.m]

4.2.1. Least-mean-square (LMS) filter

The main idea is to identify an estimated output $\hat{z}(k)$ for the system, by minimizing the error

$$e(k) = \hat{z}(k) - z(k) = \left(\sum_{i=N_{i,zy}}^{N_{f,zy}} \tilde{\mathcal{E}}_{zy}(i) y(k-i) \right) - z(k), \quad (74)$$

where $z(k)$ is the reference measurement. The unknown of the problem is the time-discrete kernel $\tilde{\mathcal{E}}_{zy}(i)$. Thus, we aim at adapt the kernel $\tilde{\mathcal{E}}_{zy}(i)$ such that at each time step the error $e(k)$ is minimized, i.e.

$$\min_{\tilde{\mathcal{E}}_{zy}} e^2(k). \quad (75)$$

The minimization can be performed using a steepest descent algorithm (Haykin 1986); thus, starting from an initial guess at $k = 0$ for $\hat{z}(k)$, $\tilde{\mathcal{E}}_{zy}$ is updated at each iteration as

$$\tilde{\mathcal{E}}_{zy}(i|k+1) = \tilde{\mathcal{E}}_{zy}(i|k) + \mu(k) \lambda(i|k), \quad (76)$$

where $\lambda(i|k)$ is the direction of the update and $\mu(k)$ is the step-length. Note that each iteration corresponds to one time step. The direction can be obtained from the local gradient, which is given by,

$$\lambda(i|k) = -\frac{\partial e^2(k)}{\partial \tilde{\mathcal{E}}_{zy}(i)} = -2 e(k) y(k-i). \quad (77)$$

This expression was obtained by forming the gradient of the error $e(k)$ with respect to $\tilde{\mathcal{E}}_{zy}(i)$ and making use of the estimated output $\hat{z}(k)$ (73).

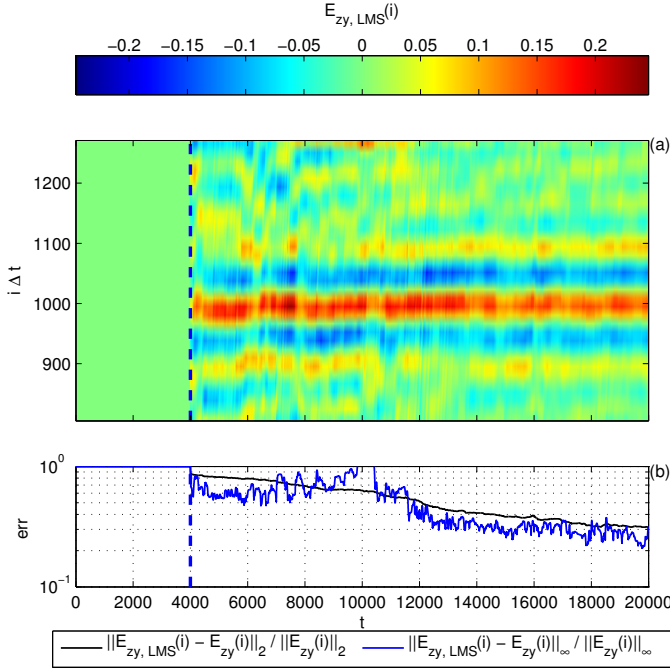


Figure 19: In (a) the evolution of $\tilde{\mathcal{E}}_{zy}(i)$ is calculated by an adaptive LMS filter and shown as a function of the discrete-time ($i\Delta t$). The estimation starts at $t = 4000$, as indicated by a blue dashed line (- -). As the iteration progresses, the error-norm constantly reduces (c). [script07.m]

The second variable that needs to be computed in (76) is the step-length $\mu(k)$. Consider the error at time-step k computed with the updated kernel $\tilde{\mathcal{E}}_{zy}(i|k+1)$

$$\begin{aligned} \tilde{e}(k) &= \left(\sum_{i=N_{i, zy}}^{N_{f, zy}} \tilde{\mathcal{E}}_{zy}(i|k+1) y(k-i) \right) - z(k) = \\ &= e(k) + \mu(k) \left(\sum_{i=N_{i, zy}}^{N_{f, zy}} \lambda(i|k) y(k-i) \right), \end{aligned} \quad (78)$$

where (75) and (76) have been used. The step-length $\mu(k)$ is calculated at each time step in order to fulfil

$$\min_{\mu(k)} \tilde{e}(k)^2 \quad (79)$$

by imposing a zero-derivative condition with respect to $\mu(k)$,

$$\frac{\partial \tilde{e}(k)^2}{\partial \mu(k)} = 2 \tilde{e}(k) \left(\sum_{i=N_{i, z_y}}^{N_{f, z_y}} \lambda(i|k) y(k-i) \right) = 0. \quad (80)$$

Assuming that

$$\sum_{i=N_{i, z_y}}^{N_{f, z_y}} \lambda(i|k) y(k-i) \neq 0 \quad (81)$$

and considering (78), the optimal step length becomes

$$\mu(k) = -\frac{e(k)}{\sum_i \lambda(i|k) y(k-i)}. \quad (82)$$

In Figure 19(a), the LMS-identified kernel $\tilde{\mathcal{E}}_{zy}(i)$ is shown as a function of time $t = k\Delta t$. When the LMS filter is turned on at $t = 4000$, the filter starts to compute the kernel, which progressively adapts. While the iteration proceeds, the error decreases as shown in Figure 19(b). In the limit of $T \rightarrow \infty$, when a steady solution can be assumed, the kernel computed by the LMS filter converges to the kernel $\tilde{\mathcal{E}}_{zy}$ obtained by the Kalman filter (see Figure 18).

The main drawback of the LMS approach is that the method is susceptible to a numerical stability (Haykin 1986). A usual way for improving the stability is to bound the step-length $\mu(k)$ by introducing an upper limit. In particular, it can be proven that in order to ensure the convergence of the algorithm, the following condition has to be satisfied

$$0 < \mu(k) < \bar{\mu} = \frac{2}{R_y}, \quad (83)$$

where the upper-bound $\bar{\mu}$ is defined by the variance R_y of the measurement y , i.e. the input signal to LMS filter.

5. Compensator

Using the theory developed in §3 and §4, we are now ready to tackle the full control problem (Figure 20): given the measurement $y(t)$, compute the modulation signal $u(t)$ in order to minimize a cost function based on $z(t)$. In the first part of this section we will focus on the LQG regulator, that couples a Kalman filter to a LQR controller. Then we present a compensator based on adaptive algorithms using LMS techniques.

5.1. Linear-quadratic Gaussian (LQG) regulator

By solving the control and estimation Riccati equations and the associated gains (\mathbf{L} and \mathbf{K}), we build a system that has as an input the measurement $y(t)$ and as an output the control signal $u(t)$:

$$\dot{\hat{\mathbf{v}}}(t) = (\mathbf{A} + \mathbf{B}_u \mathbf{K} + \mathbf{L} \mathbf{C}_y) \hat{\mathbf{v}}(t) - \mathbf{L} y(t) \quad (84)$$

$$u(t) = \mathbf{K} \hat{\mathbf{v}}(t). \quad (85)$$

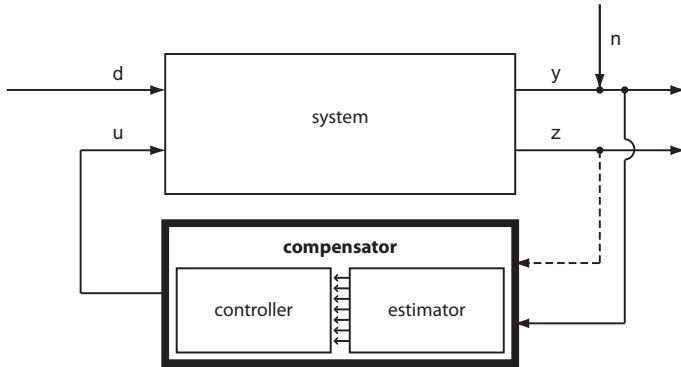


Figure 20: Block-diagram of the closed-loop system. The compensator, consisting of a controller coupled to an estimator, computes the control signal $u(t)$ given the measurement $y(t)$. The minimization of the measurement $z(t)$ is the target parameter of the controller. Note that in a feedforward controller, the output z can be used to add robustness to the compensator (for instance, in adaptive filters, §5.4).

This linear system is referred to as the LQG compensator. The estimation and control problem, discussed in the previous sections, are both optimal and guarantee stability as long as the system is observable and controllable (Glad & Ljung 2000). In particular, the disturbance d and the output z have to be placed respectively in the y -observable and u -controllable region (Figure 8). Under these conditions, a powerful theorem, known as the separation principle (Glad & Ljung 2000), states that optimality and stability transfer to the LQG compensator.

The closed-loop system obtained by connecting the compensator to the plant becomes

$$\begin{bmatrix} \dot{\mathbf{v}}(t) \\ \dot{\hat{\mathbf{v}}}(t) \end{bmatrix} = \begin{bmatrix} \mathbf{A} & \mathbf{B}_u \mathbf{K} \\ -\mathbf{L} \mathbf{C}_y & \mathbf{A} + \mathbf{B}_u \mathbf{K} + \mathbf{L} \mathbf{C}_y \end{bmatrix} \begin{bmatrix} \mathbf{v}(t) \\ \hat{\mathbf{v}}(t) \end{bmatrix} + \begin{bmatrix} \mathbf{B}_d \\ \mathbf{0} \end{bmatrix} d(t). \quad (86)$$

Figure 21 shows the response of (86) when a white random noise is considered as an input in $d(t)$. The horizontal solid black line in the top frame depicts the location of y sensor: this signal is used to force the compensator at the location depicted in the lower frame with a black dashed line. The compensator then provides a signal to the actuator (dashed black line in the upper frame) to cancel the propagating wave-packet. We let the two systems start to interact at $t = 4000$, as depicted by the dashed blue line. As soon as the first wave-packet, that is reconstructed by the compensator, reaches the actuation area, the compensator starts to provide a non-zero actuation signal back to the plant. Recall that the state $\hat{\mathbf{v}}(t)$ of the LQG compensator is an estimation of the state of the real plant $\mathbf{v}(t)$. This can be seen by comparing Figure 21(a) and

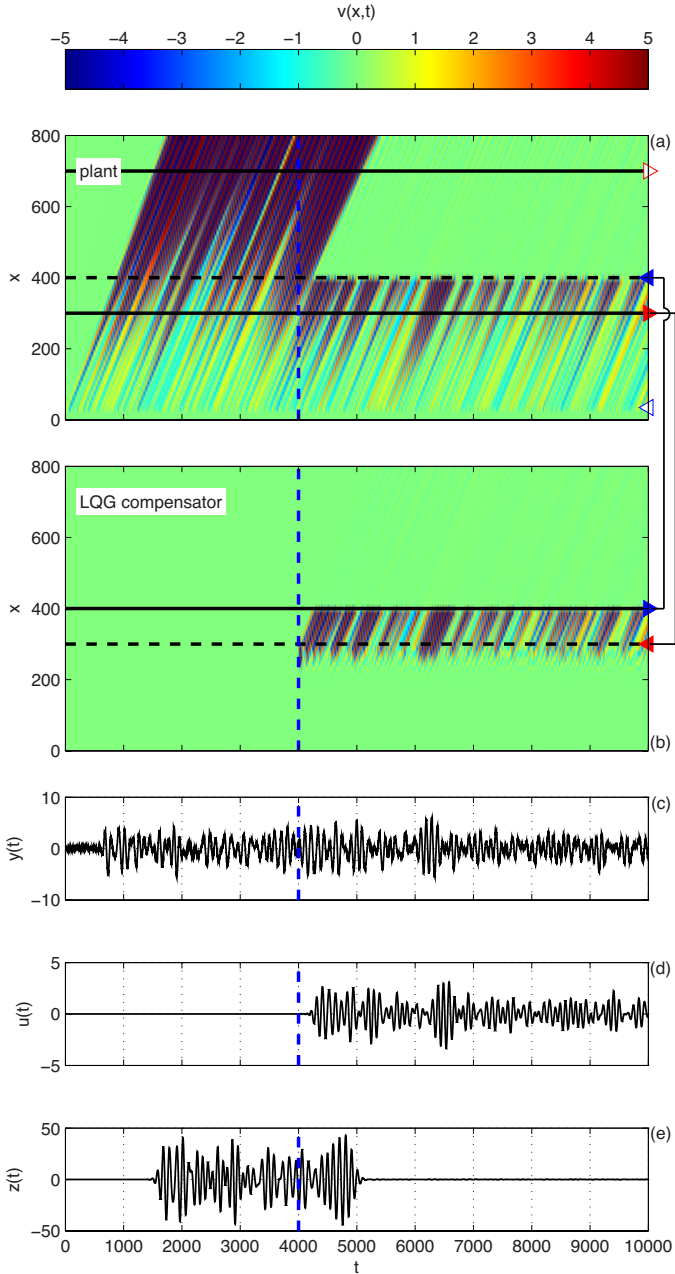


Figure 21: Spatio-temporal response in presence of a white noise input $d(t)$ for the closed-loop system (a) and the compensator (b); the disturbance is shown as a function of the streamwise direction (x) and time (t). The measurement $y(t)$, feeding the compensator, is shown in (c). At $t = 4000$ (— —), the compensator starts its action and after a short lag the actuator is fed with the computed control signal $u(t)$. The perturbation is cancelled, as shown in the contours reported in (a) and the output $z(t)$ minimized ($t > 5000$). [script08.m]

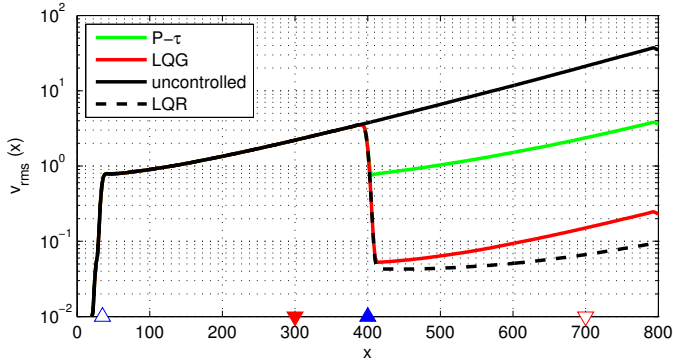


Figure 22: The *rms* velocity as a function of the streamwise location x is shown for the uncontrolled case (—), the LQG (—), the LQR (— —) and the opposition controller $P - \tau$ (—). [script08.m, script09.m]

Figure 21(b); downstream of the sensor y the state of the compensator matches the controlled plant.

Optimal controllers were applied to a large variety of flows, including oscillator flows, such as cavity and cylinder-wake flow, where the dynamic is characterized by self-sustained oscillations at well-defined frequencies, see Sipp *et al.* (2010). Note that $\mathbf{v}(t)$ and $\hat{\mathbf{v}}(t)$ have the same size: if complex systems are considered, a full-order compensator can be computationally demanding (Semeraro *et al.* 2013b); model reduction and compensator reduction enable to tackle these limitations and design low-order compensators, see §6.

5.2. Proportional controller with a time delay

One may ask how a simple proportional controller compares to the LQG for our configuration. In a proportional compensator, the control signal $u(t)$ is simply obtained by multiplying the measurement signal $y(t)$ by a constant P . Because of the strong time delays in our system, one needs to introduce also a time-delay τ between the measurement $y(t)$ and the control signal $u(t)$. The simplest control law for our system is

$$u(t) = P y(t - \tau), \quad (87)$$

where the “best” gain P and the time-delay τ can be found via a trial-and-error basis (in our case, $\tau = 250$ and $P = -0.5432$). This technique is also similar to opposition control (Choi *et al.* 1994), where blowing and suction is applied at the wall in opposition to the wall-normal fluid velocity, measured a small distance from the wall.

In Figure 22, we compare the velocity *rms* obtained with LQG compensator (red) and $P - \tau$ compensator (green). It can be observed that although both techniques reduce the perturbation amplitude downstream of the actuator

position ($x = 400$), the performance of the LQG regulator is nearly an order of magnitude better than the proportional controller. This can be mainly attributed to the additional degrees of freedom given by the $n_v \times n_v$ LQG feedback gains, as opposed to the two-degree freedom $P - \tau$ controller. Indeed, the LQG gains are computed assuming an accurate knowledge of the state-space model. Also shown (dashed-solid line) is the full-information LQR control whose performance is comparable the partial-information LQG controller: the difference between the two is due to the difference between the estimated state $\hat{\mathbf{v}}(t)$ and the real state $\mathbf{v}(t)$, i.e. the estimation error \mathbf{e} .

5.3. Model uncertainties

The LQG compensator is based on coupling an LQR controller and a Luenberger observer. Both of them are based on a model of the system and, as a consequence, their effectiveness is highly dependent on the quality of the model itself. Any difference between the model and the real plant can cause an abrupt reduction of the performances of the compensator (Doyle 1978; Belson *et al.* 2013). Model error can be attributed to, for example, nonlinearities due to the violation of the small perturbation hypothesis, nonlinearities of the actuator or sensors/actuators shape and positioning.

The robustness problem can be illustrated using a simple example. Suppose that one wants to cancel a travelling wave with a localized actuator; what one should do is to generate a wave that is exactly counter-phase with respect to the original one. Suppose that exact location of the actuation action is difficult to model. Shifting the actuator position slightly is equivalent to adding an error in the estimation of the phase of the original signal. This will in turn cause a mismatch between the wave that is meant to be cancelled and the wave created by the actuator, thus resulting in an ineffective wave cancellation – in the worst case, it may result in an amplification of the original wave.

As shown in Figure 23, when we displace the actuator further downstream by 5 spatial units and apply the compensator designed for the nominal condition to this modified system, the performance of the LQG regulator deteriorates. Since, the compensator provides a control signal that is meant to be applied in the nominal position of the actuator the control signal is not able to cancel the upcoming disturbance. Essentially, we are suffering from the lack of robustness of the feedforward configuration, since the sensor cannot measure the consequence of the defective actuator signal. There are different means to address this issue.

One can combine the feedforward configuration with a feedback action, in order to increase robustness. This can be accomplished using the second sensor z – downstream of the actuator – in combination with the estimation sensor y – placed upstream of the actuator. The combination of feedback and feedforward is the underlying idea of the MPC controller applied to our configuration (Goldin *et al.* 2013). However, there are some drawbacks due to the computational costs of the algorithm; indeed, the entries of the dynamic matrix (51) are computed during the prediction-step using time integration, whose domain increases with

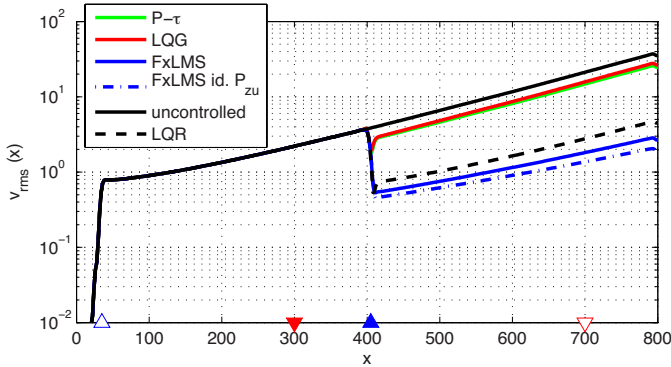


Figure 23: Robustness to uncertainties of the system: the actuator is displaced of 5 length units from its nominal position. The performance of the adaptive filter FXLMS (— and - -) are compared to the LQR (- -), LQG (-) and P - τ (-) compensators; as a reference, the uncontrolled case is shown (-). The *rms*-velocity is shown as a function of the streamwise direction (x). The adaptive filter performs reasonably well in presence of un-modelled dynamics; the performances are enhanced by the use of a on-line identified \hat{P}_{zu} (- -). The performances of the LQG (-) and P - τ (-) compensators are significantly reduced (compare with Figure 22). [script10.m]

the time-delays of the system. Thus, the integration and the dimensions of the resulting matrices can represent a bottleneck for the on-line optimization. An alternative is the use of an adaptive algorithm, which adapts the compensator response according to the information given by $z(t)$, as shown in the next section.

5.4. Filtered- X least-mean square (FXLMS)

The objective of FXLMS algorithm is to adapt the response of the compensator based on the information given by the downstream output z . The first step of the design is to describe the compensator in a suitable way in order to modify its response. The FXLMS algorithm is based on a FIR description of the compensator. Recall again that the compensator is a linear system (input is the measurement $y(t)$ and output is the control signal $u(t)$), which in time-discrete form can be represented by,

$$u(k) = \sum_{j=1}^{\infty} \tilde{\mathcal{K}}_{uy}(j) y(k-j) \approx \sum_{j=1}^{N_{uy}} \tilde{\mathcal{K}}_{uy}(j) y(k-j), \quad (88)$$

where $\tilde{\mathcal{K}}_{uy}(j)$ is a time-discrete kernel. Due to the stability of the system, we have $\tilde{\mathcal{K}}_{uy}(j) \rightarrow 0$ as $t \rightarrow \infty$, so that the sum can be truncated after N_{uy} steps.

In the case of LQG compensator $\tilde{\mathcal{K}}_{uy}$ has the form

$$\tilde{\mathcal{K}}_{uy}(j) \triangleq \mathbf{K} \exp[(\mathbf{A} + \mathbf{L}\mathbf{C}_y + \mathbf{B}_u\mathbf{K}) \Delta t(j-1)] \mathbf{L}$$

for $i = 1, 2, \dots$. The kernel $\tilde{\mathcal{K}}_{uy}(j)$ of the LQG controller is shown with red circles in Figure 24. In this case $N_{uy} = 533$, which gives $|\tilde{\mathcal{K}}_{uy}(j)| < 10^{-2}$ for $j > N_{uy}$.

The FXLMS technique modifies on-line the kernel $\tilde{\mathcal{K}}_{uy}(j)$ in order to minimize the square of measurement $z(t)$ at each time step (Sturzebecher & Nitsche 2003), i.e

$$\min_{\tilde{\mathcal{K}}_{uy}(j)} z^2(k). \quad (89)$$

The procedure is closely connected to the LMS filter discussed in §4.2.1 for the estimation problem. The kernel $\tilde{\mathcal{K}}_{uy}(j)$ is updated at each time step by a steepest-descend method:

$$\tilde{\mathcal{K}}_{uy}(j|k+1) = \tilde{\mathcal{K}}_{uy}(j|k) + \mu(k) \lambda(j|k) \quad (90)$$

where $\mu(k)$ is calculated from (82) and $\lambda(j|k)$ is the gradient of the cost function $z(k)$ with respect of the control gains $\tilde{\mathcal{K}}_{uy}(j)$. In order to obtain the update direction, consider the time-discrete convolution for $z(k)$,

$$\begin{aligned} z(k) &= \sum_{i=0}^{\infty} \tilde{\mathcal{P}}_{zd}(i) d(k-i) + \sum_{i=0}^{\infty} \tilde{\mathcal{P}}_{zu}(i) u(k-i) = \\ &= \sum_{i=0}^{\infty} \tilde{\mathcal{P}}_{zd}(i) d(k-i) + \sum_{i=0}^{\infty} \tilde{\mathcal{P}}_{zu}(i) \sum_{j=0}^{N_{uy}} \tilde{\mathcal{K}}_{uy}(j) y(k-i-j) = \\ &= \sum_{i=0}^{\infty} \tilde{\mathcal{P}}_{zd}(i) d(k-i) + \sum_{j=0}^{N_{uy}} \tilde{\mathcal{K}}_{uy}(j) \sum_{i=0}^{\infty} \tilde{\mathcal{P}}_{zu}(i) y(k-j-i). \end{aligned}$$

From this expression it is possible to obtain the gradient

$$\lambda(j|k) = -\frac{\partial z(k)^2}{\partial \tilde{\mathcal{K}}_{uy}(j)} = -2z(k) \sum_{i=0}^{\infty} \tilde{\mathcal{P}}_{zu}(i) y(k-j-i), \quad (91)$$

which can be simplified by introducing the filtered signal $y_f(k)$,

$$y_f(k) = \sum_{i=0}^{\infty} \tilde{\mathcal{P}}_{zu}(i) y(k-j-i) \approx \sum_{i=N_{i,zu}}^{N_{f,zu}} \tilde{\mathcal{P}}_{zu}(i) y(k-i) \quad (92)$$

Note that a FIR approximation of $\tilde{\mathcal{P}}_{zu}(i)$ has been used. Hence, the expression in (91) becomes,

$$\lambda(j|k) = -2z(k) y_f(k-j). \quad (93)$$

In order to get the descend direction, the measurement $y(t)$ is filtered by the plant transfer function $\tilde{\mathcal{P}}_{zu}(i)$.

Starting the on-line optimization from the compensator kernel $\tilde{\mathcal{K}}_{uy}(j)$ given by the LQG solution, the algorithm is tested on our problem. In Figure 23 we

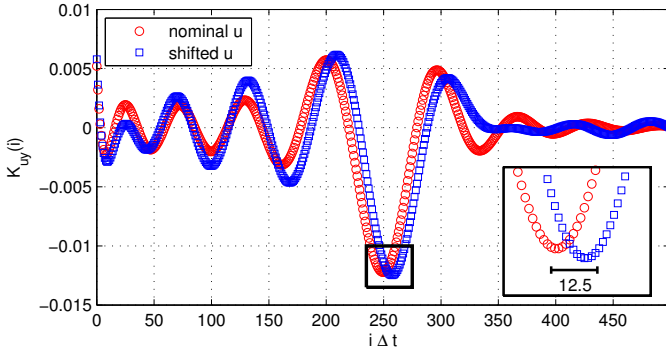


Figure 24: Robustness to uncertainties of the system: FXLMS control gain $\tilde{\mathcal{K}}_{uy}(i)$ (\square) is shifted along the time-discrete coordinate if compared to the static LQG gain (\circ) to compensate for the un-modelled shift in actuator position. [script10.m]

observe that the algorithm is able to recover some of the lost performance of LQG (due to shift in actuator position) and it is comparable to the full-information control performed by the LQR controller with the nominal gain \mathbf{K} . This is possible because of the adaptation of the kernel $\tilde{\mathcal{K}}_{uy}(j)$, to the new actuator location. Figure 24 shows how the convolution kernel has been modified by the algorithm; the kernel is shifted in time in order to restore the correct phase shift between the control signal $u(t)$ and the measurement signal $y(t)$ in the modified system. The shift in time between the two peaks (visible in the inset figure) is exactly the time that it takes for the wave-packet to cover the additional distance between the sensor and the actuator. Recalling from §2, that the wave-packet travels with a speed $V = 0.4$, it will take $\Delta x_u / V = 5 / 0.4 = 12.5$ time units to cover the extra space between u and y .

From (91), it can be noted that the FXLMS is not completely independent from a model of the system; in fact the convolution kernel $\tilde{\mathcal{P}}_{zu}(i)$ is needed to compute the gradient $\lambda(j|k)$ used by the algorithm. In the previous example, the nominal transfer function has been used, given by the model of the plant

$$\tilde{\mathcal{P}}_{zu}(i) = \mathbf{C}_z e^{\mathbf{A} \Delta t (i-1)} \mathbf{B}_u, \quad i = 1, 2, \dots \quad (94)$$

One may obtain a kernel $\tilde{\mathcal{P}}_{zu}(i)$ that is totally independent by the model – thus without any assumption on placement/shape of both actuator and sensors – by using the LMS identification algorithm derived in §4.2.1. In Figure 23, we compare $\tilde{\mathcal{P}}_{zu}(i)$ obtained from (94) using inaccurate state-space model – since actuator position has shifted (solid blue) – with $\tilde{\mathcal{P}}_{zu}(i)$ obtained by model-free identification using LMS technique (dashed blue). We observe that when combining adaptiveness with a more accurate model-free identification of $\tilde{\mathcal{P}}_{zu}(i)$, the performance is improved significantly.

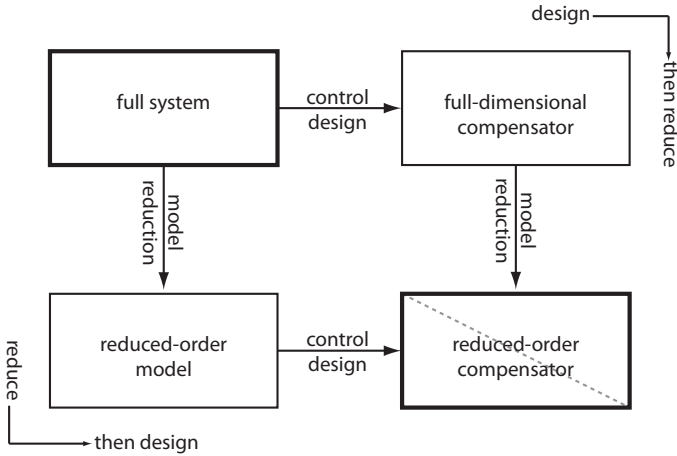


Figure 25: Two strategies are possible to compute a reduced-order compensator, reduce-then-design or a design-then-reduce. In general, the two paths do not lead at the same results.

Note that this algorithm when applied to flows dominated by convection, and thus characterized by strong time-delays, results in a feedforward controller where the feedback information is recovered by the processing of the measurements in z . This method is known to as *active noise cancellation* (Sturzebecher & Nitsche 2003; Erdmann *et al.* 2012). We can identify two time scales: a fast time-scale related to the estimation process and a slow time-scale related to the adaptive procedure (Gad-el Hak 2007). For this reason, this method is suitable for static or slowly varying model discrepancies.

6. Discussion

In this section, we discuss a few aspects that have not been addressed so far, but are important to apply the presented techniques to an actual flowing fluid. Many other important subjects such as choice of actuator and sensors, nonlinearities and receptivity are not covered by this discussion.

Low-order control design. The discretization of the Navier-Stokes system leads to high-dimensional systems that easily exceed 10^5 degrees of freedom. For instance, the full-order solution of Riccati equations for optimal control and Kalman filter problems cannot be obtained using standard algorithms (Benner 2004). One common strategy is to replace the high-dimensional system with a low-order system able to reproduce the essential input-output dynamics of the original plant. This approach is referred to as reduce-then-design (Anderson & Liu 1989), left part of Figure 25. First, a reduced-order model is identified using an appropriate model reduction or system identification technique; then the validated reduced-order model is used to design a low-order compensator.

The dual approach is called design-then-reduce or compensator reduction, right part of Figure 25. In this case, a high-order compensator is designed as first step (if possible). The second step is the reduction of the compensator to a low-order approximation.

Both the approaches lead to a low-order compensator that can be used to control the full-order plant, but they are not necessarily equivalent (Anderson & Liu 1989). In the reduce-then-design approach, we neglect a number of states during the model-order reduction of the open loop, that might become important for the dynamics of the closed-loop system. Despite these limitations, the reduce-then-design approach is the most common in flow control due to its computational advantages; indeed, the challenge of designing a high-dimensional compensator to be reduced strongly limits this alternative.

Model reduction. Following the reduce-then-design approach, the first step consists of identifying a reduced-order model, typically reproducing the I/O behaviour of the system. We can distinguish two classes of algorithms. The first category is based on a Petrov-Galerkin projection of the full-order system. In this case, the I/O behaviour of the system is reconstructed starting from a low-order approximation of the state-vector \mathbf{v}_r , characterized by a number of degree of freedom $r \ll n$; the projection can be performed on global modes (Akervik *et al.* 2007), proper orthogonal modes (POD), obtained from the diagonalization of the controllability Gramian (see §2.6), or balanced modes, for which the controllability and observability Gramians are equal and diagonal (Moore 1981; Rowley 2005; Bagheri *et al.* 2009*c*). This strategy has been widely used in the flow-control community in the past years for the identification of linear (Akervik *et al.* 2007; Ilak & Rowley 2008; Bagheri *et al.* 2009; Barbagallo *et al.* 2009; Semeraro *et al.* 2011) and nonlinear models (Noack *et al.* 2003; Siegel *et al.* 2008; Ilak *et al.* 2010). In particular, when nonlinear effects are considered, it is necessary to take into account the effect that a finite disturbance in the flow has on the base-flow, as shown by Noack *et al.* (2003) for a cylinder wake flow. At low Reynolds numbers, a small number of modes are sufficient to reproduce the behaviour of oscillators such as the cylinder wake, while a larger number of modes is required to reproduce the I/O behaviour of convective unstable flows. This is mainly due to the presence of strong time-delays (Glad & Ljung 2000) that characterize this type of systems, §2.5.

The second approach stems from the I/O analysis of the formal solution carried out in §2.5; we note that a low-order representation of the transfer function is enough to reconstruct the I/O behaviour of the system. The computation of this representation can be performed applying *system identification* algorithms (Ljung 1999). Once the transfer functions are identified, one constructs a reduced-order model in canonical form. These techniques were widely used for experimental investigations (see e.g. Lundell (2007) and Rathnasingham & Breuer (2003)) and have been recently applied also in numerical studies (Huang & Kim 2008; Hervé *et al.* 2012). Indeed, for linear systems, it can be shown that projection-based techniques and system identification techniques

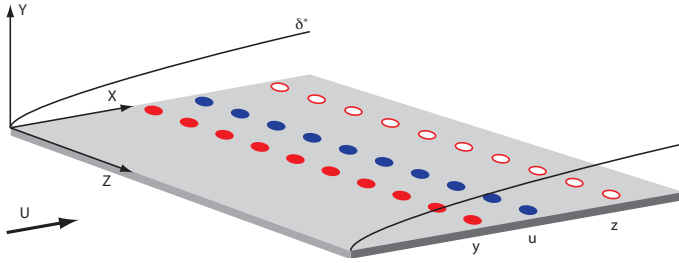


Figure 26: Control configuration for a three dimensional (3D) flow developing over a flat plate. A possible configuration consists of localized sensors and actuators placed along the spanwise direction.

can provide equivalent reduced-order models (Ma *et al.* 2011). We refer the reader to the reviews by (Bagheri & Henningson 2011) and (Sipp & Schmid 2013) for a broader overview.

Control of three-dimensional disturbances. A sketch of the three-dimensional control setup of the flow over a flat-plate is shown Figure 26. Compared to the 2D boundary-layer flow a single actuator u , sensor y and output z are now replaced by arrays of elements localized along the span-wise direction, resulting in a multi-input multi-output (MIMO) system. The localization (size and distance between elements) of sensors and actuators may significantly influence efficiency of the compensator (Semeraro *et al.* 2011, 2013). An important question one must address for MIMO systems is how to connect inputs to outputs. A first approach consists of coupling one actuator with only one sensor (for instance, the one upstream); in this case, the number of single-input single-output (SISO) *control units* equals the number of sensor/actuator pairs. This approach is called *decentralized* control-design; despite its simplicity in practical implementations, the stability in closed loop is not guaranteed (Glad & Ljung 2000). The dual approach where only one control-unit is designed and all the sensors are coupled to all the available actuators is called *centralized* control. In Semeraro *et al.* (2011), the centralized-controller strategy was found necessary for the design of a stable TS-wave controller. The main drawback of a fully centralized-control approach is that the number of connections for a flat plate of large span quickly becomes impractical due to all the wiring. One may then introduce a *semi-decentralized* controller, where small MIMO control-units are designed and connected to each other; in Dadfar *et al.* (2014), it is shown that a number of control-units can efficiently replace a full centralized control with a limited loss of performance.

Another important aspect that has been accounted for in a MIMO setting, is the choice of the objective function z . The minimization of a set of signals obtained from localized outputs with compact support does not necessarily correspond to a reduction of the actual perturbation amplitude in a global

sense. For 1D and 2D flow systems any measurement taken locally, close to the solid wall and downstream in the computational domain, is sufficient for obtaining consistency between the perturbation and signal minimization (Bagheri *et al.* 2009); this is not the case for 3D systems. An optimal way for choosing the output \mathbf{C}_z is the *output projection* suggested by Rowley (2005), where a projection on a POD basis is performed. The resulting signal $z(t)$ corresponds to the amplitude coefficients of the POD modes, i.e. the temporal behaviour of the most energetic coherent structure of the flow. This method can also provide useful guidelines for the location of output sensors.

7. Summary and conclusions

This work provides a comprehensive review on standard model-based techniques (LQR, Kalman filter, LQG, MPC) and model-free techniques (LMS, X-filtered LMS) for the delay of the transition from laminar to turbulence. We have focussed on the control of perturbation evolving in convective flows, using the linearized Kuramoto-Sivashinsky equation as a model of the flow over the flat-plate to characterize and compare these techniques. Indeed, this model provides the two important traits of convectively unstable fluid systems, namely, the amplifying behaviour of a stable system and a very large time delay.

Much research have been performed on flow control using the very elegant techniques based on LQR and LQG (Bagheri *et al.* 2009c; Semeraro *et al.* 2013; Juillet *et al.* 2013). Although, these techniques may lead to the best possible performance and they have stability guarantees (under certain restrictions), their implementation in experimental flow control settings raises a number obstacles: (1) The choice of actuator and sensor placement that yields a good performance of convectively unstable systems results in a feedforward system. We have highlighted the robustness issues arising from this configuration when using standard LQG-based techniques. (2) Disturbances, such as free-stream turbulence, and actuators, such as plasma actuators, can be difficult to model under realistic conditions. (3) The requirement of solving two Riccati equations is a major computational hassle, although it has successfully been addressed by the community using model-order reduction techniques (Bagheri *et al.* 2009) or iterative methods (Semeraro *et al.* 2013b).

Model-free techniques based on classical system-identification methods or adaptive-noise-cancellation techniques can cope with the limitations of model-based methods (Sturzebecher & Nitsche 2003). For example, we have presented algorithms that improve robustness by adapting to varying and un-modelled conditions. However, model-free techniques have their own limitations; (i) one may often encounter instabilities, which in contrast to LQR/LQG, cannot always be addressed in a straight-forward manner by using concepts such as controllability and observability. (ii) The number of free parameters (such as the limits of the sums appearing in FIR filters) that need to be modelled are many and chosen in a somewhat *ad-hoc* manner.

The conclusion is that there does not exist one single method that is able to deal with all issues, and the final choice depends on the particular conditions that must be addressed. While a model-based technique may provide optimality and physical insight, it may lack the robustness to uncertainties that adaptive methods are able to provide. We believe that future research will head towards hybrid methods, where controllers are partially designed using numerical simulations and partially using adaptive experiment-based techniques.

The authors acknowledge support the Swedish Research Council (VR-2012-4246, VR-2010-3910) and the Linné Flow Centre.

Appendix A. Numerical method

Finite-difference (FD) schemes are used to approximate the spatial derivatives in (12). In particular, a centered scheme based on stencils of five-nodes are used for the second-order and fourth-order derivatives while a one-node-backward scheme is used for the first-order derivative. The latter is required due to the convective nature of the system: a de-centered scheme reduces the spurious, numerical oscillation of the approximated solution (Quarteroni 2009).

The grid is equispaced $x_i = i \frac{L}{n_v}$, with $i = 1, 2, \dots, n_v$. Once the FD scheme is introduced, the time evolution at each of the internal node is solution of the ODE equation

$$\begin{aligned} \frac{dv'(t)}{dt} = & -V \sum_{j=-3}^1 d_{1,j}^b v'_{i+j}(t) - \frac{\mathcal{P}}{\mathcal{R}} \sum_{l=-2}^2 d_{2,l}^e v'_{i+l}(t) + \\ & - \frac{1}{\mathcal{R}} \sum_{l=-2}^2 d_{4,l}^c v'_{i+l}(t) + b_d(x_i) d(t) + b_u(x_i) u(t), \end{aligned} \quad (95)$$

where $v'_i(t) = v'(x_i, t)$ for $i = 1, 2, \dots, n_v$. The outflow boundary conditions in (10) on the right boundary of the domain lead to the linear system of equations,

$$\left. \frac{\partial v'}{\partial x} \right|_{x=L} = 0 \Rightarrow \sum_{j=-3}^1 d_{1,j}^b v'_{n_v+j}(t) = 0 \quad (96)$$

$$\left. \frac{\partial^3 v'}{\partial x^3} \right|_{x=L} = 0 \Rightarrow \sum_{j=-2}^2 d_{3,j}^c v'_{n_v+j}(t) = 0 \quad (97)$$

The solution of this system allows us to express the boundary nodes $i = n_v + 1, n_v + 2$ as a linear combination of the inner nodes. Similarly, the left boundary condition in (11) leads to an expression for the nodes $i = 0, -1$:

$$v'|_{x=0} = 0 \Rightarrow v'_0(t) = 0 \quad (98)$$

$$\left. \frac{\partial v'}{\partial x} \right|_{x=0} = 0 \Rightarrow \sum_{j=-1}^3 d_{1,j}^f v'_{0+j}(t) = 0 \quad (99)$$

where a forward FD scheme is used for the first-order derivative approximation. Equation (95) together with the boundary conditions can be rewritten in compact form as

$$\dot{\mathbf{v}}(t) = \mathbf{A} \mathbf{v}(t) + \mathbf{B}_d d(t) + \mathbf{B}_u u(t)$$

where $\mathbf{B}_d = \{b_d(x_i)\}$, $\mathbf{B}_u = \{b_u(x_i)\}$ and the matrix $\mathbf{A} \in \mathbb{R}^{n_v \times n_v}$ is a banded matrix (see also (18)).

The Crank-Nicolson method is used to march the system forward in time (18). Given a time step Δt , the value of the state $\mathbf{v}(t + \Delta t)$ is given by the expression:

$$\mathbf{v}(t + \Delta t) = \mathbf{CN}_I^{-1} [\mathbf{CN}_E \mathbf{v}(t) + \Delta t (\mathbf{B}_d d(t) + \mathbf{B}_u u(t))] \quad (100)$$

where $\mathbf{CN}_I = \mathbf{I} - \frac{\Delta t}{2} \mathbf{A}$ and $\mathbf{CN}_E = \mathbf{I} + \frac{\Delta t}{2} \mathbf{A}$. This is an implicit method, i.e. requires the solution of the linear system \mathbf{CN}_I^{-1} , and this operation can be numerically expensive.

Appendix B. Numerical code

A downloadable package of the MATLAB routines used to produce the results presented in this paper can be found at <http://www.mech.kth.se/nicolo/ks/>. The 11 scripts listed below cover all the methods that are presented in this work.

script00.m: Time evolution of a spatially localized initial condition. The time response of the plant to a Gaussian-shaped initial condition is calculated: the generated wave-packet travels downstream while growing and is detected by the outputs y and z . The spatio-temporal time evolution of $v(x, t)$ is plotted together with the output signals.

script01.m: Response to a white Gaussian disturbance $d(t)$. A white noise signal is considered as input $d(t)$ and the time-response of the plant is calculated. The statistics of the velocity are computed and visualized for comparison with the controlled cases.

script02.m: External description. An alternative description of the system, based on the Input/Output behaviour of the system is calculated. In particular, the response of the system is calculated via a FIR filter and compared with the LTI system description, i.e. internal description.

script03.m: Controllability and observability Gramians. The controllability and observability Gramians are computed solving the Lyapunov equations in (33–34).

script04.m: Linear-Quadratic Regulator. A LQR controller is applied to the plant and tested when the system is excited by a white Gaussian noise $d(t)$. The statistics of the velocity are computed and visualized in order to be compared to the other controlled cases.

script05.m: Model Predictive Control. Constrained MPC is used in presence of saturation of the actuator. The system is excited by a white Gaussian

noise $d(t)$. The statistics of the velocity are computed and visualized in order to be compared with the other controlled cases.

script06.m: Kalman filter. A Kalman filter is designed for the plant and used to estimate the system state when excited by a white Gaussian noise $d(t)$.

script07.m: Least-Mean Square filter. A LMS filter is used to identify the FIR-kernel E_{zy} . The resulting kernel is compared with the Kalman filter solution.

script08.m: Linear-Quadratic Gaussian compensator. A LQG compensator is designed coupling a LQR controller and a Kalman filter. The compensator is tested when the system is excited by a white Gaussian noise $d(t)$.

script09.m: $P - \tau$ compensator. A simple opposition control is designed using explicitly the time-delay. The system is excited by a white Gaussian noise $d(t)$. The control gain has been obtained by a trial and error procedure.

script10.m: Filtered-X Least-Mean Square algorithm. FXLMS algorithm is implemented. The initial condition is provided by the impulse response of the corresponding LQG compensator; a robustness test is carried by displacing the actuator location.

Following functions are required by the above scripts:

[A, x, I] = KS_init(nq). Given the number of degree of freedom n_v , it provides the state matrix **A** obtained by a FD discretization of the spatial derivatives. Five grid-point stencil FD schemes are used: in particular, a one grid point de-centered scheme is used to enhance the stability of the numerical solution.

d = fd_coeff(n, dx). It provides the FD coefficients used by **KS_init**.

REFERENCES

- AKERVIK, E., HÖPPFNER, J., EHRENSTEIN, U. & HENNINGSON, D. S. 2007 Optimal Growth, Model Reduction and Control in a Separated Boundary-layer Flow Using Global Eigenmodes. *J. Fluid Mech.* **579**, 305–314.
- AKHTAR, I., BORGGAARD, J., STOYANOV, M. & ZIETSMAN, L. 2010 On Commutation of Reduction and Control: Linear Feedback Control of a von Kármán Street. In *5th Flow Control Conference*, pp. 1–14. American Institute of Aeronautics and Astronautics.
- ANDERSON, B. & LIU, Y. 1989 Controller Reduction: Concepts and Approaches. *IEEE Trans. Autom. Control* **34**, 802–812.
- ANDERSON, B. & MOORE, J. 1990 *Optimal control: Linear Quadratic Methods*. Prentice Hall, New York.
- ARNOLD, W. I. & LAUB, A. 1984 Generalized eigenproblem algorithms and software for algebraic Riccati equations. *Proceedings of the IEEE* **72** (12), 1746–1754.
- ASTRÖM, K. J. & WITTENMARK, B. 1995 *Adaptive Control*, 2nd edn. Addison Wesley.
- BAGHERI, S., BRANDT, L. & HENNINGSON, D. S. 2009a Input–output analysis, model reduction and control of the flat-plate boundary layer. *J. Fluid Mech.* **620** (1), 263–298.

- BAGHERI, S. & HENNINGSON, D. S. 2011 Transition delay using control theory. *Philos. Trans. R. Soc.* **369**, 1365–1381.
- BAGHERI, S., HÖPFNER, J., SCHMID, P. J. & HENNINGSON, D. S. 2009*b* Input-Output Analysis and Control Design Applied to a Linear Model of Spatially Developing Flows. *Appl. Mech. Rev.* **62**.
- BAMIEH, B., PAGANINI, F. & DAHLEH, M. 2002 Distributed control of spatially invariant systems. *IEEE Trans. Autom. Control* **47** (7), 1091–1107.
- BANKS, H. T. & ITO, K. 1991 A numerical algorithm for optimal feedback gains in high dimensional linear quadratic regulator problems. *SIAM J. Control and Optimization* **29** (3), 499–515.
- BARBAGALLO, A., SIPP, D. & SCHMID, P. J. 2009 Closed-loop control of an open cavity flow using reduced order models. *J. Fluid Mech.* **641**, 1–50.
- BELSON, B. A., SEMERARO, O., ROWLEY, C. W. & HENNINGSON, D. S. 2013 Feedback control of instabilities in the two-dimensional Blasius boundary layer: The role of sensors and actuators. *Phys. Fluids* **25**.
- BENNER, P. 2004 Solving Large-Scale Control Problems. *IEEE Contr. Sys.* **24** (1), 44–59.
- BENNER, P., LI, J. & PENZL, T. 2008 Numerical solution of large-scale Lyapunov equations, Riccati equations, and linear-quadratic optimal control problems. *Numer. Linear Algebra Appl.* **15**, 755–777.
- BEWLEY, T. R. 2001 Flow Control: New Challenges for a New Renaissance. *Progr. Aerospace Sci.* **37**, 21–58.
- BEWLEY, T. R. & LIU, S. 1998 Optimal and Robust Control and Estimation of Linear Paths to Transition. *J. Fluid Mech.* **365**, 305–349.
- BEWLEY, T. R., MOIN, P. & TEMAM, R. 2001 DNS-based predictive control of turbulence: an optimal benchmark for feedback algorithms. *J. Fluid Mech.* **447** (1), 179–225.
- BOYD, S. & VANDENBERGHE, L. 2004 *Convex optimization*. Cambridge university press.
- BRYD, R. H., HRIBAR, M. E. & NOCEDAL, J. 1999 An Interior Point Algorithm for Large-Scale Nonlinear Programming. *SIAM Journal on Optimization* .
- BUSHNELL, D. M. & MOORE, K. J. 1991 Drag Reduction in Nature. *Ann. Rev. Fluid Mech.* **23** (65–79).
- CHARRU, F. 2011 *Hydrodynamic Instabilities*, 1st edn. Cambridge.
- CHEVALIER, M., HÖPFNER, J., AKERVIK, E. & HENNINGSON, D. S. 2007*a* Linear Feedback Control and Estimation Applied to Instabilities in Spatially Developing Boundary Layers. *J. Fluid Mech.* **588**, 163–187.
- CHEVALIER, M., HÖPFNER, J., BEWLEY, T. R. & HENNINGSON, D. S. 2006 State Estimation in Wall-bounded Flow Systems. Part 2: Turbulent Flows. *J. Fluid Mech.* **552**, 167–187.
- CHEVALIER, M., SCHLATTER, P., LUNDBLADH, A. & HENNINGSON, D. S. 2007*b* A pseudo-spectral solver for incompressible boundary layer flows. *Tech. Rep. TRITA-MEK 2007:07*. KTH Mechanics, Stockholm, Sweden.
- CHOI, H., MOIN, P. & KIM, J. 1994 Active Turbulence Control for Drag Reduction in Wall-bounded Flows. *J. Fluid Mech.* **262**, 75–110.
- COLEMAN, T. F. & LI, Y. 1996 A reflective Newton method for minimizing a

- quadratic function subject to bounds on some of the variables. *SIAM Journal on Optimization* **6** (4), 1040–1058.
- COLLIS, S. S., JOSLIN, R. D., SEIFERT, A. & THEOFILIS, V. 2004 Issues in active flow control: theory, control, simulation, and experiment. *Progr. Aerospace Sci.* **40** (4), 237–289.
- CORBETT, P. & BOTTARO, A. 2001 Optimal control of nonmodal disturbances in boundary layers. *Theoretical and Computational Fluid Dynamics* **15** (2), 65–81.
- CORKE, T. C., ENLOE, C. L. & WILKINSON, S. P. 2010 Dielectric Barrier Discharge Plasma Actuators for Flow Control. *Ann. Rev. Fluid Mech.* **42** (1), 505–529.
- CORTELEZZI, L., SPEYER, J. L., LEE, K. H. & KIM, J. 1998 Robust Reduced-Order Control of Turbulent Channel Flows via Distributed Sensors and Actuators. *IEEE 37th Conf. on Decision and Control* pp. 1906–1911.
- CVITANOVIĆ, P., ARTUSO, R., MAINIERI, R., TANNER, G. & VATTAY, G. 2012 Turbulence? In *Chaos: Classical and Quantum*, chap. 4. Niels Bohr Institute, Copenhagen, <http://ChaosBook.org/version14>.
- DADFAR, R., FABBIANE, N., BAGHERI, S. & HENNINGSON, D. S. 2014 Centralised versus decentralised active control of boundary layer instabilities. *Flow, Turb. and Comb.* **93** (4), 537–553.
- DOYLE, J. C. 1978 Guaranteed Margins for LQG Regulators. *IEEE Trans. Autom. Control* **AC-23** (4), 756–757.
- DOYLE, J. C., GLOVER, K., KHARGONEKAR, P. P. & FRANCIS, B. A. 1989 State-Space Solutions to Standard H_2 and H_∞ Control Problems. *IEEE Trans. Autom. Control* **34**, 831–847.
- ELLIOTT, S. & NELSON, P. 1993 Active noise control. *Signal Processing Magazine, IEEE* **10** (4), 12–35.
- ERDMANN, R., PÄTZOLD, A., ENGERT, M., PELTZER, I. & NITSCHKE, W. 2012 On active control of laminar-turbulent transition on two-dimensional wings. *Philos. Trans. R. Soc.* **369**, 1382–1395.
- GARCIA, C. E., PRETT, D. M. & MORARI, M. 1989 Model Predictive Control: Theory and Practice – A Survey. *Automatica* **25** (3), 335–348.
- GLAD, T. & LJUNG, L. 2000 *Control Theory*. London: Taylor & Francis.
- GOLDIN, N., KING, R., PÄTZOLD, A., NITSCHKE, W., HALLER, D. & WOIAS, P. 2013 Laminar Flow Control With Distributed Surface Actuation: Damping Tollmien-Schlichting Waves with Active Surface Displacement. *Exp. Fluids* **54** (3), 1–11.
- GRUNDMANN, S. & TROPEA, C. 2008 Active Cancellation of Artificially Introduced Tollmien-Schlichting Waves using Plasma Actuators. *Exp. Fluids* **44** (5), 795–806.
- GUNZBURGER, M. 2003 *Perspectives in Flow Control and Optimization*. SIAM.
- GAD-EL HAK, M. 1996 Modern Developments in Flow Control. *Appl. Mech. Rev.* **49**, 365–379.
- GAD-EL HAK, M. 2007 *Flow control: passive, active, and reactive flow management*. Cambridge University Press.
- HAYKIN, S. 1986 *Adaptive Filter Theory*. Prentice-Hall.
- HERVÉ, A., SIPP, D., SCHMID, P. J. & SAMUELIDES, M. 2012 A physics-based approach to flow control using system identification. *J. Fluid Mech.* **702**, 26–58.
- HÖGBERG, M. & BEWLEY, T. R. 2000 Spatially Localized Convolution Kernels for Feedback Control of Transitional Flows. *IEEE 39th Conf. on Decision and Control* **3278-3283**.

- HÖGBERG, M., BEWLEY, T. R. & HENNINGSON, D. S. 2003a Linear Feedback Control and Estimation of Transition in Plane Channel Flow. *J. Fluid Mech.* **481**, 149–175.
- HÖGBERG, M., BEWLEY, T. R. & HENNINGSON, D. S. 2003b Relaminarization of $Re_\tau = 100$ Turbulence Using Gain Scheduling and Linear State-feedback Control Flow. *Phys. Fluids* **15**, 3572–3575.
- HUANG, S. & KIM, J. 2008 Control and system identification of separated flow. *Phys. Fluids* **20**, 101509.
- HUERRE, P. & MONKEWITZ, P. A. 1990 Local and Global Instabilities in Spatially Developing Flows. *Ann. Rev. Fluid Mech.* **22**, 473–537.
- ILAK, M., BAGHERI, S., BRANDT, L., ROWLEY, C. W. & HENNINGSON, D. S. 2010 Model Reduction of the Nonlinear Complex Ginzburg-Landau Equation. *SIAM J. Appl. Dyn. Sys.* **9** (4), 1284–1302.
- ILAK, M. & ROWLEY, C. W. 2008 Modeling of Transitional Channel Flow Using Balanced Proper Orthogonal Decomposition. *Phys. Fluids* **20**, 034103.
- JACOBSON, S. A. & REYNOLDS, W. C. 1998 Active control of streamwise vortices and streaks in boundary layers. *J. Fluid Mech.* **360**, 179–211.
- JOSHI, S. S., SPEYER, J. L. & KIM, J. 1997 A Systems Theory Approach to the Feedback Stabilization of Infinitesimal and Finite-amplitude Disturbances in Plane Poiseuille Flow. *J. Fluid Mech.* **332**, 157–184.
- JOVANOVIĆ, M. R. & BAMIEH, B. 2005 Componentwise Energy Amplification in Channel Flows. *J. Fluid Mech.* **534**, 145–183.
- JUILLET, F., SCHMID, P. J. & HUERRE, P. 2013 Control of amplifier flows using subspace identification techniques. *J. Fluid Mech.* **725**, 522–565.
- KIM, J. & BEWLEY, T. R. 2007 A Linear Systems Approach to Flow Control. *Ann. Rev. Fluid Mech.* **39**, 39–383.
- KRIEGSEIS, J. 2011 Performance Characterization and Quantification of Dielectric Barrier Discharge Plasma Actuators. PhD thesis, TU Darmstadt.
- KURAMOTO, Y. & TSUZUKI, T. 1976 Persistent Propagation of Concentration Waves in Dissipative Media Far from Thermal Equilibrium. *Progr. Theoretical Physics* **55** (2), 356–369.
- LEE, K. H., CORTELEZZI, L., KIM, J. & SPEYER, J. 2001 Application of Reduced-order Controller to Turbulent Flow for Drag Reduction. *Phys. Fluids* **13**, 1321–1330.
- LEWIS, F. L. & SYRMOUS, L. V. 1995 *Optimal Control*. John Wiley & Sons, New York.
- LJUNG, L. 1999 *System identification*. Wiley Online Library.
- LUENBERGER, D. G. 1979 *Introduction to Dynamic System*. John Wiley & Sons, New York.
- LUNDELL, F. 2007 Reactive control of transition induced by free-stream turbulence: an experimental demonstration. *J. Fluid Mech.* **585**, 41–71.
- MA, Z., AHUJA, S. & ROWLEY, C. W. 2011 Reduced-order models for control of fluids using the eigensystem realization algorithm. *Theoretical and Computational Fluid Dynamics* **25** (1-4), 233–247.
- MANNEVILLE, P. 1995 *Dissipative structures and weak turbulence*. Springer.
- MARTENSSON, K. & RANTZER, A. 2011 Synthesis of structured controllers for large-scale systems. *IEEE Trans. Autom. Control* .
- MCKEON, B. J., SHARMA, A. S. & JACOBI, I. 2013 Experimental manipulation of wall turbulence: A systems approach. *Phys. Fluids* **25** (3), –.

- MILLING, R. W. 1981 Tollmien–Schlichting wave cancellation. *Phys. Fluids* **24**, 979.
- MONOKROUSOS, A., BRANDT, L., SCHLATTER, P. & HENNINGSON, D. S. 2008 DNS and LES of estimation and control of transition in boundary layers subject to free-stream turbulence. *Intl J. Heat and Fluid Flow* **29** (3), 841–855.
- MOORE, B. 1981 Principal Component Analysis in Linear Systems: Controllability, Observability, and Model reduction. *IEEE Trans. Autom. Control* **26** (1), 17–32.
- NOACK, B. R., AFANASIEF, K., MORZYNSKI, M., TADMOR, G. & THIELE, F. 2003 A hierarchy of low-dimensional models for the transient and post-transient cylinder wake. *J. Fluid Mech.* **497**, 335–363.
- NOACK, B. R., MORZYNSKI, M. & TADMOR, G. 2011 *Reduced-Order Modelling for Flow Control*, , vol. 528. Springer Verlag.
- PENROSE, R. 1955 A generalized inverse for matrices. *Mathematical Proceedings of the Cambridge Philosophical Society* **51**, 406–413.
- PRALITS, J. O. & LUCHINI, P. 2010 Riccati-less optimal control of bluff-body wakes. In *Seventh IUTAM Symposium on Laminar-Turbulent Transition* (ed. P. Schlatter & D. S. Henningson), , vol. 18. Springer.
- PRESS, W. H., TEUKOLSKY, S. A., VETTERLING, W. T. & FLANNERY, B. P. 2007 *Numerical Recipes 3rd Edition: The Art of Scientific Computing*, 3rd edn. Cambridge University Press.
- QIN, S. J. & BADGWELL, T. A. 2003 A Survey of Industrial Model Predictive Control Technology. *Contr. Eng. Pract.* **11** (7), 733–764.
- QUARTERONI, A. 2009 *Numerical Models for Differential Problems*. Springer.
- RATHNASINGHAM, R. & BREUER, K. S. 2003 Active control of turbulent boundary layers. *J. Fluid Mech.* **495**, 209–233.
- ROWLEY, C. W. 2005 Model reduction for fluids, using balanced proper orthogonal decomposition. *Intl J. of Bifurcation and Chaos* **15** (03), 997–1013.
- SARIC, W. S., REED, H. L. & KERSCHEN, E. J. 2002 Boundary-layer Receptivity to Freestream Disturbances. *Ann. Rev. Fluid Mech.* **34** (1), 291–319.
- SCHLICHTING, H. & GERSTEN, K. 2000 *Boundary-Layer Theory*. Springer Verlag, Heidelberg.
- SCHMID, P. J. 2007 Nonmodal Stability Theory. *Ann. Rev. Fluid Mech.* **39**, 129–62.
- SCHMID, P. J. & HENNINGSON, D. S. 2001 *Stability and Transition in Shear Flows*. *Applied Mathematical Sciences* v. 142. Springer-Verlag.
- SEMERARO, O., BAGHERI, S., BRANDT, L. & HENNINGSON, D. S. 2011 Feedback control of three-dimensional optimal disturbances using reduced-order models. *J. Fluid Mech.* **677**, 63–102.
- SEMERARO, O., BAGHERI, S., BRANDT, L. & HENNINGSON, D. S. 2013a Transition delay in a boundary layer flow using active control. *J. Fluid Mech.* **731** (9), 288–311.
- SEMERARO, O., PRALITS, J. O., ROWLEY, C. W. & HENNINGSON, D. S. 2013b Riccati-less approach for optimal control and estimation: an application to two-dimensional boundary layers. *J. Fluid Mech.* **731**, 394–417.
- SIEGEL, S. G., SIEGEL, J., FAGLEY, C., LUCHTENBURG, D. M., COHEN, K. & MCLAUGHLIN, T. 2008 Low Dimensional Modelling of a Transient Cylinder Wake Using Double Proper Orthogonal Decomposition. *J. Fluid Mech.* **610**, 1–42.
- SIPP, D., MARQUET, O., MELIGA, P. & BARBAGALLO, A. 2010 Dynamics and Control

- of Global Instabilities in Open-Flows: a Linearized Approach. *Appl. Mech. Rev.* **63** (3), 30801.
- SIPP, D. & SCHMID, P. J. 2013 Closed-Loop Control of Fluid Flow: a Review of Linear Approaches and Tools for the Stabilization of Transitional Flows. *AerospaceLab Journal*.
- SIVASHINSKY, G. I. 1977 Nonlinear Analysis of Hydrodynamic Instability in Laminar Flames – I. Derivation of Basic Equations. *Acta Astronautica* **4**, 1177–1206.
- SKOGESTAD, S. & POSTLETHWAITE, I. 2005 *Multivariable Feedback Control, Analysis to Design*, 2nd edn. Wiley.
- STURZEBECHER, D. & NITSCHKE, W. 2003 Active cancellation of Tollmien–Schlichting instabilities on a wing using multi-channel sensor actuator systems. *Intl J. Heat and Fluid Flow* **24**, 572–583.
- SUZEN, Y., HUANG, P., JACOB, J. & ASHPIS, D. 2005 Numerical Simulations of Plasma Based Flow Control Applications. *AIAA J.* **4633**, 2005.
- ZHOU, K., DOYLE, J. C. & GLOVER, K. 2002 *Robust and Optimal Control*. Prentice Hall, New Jersey.

Paper 2

2

On the role of adaptivity for robust laminar-flow control

Nicolò Fabbiane¹, Bernhard Simon², Felix Fischer²,
Sven Grundmann², Shervin Bagheri¹ and Dan S. Henningson¹

¹ Linné FLOW Centre, KTH Mechanics, S-100 44 Stockholm, Sweden

² Center of Smart Interfaces, TU Darmstadt, 64347 Griesheim, Germany

Journal of Fluid Mechanics (2015), vol. **767**, R1

In this work, we use numerical simulations and experiments to compare the robustness of adaptive and model-based techniques for reducing the growth of two-dimensional TS disturbances. In numerical simulations, the optimal Linear Quadratic Gaussian (LQG) regulator shows the best performance under the conditions it was designed for. However, it is found that the performance deteriorates linearly with the drift of the Reynolds number from its nominal value. As a result, an order-of-magnitude loss of performance is observed when applying the computation-based LQG controller in wind-tunnel experiments. In contrast, it is shown that the adaptive Filtered-X Least-Mean-Squares (FXLMS) algorithm is able to maintain an essentially constant performance for significant deviations of nominal values of disturbance amplitude and Reynolds number.

Key words: boundary-layer control, flow control, instability control

1. Introduction

Over the last decades the spatiotemporal behavior of the instabilities leading to transition from a laminar to a turbulent regime in boundary-layer flows has been thoroughly characterized. In a low-turbulence environment the initial phase of the transition process is an exponential growth of Tollmien Schlichting (TS) waves (Saric *et al.* 2002). Both numerical and laboratory experiments have shown that it is possible to use linear control techniques to damp the amplitude of the instabilities by several orders of magnitude, with the consequences that the transition is delayed and the skin-friction drag is reduced (Lundell 2007; Bagheri & Henningson 2011; Semeraro *et al.* 2013; Goldin *et al.* 2013). However, the linear control approach have not yet been established as a competitive technique in applied settings, and essentially all work is at a proof-of-concept level. Understanding how linear controllers perform under varying conditions is a first step towards making this flow control approach a realistic and competitive alternative in applications.

One of the first attempts to design a compensator in order to delay the laminar-to-turbulent transition was presented by Bewley & Liu (1998). Optimal

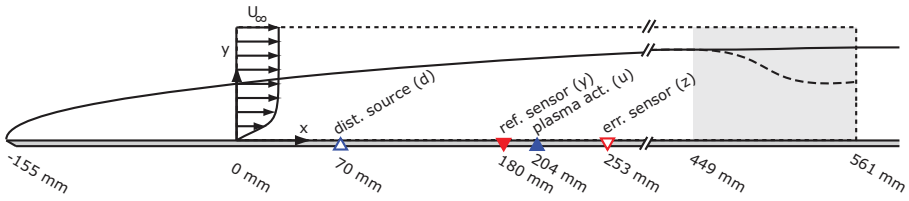


Figure 1: Experimental set-up. The computational domain used in the DNS simulations (dashed line) starts at $(x, y) = (0, 0)$ and it extends $750 \delta_0^*$ in streamwise direction and $30 \delta_0^*$ in the wall-normal direction, where $\delta_0^* = 0.748$ mm is the displacement thickness at the beginning of the domain. In the last part of the domain (grey area) a fringe region enforces the periodicity along the streamwise direction (Nordström *et al.* 1999).

and robust control theory were used to precompute the compensator based on a state-space formulation of the governing equations. It was a natural extension of the classical Orr-Sommerfeld theory; by connecting the inputs to outputs via a compensator, all aspect of disturbance dynamics – which was previously performed for the open-loop system – could now be performed for the closed-loop system. The optimality and the guaranteed stability of the closed-loop system (under certain conditions, Glad & Ljung 2000; Doyle 1978), resulted in a rapid spread in the stability community (Barbagallo *et al.* 2009; Bagheri *et al.* 2009; Semeraro *et al.* 2013b; Juillet *et al.* 2014). In this class of *static* methods the compensator is first precomputed off-line based on a linear model of the flow and then applied to the laboratory or numerical experiment. The most widely used compensator in this context is the Linear Quadratic Gaussian (LQG) regulator. In contrast, in *adaptive* control techniques, which was first employed in the work of Sturzebecher & Nitsche (2003), the control law is not precomputed but it is identified on-line, i.e. the algorithm is able to adjust the compensator through measurements and only partial modelling of the flow response is required. In this category of methods – with the Filtered-X Least Mean Square (FXLMS) algorithm being the most common one – the stability of the closed-loop system is not guaranteed and the disturbance energy is not reduced in an optimal way (Aström & Wittenmark 1995).

The aim of this work is to compare the robustness of static and adaptive controllers and assess their advantages and limitations. First, we investigate robustness of the closed-loop system in experiments by applying a LQG compensator that is designed based on a numerical model of the experimental configuration. This approach has many uncertainties incorporated, since a perfectly exact model of the flow, actuators, sensors and disturbances is not possible to obtain. Second, we compare the performance of LQG and FXLMS by systematically inducing a drift in the Reynolds number and the disturbance amplitude.

2. Experimental set-up

A 2D TS wave is generated by a disturbance source (denoted by d in Figure 1) in a flat-plate boundary-layer flow and is detected further downstream by a surface hot-wire (y in Figure 1). This sensor provides the reference signal to the compensator to compute the control action and a dielectric barrier discharge (DBD) plasma actuator (u) provides the prescribed forcing on the flow. A second surface hot-wire sensor (z) is positioned downstream of the actuator to evaluate the compensator performance.

The experiments are conducted in an open-circuit wind tunnel at TU Darmstadt, which provides a $450 \text{ mm} \times 450 \text{ mm}$ test section and an averaged turbulence intensity of $Tu = 0.1\%$, measured at the end of the 1:24 contraction nozzle. A 1600 mm long flat plate with an 1:6 elliptical leading edge and adjustable trailing edge is mounted horizontally in the middle of the test section. Figure 1 shows a sketch of the flat plate containing surface mounted sensors, the disturbance source and the plasma actuator. The zero position is chosen to be 70 mm upstream of the disturbance source as the DNS computational box starts at this point.

A dSPACE system consisting of a DS1006 processor board, a DS2004 A/D board as well as a DS2102 high resolution D/A Board provides the computational power for the flow control algorithm. An additional 16bit NI PCI 6254 A/D board is used for data acquisition of hot wire sensors signals as well as the disturbance source signals.

Disturbances are created by pressure fluctuations at the wall, caused by conventional loudspeakers. The disturbance source consists of 16 Visaton BF 45 speakers, amplified by 16 Kemo M031N, which can be controlled individually by the 16 channels analog output module NI9264. The set of loudspeakers is placed outside of the test section and 1.2 m long tubes are led into the test section from below the flat plate. The tubes are arranged along a line in spanwise direction beneath a 0.2 mm wide slot in the flat plate surface while the construction principle is similar to Borodulin *et al.* (2002); Würz *et al.* (2012). Five tubes with an outer diameter of 3 mm are connected to every loudspeaker leading to a total width of the disturbance source of 240 mm. Two spanwise rows of 30 Sennheiser KE 4-211-2 microphones enable the on-line monitoring of the phase and amplitude of the artificially excited TS waves in order to assure an even 2D wave front (Figure 2). The first row is positioned upstream of the plasma actuator at $x = 164 \text{ mm}$ while the second row downstream of the plasma actuator at $x = 224 \text{ mm}$. All microphones are mounted below the surface and are connected to the surface through a 0.2 mm circular orifice with a spacing of only 9 mm in spanwise direction. All channels are sampled by two NI 9205 A/D converter modules with 4 kHz.

In addition, a boundary-layer hot wire probe Dantec 55P15 is mounted on a 2D traverse for phase-averaged boundary layer measurements. The DC signal is filtered with an 1 kHz low pass filter to avoid aliasing.

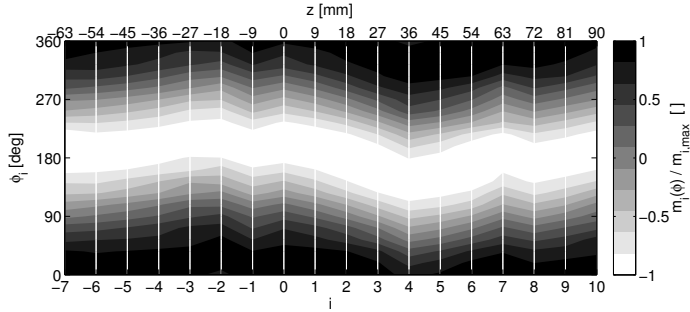


Figure 2: Phase-averaged microphone signals $m_i(\phi)$ for a 200 Hz TS-wave: the wave front is aligned along the spanwise direction resulting in a 2D disturbance. The signals are from the upstream microphone row are sampled at 4 kHz and time-average for 10 s.

2.1. Actuator and sensors for flow control

The plasma actuator consists of a 10 mm wide grounded lower electrode of $35 \mu\text{m}$ thickness and a 5 mm wide upper electrode, which are divided in the vertical direction by five layers of Kapton tape with a total thickness of 0.3 mm. A GBS Minipuls 2.1 high voltage supply is driving the 230 mm long plasma actuator, which is installed flush mounted to a spanwise groove in order to minimize roughness of the surface.

The plasma actuator driving frequency f_{PA} is chosen to be 10 kHz, which is more than one order of magnitude higher than the unstable TS wave frequency band for this experiment. In order to assure a stable discharge in time and space, an operation range from $V = 5 \text{ kV}_{pp}$ to 13 kV_{pp} has to be maintained for this actuator design (Barckmann 2014): therefore a mean voltage supply $V = 7 \text{ kV}_{pp}$ is chosen for all experiments. The compensator can modulate the amplitude of the high voltage supply via the control signal $u(t)$ and, as consequence, vary the plasma actuator force on the time scale of the TS waves. The control signal $u(t)$, fed into the high voltage generator, is a linearized function with respect to the plasma actuator force at that working point.

Two surface hot-wires sensors are used to provide the compensator the required information to compute a suitable control signal $u(t)$. As introduced by Sturzebecher & Nitsche (2003), the surface hot-wire has proven to be an excellent sensor type for reactive flow control (Lundell 2007; Kurz *et al.* 2013). Due to the high electromagnetic interference of the plasma actuator, a classic hot-wire design with prongs is preferred and modified to serve as a surface hot-wire. Two conventional needles are moulded in a plastic case, which can be flush mounted on the flat plate. A small groove between the needle tips avoids heat loss to the structure and improves the signal-to-noise ratio. The $5 \mu\text{m}$ thin and 1.25 mm long gilded-tungsten wire is heated with an overheat ratio of 1.7. Due to shielded

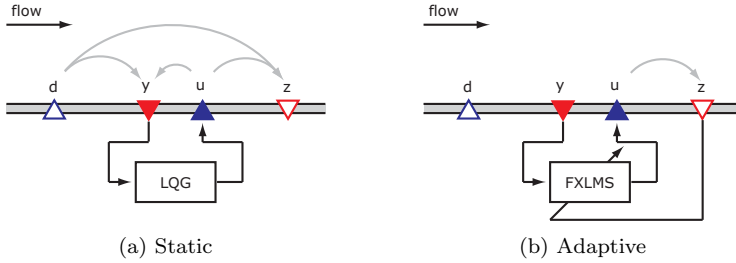


Figure 3: Compensator schemes for static (LQG) and adaptive (FXLMS) strategies. The measurements by the error sensor z are used by the FXLMS algorithm to adapt to the current flow conditions. The grey lines indicate the I/O relations required to be modelled by each strategy.

signal lines, this sensor is less sensitive for electromagnetic interferences than the conventional surface hot-wire design based on photo-etched printed circuit boards. A 4 channels Dantec Streamline constant temperature anemometer (CTA) provides the band pass filtered AC signal of the sensors (10 Hz – 1 kHz). All hot wire sensor signals are acquired with a sample rate of 10 kHz. The surface hot-wires are calibrated for quantifying the TS wave amplitude according to the definition in (2). The calibration was conducted by exciting 2D TS waves whose maximum amplitude was measured above the surface hot-wire using the traversable boundary-layer hot-wire probe as a reference.

3. Static and adaptive compensators

Given the sensor measurements the compensator provides the control sign to the actuator (Figure 3). The compensator response is described by the finite impulse response (FIR) filter (Haykin 1986),

$$u(n) = \sum_{i=1}^{N_k} K(i) y(n-i) \quad (1)$$

where $u(n) = u(n \Delta t)$ and $y(n) = y(n \Delta t)$ are the time-discrete representation of the time-continuous signals $u(t)$ and $y(t)$ and $\Delta t = 1$ ms is the sampling time. The N_K coefficients $K(i)$ are the kernel of the filter and they describe how the compensator filters the measurements $y(n)$ in order to provide the control action $u(n)$.

One may identify two types of compensators depending on whether the kernel is static or adaptive. In this work, the LQG regulator is chosen as representative of the static compensator class (Figure 3a). It is designed by solving two independent optimization problems based on a state-space model of the plant (Glad & Ljung 2000). The estimation problem constructs a low-dimensional approximation of the flow from the measurements $y(t)$. The optimal

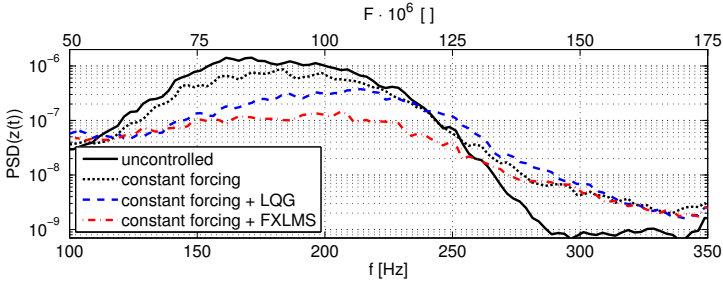


Figure 4: Experimental time-averaged Power Spectral Density (PSD) functions for $z(t)$. The flow is excited by a white-noise signal $d(t)$. The top axis reports the non-dimensional frequency $F = (2\pi\nu/U_\infty^2) f$. The Reynolds number at error sensor location is $Re_{x,z} = 375 \cdot 10^3$

control problem, computes the signal $u(t)$ from the estimated state. A FXLMS algorithm represents the class of adaptive compensators (Sturzebecher & Nitsche 2003; Engert *et al.* 2008). As reported in Figure 3b, it uses the measurement signal of the error sensor $z(t)$ to dynamically adapt and is therefore able to adjust to varying conditions (such as Reynolds number) of the flow. The design requires a model of the input-output relation between the plasma actuator and the error sensor ($u \rightarrow z$). Compared to LQG algorithm, FXLMS is only sub-optimal; we refer to Fabbiane *et al.* (2014) for more detailed information on both approaches.

Figure 4 compares the performance of the two compensators when the disturbance source is fed with a white-noise signal $d(t)$ for a wind tunnel speed $U_{WT} = 12 \text{ m s}^{-1}$. The flow filters the introduced disturbances and amplifies only a band of frequencies (Schmid & Henningson 2001): the spectrum of $z(t)$ that results from this process is depicted by the solid line. Note that $z(t)$ is a measure of the wall-stress fluctuations and therefore related to the amplitude of the TS wave-packets that are generated by the disturbance $d(t)$. The dashed and dot-dashed lines depict the spectrum $z(t)$ when the LQG and FXLMS compensators are applied: the FXLMS algorithm appears to be more effective than the LQG regulator. As mentioned in §2.1, the plasma actuator is operated at a mean high voltage $V = 7 \text{ kV}_{pp}$, corresponding to an average specific-power consumption of $P = 16 \text{ W m}^{-1}$. The resulting constant forcing is small and has therefore only a marginal stabilizing effect on the flow, as it is shown by the dotted line in Figure 4.

4. A DNS model of the flow

In order to provide a model for the LQG design, numerical simulations are used to simulate the flow in the test section. The experimental set-up described in §2, produces sufficiently small perturbations in order to not trigger non-linear phenomena. Therefore, the linearized Navier-Stokes (NS) equations around a

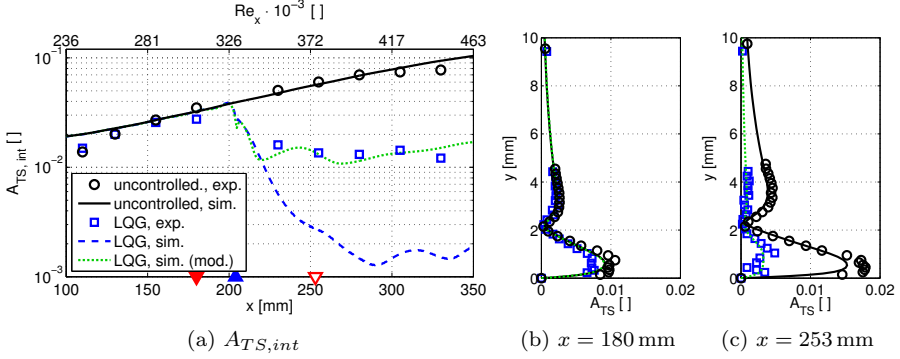


Figure 5: TS-wave amplitude for $f_d = 200$ Hz. Lines and circles depict simulated and experimental data respectively. (a) shows the integral TS-wave amplitude ($A_{TS,int}$) as a function of the streamwise position. The top axis reports $Re_x = \frac{(x-x_{LE})U_\infty}{\nu}$, where x_{LE} is the leading-edge position. (b) and (c) show the TS-wave shape at two different x positions upstream and downstream the actuator. The triangles indicate where the reference sensor, plasma actuator, and error sensor are positioned, cfr. Figure 1.

laminar zero-pressure-gradient boundary-layer flow are considered to describe the temporal evolution of the disturbances. The free-stream velocity $U_\infty = 14 \text{ m s}^{-1}$ and the displacement thickness in the beginning of the domain $\delta_0^* = 0.748 \text{ mm}$ are identified by a parameter fitting procedure of the laminar solution over 10 measured mean-velocity profiles between $x = 0 \text{ mm}$ and $x = 330 \text{ mm}$. The resulting Reynolds number is $Re = U_\infty \delta_0^* / \nu = 656$. A pseudo-spectral DNS code is used to perform the simulations (Chevalier *et al.* 2007). Fourier expansion over $N_x = 768$ modes is used to approximate the solution along the streamwise direction, while Chebyshev expansion is used in the wall-normal direction on $N_y = 101$ Gauss-Lobatto collocation points. The computational domain is shown in Figure 1.

The disturbance source and the plasma actuator are modelled by volume forcings. Each forcing term is decomposed into a constant spatial shape and in a time dependent part (i.e. the input signal). The forcing shape for the disturbance source is a synthetic vortex localized at the disturbance source position (Bagheri *et al.* 2009). The plasma actuator shape, instead, is modelled by a distributed streamwise forcing, according to the results by Krieger *et al.* (2013). As the forcing shape depends on the high-voltage supply to the actuator, a linearisation around $V = 7 \text{ kV}_{pp}$ is considered. The surface hot-wires sensors $y(t)$ and $z(t)$ are modelled as point-wise measurements of the skin-friction fluctuations.

Numerical simulations and experimental measurements of the performance of the LQG compensator are reported in Figure 5. The flow is excited by a

single-frequency constant-amplitude signal $d(t)$ with frequency $f_d = 200$ Hz. The amplitude of the velocity fluctuation in the flow is measured by an hot-wire probe mounted on a traverse system. A non-dimensional measure for the TS-wave amplitude is introduced:

$$A_{TS,int}(x) = \frac{1}{\delta_0^*} \int_0^\infty \frac{|\mathcal{U}(x, y, f_d)|}{U_\infty} dy = \frac{1}{\delta_0^*} \int_0^\infty A_{TS}(x, y) dy \quad (2)$$

where $\mathcal{U}(x, y, f)$ is the Fourier transform of the streamwise component of the velocity. From Figure 5a it can be observed that the direct simulations (black solid line) of the flow matches very well the experimental data (black circles). When the LQG-controller is active in experiments (blue squares), one order-of-magnitude reduction of disturbance amplitude is observed. This is, to the authors knowledge, the first time a computation-based LQG controller, designed without any fitting parameters nor system identification, suppresses disturbances in wind-tunnel experiments. However, LQG controller is optimal for the exact model only, which it was designed for; as shown in Figure 5a, the attainable reduction of disturbance is two-orders of magnitude, when the controller is applied to the numerical simulation (dashed-blue line). The difference of one-order of magnitude is due to the fact that in experiments a steady forcing was applied in addition to LQG control signal (see Sec. 2). The performance prediction is improved if the average constant forcing by the plasma actuator is considered when computing the baseflow used for testing the compensator (green dotted line). This shows that there is a small difference between the modelled flow and the experimental flow.

In Figure 5(b-c) the profile of TS disturbance is compared with and without controller active. The profiles are measured at the streamwise location of the reference sensor y and the error sensor z . From Figure 5c, one observes that the disturbance is damped all along the wall-normal direction, both in simulation (green dotted line) and experiment (blue squares). A double-peaked shape is visible near the wall that can be explained by the proximity to the plasma actuator. In fact, the lower peak of the TS amplitude is located at the wall-normal position where Kriegseis *et al.* (2013) measured the maximum forcing of a similar plasma actuator. However, as the controlled TS-wave evolves further downstream the double peak structure is less pronounced.

From Figure 5(b-c) it can be seen that the maximum amplitude of the disturbance goes from $0.01 U_\infty$ at y -sensor location to $0.02 U_\infty$ at z -sensor location. These small amplitudes confirm the small-perturbation hypothesis, for which the linear model and control are based on. In order to cancel the disturbance, the plasma actuator induces velocity fluctuations of the same order of magnitude as the TS disturbance, i.e. between $\pm 0.14 \text{ m s}^{-1}$ and $\pm 0.28 \text{ m s}^{-1}$.

5. Robustness

In this section, the robustness of the two control techniques is analysed. In the present context, *robustness* refers to the capacity of the compensator to overcome differences between design and working conditions. In particular, the

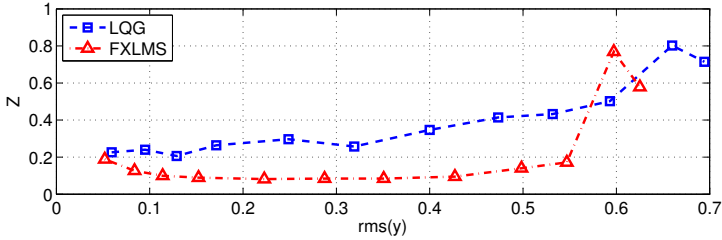


Figure 6: Effect of the TS-wave amplitude on the performance indicator Z . The flow is excited by the disturbance source operated with a 200 Hz single-frequency signal.

effect of deviations of disturbance amplitude and the free-stream velocity on the control performance is investigated. It has been shown by Belson *et al.* (2013) and Fabbiane *et al.* (2014), that the current sensor/actuator configuration results in a feed-forward control, which is well-known to have robustness issues. The type of robustness analysis performed here is ad-hoc in the sense that model uncertainties have systematically been introduced in order to assess the performance.

A 200 Hz single-frequency disturbance is used to investigate the robustness of the LQG controller against higher TS-wave amplitude. The amplitude is gradually increased and the rms of the reference sensor signal $y(t)$ is used as an indicator of disturbance amplitude. A performance index is defined as the ratio between the root-mean-square (rms) of the controlled and uncontrolled sensor signals, i.e.

$$Z = \frac{\text{rms}(z_{ctr}(t))}{\text{rms}(z_{unctr}(t))}. \quad (3)$$

In Figure 6, it can be observed that controller performance is gradually degraded while the amplitude rises and saturated around $rms(y) = 0.6$. The FXLMS compensator, instead, is able to maintain good performance until an abrupt breakdown of the performance around $rms(y) = 0.6$. At these large amplitudes, the compensator adaptivity can not compensate the strong non-linearities of the flow.

Variation of the free stream conditions may also degrade the control performance, since it changes the baseflow. The wind-tunnel speed is varied around the design condition $U_{WT} = 12 \text{ m s}^{-1}$, changing the Reynolds number and, as a consequence, the stability properties of the flow (Schmid & Henningson 2001). A white-noise is low-pass filtered with a cut-off frequency of 4 kHz and considered as disturbance signal $d(t)$. The disturbance is monitored in order to ensure a 2D wave-front. The ratio between $rms(y)$ and the wind-tunnel speed U_{WT} is kept constant and equal to $6.5 \cdot 10^{-3}$ in order to avoid non-linear effects. Note that the asymptotic velocity U_{∞} differs from U_{WT} because of blockage effects due to the presence of the flat-plate and experimental equipment.

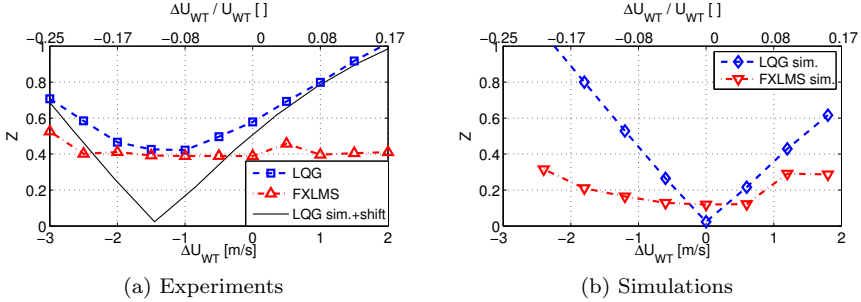


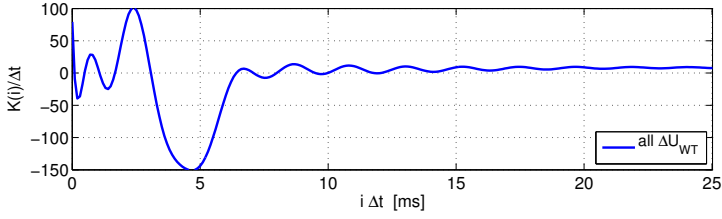
Figure 7: Effect of wind-tunnel speed variation ΔU_{WT} on the performance indicator Z . The solid line in (b) depicts the DNS data shifted to fit the experimental curve. The flow is excited by the disturbance source operated with a white noise signal $d(t)$.

Figure 7a shows Z as a function of the wind-tunnel speed variation ΔU_{WT} . It is observed (blue dashed line) that the LQG performance is sensitive to variation of the free-stream velocity. Note that the best performance is obtained for a velocity lower than the design speed. This shift can be attributed to the fact that an experimental flow can only be modelled numerically up to a certain accuracy. Uncertainties such as for example fluctuations in temperature (and thus a shift in Reynolds number) are unavoidable and lead to loss of performance, as described in the previous section. The FXLMS compensator, on the other hand, is able to adapt to the changed conditions. Even if the required input-output relation $u \rightarrow z$ – which is a static part of the FXLMS algorithm – is changed by the speed variation, the adaptive nature of the controller is able to compensate for this error and provide an almost unaltered performance for significant wind-tunnel speed variations.

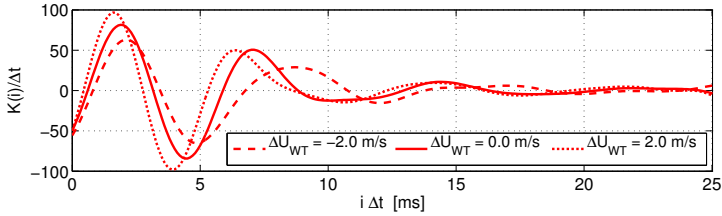
The robust property of FXLMS is also confirmed by the numerical experiments (Figure 7b). Similar to the experiment, the free-stream velocity is varied with respect to its nominal value and the performance of the control action is monitored. At the design conditions $\Delta U_{WT} = 0 \text{ m s}^{-1}$, the model for which the LQG was designed is a very accurate representation of disturbance behavior. Interestingly, the attenuation achieved by the FXLMS algorithm is very close to the optimal performance of the LQG regulator. For the latter compensator however, Z increases linearly with ΔU_{WT} . This can be explained as follows. Assume that $z(t)$ is the superposition of the two counter-phase TS-waves, one generated by the disturbance source and one by the plasma actuator,

$$z(t) = z_d(t) + z_u(t) = a \sin(\omega(t + \Delta\tau)) - a \sin(\omega t). \quad (4)$$

The leading order effect of a change in the free-stream is on the phase-speed of the TS-wave, which in turn results in a modification of the phase-shift parameter



(a) LQG kernel



(b) FXLMS kernel

Figure 8: Compensator kernels $K(i)$ for different wind-tunnel speeds for LQG (a) and FXLMS (b). The solid line represents the design condition. When U_{WT} decreases (dashed line) or increases (dotted line), the FXLMS compensator adapts to the new conditions by stretching or shrinking the compensator kernel.

$\Delta\tau$. Rewriting expression (4) to highlight the role of $\Delta\tau$,

$$z(t) = 2a \sin\left(\omega \frac{\Delta\tau}{2}\right) \cos\left(\omega \left(t - \frac{\Delta\tau}{2}\right)\right) \approx a\omega\Delta\tau \cos\left(\omega \left(t - \frac{\Delta\tau}{2}\right)\right). \quad (5)$$

it is observed that for small values of $\omega\Delta\tau$, the amplitude of $z(t)$ is a linear function of $\Delta\tau$. The black solid line in Figure 7a shows the simulated LQG performance (dashed-blue in Figure 7b) when it is shifted to the left to coincide with minima of experimental control values of Z . Note that Z corresponding to numerical data asymptotically approaches the experimental data (blue dashed line), showing the same linear behaviour predicted by (5).

The solid lines in Figure 8 depict LQG and FXLMS kernels for the design condition, i.e. $\Delta U_{WT} = 0 \text{ m s}^{-1}$. When the wind-tunnel speed is decreased, the amplification of the TS wave is reduced and the propagation speed of the TS wave decreases, i.e. the TS wave moves slower than under design conditions. In this particular new condition, the FXLMS algorithm reacts by stretching the convolution kernel in time and reducing the magnitude of the $K(i)$ coefficients (dashed line in Figure 8b). On the other hand, if the speed increases, the effect on the flow is opposite; the TS wave moves faster and is more amplified. Hence, the compensator reacts by shrinking the kernel and increasing the magnitude of the $K(i)$ coefficients (dotted line). The LQG kernel, instead, is fixed and does not adapt to the actual flow conditions.

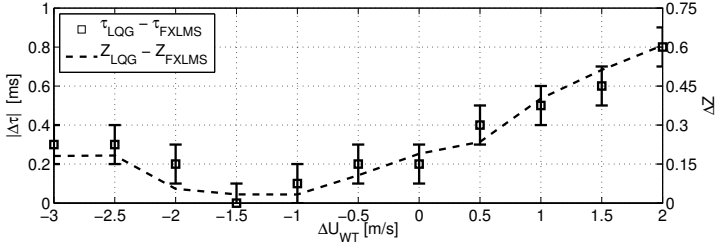


Figure 9: Correlation between phase error $|\Delta\tau|$ (squares) and performance loss ΔZ (dashed line) when the wind-tunnel speed is changed. The error bars report an interval $\pm\Delta t$ around each $\Delta\tau(U_{WT})$ point.

To quantify the phase-shift in the kernel, let τ represent the time for which the kernel attains its minimum value. Further, one may define the difference between the phase-shift of the two compensator kernels by $|\Delta\tau| = |\tau_{LQG} - \tau_{FXLMS}|$. In Figure 9, a strong correlation between $|\Delta\tau|$ and the performance loss ΔZ (i.e. the gap between the two curves in Figure 7a) is observed. This correlation shows that the compensator performance is mainly depending on a correct prediction of the time it takes for the TS wave to propagate from the reference-sensor and to the plasma-actuator. In the LQG approach, this information is given by the designed static model: any inaccuracy in this model may lead to an incorrect computation of the phase-shift and, eventually, to a performance loss.

The FXLMS adaptive algorithm is not equivalent to a feedback sensor/actuator configuration (Belson *et al.* 2013). The FXLMS algorithm is able to adapt to modified flow conditions (i.e. weak nonlinearities, free-stream variation, etc.) by adapting its response (e.g. by stretching/shrinking the kernel when velocity fluctuations occur). However, it has to be noted that (i) the measurement signal $z(t)$ has not a direct influence on the control signal but on the kernel only and (ii) the adaptation time-scale – approximately 15 s from zero initial condition to the asymptotic value – is significantly larger than the TS-wave time-scale. Therefore the compensator is able to adapt only to *slow* changes in the flow and the adaptation loop can not be characterized as a conventional feedback. These results extend and confirm our earlier work on the Kuramoto-Sivashinsky equation to a physical fluid flow (Fabbiane *et al.* 2014).

6. Conclusions

From a general viewpoint, the role of optimality have been overemphasized in investigations with linear theoretical approach to transition and turbulence control. Although, these studies provide important physical insight into performance limitations as well as the best achievable flow control performance, they remain at a proof-of-concept level, since any deviation of the design conditions can destabilize the controller; at best it will render the control performance

suboptimal. In this paper, it is shown that adaptivity plays a crucial role to achieve robustness in transition control, even when a simple 2D-disturbance case is considered. Whereas the optimal LQG outperforms simple wave-cancellation techniques significantly (Fabbiane *et al.* 2014), FXLMS obtains nearly as good performance as LQG but in addition possess the robustness, making it the choice for transition control.

The authors acknowledge support the Swedish Research Council (VR-2012-4246, VR-2010-3910), German Research Foundation, and the Linné FLOW Centre.

REFERENCES

- ASTRÖM, K. J. & WITTENMARK, B. 1995 *Adaptive Control*, 2nd edn. Addison Wesley.
- BAGHERI, S., BRANDT, L. & HENNINGSON, D. S. 2009 Input–output analysis, model reduction and control of the flat-plate boundary layer. *J. Fluid Mech.* **620** (1), 263–298.
- BAGHERI, S. & HENNINGSON, D. S. 2011 Transition delay using control theory. *Philos. Trans. R. Soc.* **369**, 1365–1381.
- BARBAGALLO, A., SIPP, D. & SCHMID, P. J. 2009 Closed-loop control of an open cavity flow using reduced order models. *J. Fluid Mech.* **641**, 1–50.
- BARCKMANN, K. 2014 Active Vortex Generation using Dielectric Barrier Discharge Plasma Actuators in Laminar Boundary Layers. PhD thesis, Technischen Universität Darmstadt.
- BELSON, B. A., SEMERARO, O., ROWLEY, C. W. & HENNINGSON, D. S. 2013 Feedback control of instabilities in the two-dimensional Blasius boundary layer: The role of sensors and actuators. *Phys. Fluids* **25**.
- BEWLEY, T. R. & LIU, S. 1998 Optimal and Robust Control and Estimation of Linear Paths to Transition. *J. Fluid Mech.* **365**, 305–349.
- BORODULIN, V. I., KACHANOV, Y. S. & KOPTSEV, D. B. 2002 Experimental Study of Resonant Interactions of Instability Waves in Self-Similar Boundary Layer with an Adverse Pressure Gradient: II. Detuned Resonances*. *Journal of Turbulence* **3** (062).
- CHEVALIER, M., SCHLATTER, P., LUNDBLADH, A. & HENNINGSON, D. S. 2007 A pseudo-spectral solver for incompressible boundary layer flows. *Tech. Rep. TRITA-MEK 2007:07*. KTH Mechanics, Stockholm, Sweden.
- DOYLE, J. C. 1978 Guaranteed Margins for LQG Regulators. *IEEE Trans. Autom. Control* **AC-23** (4), 756–757.
- ENGERT, M., PÄTZOLD, A., BECKER, R. & NITSCHKE, W. 2008 Active Cancellation of Tollmien-Schlichting Instabilities in Compressible Flows Using Closed-Loop Control. In *IUTAM Symposium on Flow Control and MEMS*, , vol. 7, pp. 319–331. Springer Netherlands.
- FABBIANE, N., SEMERARO, O., BAGHERI, S. & HENNINGSON, D. S. 2014 Adaptive and Model-Based Control Theory Applied to Convectively Unstable Flows. *Appl. Mech. Rev.* **66** (6), 060801.
- GLAD, T. & LJUNG, L. 2000 *Control Theory*. London: Taylor & Francis.
- GOLDIN, N., KING, R., PÄTZOLD, A., NITSCHKE, W., HALLER, D. & WOIAS, P. 2013

- Laminar Flow Control With Distributed Surface Actuation: Damping Tollmien-Schlichting Waves with Active Surface Displacement. *Exp. Fluids* **54** (3), 1–11.
- HAYKIN, S. 1986 *Adaptive Filter Theory*. Prentice-Hall.
- JUILLET, F., MCKEON, B. J. & SCHMID, P. J. 2014 Experimental Control of Natural Perturbations in Channel Flow. *J. Fluid Mech.* **752**, 296–309.
- KRIEGSEIS, J., SCHWARZ, C., TROPEA, C. & GRUNDMANN, S. 2013 Velocity-Information-Based Force-Term Estimation of Dielectric-Barrier Discharge Plasma Actuators. *J. Phys. D* **46** (5), 055202.
- KURZ, A., GOLDIN, N., KING, R., TROPEA, C. D. & GRUNDMANN, S. 2013 Hybrid Transition Control Approach for Plasma Actuators. *Exp. Fluids* **54** (11), 1–4.
- LUNDELL, F. 2007 Reactive control of transition induced by free-stream turbulence: an experimental demonstration. *J. Fluid Mech.* **585**, 41–71.
- NORDSTRÖM, J., NORDIN, N. & HENNINGSON, D. S. 1999 The fringe region technique and the Fourier method used in the direct numerical simulation of spatially evolving viscous flows. *SIAM J. Sci. Comp.* **20** (4), 1365–1393.
- SARIC, W. S., REED, H. L. & KERSCHEN, E. J. 2002 Boundary-layer Receptivity to Freestream Disturbances. *Ann. Rev. Fluid Mech.* **34** (1), 291–319.
- SCHMID, P. J. & HENNINGSON, D. S. 2001 *Stability and Transition in Shear Flows. Applied Mathematical Sciences* v. 142. Springer-Verlag.
- SEMERARO, O., BAGHERI, S., BRANDT, L. & HENNINGSON, D. S. 2013a Transition delay in a boundary layer flow using active control. *J. Fluid Mech.* **731** (9), 288–311.
- SEMERARO, O., PRALITS, J. O., ROWLEY, C. W. & HENNINGSON, D. S. 2013b Riccati-less approach for optimal control and estimation: an application to two-dimensional boundary layers. *J. Fluid Mech.* **731**, 394–417.
- STURZEBECKER, D. & NITSCHKE, W. 2003 Active cancellation of Tollmien-Schlichting instabilities on a wing using multi-channel sensor actuator systems. *Intl J. Heat and Fluid Flow* **24**, 572–583.
- WÜRZ, W., SARTORIUS, D., KLOKER, M., BORODULIN, V. I., KACHANOV, Y. S. & SMORODSKY, B. V. 2012 Nonlinear Instabilities of a Non-Self-Similar Boundary Layer on an Airfoil: Experiments, DNS, and Theory. *Euro. J. Mech. B* **31**, 102–128.

Paper 3

3

In-flight active-wave-cancelation via delayed-x-LMS control algorithm in a laminar boundary layer

Bernhard Simon², Nicolò Fabbiane¹, Timotheus Nemitz²,
Shervin Bagheri¹, Dan S. Henningson¹ and Sven Grundmann³

¹ Linné FLOW Centre, KTH Mechanics, S-100 44 Stockholm, Sweden

² Center of Smart Interfaces, TU Darmstadt, 64347 Griesheim, Germany

³ Department of Fluid Mechanics, University of Rostock, Germany

Under review for publication in Experiments in Fluids

This manuscript demonstrates the first successful application of the delayed-x-LMS (dxLMS) control algorithm for TS-wave cancelation. Active wave cancelation of two-dimensional broad-band Tollmien-Schlichting (TS) disturbances is performed with a single DBD plasma actuator. The experiments are conducted in flight on the pressure side of a laminar flow wing glove, mounted on a manned glider. The stability properties of the controller are investigated in detail with experimental flight data, DNS and stability analysis of the boundary layer. Finally, a model-free approach for dxLMS operation is introduced to operate the controller as a “black box” system, which automatically adjusts the controller settings based on a group speed measurement of the disturbance wave packets. The modified dxLMS control algorithm allows to operate the controller without a model and an adaption based on varying conditions that may occur during flight in atmosphere.

Key words: active flow control, active wave cancelation, fxLMS, dxLMS, in-flight measurements, DNS, DBD plasma actuator.

1. Introduction

Delaying laminar-turbulent transition of a boundary layer has been a major topic of fluid mechanic-research during the last decades. Besides passive control techniques which are related to the favourable pressure distribution of natural laminar flow (NLF) airfoils, active methods can be used to attenuate disturbances in the boundary layer and move the transition to turbulence further downstream. Predetermined flow control techniques (Gad-el Hak 2000) e.g steady boundary-layer suction have been investigated intensively but require relatively high actuation power levels because the mean boundary layer profile is altered. Reactive flow control techniques such as the active wave cancelation (AWC)

only act on the fluctuations in the laminar boundary layer and therefore require less energy.

Early attempts of AWC with moving wall actuators by Thomas (1983) successfully attenuated the amplitude of artificially generated TS-disturbances in a laminar boundary layer while Sturzebecher & Nitsche (2003) showed the cancelation of natural occurring TS-waves on a glider wing in flight. Motivated by the previous work with moving wall actuators, Grundmann & Tropea (2008) first showed that the plasma actuator (PA) is also able to cancel out TS-waves in a laminar boundary layer. Further studies with PAs by Kurz *et al.* (2013) and Kotsonis *et al.* (2013, 2015) suggest that PAs can be used to delay the onset of transition.

Several in-flight measurement projects have been conducted with the PA at Technische Universität Darmstadt by Duchmann *et al.* (2014), Kurz *et al.* (2014) and Simon *et al.* Simon *et al.* (2016). Despite the low fluid-dynamic efficiency Kriegseis *et al.* (2013a) and the limited body force of the PA, the actuator is well-suited for research applications on flow control topics. The lack of moving parts and short response times make PAs attractive for many applications. Recent articles by Wang *et al.* (2013) and Kriegseis *et al.* (2016, accepted) show comprehensive reviews of PAs as flow control devices, in particular for boundary-layer flow-control.

Model-based AWC algorithms showed promising results in DNS as reported by Semeraro *et al.* (2013) and Dadfar *et al.* (2013), whereas experiments were mainly conducted with adaptive control algorithms as the filtered-x-LMS (fxLMS) algorithm (Sturzebecher & Nitsche 2003; Kotsonis *et al.* 2013, 2015). The fxLMS is an extended version of the adaptive 'least mean square' (LMS) algorithm Elliott & Nelson (1993) that compensates the distance and therefore the transfer path from the actuator to the error sensor downstream. Fabbiane *et al.* (2015a) and Simon *et al.* (2015) investigated the adaptivity of the fxLMS algorithm and its limits. The required model of the so called secondary path, between actuator and error sensor, should not change significantly during the experiment otherwise the algorithm becomes unstable.

For narrowband disturbances in laminar boundary layers the dxLMS algorithm can be used as shown later in this manuscript. Until now the dxLMS algorithm has only been applied to acoustic problems (Kuo & Morgan 1995; Kim & Park 1998; Snyder & Hansen 1990; Hansen & Snyder 1996) but the savings in computational power makes its application promising for future 3D application with multiple PAs in spanwise direction for the delay of natural transition. The reduction of the complexity of the secondary-path model to a simple delay N combined with a model free approach for the determination of the required N leads to a promising "black box" system as shown in this manuscript for the first time.

This work presents a detailed study on the application of the dxLMS algorithm for laminar flow control. It is structured as follows:

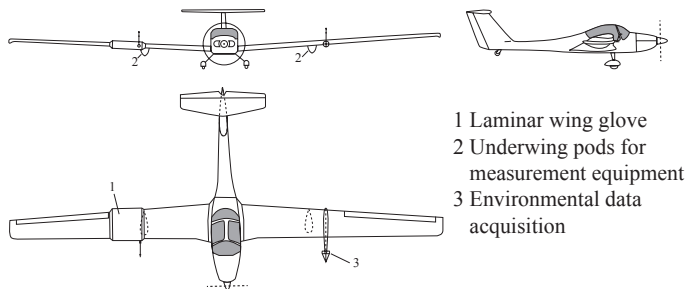


Figure 1: Grob G109b motor glider.

Section 2 gives an overview of the experimental setup while section 3 presents the applied control theory. The numerical tools used in this work are described in section 4 and the in-flight measurements of the base flow as well as the DNS results are shown section 5. Section 6 and section 7 deal with the dxLMS operation in flight and a model-free approach for online-delay adaption, respectively. Concluding remarks summarize the content in section 8.

2. Experimental Setup

The in-flight experiments are conducted with a manned Grob G109b motorized glider, which combines the advantages of vibrationless gliding flight with a 96 kW engine for take off and altitude gain. The three-view drawing in Fig. 1 shows the glider with a wing span of 17.4 m and an aspect ratio of 15.9. The sweep angle is close to zero which leads to a negligible spanwise pressure gradient and an almost two-dimensional flow along the chord. A temporary 'permit to fly' allows an additional payload for the measurement equipment and leads to a maximum take-off weight of $m_{\text{MTOW}} = 950$ kg. Due to flight speed limitations the angle of attack exploitable for the experiments ranges between $\alpha_{\text{min}} = -3^\circ$ and $\alpha_{\text{max}} = 13^\circ$ close to stall speed. The flight speed is around $U_\infty = 41$ m/s for $\alpha = 2.5^\circ$, the actual value depends on the environmental conditions at flying altitude. The chord-based Reynolds number is $Re \approx 3.75 \cdot 10^6$.

The right wing of the glider can be equipped with a natural laminar flow (NLF) airfoil wing glove. The airfoil (Fig. 2) was developed by Weismüller (2012) to quantify the influence of atmospheric turbulence on NLF airfoils and Reeh & Tropea (2015) intensively investigated the flow around the airfoil in flight. The flat airfoil shape on the pressure side creates an almost linear pressure gradient which is adjustable between moderate positive and negative values. The flow was shown to be 2D in the inner region of the wing glove by Reeh (2014). All base flow considerations and resulting pressure distributions are discussed later in section 5.

The wing glove itself (Fig. 3) forms a square shape with a chord length of $c = 1.35$ m and is slipped over the wing. The pressure distribution is measured



Figure 2: Airfoil shape.

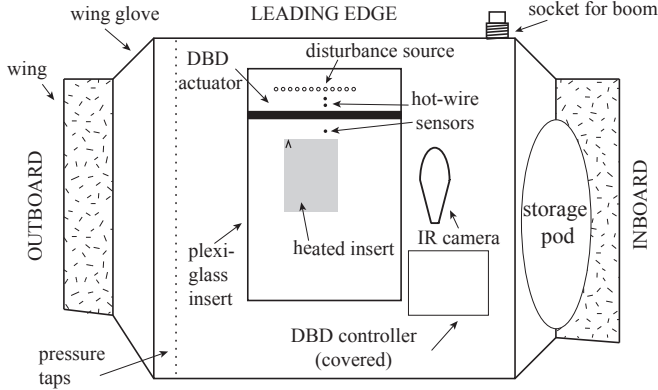


Figure 3: Sketch of the wing glove pressure side.

with 64 pressure taps distributed over the suction and pressure side of the wing glove and acquired by a Pressure Systems ESP-64HD pressure transducer. The reference atmospheric pressure p_∞ is gained at a boom protruding upstream into the flow mounted at the wing glove.

An exchangeable plexi-glass insert is arranged flush mounted to the surface (see Fig. 3) and accommodates the sensors and actuators. The disturbance source d is located at $x_d/c = 0.18$ and consists of 12 miniature loudspeakers installed underneath the measurement insert in spanwise direction with a spacing of 20 mm. A circular array of six 0.2 mm holes connects each speaker to the aerodynamic surface.

Three surface hot-wires probes p , r and e are located at $x_p/c = 0.26$, $x_r/c = 0.29$ and $x_e/c = 0.38$. The in-house manufactured hot-wire sensors are flush mounted to the surface and consist of two needles molded in a plastic case with a 1.25 mm long and $5\ \mu\text{m}$ thin gold plated tungsten wire welded on top. All hot-wires are operated by Dantec MiniCTA constant temperature anemometers. A signal conditioner filters the analog signals (first order bandpass 50 Hz to 3.8 kHz) and amplifies the signal fluctuations by a factor of 400. The following geometrical distances between sensors and actuator have been measured at the wing glove:

- $\overline{pr} = 35\ \text{mm}$
- $\overline{rc} = 47\ \text{mm}$

- $\bar{c}e = 76$ mm.

The PA c is positioned flush mounted in a groove at $x_c/c = 0.33$. It consists of a 10 mm wide grounded lower copper electrode of $35 \mu\text{m}$ thickness and a 5 mm wide upper electrode divided by five layers of polyimide tape with a total thickness of 0.3 mm. The driving high voltage signal is generated at a fixed frequency of $f_{\text{PA}} = 9.8$ kHz by a GBS Minipuls 2.1 while the high voltage amplitude can be modulated with an analog input signal. The modulation of the driving frequency allows the generation of a variable volume force in time (Kurz *et al.* 2013) which can be divided in a stabilizing steady 'force offset' and an unsteady part which is used for active wave cancellation. In spanwise direction the PA is 230 mm long and a 2D behavior is assumed in the following.

A dSPACE digital signal processor, consisting of a DS1007 processor board, a DS2004 A/D board and a DS2102 D/A board mounted in a dSPACE AutoBox acquires the hot-wire signals and generates the input signals for the disturbance source and the high-voltage generator. Data acquisition and the control algorithm (section 3) run at a sampling frequency of $f_S = 20$ kHz.

An environmental data acquisition setup mounted on the left glider wing completes the in-flight testing setup (see Fig. 1). The angle of attack α and the side-slip angle β are measured with a *Dornier Flight Log*, which is a wind vane mounted on a second boom. In addition the atmospheric pressure p_∞ , dynamic pressure q and temperature T_∞ are measured upstream of the left wing. All ambient flow conditions are acquired with a sampling frequency of 1 kHz by a NI6221 USB A/D converter, synchronized to the other measurement data with a digital trigger.

All measurement equipment is operated by an onboard DC 24 V lead acid battery with a capacity of 16 Ah which allows a system operation time of about one hour. More details about the measurement procedure is given in section 5.1.

3. Control Theory

This section briefly explains the implemented control algorithms and gives an insight on the application of these algorithms for active flow control in a laminar boundary layer. Further detailed information on the control theory background can be found in several text books (Elliott & Nelson 1993; Kuo & Morgan 1995).

3.1. Filtered- x -LMS Control Algorithm

The flow-control system sketched in Fig. 4 is a single-input-single-output (SISO) system as it consists of one reference sensor r , an error sensor e and the actuator c . An adaptive feed-forward least mean squares (LMS) control algorithm which is applied adapts a digital finite impulse response (FIR) filter in order to minimize the signal at the error sensor. The filter output $y(n)$ of a

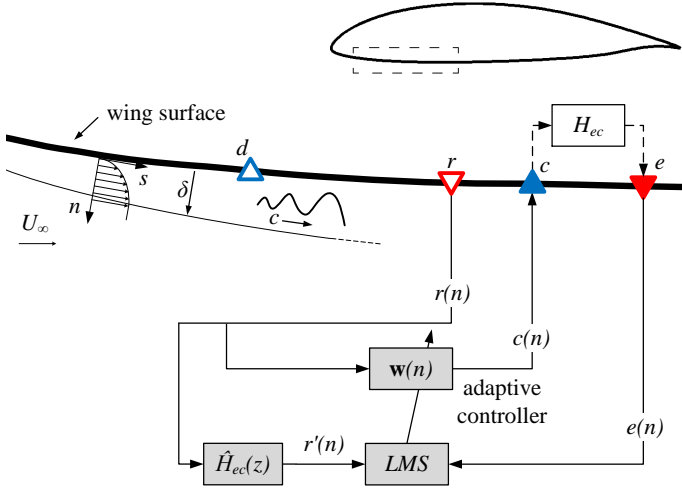


Figure 4: 2D wing setup and extended fxLMS control algorithm sketched below.

FIR filter $\mathbf{w} = [w_0 \dots w_{M-1}]^T$ and an input signal x is given by

$$y(n) = \sum_{i=0}^{M-1} w_i x(n-i). \quad (1)$$

The variable n indicates the discrete-time step and the filter order is $M = 256$ for most examples presented in this manuscript. The filter \mathbf{w} is adapted by the LMS control algorithm as indicated in Fig. 4 by the arrow. The adaptation is based on

$$\mathbf{w}(n+1) = \mathbf{w}(n) + \alpha \mathbf{r}(n) e(n), \quad (2)$$

where α is the step size, which is set to $\alpha = 10^{-3}$, and $\mathbf{r} = [r(n) \dots r(n-M+1)]^T$ a vector of the last M values of the reference sensor signal.

The transfer function from x to y is defined as H_{yx} (to actuator/sensor y , from actuator/sensor x) therefore H_{er} denotes the primary path (to e , from r) while H_{ec} is the secondary path (to e , from c). Thus, the secondary path describes the transfer function between the plasma actuator c and the error sensor e while the primary path describes the transmission behavior between reference sensor r and error sensor e . The feedback path H_{rc} (to r , from c) is negligible in the presented flow control system as the Tollmien-Schlichting disturbances in the laminar boundary layer only propagate downstream.

The LMS control algorithm adapts the filter \mathbf{w} which describes the behavior of the control path H_{cr} . The LMS algorithm alone requires the same position for the actuator c and the error sensor e otherwise the phase-angle shift due to the secondary path H_{ec} would lead to an unstable controller behavior (Elliott & Nelson 1993). The experimental setup does not allow to place the sensors

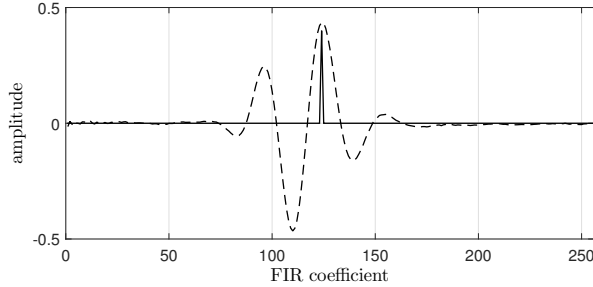


Figure 5: Secondary path model \hat{H}_{ec} and corresponding delay of $N_P = 124$ samples for the dxLMS algorithm.

very close to the plasma actuator due to the high voltage and geometrical concerns. This is often the case also for acoustic or structural vibration problems. Therefore, the physical secondary path H_{ec} is modelled with another FIR filter \hat{H}_{ec} to filter the reference signal $r(n)$ and compensate the phase shift. An example for a filter \hat{H}_{ec} is presented in Fig. 5 which shows the convective behavior of the transmission path. The filtered signal $r'(n)$ is now fed into the LMS algorithm as shown in Fig. 4 and the algorithm is now called filtered-x-LMS or fxLMS:

$$\mathbf{w}(n+1) = \mathbf{w}(n) + \alpha \mathbf{r}'(n) e(n). \quad (3)$$

Former investigations by the authors (Fabbiane *et al.* 2015a; Simon *et al.* 2015) showed a robust controller behavior as long as the phase-angle error between the physical secondary path H_{ec} and the secondary path model \hat{H}_{ec} is between $\pm 90^\circ$. This is a well known boundary for the controller stability (Elliott & Nelson 1993; Hansen & Snyder 1996).

3.2. Delayed-x-LMS Control Algorithm

For a narrow band disturbance problem, such as TS-waves in the laminar boundary layer, a delay z^{-N} with N samples might be good enough to approximate a model for the convective behavior of the secondary path. Fig. 5 shows such a model for the secondary path \hat{H}_{ec} as well as the approximation of H_{ec} with a delay of $N_P = 124$ samples. The index P indicates a delay corresponding to the global maximum (peak) of \hat{H}_{ec} . Li & Gaster (2006) proposed a related approach for the simplification of a transfer function for active flow control by simplifying the already calculated control kernel with a delay. With the delay z^{-N} the LMS algorithm (equation (2)) can be written as follows and is now called delayed-x-LMS (dxLMS):

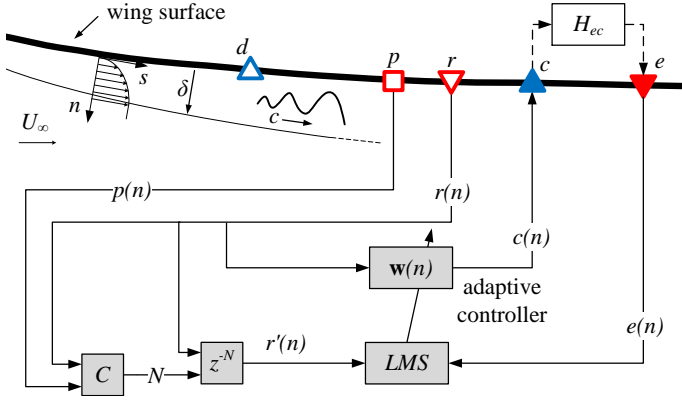


Figure 6: 2D wing setup and dxLMS control algorithm sketched below.

$$\begin{aligned}\mathbf{w}(n+1) &= \mathbf{w}(n) + \alpha \mathbf{r}(n) z^{-N} e(n) \\ &= \mathbf{w}(n) + \alpha \mathbf{r}(n-N) e(n).\end{aligned}\quad (4)$$

Snyder & Hansen (1990) as well as Kim & Park (1998) applied the dxLMS algorithm for acoustic problems with narrow-band noise. The experiments presented in this manuscript show its application for laminar boundary layer flow control for the first time.

Fig. 6 shows the dxLMS controller sketched below the 2D wing setup. Besides the dxLMS algorithm a second upstream sensor p is introduced which serves as an input signal $p(n)$ for the block C together with the reference sensor signal $r(n)$. Block C is responsible for the identification of the delay N in equation (4). In the following the procedure for calculating the time-delay N is described.

3.2.1. Delay identification

The downstream propagating disturbance a is a superposition of travelling-waves:

$$a(x, t) = A e^{i(\omega t - kx)} = A e^{i\Phi}, \quad (5)$$

where ω is the angular frequency, k the streamwise wave-number and Φ the phase angle of the wave. The growth in amplitude A is neglected, since it is not relevant for the following analysis. The phase speed c is defined by $c = \frac{\omega}{k}$ while group speed c_g is defined as the derivative of ω with respect to the modulus of the wave number k :

$$c_g = \frac{\partial \omega}{\partial k}. \quad (6)$$

Assuming a group speed c_g , the cross correlation function of two sensor signals at location x_1 and x_2 gives the time shift between both sensor signals τ :

$$\tau(\omega) = \int_{x_1}^{x_2} \frac{1}{c_g(\omega)} dx. \quad (7)$$

If a parallel flow or a slowly varying boundary layer is considered, the group speed is constant between the two locations ($x_2 - x_1 = \Delta x$). If a constant group-speed is assumed in the range of the amplified frequencies, equation (7) reduces to

$$\tau(\omega) \approx \tau = \frac{x_2 - x_1}{c_g} = \frac{\Delta x}{c_g}. \quad (8)$$

This translates in a time-discrete delay or lag L between the sensors p and r

$$L = f_S \tau = f_S \frac{\Delta x}{c_g}, \quad (9)$$

where f_S is the sampling frequency.

As the dSPACE digital signal processor executes the algorithm at a rather low frequency of $f_S = 20$ kHz the phase-angle resolution $\delta\Phi(f) = \frac{f}{f_S} 360^\circ$ has to be taken into account for the accuracy of the signal shift measurement L . If the assumption of an almost constant average group speed is correct, the signal shift L in samples can be normalized by the distance between the sensors p and r (\overline{pr}) and a specific time delay γ is introduced as follows:

$$\gamma = \frac{L}{\overline{pr}} = \frac{N}{\overline{ce}} = \frac{f_S}{c_g}. \quad (10)$$

This is valid if the group speed is constant between the sensors p and r : this assumption is verified later in the manuscript in section 5.2.

Equation (10) indicates that the required delay N for the dxLMS operation can then directly be calculated from a measurement of the signal-shift L by

$$N = \gamma \cdot \overline{ce}, \quad (11)$$

where N is rounded to the closest integer. This link leads to a 'black box' system which could operate the controller without any knowledge of the laminar boundary layer flow around the wing glove. Section 7 discusses the application of the dxLMS in real flight application and the advantages in comparison to the well known fxLMS approach.

The key to this reduction of the complexity of the secondary path is the similarity between the phase response given by the time-delay and the actual phase response by a TS-wave. The phase response associated to a time delay reads:

$$\Delta\Phi = - \left(360^\circ \frac{N}{f_S} \right) f. \quad (12)$$

As mentioned before, a similar expression can be derived for the disturbances in the TS-wave band. A downstream propagating wave in (equation (5)) causes a phase-angle shift $\Delta\Phi$ of the sensor signals between the two different stream-wise positions. It can be shown that the derivative of the phase-angle shift $\Delta\Phi$ with

respect to the angular frequency ω is equal to minus the previously computed time-delay τ :

$$\begin{aligned}\frac{\partial}{\partial\omega}(\Delta\Phi) &= \frac{\partial}{\partial\omega}(-k \Delta x) \\ &= -\frac{\partial k}{\partial\omega} \Delta x = -\frac{\Delta x}{c_g} = -\tau.\end{aligned}\quad (13)$$

Hence, by integrating $\frac{\partial}{\partial\omega}(\Delta\Phi)$ in this region, we obtain that the phase-angle shift (in deg) is given by:

$$\Delta\Phi(f) = -\left(360^\circ \frac{\Delta x}{c_g}\right) f + \Delta\Phi_0, \quad (14)$$

where $f = 2\pi\omega$ is the frequency and $\Delta\Phi_0 \in [0^\circ, 360^\circ)$ is the zero-cross phase. By comparing equations (12) and (14), the possible values of $\Delta\Phi_0$ reduce to 0° , if a positive gain is used in front of the time delay, or 180° , if a negative gain is considered. Hence, once the time-delay τ is identified via a measurement of the group speed c_g , the only free parameter for the dxLMS design is the positive/negative gain associated with the time-delay.

3.3. Offline Controller Simulation

The knowledge of all transmission paths of the flow control problem makes an offline investigation of the fxLMS and dxLMS controller behavior possible. Either the sensor signals of a test flight or the DNS solution of a flow field can describe the required paths between sensors and actuators. This offline-controller simulation in MATLAB-Simulink saves measurement time and allows a detailed preparation for the test flights, where time is valuable. In the following, the controller simulation based on flight data and DNS are discussed.

For the identification of the secondary path model \hat{H}_{ec} during an experiment, the Minipuls high voltage amplifier is operated with a pseudo random binary signal (PRBS). This results in a modulated high voltage signal at the PA which creates broad-band TS-waves travelling downstream. The transmission behavior of H_{ec} can either be estimated online with a LMS or calculated offline with the power spectral density $S_{cc}(\Omega)$ and the cross-spectral density $S_{ec}(\Omega)$ (Elliott & Nelson 1993):

$$S_{cc}(\Omega) = \lim_{n \rightarrow \infty} \frac{1}{\sqrt{2T}} (C_T^*(\Omega)C_T(\Omega)) \quad (15)$$

$$S_{ec}(\Omega) = \lim_{n \rightarrow \infty} \frac{1}{\sqrt{2T}} (E_T^*(\Omega)C_T(\Omega)). \quad (16)$$

The transmission behavior $\hat{H}_{ec}(\Omega)$ is defined as follows:

$$\hat{H}_{ec}(\Omega) = \frac{S_{ec}}{S_{cc}}. \quad (17)$$

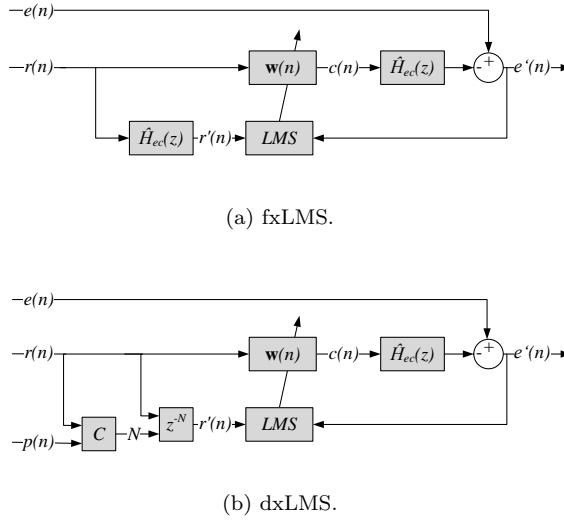


Figure 7: Block diagram for controller simulation with recorded flight data.

The magnitude and phase information, which is contained in $\hat{H}_{ec}(\Omega)$ can then be converted to a digital FIR filter $\hat{H}_{ec}(z)$, e.g. with the *invfreqz* command in MATLAB. For offline controller simulation $\hat{H}_{ec}(z)$, a record of a flight case with only disturbance source in operation is required (uncontrolled case). The discrete reference and error sensor signals $r(n)$ and $e(n)$ are the input signals for the fxLMS offline controller simulation as indicated in Fig. 7a. The incoming reference sensor signal $r(n)$ is therefore the same as if the controller would be operated during flight and the filtering of $r(n)$ with \hat{H}_{ec} is exactly the same as in flight. Because the controller actuation is only performed offline the physical transmission path H_{ec} has to be modelled and $c(n)$ is filtered by \hat{H}_{ec} . The result is then subtracted from the measured 'desired' signal $e(n)$ and the simulated error sensor signal $e'(n)$ is the second input for the LMS adaptation algorithm. It is obvious that this procedure does not completely describe the flight conditions because the estimated paths \hat{H}_{ec} in the upper and lower row in Fig. 7a are exactly the same. In a real case the physical transmission path H_{ec} changes due to varying inflow conditions and can even cause an unstable controller behavior as discussed later in section 7 and shown by Simon *et al.* (2015).

Fig. 7b shows the block diagram for the dxLMS offline-controller simulation with recorded flight data. The only difference to the fxLMS approach in Fig. 7a is the filtering of $r(n)$ and the online-adaptation of the delay N as described earlier in this section.

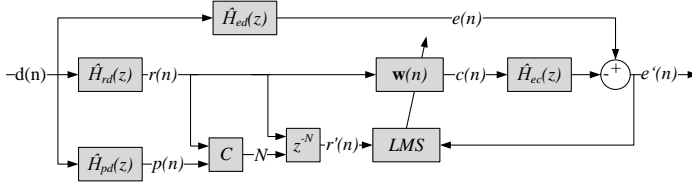


Figure 8: Block diagram for controller simulation with transfer paths obtained with DNS.

Direct numerical simulations (DNS) allow to extract detailed information of the boundary layer transmission behavior. For the given problem, the FIR filter coefficients of the transfer path models \hat{H}_{pd} , \hat{H}_{rd} , \hat{H}_{ed} and \hat{H}_{ec} are available and implemented in the controller simulation as shown in Fig. 8. Analogous to the in-flight data controller simulation the reference sensor filtering can be changed for the fxLMS controller simulation, see Fig. 7. The incoming disturbances are not given by in-flight sensor data, a white noise signal $d(n)$ is the only input signal required for the DNS data controller simulation.

4. Numerical Tools

A spectral-element method (SEM) code – Nek5000 – is used to perform two-dimensional (2D) direct numerical simulations (DNS) of the incompressible flow close to the wing, Fischer *et al.* (2008). The code is based on a discretisation of the computational domain in spectral elements (Patera 1984) and in each element the flow is approximated by 2D Legendre-Gauss-Lobatto polynomials up to degree N .

The Reynolds number $Re = \frac{U_\infty c}{\nu}$ for the simulations is $3.75 \cdot 10^6$. The computational domain extends along the airfoil from $x/c = 0.1$ of its upper surface to $x/c = 0.65$ on the lower side, see Fig. 9. The domain is discretized in 20000 2D spectral elements of order $N = 12$ on both directions: 400 elements are distributed along the airfoil surface and 50 along the wall normal direction with cosine distribution to form a curvilinear grid. The wall-normal and wall-wise size of the elements goes respectively from a minimum of $4 \cdot 10^{-5}$ and $7 \cdot 10^{-4}$ close to the wall to a maximum of $1 \cdot 10^{-2}$ and $7 \cdot 10^{-3}$ in the free-stream.

No slip boundary condition is enforced on the airfoil surface. On the free-stream boundary, a Dirichlet boundary-condition enforces the solution to the potential solution of the flow, corrected for the presence of a boundary-layer. The two outflow boundaries are treated according to Brynjell-Rahkola (2015): on the boundary pressure and velocity are linked by the relation

$$\frac{1}{Re} \frac{\partial u_n}{\partial n} - p = -p_a, \quad (18)$$

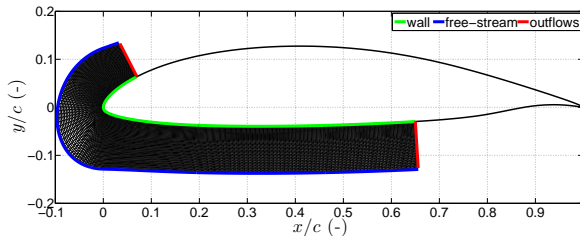


Figure 9: DNS mesh.

where n is the boundary-normal direction and u_n the component of the velocity normal to the boundary. The pressure is indicated by p and the boundary pressure p_a is computed from the superposition of the potential flow and Falkner-Skan boundary-layer solution.

4.1. Linear simulations

Linear simulations are performed with respect to the steady solution. The boundary condition for the perturbation velocity are similar to the baseflow boundary conditions: no-slip on the surface, homogeneous Dirichlet on the free-stream boundary and homogeneous outflows (i.e. $p_a = 0$). In addition, sponges are placed in front of each outflow in order to avoid reflections: both upper and lower sponges have the tickness $\Delta x/c = 0.05$.

Input and output devices used in the experimental setup are modelled in the numerical simulations. Surface hot wires are represented by a weighted-average of the wall-shear stress: a Gaussian function with variance $10^{-3}c$ is used as a weight function. The disturbance introduced by the loud-speakers is modelled by a train of synthetic vortices introduced at the same location as the loudspeakers in the experimental set-up, Bagheri *et al.* (2009). The plasma actuator, instead, is represented by a volume forcing based on the experimental results by Kriegseis *et al.* (2013b) at the PA's location, Fabbiane *et al.* (2015b).

5. Base Flow

All test flights are conducted in gliding flight without engine which requires a special in-flight testing procedure, explained in section 5.1. Based on this experiments the base flow around the wing is characterized and the boundary layer properties are investigated in section 5.2.

5.1. In-Flight Testing Procedure

The in-flight tests presented in this paper enable boundary layer measurements in a realistic flight environment. It does not, however, determine the performance parameters of the aircraft as flight testing is usually understood. Nonetheless, the measurements are related to flight mechanics, environmental conditions

and flight planning - challenges which only exist for measurements under flight conditions (Joslin 1998). Despite the difficulties of in-flight measurements compared to wind-tunnel tests, there are reasons for experiments on a airplane wing in flight. The investigations of Weismüller (2012) on the atmospheric turbulence indicate the need for in-flight experiments as the turbulence intensity is very low. More importantly, isentropic turbulence is achievable for high Reynolds numbers. In addition acoustic disturbances make the investigation on natural transition in the wind tunnel difficult as the ambient noise can trigger laminar-turbulent transition. Last but not least, a flow control technology in flight is very close to application.

The measurement time, preparation, maintenance and costs exceed the effort for wind tunnel experiments by far. For the current setup, one test flight of 1.5 h includes only 20 min of measurement time, the rest of the time is spend on cruise flight and altitude gain. During a measurement flight, the glider climbs up to altitude of 10,000 ft and the pilot switches off the engine. As soon as the propeller is turned away from the wind the pilot starts to adjust the angle of attack α according to the flight display in front of him; an online-visualization of the low-pass filtered values for α and the slideslip-angle β assists the pilot in setting and maintaining the desired flight state. Flight mechanics couple flight speed U_∞ and α depending on the weight, required lift, density of the air and other parameters and therefore do not allow the same boundary conditions for each flight, even during one single gliding flight. Numerical studies based on linear stability analysis concerning these issues have been conducted by Duchmann (2012). They revealed a stronger sensitivity of the streamwise position of the naturally occurring transition to changes of the angle of attack than to a slowly drifting Reynolds number. Therefore, the active flow control experiments in gliding flight were conducted for constant angle of attack conditions instead of constant Reynolds number condition. Nevertheless, only small Reynolds number fluctuations are observed in the presented data. The first measurement run can be recorded in gliding flight at 9,000 ft and the measurements have to be stopped at an altitude of about 3,000 ft to turn back on the engine. The measurement time of one gliding flight is about 10 min while typically 15 measurement runs of 20 to 40 s are recorded. All experiments have been conducted early in the morning under calm conditions to avoid changes in α . Unavoidable limitations to in-flight experiments are given by traffic, inversion layers and battery power supply, which operates the whole measurement equipment.

5.2. Base Flow Characterization

As discussed before, the angle of attack measurement with the *Dornier Flight Log* only gives a rough estimate of the in-flow conditions as the systematical error due to positioning of the probe is not taken into account. Because of this the pressure distribution around the wing glove as well as the dynamic pressure q measured upstream of the wing are the reference values for comparison with

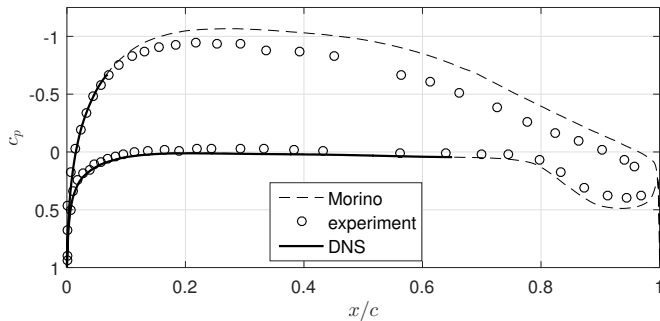


Figure 10: Measured and calculated pressure distribution, $\alpha = 2.5^\circ$.

numerical investigations. Fig. 10 shows a pressure distribution measured in flight. The boundary layer is tripped artificially on the suction side of the wing glove by surface roughness, which can be seen in the pressure distribution as a rising pressure at $x/c = 0.3$.

Due to the high Reynolds number, small displacement thickness and moderate α potential flow theory provides a good estimate of the pressure around the wing glove. The potential flow solution, calculated with a Morino method, is drawn as a dashed line in Fig. 10. All experiments are conducted on the pressure side of the wing glove. Therefore the angle of attack is iterated for the potential flow solution in order to match the pressure distribution and, more important, the pressure gradient on the lower side. In the following discussions only the value for α measured during the experiment in flight is given.

The potential flow solution serves as an initial condition for DNS calculations which aim at two points;

1. comparison between flight and numerical simulations;
2. parameter studies under controlled conditions.

A comparison between numerical and experimental baseflow is presented in Fig. 10. It shows a good agreement on the pressure side.

Active wave cancellation in the laminar boundary layer requires a sufficiently low amplitude of the disturbances at the actuator position such that the transition process is in the linear regime. For the in-flight experiments this leads to a range of $1.5^\circ < \alpha < 3.5^\circ$ in which the experiments with artificially introduced 2D disturbances are reasonable. The pressure distributions for the considered range is shown in Fig. 11. It is obvious that the pressure gradient in this region can be altered from slightly negative for high α to slightly positive for lower α .

The boundary layer profiles extracted from DNS calculations enable investigations on the linear stability of the boundary layer in the considered range of flight states. Three neutral stability curves and N-factor contour plots,

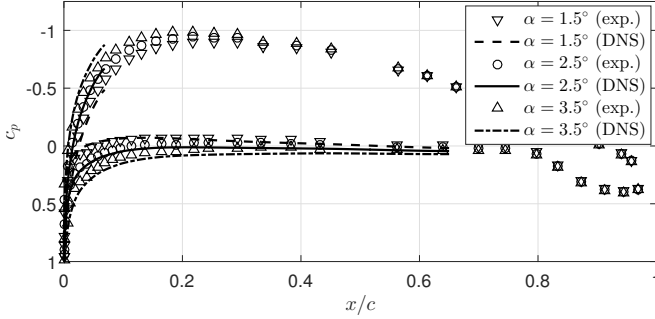


Figure 11: Measured and calculated pressure distribution for different angles of attack.

calculated with PSE (Juniper *et al.* 2014), are shown in Fig. 12. The sensor positions are indicated as triangles (see Fig. 6) and the disturbance source d with a Δ . Because the experiments are conducted on the pressure side of the wing glove, the pressure gradient is decreasing for higher α and therefore stabilizes the laminar boundary layer. This results in a downstream shifted neutral stability curve ($\alpha_i = 0$) and a slightly shifted amplified frequency band. The flat shape of the middle region of the airfoil (Fig. 2) leads to rather low amplification transition scenarios but also a significant movement of the transition region for a change of α which was shown by Reeh (2014) for the same airfoil in flight. For all three presented cases, the actuation with the PA (\blacktriangle) is active in a low amplified region where $N \approx 4$. The low amplification rates are necessary to introduce artificial 2D waves which dominate the natural disturbances. Future experiments on wave cancellation of natural disturbances with distributed actuators would not require such a low amplification (Peltzer *et al.* 2009).

Based on the PSE results the propagation behavior of the disturbances can be investigated more in detail. Fig. 13 shows the non-dimensionalized phase speed c and group speed c_g for the local maximum N-factor N_{\max} and $1.5^\circ \leq \alpha \leq 3^\circ$. The PSE results allow the calculation of the phase speed c .

As indicated in Fig. 13 the phase speed c and the group speed c_g slow down about 5% in the region between the sensors p (\square) and e (\blacktriangledown). The consequences of a changing group speed c_g for the specific time delay γ (equation (10)) is discussed later in section 7.

The flow control setup is a SISO system as mentioned before in section 3. Since only one actuator is mounted in spanwise direction a 2D wave front is required for the experiment. Natural TS-waves occur in wave packets with a modulation in spanwise direction (Peltzer *et al.* 2009; Saric *et al.* 2002). Therefore artificial disturbances with an even wave front are created by the disturbance source. Fig. 14 shows the power spectra of the reference sensor

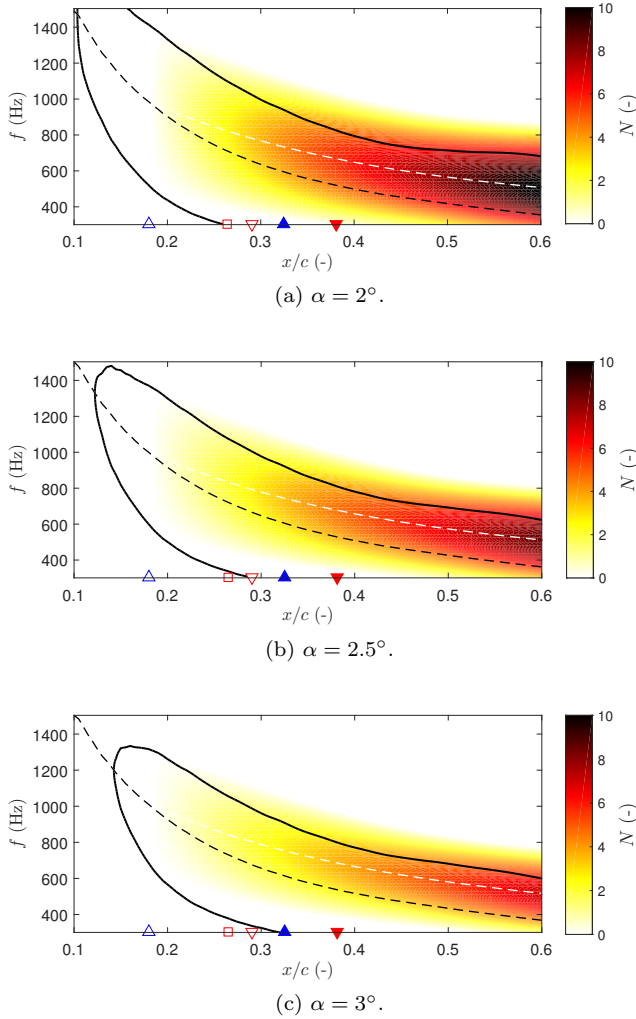


Figure 12: Neutral stability curve ($\alpha_i = 0$, black solid line) and N -factor contours for different α and $Re = 3.75 \cdot 10^6$. The dashed black line shows the most amplified frequency ($\alpha_i = \min$) while the dashed white line indicates the local N -factor maximum N_{\max} . The triangles below indicate the sensor and actuator positions (see Fig. 6).

signal $r(t)$ for the natural and artificial case (disturbance source on). The artificially created 2D waves show amplitudes which are 12 to 15 dB higher compared to the natural case, depending on the angle of attack α . This emphasises that the naturally occurring 3D waves can be neglected and a

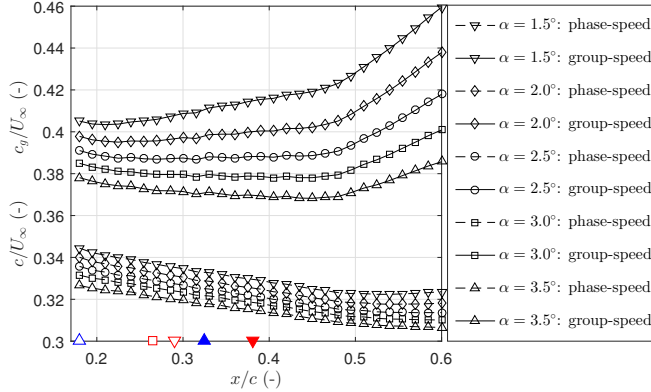


Figure 13: Non-dimensionalized phase speed c/U_∞ and group speed c_g/U_∞ of the disturbances at the frequency for N_{\max} . The triangles below indicate the sensor and actuator positions (see Fig. 6).

2D problem is present for the experiments. Limited space for sensors and measurement time does not allow a measurement of the 2D character of the wave front as it was conducted by the authors in wind-tunnel experiments (Fabbiane *et al.* 2015a). The speakers are positioned directly beneath the surface and the resulting small dead volume leads to the assumption that the speakers create a 2D wave. The steady part of the PA force alters the boundary layer profile and therefore also the stability properties of the boundary layer (Duchmann *et al.* 2014). For the present case, the high flight speed in combination with the rather low steady forcing of the PA leads to the assumption of a negligible effect of the boundary-layer stabilization. Changing flow conditions during flight do not allow to extract this small effect for the low actuator power levels from the recorded data, see section 5.1.

6. Controller Operation in Flight

Several experiments with successful TS-wave cancellation of broad-band disturbances with adaptive fxLMS algorithms have been reported in literature (Fabbiane *et al.* 2015a; Simon *et al.* 2015; Sturzebecher & Nitsche 2003). The successful application of the fxLMS controller for $U_\infty = 40.3 \text{ m/s}$ and $\alpha = 3^\circ$ with a broad-band disturbance is shown in Fig. 15a. The disturbances at the error sensor e , which range from about 500 Hz to 1100 Hz are almost completely damped.

The dxLMS control algorithm works as good as the fxLMS algorithm even with this very simplified model of the transmission behavior of the secondary path H_{ec} . Fig. 15b shows a amplitude reduction of 12 to 15 dB, if the controller is operated. For dxLMS controller operation, a digital bandpass filter (400 to

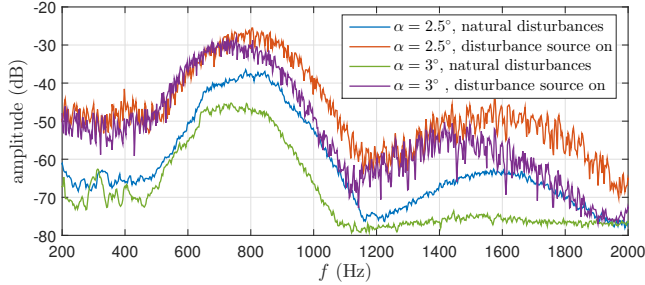


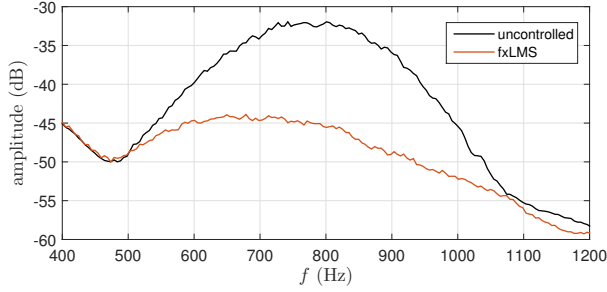
Figure 14: Power density spectra of the error sensor signal $e(t)$ for natural and artificially induced TS-wave disturbances.

1100 Hz) is implemented in the Simulink model for all sensor signals. The filter is necessary because the dxLMS controller adaptation can become unstable for low frequency disturbances due to a phase-angle error, which is discussed later in this section.

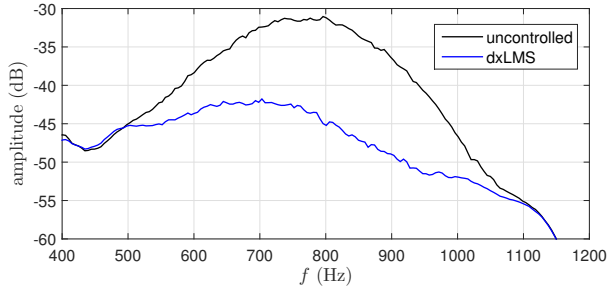
For direct comparison of both controller concepts the boundary conditions have to be the same. Wind-tunnel experiments can fulfill this requirement but for the flight test case an offline simulation of the controller behavior is necessary, see section 3.3. The physical secondary path H_{ec} is modelled with a FIR filter \hat{H}_{ec} . Fig. 16 shows the offline simulated controller behavior for exactly the same boundary conditions. The direct comparison shows that both controllers perform equally well while small deviations are caused by an adaptation of the LMS algorithm. It should be noted here, that the dxLMS controller shows almost exactly the same signal reduction for $N_P = 118$ samples compared to a shorter delay of $N = 115$ samples.

The LMS adaptation algorithm estimates the control path H_{cr} with a FIR filter \mathbf{w} , which describes the transmission behavior from the reference sensor r to the PA c . The filter \mathbf{w} is also known as “kernel” and shown in Fig. 17 for the offline simulated cases presented in Fig. 16. The FIR filters differ only for the first twenty coefficients but the most characteristic peaks, which are responsible for a successful TS-wave damping (Fabbiane *et al.* 2015a), match perfectly.

The control success with the dxLMS algorithm can be explained by looking at the phase response of the transmission paths. As shown by Simon *et al.* (2015), the fxLMS controller performance is almost constant for the stable controller parameters but decreases abruptly if $\pm 90^\circ$ phase-angle error of the secondary path model is exceeded. The solid blue line in Fig. 18 shows the phase response of the secondary path model filter \hat{H}_{ec} while the dotted lines indicate the $\pm 90^\circ$ boundary. The phase response of a delay is a straight line with the slope $\frac{\partial \Phi}{\partial f} = -\frac{360^\circ N}{f_s}$ and for the presented case with $N_P = 118$ the phase response lies in-between the $\pm 90^\circ$ boundary for the amplified region of the boundary layer. The frequency response of \hat{H}_{ec} is plotted as a black



(a) fxLMS.



(b) dxLMS.

Figure 15: Control success of the active wave cancelation for fxLMS and dxLMS ($N_P = 128$) algorithm at $\alpha = 3^\circ$. The spectra show the signal reduction at the error sensor e .

solid line and marks the important region below the TS-wave 'hump' where the disturbances in the boundary layer are amplified. For the optimal delay of $N_P = 118$ the phase responses of \hat{H}_{ec} and the delay meet at the most amplified frequency $f \approx 720$ Hz whereas the curve for $N = 115$ intersect above the amplified band at $f \approx 1030$ Hz. Both lie in-between the $\pm 90^\circ$ boundary for the whole band as indicated in Fig. 18. The dxLMS controller requires an additional bandpass filter to avoid an unstable controller adaptation caused by disturbances below the TS-wave frequency band which are not amplified by the boundary layer but can exceed the $\pm 90^\circ$ boundary.

The in-flight measurements are limited to the measurement with uncalibrated surface hot-wires. A measurement of the control success in terms of disturbance amplitude growth along the streamwise direction is not possible. The DNS results allow to measure the control success from the flow field. Fig. 19a shows the error-sensor spectra for the uncontrolled case as well as for dxLMS and fxLMS operation. The fxLMS controller reaches about 15 dB reduction in the amplified region while the dxLMS control algorithm performs equally

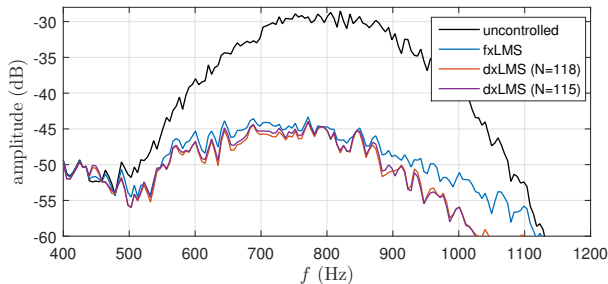


Figure 16: Controller simulation (offline) of fxLMS and dxLMS for the same test case. The transmission path is recorded at $\alpha = 2.5^\circ$ and the dxLMS algorithm operated with delays of $N_P = 118$ and $N = 115$.

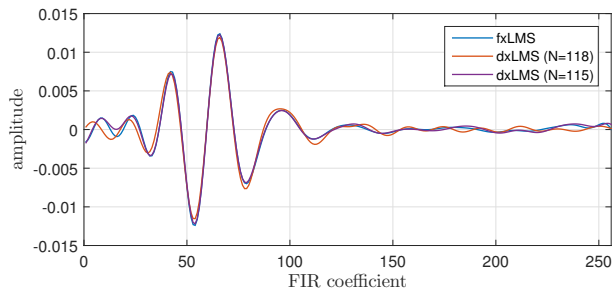


Figure 17: Kernel \mathbf{w} of the dxLMS and fxLMS controller for the test case shown in Fig. 16.

well for $f < 900$ Hz but slightly better for $f > 900$ Hz, which is consistent with the experimental results in Fig. 16. The converged kernels \mathbf{w} for both control approaches (Fig. 19b) match well but the dxLMS kernel differs slightly, similar to the experimental case shown in Fig. 17.

An evaluation of the whole flow control approach is not possible only by analyzing the error sensor signals because it includes only the performance at one point. The flow field obtained by DNS allows a prediction of the perturbation energy evolution for both control approaches, dxLMS and fxLMS. An integral value for the perturbation amplitude at a certain streamwise location is defined as follows:

$$A(x) = \int_{y=0}^{\infty} \langle (u'(x, y))^2 \rangle dy. \quad (19)$$

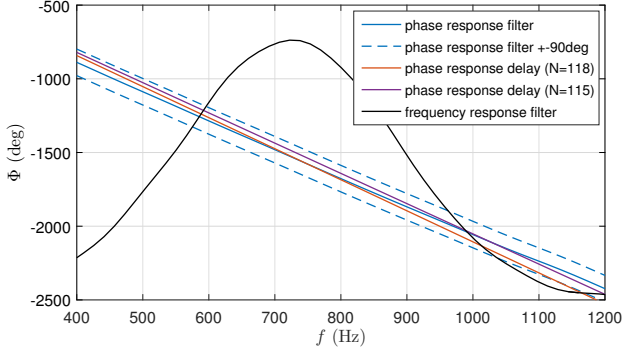


Figure 18: Phase response of the secondary path model filter \hat{H}_{ec} and a delay of $N_P = 118$ for dxLMS operation for the test case shown in Fig. 16.

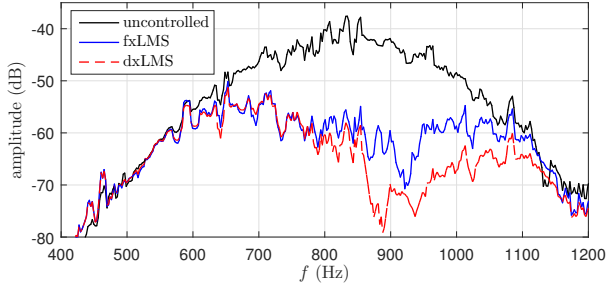
Fig.19c shows the streamwise evolution of A . The amplitude drops down at the actuator position PA (\blacktriangle) and grows again. The DNS results demonstrate that $e(t)$ is a good measure for the control success and the wave cancelation has a sustained effect on the disturbance amplitude downstream.

6.1. Variable Flow Conditions in Flight

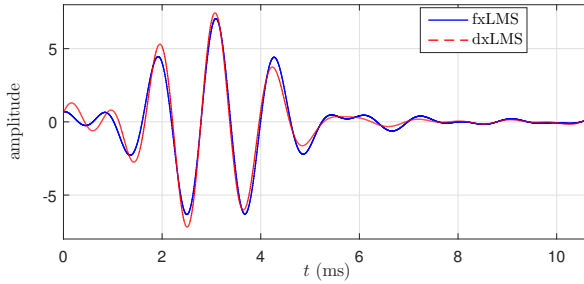
The stability and robustness of the fxLMS and dxLMS control algorithm is mainly dependent on the secondary path model \hat{H}_{ec} and the delay N . The corresponding FIR filters are shown in Fig. 20 for different angles of attack α and flight speeds U_∞ . It is obvious that the curves of \hat{H}_{ec} are stretched for higher angles of attack α and the amplitude is higher for lower α .

Simon *et al.* (2015) introduced scaling and stretching factors for a model adaptation and extended the stable operation range in a wind tunnel experiment for the fxLMS controller. This was done by a system identification and controller calibration for a certain range of wind tunnel speeds and an online-adaptation during the experiment. The black curve ($\alpha = 2.5^\circ, U_\infty = 37.2 \text{ m/s}$) in Fig. 20 shows that such a pre-calibration of the system is not possible. Because of flight mechanics the flow around the wing changes during flight. All transfer functions but the black curve are recorded at a flight altitude of about 8000 ft while the other curve is recorded at 3000 ft during the same gliding flight. Even if the mass of the glider (wing surface area S) and required lift F_L remain the same, the air density ρ changes with altitude and therefore the flight speed U_∞ changes for a constant α (or lift coefficient c_L):

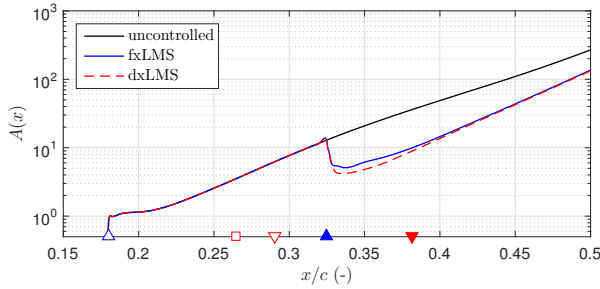
$$F_L = c_L \cdot \frac{\rho}{2} U_\infty^2 S. \quad (20)$$



(a) Power density spectra of the error sensor signal.



(b) Kernel w .



(c) Perturbation energy development.

Figure 19: Comparison between fxLMS and dxLMS by linear DNS for $\alpha = 2.5^\circ$ and $Re = 3.75 \cdot 10^6$. Data are normalized with respect to the introduced disturbance.

The increased density ρ at the lower altitude leads to a lower flight speed U_∞ and therefore to a lower group speed c_g of the Tollmien-Schlichting waves which is visible in a shift to the right in Fig. 20. The amplification of the disturbances is mainly influenced by the pressure gradient or α , respectively. This is why the amplitude of both measurements for $\alpha = 2.5^\circ$ remains constant.

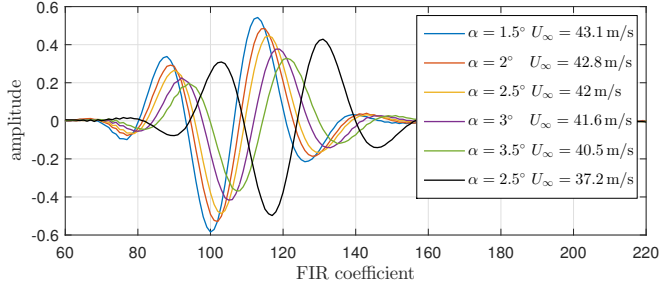


Figure 20: Secondary path model \hat{H}_{ec} for different angles of attack and flight altitudes.

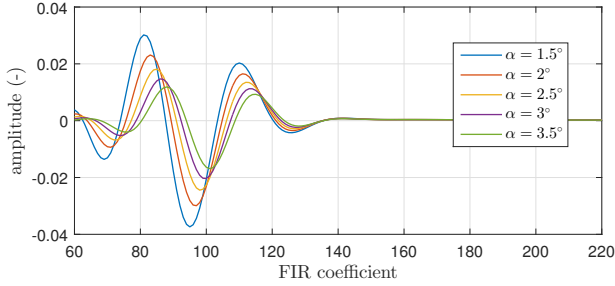
A pre-calibrated system would lead to an unstable controller behavior, if the phase-angle shift because the decreased group speed is higher than 90° .

Due to the changing boundary conditions the flight data are not ideal for a parametric study of α and U_∞ . The DNS calculations shown in Fig. 21 enable to investigate the influence of each parameter independently. A variation of α in Fig. 21a is associated with an increasing amplification for lower α but also the shape of the filter \hat{H}_{ec} is shifted to the left because of the increased group speed c_g , see Fig. 13. The flow speed U_∞ is varied by $\pm 10\%$ at $\alpha = 2.5^\circ$ and the resulting secondary path model \hat{H}_{ec} is shown in Fig. 21b. The shift of the curves is more significant for the change of U_∞ compared to α but the amplification is almost not influenced by U_∞ . Compared to the experimental values the DNS results do not match exactly because α and U_∞ are coupled in-flight but the observations of the parameter study can also be made with the experimental results in Fig. 20.

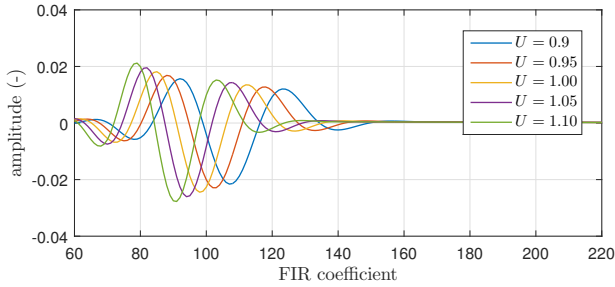
7. dxLMS Stability and a Model-Free Approach for Online-Delay Adaptation

The discussion of the varying flow conditions during flight in the last paragraphs shows the need for a model adaptation during operation of the LMS algorithm. In section 3 the calculation of the required delay N with an online-measured specific time delay γ was introduced (equation (11)).

Fig. 22 shows two upstream sensor signals $p(t)$ and $r(t)$ extracted from the test case shown in Fig. 16. The characteristics of the signals are almost the same while $r(t)$ is slightly shifted to the right due to the sensor distance $\bar{p}r$ and the group speed c_g of the downstream traveling waves. The shift between the signals, L , is extracted from the cross-correlation of both signals, presented in Fig. 23. A number of 2000 samples was found to give reliable results for the online-calculation on the dSPACE system which, implies an update of L every 0.01 s. The determined value of $L = 53$ samples can now be used to determine γ . For the presented example this leads to



(a) Variation of α .



(b) Variation of the normalized flow speed $U = \frac{U_\infty}{U_{\infty,ref}}$.

Figure 21: Parameter study of the secondary path model \hat{H}_{ec} for parameters α and U_∞ , computed with DNS data .

$$\gamma = \frac{L}{\bar{p}\bar{r}} = \frac{53 \text{ samples}}{35 \text{ mm}} = 1.514 \text{ samples/mm.} \quad (21)$$

The required delay N can now be calculated based on γ :

$$N = \gamma \cdot \bar{c}\bar{e} = 115 \text{ samples.} \quad (22)$$

Compared to the optimal delay $N_P = 118$ samples the delay determined by cross-correlation is slightly underestimated. The change of the group speed c_g leads to an error of $\Delta N = -3$ samples but it can be compensated by the adaptive character of the LMS algorithm as shown earlier in Fig. 16.

The phase-angle resolution $\delta\Phi(f)$ of a disturbance with the frequency f is critical for the stability of the controller because a phase-angle error for the secondary path model \hat{H}_{ec} of less than $\pm 90^\circ$ is required as explained in section 3. A sample rate of $f_S = 20$ kHz leads to a phase-angle resolution $\delta\Phi = 14.4^\circ$ for a disturbance with a frequency of $f = 800$ Hz. Flow control at higher flow speeds requires higher sampling rates. The model-free approach can only work,

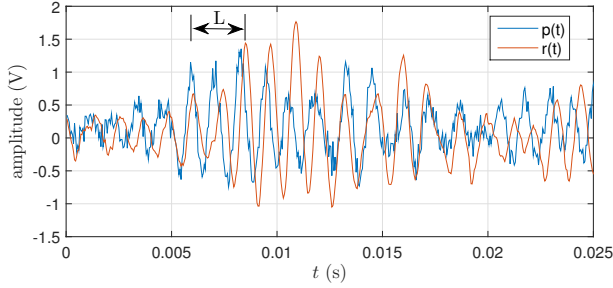


Figure 22: Upstream sensor signals $p(t)$ and $r(t)$. The lag sensor signal $p(t)$ is amplified by a factor of 2 for better comparison.

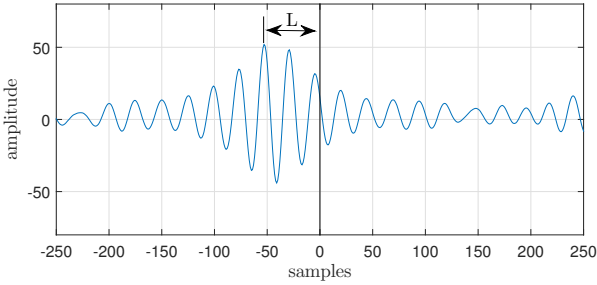


Figure 23: Cross-correlation of two upstream sensor signals $p(t)$ and $r(t)$, presented in Fig. 22.

if the phase-angle shift $\Delta\Phi$ can be resolved. In addition the ratio of the sensor distance \overline{pr} compared to the distance \overline{ce} influences the resolvable signal shift. For the given example the required delay N can only be determined with a resolution of

$$\delta N = 1 \text{ sample} \frac{\overline{ce}}{\overline{pr}} = 2.17 \text{ samples.} \quad (23)$$

In conclusion the sample rate and the upstream sensor distance are most important for the success of the presented model-free control approach. The positioning of the lag sensor p between r and c could provide a possibility to minimize the influence of a changing group speed in the streamwise direction.

The numerical simulation results allow the computation of the time delay N based on different methods;

- **group speed** c_g , based on the stability properties;
- based on a **peak** in the secondary path model \hat{H}_{ec} ;

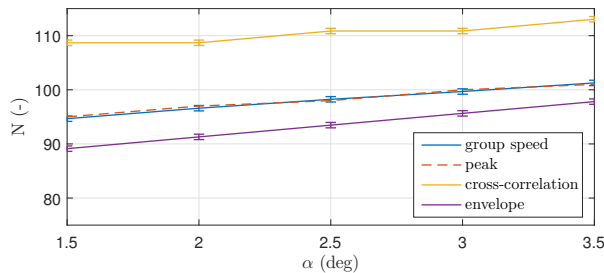


Figure 24: Delay N for dxLMS operation, computed using group speed, the (negative) peak of H_{ec} and the cross-correlation or the envelope of the cross-correlation from $p(t)$ and $r(t)$, respectively. The data is obtained from the DNS results.

- **correlation** techniques, based on the sensor signals $p(t)$ and $r(t)$

Fig. 24 shows a comparison between the listed methods for determining the required delay N for the dxLMS algorithm. Based on the stability of the boundary layer the average group speed c_g between PA (c) and e can be calculated (see Fig. 13). Equations (8) and (9) then translate the time shift τ with the sample rate f_S to a delay N . The resulting N increases with α because c_g slows down due to the decreasing flight speed U_∞ .

Plotting the position of the delay in a secondary path FIR filter curve (Fig. 25) shows an interesting fact: the group speed is represented by the global minimum of the impulse response curve. A reason for this behaviour, is that the peak (global minimum) of the impulse response is a very good measurement of the center of the wave packet. A model-free dxLMS operation based on the cross-correlation of the upstream sensor signals $p(t)$ and $r(t)$ has been introduced and works well for the data recorded in flight, see Fig. 23. However, for the cases calculated by DNS, the dxLMS controller is unstable because the second positive peak is lower in amplitude, compared to the experimentally obtained curves in Fig. 20 which leads to a slightly changed phase response.

Another correlation technique is a time shift measurement based on the envelope of the cross-correlation, see Fig. 26. The maximum of the envelope is the lag L between the sensor signals $p(t)$ and $r(t)$. Due to the envelope technique, the corresponding delay N is now close to the group speed c_g and therefore the minimum-peak in Fig. 25. As already discussed earlier c_g is decreasing with x and the envelope technique underestimates the delay slightly.

The most critical part which can be well investigated with the DNS results is the phase-angle error $\Delta\Phi_e$ between the secondary path model \hat{H}_{ec} and the actual secondary path H_{ec} . Fig. 27 shows $\Delta\Phi_e$ for all four different delay approaches. The two methods based on the group speed c_g and the (negative) peak lie on top of each other due to the same delay N . The curves are shifted

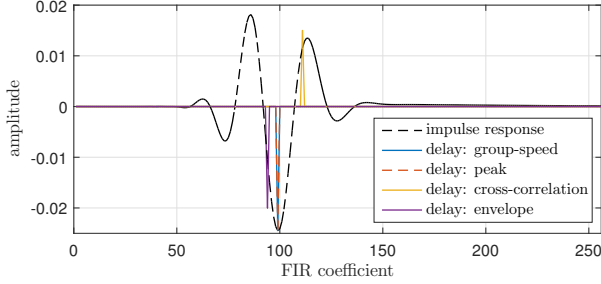


Figure 25: Secondary paths for fxLMS operation and different delays for the dxLMS approach. The data are obtained via DNS simulations at $\alpha = 2.5^\circ$.

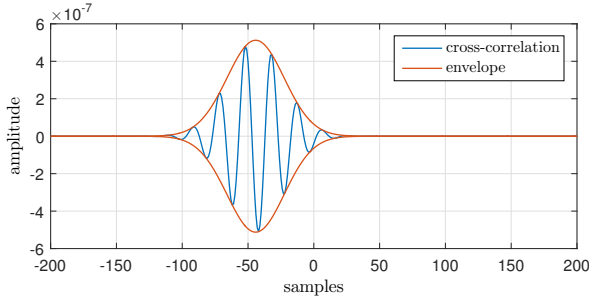


Figure 26: Cross-correlation of two upstream sensor signals $p(t)$ and $r(t)$ computed from DNS data at $\alpha = 2.5^\circ$.

by a zero-cross phase of $\Delta\Phi_0 = 180^\circ$ because of the negative gain, described in equation (14). In comparison to the group speed method, the cross-correlation method fulfills the stability criteria of the LMS ($\pm 90^\circ$ limit) only in a short band and does not match the slope of H_{ec} well but crosses the phase response, as already seen in the experimental results in Fig. 18. The group speed and peak based delay match the slope much better which leads to a phase-angle error $\Delta\Phi_e$ close to zero for a wide range of the amplified frequency band, see Fig. 12b. A model-free dxLMS operation is more robust in terms of LMS controller stability with the envelope method introduced above; the DNS results in Fig. 19 are obtained by using this method.

For dxLMS controller operation the zero-cross phase of $\Delta\Phi_0 = 180^\circ$ can be realized by adjusting the control law (equation (4)) with a negative gain (-1) as follows:

$$\mathbf{w}(n+1) = \mathbf{w}(n) + (-1)\alpha r(n)z^{-N}e(n) \quad (24)$$

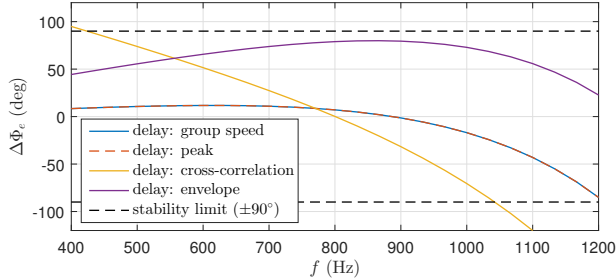


Figure 27: Phase error $\Delta\Phi_e$ with respect to the secondary path H_{ec} . The data is obtained via DNS simulations at $\alpha = 2.5^\circ$. A negative gain is used in the time-delay approximations, i.e. $\Delta\phi_0 = \pi = 180^\circ$, for the time delays N computed via group speed, (negative) peak of H_{ec} and the cross-correlation or the envelope of the cross-correlation from $p(t)$ and $r(t)$, respectively.

The discussion above illustrates that particular care has to be taken in identifying the center of the wave-packet trace. A cross-correlation method may lead to an error in the time-delay or phase-angle, respectively. Moreover, the error of the correlation is also due to the variation in the group-speed between p - r and c - e location: in this setup, this error does not compromise the stability of the control algorithm and the error reduces by increasing the angle of attack, see Fig. 24. However, a small systematic error will always be present.

8. Conclusions

The main focus of the work is the controller stability paired with a detailed investigation of the boundary layer transmission behaviour, supported by DNS. The performance of the reliable fxLMS control algorithm and the newly introduced modified dxLMS control algorithm has been investigated for active wave cancelation in flight under realistic atmospheric conditions.

Performance-wise the dxLMS and fxLMS control algorithms work equally well, if the delay N is chosen in such a way that the phase-angle error $\Delta\Phi \leq \pm 90^\circ$. In-flight measurements and DNS simulations showed that the group speed of the TS-wave disturbances change significantly dependent on the environmental conditions and therefore also e.g. on the altitude. The resulting phase-angle error $\Delta\Phi$ therefore leads to an unstable controller behaviour, if a previously identified model of the boundary layer transmission is not valid any more.

The introduced model-free “black box” system successfully works without any previous information about the environmental conditions and successfully cancel out TS-wave disturbances with the presented SISO system. An advanced method for dxLMS controller operation and the determination of N , based on the group speed measurement, has been introduced and theoretically derived. In addition, the dxLMS algorithm requires less computational power because

a FIR filter is replaced by a simple delay N . With regard to future MIMO systems for active wave cancelation of naturally occurring wave packets the dxLMS approach is a key development for less complex controllers and lower requirements on the computational power.

This work was supported by the German research foundation (DFG) under the grant No.GR3524/4-1. Simulations have been performed at the National Supercomputer Centre (NSC) with computer time granted by the Swedish National Infrastructure for Computing (SNIC). We also wish to thank Jens Rohlfing from Fraunhofer LBF (Darmstadt) for the fruitful discussions. Finally we appreciate the support of our student and flight test pilot Tobias Hofmann.

REFERENCES

- BAGHERI, S., BRANDT, L. & HENNINGSON, D. S. 2009 Input–output analysis, model reduction and control of the flat-plate boundary layer. *J. Fluid Mech.* **620** (1), 263–298.
- BRYNJELL-RAHKOLA, M. 2015 Global stability analysis of three-dimensional boundary-layer flows. Lic. thesis, KTH, Stockholm.
- DADFAR, R., SEMERARO, O., HANIFI, A. & HENNINGSON, D. S. 2013 Output feedback control of flow on a flat plate past a leading edge using plasma actuators. *AIAA Journal* QP 2013.
- DUCHMANN, A. 2012 Boundary-layer stabilization with dielectric barrier discharge plasmas for free-flight application. PhD thesis, TU Darmstadt.
- DUCHMANN, A., SIMON, B., C. & GRUNDMANN, S. 2014 Dielectric barrier discharge plasma actuators for in-flight transition delay. *AIAA Journal* .
- ELLIOTT, S. & NELSON, P. 1993 Active noise control. *Signal Processing Magazine, IEEE* **10** (4), 12–35.
- FABBIANE, N., SIMON, B., FISCHER, F., GRUNDMANN, S., BAGHERI, S. & HENNINGSON, D. S. 2015a On the role of adaptivity for robust laminar flow control. *Journal of Fluid Mechanics* **767**.
- FABBIANE, N., SIMON, B., FISCHER, F., GRUNDMANN, S., BAGHERI, S. & HENNINGSON, D. S. 2015b On the Role of Adaptivity for Robust Laminar-Flow Control. *J. Fluid Mech.* **767**, R1.
- FISCHER, P. F., LOTTES, J. S. & KERKEMEIER, S. G. 2008 Nek5000 - open source spectral element cfd solver.
- GRUNDMANN, S. & TROPEA, C. 2008 Active Cancellation of Artificially Introduced Tollmien–Schlichting Waves using Plasma Actuators. *Exp. Fluids* **44** (5), 795–806.
- GAD-EL HAK, M. 2000 *Flow control: passive, active, and reactive flow management*. Cambridge Univ Pr.
- HANSEN, C. & SNYDER, S. 1996 *Active control of noise and vibration*. CRC Press.
- JOSLIN, R. 1998 Aircraft laminar flow control 1. *Annual review of fluid mechanics* **30** (1), 1–29.
- JUNIPER, M. P., HANIFI, A. & THEOFILIS, V. 2014 Modal stability theory lecture notes from the flow-nordita summer school on advanced instability methods for complex flows, stockholm, sweden, 2013. *Applied Mechanics Reviews* **66** (2), 024804.

- KIM, H.-S. & PARK, Y. 1998 Delayed-x lms algorithm: An efficient and algorithm utilizing robustness of cancellation path model. *Journal of sound and vibration* **212** (5), 875–887.
- KOTSONIS, M., GIEPMAN, R., HULSHOFF, S. & VELDHUIS, L. 2013 Numerical study of the control of Tollmien–Schlichting waves using plasma actuators. *AIAA Journal* **51** (10), 2353–2364.
- KOTSONIS, M., SHUKLA, R. K. & PRÖBSTING, S. 2015 Control of natural tollmien-schlichting waves using dielectric barrier discharge plasma actuators. *International Journal of Flow Control* **7** (1-2), 37–54.
- KRIEGSEIS, J., DUCHMANN, A., TROPEA, C. & GRUNDMANN, S. 2013a On the classification of dielectric barrier discharge plasma actuators: A comprehensive performance evaluation study. *Journal of Applied Physics* **114** (5), 053301.
- KRIEGSEIS, J., SCHWARZ, C., TROPEA, C. & GRUNDMANN, S. 2013b Velocity-information-based force-term estimation of dielectric-barrier discharge plasma actuators. *Journal of Physics D: Applied Physics* **46** (5), 055202.
- KRIEGSEIS, J., SIMON, B. & GRUNDMANN, S. 2016, accepted Towards In-Flight Applications? A Review on DBD-based Boundary-Layer Control. *Appl. Mech. Rev.* .
- KUO, S. M. & MORGAN, D. 1995 *Active noise control systems: algorithms and DSP implementations*. John Wiley & Sons, Inc.
- KURZ, A., GOLDIN, N., KING, R., TROPEA, C. & GRUNDMANN, S. 2013 Hybrid transition control approach for plasma actuators. *Experiments in Fluids* **54** (11), 1–4.
- KURZ, A., SIMON, B., TROPEA, C. & GRUNDMANN, S. 2014 Active wave cancellation using plasma actuators in flight. In *52nd Aerospace Sciences Meeting, AIAA SciTech. American Institute of Aeronautics and Astronautics*.
- LI, Y. & GASTER, M. 2006 Active control of boundary-layer instabilities. *Journal of Fluid Mechanics* **550**, 185–206.
- PATERA, A. T. 1984 A spectral element method for fluid dynamics: Laminar flow in a channel expansion. *J. Comp. Phys.* **54** (3), 468–488.
- PELTZER, I., PÄTZOLD, A. & NITSCHKE, W. 2009 In-flight experiments for delaying laminar-turbulent transition on a laminar wing glove. *Proceedings of the Institution of Mechanical Engineers, Part G: Journal of Aerospace Engineering* **223** (6), 619–626.
- REEH, A. D. 2014 Natural laminar flow airfoil behavior in cruise flight through atmospheric turbulence. PhD thesis, TU Darmstadt.
- REEH, A. D. & TROPEA, C. 2015 Behaviour of a natural laminar flow aerofoil in flight through atmospheric turbulence. *Journal of Fluid Mechanics* **767**, 394–429.
- SARIC, W. S., REED, H. L. & KERSCHEN, E. J. 2002 Boundary-layer Receptivity to Freestream Disturbances. *Ann. Rev. Fluid Mech.* **34** (1), 291–319.
- SEMERARO, O., BAGHERI, S., BRANDT, L. & HENNINGSON, D. S. 2013 Transition delay in a boundary layer flow using active control. *J. Fluid Mech.* **731** (9), 288–311.
- SIMON, B., NEMITZ, T., ROHLFING, J., FISCHER, F., MAYER, D. & GRUNDMANN, S. 2015 Active flow control of laminar boundary layers for variable flow conditions. *International Journal of Heat and Fluid Flow* **56**, 344–354.
- SIMON, B., SCHNABEL, P. & GRUNDMANN, S. 2016 Ir measurements for quantification

- of laminar boundary layer stabilization with dbd plasma actuators. In *New Results in Numerical and Experimental Fluid Mechanics X*. Springer.
- SNYDER, S. & HANSEN, C. 1990 The influence of transducer transfer functions and acoustic time delays on the implementation of the lms algorithm in active noise control systems. *Journal of Sound and Vibration* **141** (3), 409–424.
- STURZEBECKER, D. & NITSCHKE, W. 2003 Active cancellation of Tollmien–Schlichting instabilities on a wing using multi-channel sensor actuator systems . *Intl J. Heat and Fluid Flow* **24**, 572–583.
- THOMAS, A. S. 1983 The control of boundary-layer transition using a wave-superposition principle. *Journal of Fluid Mechanics* **137**, 233–250.
- WANG, J.-J., CHOI, K.-S., FENG, L.-H., JUKES, T. N. & WHALLEY, R. D. 2013 Recent developments in dbd plasma flow control. *Progress in Aerospace Sciences* **62**, 52–78.
- WEISMÜLLER 2012 A new approach to aerodynamic performance of aircraft under turbulent atmospheric conditions. PhD thesis, TU Darmstadt.

Paper 4

Centralised versus decentralised active control of boundary layer instabilities

Reza Dadfar, Nicolò Fabbiane, Shervin Bagheri
and Dan S. Henningson

Linné FLOW Centre, KTH Mechanics, S-100 44 Stockholm, Sweden

Flow, Turbulence and Combustion (2014), vol. **93** (4), 537–553

We use linear control theory to construct an output feedback controller for the attenuation of small-amplitude three-dimensional Tollmien-Schlichting (TS) wavepackets in a flat-plate boundary layer. A three-dimensional viscous, incompressible flow developing on a zero-pressure gradient boundary layer in a low Reynolds number environment is analyzed using direct numerical simulations. In this configuration, we distribute evenly in the spanwise direction up to 72 localized objects near the wall (18 disturbances sources, 18 actuators, 18 estimation sensors and 18 objective sensors). In a fully three-dimensional configuration, the interconnection between inputs and outputs becomes quickly infeasible when the number of actuators and sensors increases in the spanwise direction. The objective of this work is to understand how an efficient controller may be designed by connecting only a subset of the actuators to sensors, thereby reducing the complexity of the controller, without comprising the efficiency. If n and m are the number of sensor-actuator pairs for the whole system and for a single control unit, respectively, then in a decentralised strategy, the number of interconnections decreases mn compared to a centralized strategy, which has n^2 interconnections. We find that using a semi-decentralized approach – where small *control units* consisting of 3 estimation sensors connected to 3 actuators are replicated 6 times along the spanwise direction – results only in a 11% reduction of control performance. We explain how “wide” in the spanwise direction a control unit should be for a satisfactory control performance. Moreover, the control unit should be designed to account for the perturbations that are coming from the lateral sides (crosstalk) of the estimation sensors. We have also found that the influence of crosstalk is not as essential as the spreading effect.

Key words: active control, boundary layer instabilities, decentralised controller

1. Introduction

Drag reduction methodologies in vehicles and aircrafts have received considerable attention during the past decades (Thomas 1984). These techniques provide the

possibility to significantly reduce the operational cost in transportation sector and also improve the environmental consequences. In boundary layer flows, drag reduction can be achieved by extending the laminar region on the aerodynamics parts of vehicles by delaying the transition from laminar to turbulence. Although, different techniques are used to delay the transition, currently significant efforts are devoted to active control strategies *e.g.* opposition control (Hammond *et al.* 1998), wave cancellation (Sturzebecher & Nitsche 2003), optimal controller (Dadfar *et al.* 2013) and etc. This approach adds external energy to the system in terms of predetermined actuation (open loop) or on-line computation of the actuation law using feedback information from the measurement sensors (reactive control). One particular reactive control strategy employed in this study is output feedback control (Doyle *et al.* 1989), where the actuation is determined by measuring external disturbances.

In an environment characterised by low turbulence levels, two-dimensional perturbations – Tollmien-Schlichting (TS) – wavepackets are triggered inside the boundary layer. The TS waves grow exponentially in amplitude as they move downstream until a point where nonlinear effects are significant and transition to turbulence is triggered. An important trait of this transition scenario, which also enables the use of linear control theory, is that the initial stage of the perturbation growth inside the boundary layer is well described by a linear system. Moreover, due to the large sensitivity of such flows to an external excitation, one can influence the TS waves by introducing small local perturbation in small region of the flow via proper localised devices requiring minute energy. There is now substantial literature where linear control theory is combined with numerical simulations to control transition in wall-bounded flows. Pioneering work include the control of Orr-Sommerfeld equations (Joshi *et al.* 1997), distributed control using convolution kernels (Cortelezzi *et al.* 1998; Högberg *et al.* 2003) and a localised control approach (Dadfar *et al.* 2013; Bagheri *et al.* 2009). The term *localized* in the latter approach refers to the use of a limited number of small compact actuation and estimation devices positioned in specific manner to allow efficient control. The fact that the number of inputs/outputs ($\mathcal{O}(10)$) is order of magnitudes smaller than the dimensions of flow system ($\mathcal{O}(10^7)$) provides amenable conditions for reducing the order of the system by constructing a low-dimensional model (ROM). Here, we report on our most advanced configuration (placing up to 72 inputs/outputs) so far. In order to have a physically realizable configuration, our numerical system is chosen as to resemble the experimental study performed by Li & Gaster (2006). This investigation extends or complements our previous work on two-dimensional disturbances using blowing/suction and shear stress measurements (Bagheri *et al.* 2009a), three-dimensional linear (Semeraro *et al.* 2011) and nonlinear (Semeraro *et al.* 2013) investigations. Relevant reviews on this subject are provided in Bewley (2001), Kim & Bewley (2007) and Bagheri & Henningson (2011).

We will report on the efficiency of a centralised and a decentralised control strategy (Glad & Ljung 2000; Lewis & Syrmos 1995). In the former approach all the sensors are connected to all the actuators. Since the complexity of a controller is related to the number of interconnections, this approach becomes infeasible when reaching $\mathcal{O}(10^2)$ inputs and outputs. This is certainly a restrictive issue, since in a localized control approach the number of required sensors and actuators increase with the span of the plate. A solution to this restriction is a decentralised controller where one disregards some of the interconnections which are not essential to the dynamics of the system. Then one replicates the same controller (called control unit) along the span of the system to cover a larger spanwise distance. In this study, several different control units are designed and their performances are compared.

2. Flow and Control Configuration

2.1. Governing equations

The dynamics and control of small-amplitude perturbations in a viscous, incompressible flow developing over an unswept flat plate are investigated using direct numerical simulation (DNS). The disturbance dynamics is governed by the Navier-Stokes equation linearised around a spatially developing zero-pressure-gradient boundary layer flow as

$$\frac{\partial u}{\partial t} = -(U \cdot \nabla)u - (u \cdot \nabla)U - \nabla p + \frac{1}{Re} \nabla^2 u + \lambda_f(x)u, \quad (1a)$$

$$\nabla \cdot u = 0, \quad (1b)$$

$$u = u_0 \quad \text{at} \quad t = t_0, \quad (1c)$$

where the disturbance velocity and pressure fields are denoted by $u(x, y, z, t)$ and $p(x, y, z, t)$; x , y and z denote the streamwise, wall normal and spanwise direction, respectively. Furthermore, $U(x, y)$ and $P(x, y)$ represent the baseflow velocity and pressure; they are a solution to the steady, nonlinear Navier-Stokes equation. In this study, all the spatial coordinates are normalised with the displacement thickness δ^* at the inlet of the computational box. The Reynolds number is defined based on the displacement thickness as $Re = U_\infty \delta^* / \nu$ where the U_∞ denotes the uniform free stream velocity and ν is the kinematic viscosity; all the simulations are performed at $Re = 915$ which correspond to a distance of $312\delta^*$ from the origin of the plate to the inlet of the computational box. The no-slip boundary condition is considered at the wall ($y = 0$), while Dirichlet boundary condition with vanishing velocity is employed at the upper boundary ($y = L_y$); this boundary condition is applied far enough from the boundary layer to ensure negligible influence on the dynamics of the perturbations. Periodicity is assumed in the spanwise and streamwise directions. In the latter, the term $\lambda(x)$ is implemented to enforce this periodicity so that a spectral Fourier expansion technique can be employed. The function $\lambda(x)$ is zero inside the physically relevant part of the domain where the dynamics are investigated and has nonzero

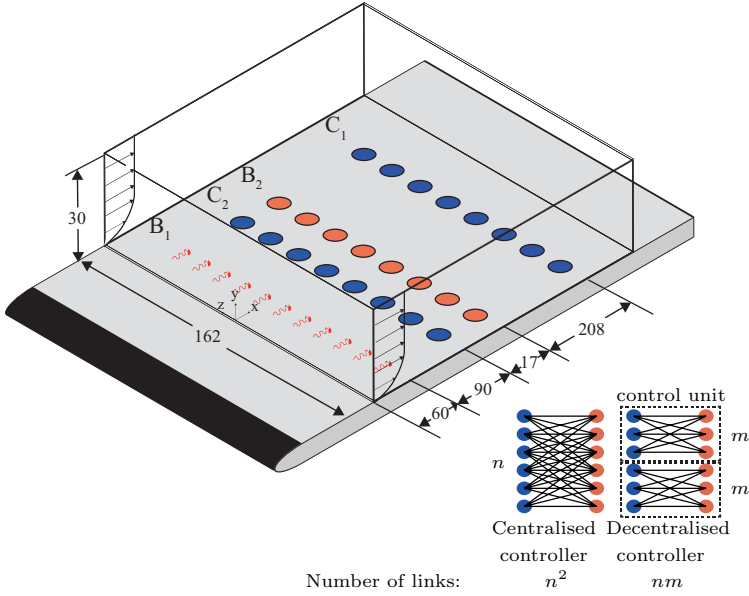


Figure 1: Input-output configuration of the system. The input B_1 is a row of localised disturbances located at $x = 60$, convected downstream and converted to a TS wavepacket. The control action is provided by the input B_2 , consists of a row of actuators located at $x = 167$. A set of localised estimation sensors, at $x = 150$ upstream of the actuator is employed. A row of output sensors at $x = 375$ is implemented as the objective function of the controller. Two control strategies, centralised and decentralised are used. In the former all the sensors and actuators are wired together while in the latter, a control unit with a limited interconnections is designed and replicated along the span. There are in total 18 disturbances B_1 , 18 sensors C_2 , 18 actuators B_2 and 18 outputs C_1 . Only 8 of those are depicted in the figure. For a centralised controller with n sensor-actuator pairs, the connections are n^2 while in a decentralised controller, each control unit contains m sensor-actuator pairs, the connections are mn .

value at the end of the domain where a fringe region is applied (Nordström *et al.* 1999). The simulation is performed using a pseudo-spectral DNS code (Chevalier *et al.* 2007) where Fourier series are employed in the wall-parallel directions and the wall-normal direction is expanded in Chebyshev polynomials. The computational domain $\Omega = (0, 500) \times (0, 30) \times (0, 162)$ is discretized with $384 \times 101 \times 128$ grid points in x, y and z directions, respectively. The time integration is performed using a Crank-Nicolson scheme for the linear terms and a third order Runge-Kutta method for the advective terms (Chevalier *et al.* 2007). The time step is $0.4\delta^*/U_\infty$ for the current simulations.

2.2. Input-Output System

A schematic representation of the input-output configuration is depicted in Figure 1. The linearised Navier-Stokes equation with inputs and outputs can be written in state space form as

$$\dot{u}(t) = Au(t) + B_1w(t) + B_2\phi(t), \quad (2a)$$

$$v(t) = C_2u(t) + \alpha g(t), \quad (2b)$$

$$z(t) = \begin{pmatrix} C_1 \\ 0 \end{pmatrix} u(t) + \begin{pmatrix} 0 \\ R^{1/2} \end{pmatrix} \phi(t). \quad (2c)$$

Henceforth, $u(t) \in \mathbb{R}^n$ denotes the state vector, whereas $w(t) \in \mathbb{R}^d$, $\phi(t) \in \mathbb{R}^m$, $v(t) \in \mathbb{R}^p$, $g(t) \in \mathbb{R}$ and $z(t) \in \mathbb{R}^k$ denote time signals. The matrix $A \in \mathbb{R}^{n \times n}$ represents the linearised and spatially discretised Navier-Stokes equation. The above form has been reported in numerous works (see e.g. Semeraro *et al.* (2010)) and only a short description is provided here:

- The first input ($B_1w(t)$) is composed of $B_1 \in \mathbb{R}^{n \times d}$ representing the spatial distribution of d localised disturbances located at the upstream end of the domain and white noise signals $w(t) \in \mathbb{R}^d$. These inputs represent a model of perturbations introduced inside the boundary layer by e.g. roughness and free-stream perturbations.
- In the second input ($B_2\phi(t)$), $B_2 \in \mathbb{R}^{n \times m}$ represents the spatial support of m actuators located inside the boundary layer near the wall. They are fed by the control signal $\phi(t) \in \mathbb{R}^m$, which is to be determined by an appropriate controller.
- The p output measurement provided by $v(t) \in \mathbb{R}^p$ detect information about the travelling structures by the localised sensors $C_2 \in \mathbb{R}^{p \times n}$. These measurements are corrupted by $\alpha g(t)$. More precisely, $g(t) \in \mathbb{R}^p$ is a white noise signal and α the level of noise.
- The output $z(t) \in \mathbb{R}^k$ extracts information from the flow in order to evaluate the performance of the controller. This is done by localised outputs $C_1 \in \mathbb{R}^{k \times n}$ with a spatial distribution located far downstream in the computational box. It also contains the weighted control input. In fact, the minimisation of the output signal detected by C_1 is the objective of our LQG controller; the aim is to find a control signal $\phi(t)$ able to attenuate the amplitude of the disturbance detected by C_1 . Hence, the objective function reads

$$\|z\|_{L^2_{[0,\infty]}}^2 = \mathcal{E} \{ u^T C_1^T C_1 u + \phi^T R \phi \}, \quad (3)$$

where $\mathcal{E}(\cdot)$ is the expectation operator. The matrix $R \in \mathbb{R}^{m \times m}$ contains the control penalty l^2 in each diagonal entry and represents the expense of the control. This parameter is introduced as a regularisation term accounting for physical restrictions. Large values of control penalty results in weak actuation and creates low amplitude control signal whereas low values of control penalty leads to strong actuation.

Element	Symbol	Number	Location	Parameters
–	–		(x_0, y_0)	$(\sigma_x, \sigma_y, \sigma_z)$
Disturbances	B_1	18	(60, 0)	(6, 1.5, 8)
Sensors	C_2	18	(150, 0)	(2, 1.5, 2)
Actuators	B_2	18	(167, 0)	(6, 1.5, 8)
Outputs	C_1	18	(375, 0)	(5, 1.5, 6)

Table 1: The main parameters characterising the spatial distribution of the sensors and the actuators. All the elements are located at $z_0 = -76.5$ and distributed along the span with the spanwise spacing $\Delta_z = 9$.

Following Semeraro *et al.* (2011), we define the spatial distribution of the sensors and actuators with a Gaussian divergence-free function as

$$h(x, y, z) = a \begin{pmatrix} \sigma_x \gamma_y \\ -\sigma_y \gamma_x \\ 0 \end{pmatrix} e^{-\gamma_x^2 - \gamma_y^2 - \gamma_z^2}, \quad (4)$$

where

$$\gamma_x = \frac{x - x_0}{\sigma_x}, \quad \gamma_y = \frac{y - y_0}{\sigma_y}, \quad \gamma_z = \frac{z - z_0}{\sigma_z}, \quad (5)$$

and (x_0, y_0, z_0) is the centre of the Gaussian distribution. The scalar quantities $(\sigma_x, \sigma_y, \sigma_z)$ represent the corresponding size (values given in Table 1). The scalar a represents an amplitude which is equal to 2×10^{-3} for the actuators and one for the sensors. Most of our simulation is performed for the setup reported in Table 1. We denote the i th element of the disturbance vector B_1 by $B_{1,i}$ corresponding to the signal $w_i(t)$.

2.3. Model Reduction

We construct a reduced-order model of the system by projecting the n -dimensional state onto a low-dimensional subspace of dimension r . Expanding the state in a linear combination of columns of the expansion basis $\Phi = (\phi_1, \phi_2, \dots, \phi_r) \in \mathbb{R}^{n \times r}$ as

$$u = \Phi \hat{u} \quad (6a)$$

$$\hat{u} = \Psi^T u, \quad (6b)$$

where $\Psi = (\psi_1, \psi_2, \dots, \psi_r) \in \mathbb{R}^{n \times r}$ are the adjoint modes, bi-orthogonal to the expansion basis Φ , i.e. $\Psi^T \Phi = I$. Substituting Eq. (6a) into the system Eq. (2) and using the bi-orthogonality of the basis, the reduced system of order r is

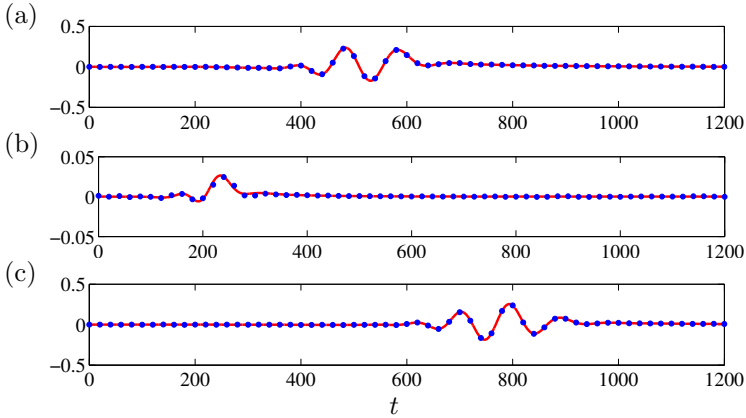


Figure 2: Impulse response of the system (a) from the input $B_{2,8}$ to the output $C_{1,8}$, (b) from the input $B_{1,8}$ to the output $C_{2,8}$ and (c) from the input $B_{1,8}$ to the output $C_{1,8}$. The red line shows the DNS results, while the dotted lines indicates the impulse response of the reduced model (Case N Table 2)

obtained as

$$A_r = \Psi^T A \Phi, \quad (7a)$$

$$B_{1r} = \Psi^T B_1, \quad B_{2r} = \Psi^T B_2, \quad (7b)$$

$$C_{1r} = C_1 \Phi, \quad C_{2r} = C_2 \Phi. \quad (7c)$$

The choice of the basis function is crucial for the performance of the reduced order system (Bagheri *et al.* 2009c; Barbagallo *et al.* 2009). We use a balanced-mode-basis (Moore 1981; Willcox & Peraire 2002; Rowley 2005) that preserves the dynamics between the inputs and outputs of the system. The states that are equally observable and controllable form a hierarchy of so-called balanced modes. The method is based on the concepts of observability and controllability (Zhou *et al.* 2002), which provide a means to characterize the states in terms of how easily triggered they are by the inputs and observed by the outputs, respectively. The states which are neither controllable nor observable or the ones that are weakly controllable or observable are redundant for the input-output behaviour of the system. A limitation pertaining to this method is the necessity of computing the adjoint balanced modes. The Eigensystem Realisation Algorithm (ERA) (Juang & Pappa 1985; Ma *et al.* 2011) is a system identification technique that allows to circumvent this limitation. It is only based on sampling measurements extracted directly from the flow, see a detailed description of the method in Ma *et al.* (2011).

As an example of the performance of the reduced-order model with $r = 435$, in Figure 2 we show the impulse responses:

$$\phi_8 \rightarrow z_8, \quad w_8 \rightarrow v_8, \quad w_8 \rightarrow z_8.$$

In the figure, the solid lines are the impulse response of the full system obtained from solving Navier-Stokes equation while the dotted lines presents the results of the reduced-order model. We observe an equally good agreement for all the inputs and output, when comparing the full system and the ROM. Now that an efficient ROM is constructed, may design a linear controller.

2.4. Control Design

We use a classical LQG-approach to determine a controller that minimises the energy of disturbances captured by output C_1 (Lewis & Syrmos 1995; Zhou *et al.* 2002). The control signal $\phi(t)$ is designed for the actuator B_2 such that the mean of the output energy, $z(t)$, is minimised (see Eq. 3). The LQG design procedure involves a two-step process: first the full state - represented in this case by the velocity field - is reconstructed from the noisy measurement $v(t)$ via an estimator. Once the estimated state \hat{u} is computed the control signal can be computed by the following linear relationship

$$\phi(t) = K\hat{u}(t), \quad (8)$$

where $K \in \mathbb{R}^{m \times r}$ is referred to as the control gain. When the disturbances are modelled as white Gaussian noise, the separation principle allows the two steps (estimation and full-information control) to be performed independently. Furthermore, both problems are optimal and stable and the resulting closed loop is also optimal and stable (Zhou *et al.* 2002). The final form of the reduced order controller (also called compensator) of size r is

$$\dot{\hat{u}}(t) = (A_r + B_{2r}K + LC_{2r})\hat{u}(t) - Lv(t), \quad (9a)$$

$$\phi(t) = K\hat{u}(t), \quad (9b)$$

where the term $L \in \mathbb{R}^{r \times p}$ is the estimator gain and can be computed by solving a Riccati equation (Glad & Ljung 2000), such that the error $\epsilon = \|\hat{u} - u\|^2$ is minimised. The controller is thus a state-space system with the measurements $v(t)$ as input and the control signal $\phi(t)$ as output. The evolution of the perturbations is simulated by marching in time the full DNS, while the controller runs on-line, simultaneously. Eq. 9a is based on the reduced-order model and is solved by using a standard Crank-Nicholson scheme.

2.5. Centralised and Decentralised Controllers

A multivariable control approach is necessary since our system has more than one actuator and sensor. The degree of control complexity in a multivariable approach depends on the degree of coupling between inputs and outputs. For example consider the transfer function between the input w_j to the output v_k . Then the effect on v_k due to a small change in w_j may depend on one, a few or all other inputs w_h for $h \neq j$, if the system is uncoupled, weakly coupled or fully coupled, respectively. The degree of coupling depends usually not only on the actuator/sensor placement but also on the dynamics of the TS wavepackets. As we shall see, we have a situation of a weakly coupled system, due to the fact

that a TS wavepacket generated from a point source spreads only in a limited spanwise region.

The most straight-forward approach is the so called centralised controller where all the inputs and outputs are connected together. The main disadvantage is that the number of interconnections – thus the complexity of the controller – increase significantly as we aim to control perturbations over a larger span of the domain. In contrast, a fully decentralised controller connects only one sensor to one actuator, and thus requires by definition the same number of actuators and sensors. This approach disregards any influence of an input which is not placed directly upstream the output; this is a risky model assumption, as the influence that may exist in reality will induce an over- or underestimation of the signals, causing instabilities. A compromise between the centralised and fully decentralised approach is a semi-decentralised approach (henceforth only referred to as decentralised), where the system is divided into a collection of independent sub-systems. For each sub-system a controller is designed – called a control unit – for a few number of sensors and actuators. Then, the same controller is replicated along the span to cover a broader region. As we will see the division into control units provides an efficient means for control of TS waves, since the disturbance source upstream is only observable at a subset of sensors; thus some of the interconnections which are not relevant to the dynamics of the system are neglected (see Figure 1).

The number of interconnections in a control system determines the complexity of a controller. Reducing the complexity has a number of advantages including, easier implementation (less hardware) low-dimensionality of the system (faster system). In a system with a centralised controller using n sensors and n actuators, n^2 interconnections are required. However if we split this system into $\sim n/m$ control units with m sensors and m actuators each, the total number of interconnections becomes $n/m \times m^2 = nm$. This is a linear function of n instead of a quadratic function. The net gain of a decentralised controller is more evident when the number of sensors and actuators increases in the system *e.g.* when the objective is to control a larger span of the boundary layer.

3. Results

In the following sections, we first design and analyse a centralised controller for the attenuation of small-amplitude TS wavepackets. After a parametric study of the control penalty, we identify a reference controller, as the centralised controller that for the chosen flow parameters (*Re*, domain, etc) provides the best performance. Second, we design a set of decentralised controllers by assembling several control units of different sizes. Their control efficiency in terms of performance (robustness is left for future studies) will be compared to the reference controller. In order to determine the performance of the controller, we use the 2-norm of a system G . When the inputs of the system are white

Case	Description	Control Penalty	Order	Norm Reduction	Energy Reduction
k	–	l	r	$1 - \frac{\ G_k\ _2^2}{\ G_n\ _2^2}$	\bar{E}_k
N	18/18 – 18 – 18 – 18/1	–	–	0%	0.00
A	18/18 – 18 – 18 – 18/1	100	435	45%	0.27
B	18/18 – 18 – 18 – 18/1	10	435	98%	0.80
C	18/18 – 18 – 18 – 18/1	1	435	98%	0.80

Table 2: The performance of a LQG controller designed with different control penalties. The noise autocovariance on the estimation sensors and for all cases are assumed constant $\alpha^2 = 10^{-6}$. The norms are computed in the time interval $t \in [2000, 8000]$. The description identifier is defined as the following; number of disturbances B_1 / the design configuration of the system consists of $d-p-m-k$ disturbances-estimation sensors-actuators-outputs/ number of control units.

noises with variance σ_w^2 , $\|G\|_2^2$ can be computed as:

$$\|G\|_2^2 = \frac{1}{d\sigma_w^2} \sum_i \frac{1}{T} \int_{t_0}^{t_1} (C_{1i}u)^2 dt \quad (10)$$

where $T = t_1 - t_0$ is the period over which the performance is evaluated. In Table 2-4, we compare the norm of the uncontrolled system $\|G_n\|_2^2$ to the ones with control $\|G_k\|_2^2$.

3.1. Centralised Controller

In Table 2 the effect of different control penalties (parameter l in Eq. 3) on the performance of the closed-loop system is investigated for a centralized LQG controller and the setup in Table 1. The optimal value of the control penalty is usually not known before applying the controller to the full DNS and involves an iterative procedure. In general, small values of the control penalty correspond to a reduction of the perturbation amplitude; however, too low values of control penalties may result in unfavourable behaviour such as unphysical control signal (Semeraro *et al.* 2011). Case *C* in Table 2 is selected as the baseline reference controller, for which all decentralized controller will be compared to, while case *N* represents the system without implementing the control (uncontrolled case) and is used to compute the performance of the controller.

First, we characterize the performance of controller *C* using a number of different observables. Figure 3 represents the input-output behaviour of the closed-loop system for case *C*. In this setup, there are totally 18 inputs B_1 ; each of them are excited by an independent white noise of variance $\frac{1}{3}$. In the first frame (Figure 3a), the disturbance input w_8 is shown. It is a white noise signal that provides a continuous forcing at $B_{1,8}$. Figure 3b shows the measurement

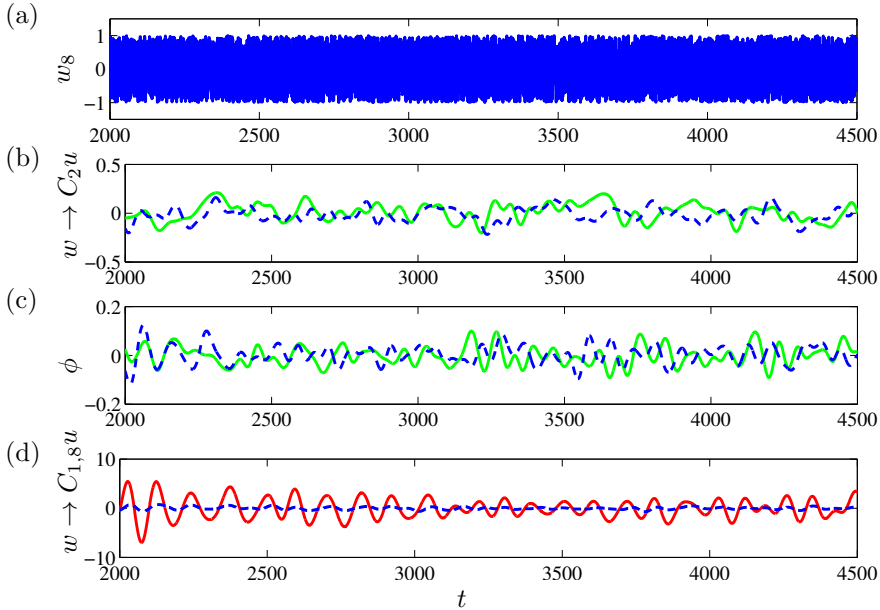


Figure 3: Noise response of the closed-loop system: Stochastic excitation of the input $B_{1,8}$ is shown in (a), estimation signals $C_{2,8}$ (dashed blue line) and $C_{2,18}$ (solid green line) in (b), control signal feeding the actuator $B_{2,8}$ (dashed blue lines) and $B_{2,18}$ (solid green line) in (c) and measurement extracted by sensor $C_{1,8}$ for uncontrolled (solid line) and controlled and dashed (dashed line) system (cases N and C in Table 2) in (d).

detected by upstream sensors $C_{2,8}$ and $C_{2,18}$. The sensors are located close to the wall, inside of the boundary layer and can register the evolution of the disturbance. One clearly observes that certain frequencies are amplified by the system, whereas others are damped. Figure 3c reports the control signals related to actuators $B_{2,8}$ and $B_{2,18}$. Since the disturbances are uncorrelated, we can observe independent behaviour for different actuators. Finally, in Figure 3d, the signal extracted from output $C_{1,8}$ for the uncontrolled and controlled cases is shown. The root mean square (r.m.s) of the signal is reduced up to 89%.

The input-output behaviour of the closed-loop system in frequency domain is shown in Figure 4. The power spectrum density of the input signal w_8 together with the output signal $C_{1,8u}$ in the controlled and uncontrolled configuration are plotted (cases N and C). In this configuration the most amplified frequency in the system is 0.00171, where its energy is damped up to one order of magnitude.

In a three-dimensional configuration, the minimisation of the sensor measurements near the wall, does not guarantee the reduction of the perturbation energy in the full domain. This has to be evaluated a posteriori. Figure 5 shows

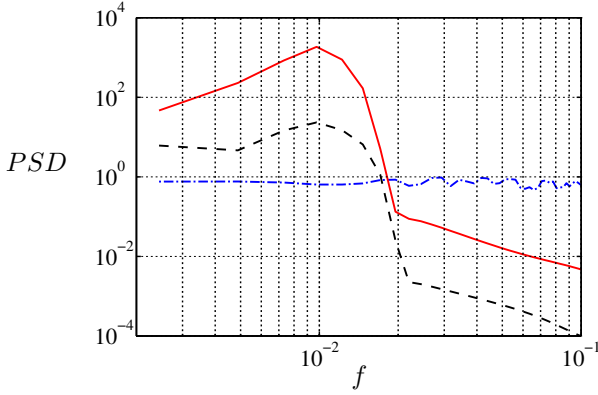


Figure 4: Power spectrum density (PSD) of the input signal w_8 (dashed-dots blue – cases $N - C$), uncontrolled output signal $C_{1,8}u$ (solid red – case N) and the controlled output signal $C_{1,8}u$ (dashed black – case C) are shown.

the energy, $E(t) = u^T u / 2$, of the perturbation as a function of time. The mean value of the energy reduction \bar{E}_k is defined as

$$\bar{E}_k = \frac{\int_{t_0}^{t_1} E_N dt - \int_{t_0}^{t_1} E_k dt}{\int_{t_0}^{t_1} E_N dt}, \quad (11)$$

where $[t_0, t_1]$ is the time interval in which the statistics are computed. In Figure 5, the uncontrolled energy E_N is shown by a solid red line while the controlled energy, E_k is shown with a blue line. We observed that the energy is reduced by approximately 80%.

Finally, in order to gain an insight into where in the physical domain, the controller has a strong effect, we show in Figure 6 the distribution of the r.m.s value of the streamwise velocity of disturbances in horizontal plane (streamwise-spanwise) averaged along wall normal direction. The disturbances B_1 are located at $x = 60$ from the beginning of the computational box. We expect the amplitude of the perturbations to grow as we move toward the end of the domain in uncontrolled case N (Figure 6a). Figure 6b shows the resulting r.m.s value of the perturbations when the controller is active. The suppression of the perturbations begin from $x = 167$ where the actuators are located. Figure 6c reports the percentage of the reduction in r.m.s of the perturbation. Since the objective function of the controller is to attenuate the amplitude of the perturbation where the outputs are located, a significant reduction is observed at that region; the reduction is also homogeneous in spanwise direction.

3.2. Decentralised Controllers

Having shown that centralized controller with a very high complexity may reduce energy by nearly an order of magnitude, we now investigate how decentralized

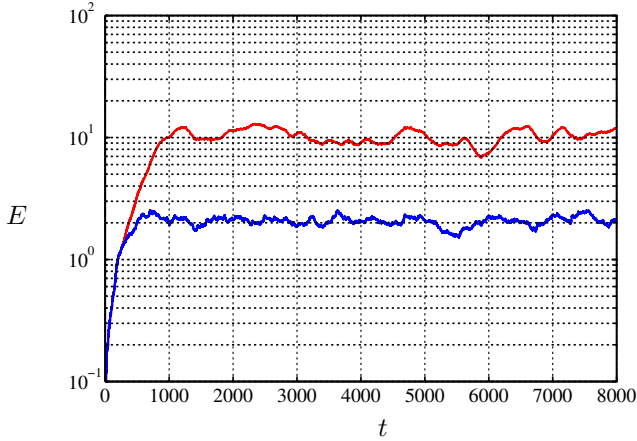


Figure 5: Energy of the perturbations E as a function of time t ; solid red line corresponds to the energy of uncontrolled case E_N and solid blue line to the controlled case E_C . The statistics are computed for the time interval $t \in [3000 \ 8000]$.

Case	Description	Control penalty	Order	Norm Reduction	Energy Reduction
k	—	l	r	$1 - \frac{\ G_k\ _2^2}{\ G_N\ _2^2}$	\bar{E}_k
D	18/5 – 3 – 3 – 9/1	20	155	4.6%	0.109
E	18/5 – 1 – 3 – 9/1	20	155	2.2%	0.044
F	18/3 – 3 – 3 – 9/1	20	119	3.4%	0.087
G	18/5 – 3 – 3 – 3/1	10	87	8.4%	0.083

Table 3: In each case only one control unit is employed. The noise autocovariance for all the cases are assumed as $\alpha^2 = 10^{-6}$ and the norms are computed for time $t > 2000$.

controllers of lower complexity compare in performance. As already mentioned, the decentralized controllers are designed in two steps; (i) constructing a control unit using only a few actuators and sensors; (ii) by replicating the units in the spanwise direction.

3.2.1. Design and Performance of Single Control Units

The simplest control unit is obtained by to connecting one sensor C_2 to one actuator B_2 . Despite the relative simplicity of this configuration both in terms

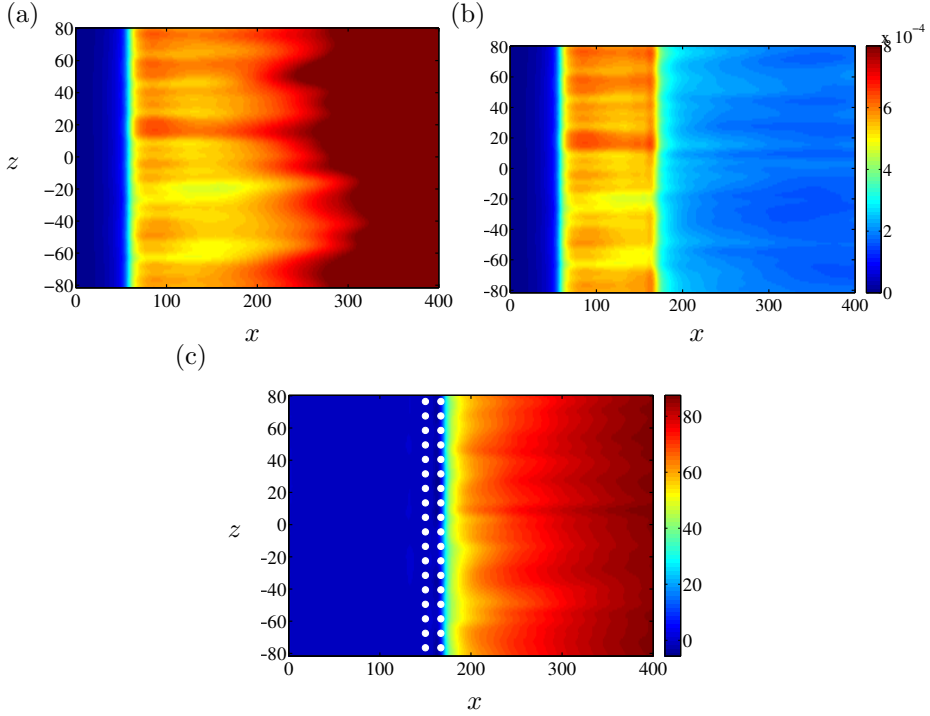


Figure 6: Streamwise root mean square velocity averaged along wall normal direction for the uncontrolled case N (a) and controlled case C (b) and the corresponding percentage of the reduction (c). The statistics are computed for the time interval $t \in [3000, 8000]$. The white dots indicate the location of estimation sensors C_2 and the actuators B_2 .

of the design and implementation, the results are prone to the stability problems and poor control performance (Li & Gaster 2006; Semeraro *et al.* 2011).

Motivated by the experimental work of Li & Gaster (2006), we choose to investigate two control units:

1. The first one consists of three actuators (the center actuator $B_{2,8}$ and two adjacent to the center $B_{2,7}$ and $B_{2,9}$), three estimation sensors ($C_{2,7}$, $C_{2,8}$ and $C_{2,9}$) and 9 objective sensors $C_{1,(4,5,\dots,12)}$. During the design process of the control unit, we assume that there exists 5 upstream disturbances $B_{1,(6,7,\dots,10)}$, but the actual performance of the controller is assessed when 18 disturbance sources are active (see sketch in Figure 7a). The description identifier of this control unit is $(18/5 - 3 - 3 - 9/1)$, where the different numbers are respectively; number of disturbances B1 / the design configuration of the system consists of $d - p - m - k$

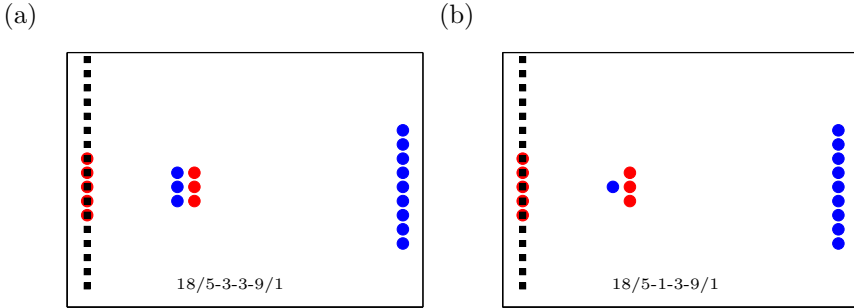


Figure 7: A schematic view of two control units. The controller shown in (a) is designed considering 5 upstream disturbances $B_{1,(6,7,\dots,10)}$, 3 estimation sensors $C_{2,(7,8,9)}$, 3 actuators $B_{2,(7,8,9)}$ and 9 outputs $C_{1,(4,5,\dots,12)}$ as the objective function (circles). This control unit performs when 18 disturbances are evolving into the domain (squares). The layout and the number of sensors and actuators remain the same for the control unit depicted (b), but only one estimation sensor $C_{2,8}$ is used.

(disturbances-estimation sensors-actuators-outputs) / number of control units.

2. The second one ($18/5 - 1 - 3 - 9/1$) has only one estimation sensor, namely the center one ($C_{2,8}$) as shown in Figure 7b. The remaining parameters are the same the first control unit.

Figure 8 shows the control signal for the two lateral actuators $B_{2,7}$ and $B_{2,9}$ for both control unit one and two. It is obvious that the two actuators behave in the same manner for the second controller (case *E* in Table 3) while they are acting independently for the multiple sensor control unit (case *D* in Table 3). After designing the control units, their performances are monitored while 18 disturbances B_1 evolve and convect downstream ($18/5 - 3 - 3 - 9/1$). Figure 8 depicts the control signal for the two lateral actuators $B_{2,7}$ and $B_{2,9}$ for both cases. It is obvious that the two actuators behave in the same manner for the symmetric controller (case *E*) while they are acting independently for the asymmetric one (case *D*).

Figure 9 shows the streamwise velocity cancellation at two different planes $z = -13.5$ and $y = 0.6$ for case *D*. The maximum rms reduction in this case is 48%. The same number of sensor and actuators (1 sensor - 3 actuators) are used in the experimental setup by Li & Gaster (2006). The maximum rms reduction in this case is similar to the one obtained in the experiment. In the experimental setup the data is extracted at a lower plane $y = 0.36$ but the maximum reduction in case *D* occurs at $y \approx 0.6$. The difference between the two cases may arise from the fact that the effect of the actuators are different

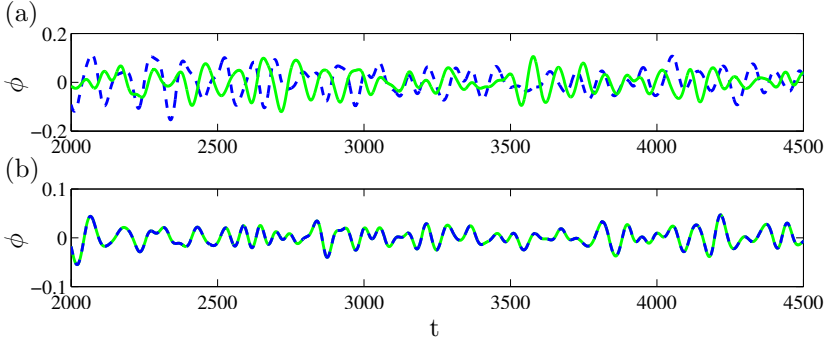


Figure 8: Control signal driving the actuators $B_{2,7}$ (solid line) and $B_{2,9}$ (dotted line) are shown in (a) for a three-estimation sensors-based control unit (case D in Table 3) and in (b) for single-estimation sensors-control unit (case E in Table 3).

in both cases. Moreover, in this case we use 18 sources of disturbance with a periodic boundary condition which numerically analogues to using an infinite number of actuators while in the experimental setup, they only used 15 sources of disturbance. Figure 10 shows the streamwise velocity cancellation averaged along wall normal direction. The white dots indicate the spatial configuration of the sensors and actuators for the two cases D and E . The Figs. 10a and 10b confirm that a level of cancellation up to 40% is achieved in the central area downstream of the actuators while it faded away as we move downstream. Controller based on only one upstream sensor can act on a limited region while the controller based on three sensors is able to influence a broader domain. The reason is that the latter controller can identify the discrepancy between the disturbances coming from lateral sides, i.e. the observability of the system is significantly larger. This controller can attenuate the energy of the system up to 10.9% (see Table 3 case D), while the single-sensor controller can only suppress the energy up to 4.4%. Furthermore, in terms of norms of the system, the corresponding reduction between the two controllers are 4.6% and 2.2%. In the following section we use the control unit, case F .

3.2.2. Effect of Crosstalk

As a localised disturbance propagates downstream, it will – after a short transient – develop into a wavepacket that grows in size and spreads along the spanwise direction. Each estimation sensor $C_{2,j}$ does not only receive a signal from the disturbance source directly upstream of it (w_j), but also the lateral sources (w_h , for $h \neq j$) contribute to the total measured signal. The additional perturbations, originated from the lateral sources and detected by the estimation sensors C_2 , are referred to as *crosstalk* (see Figure 12).

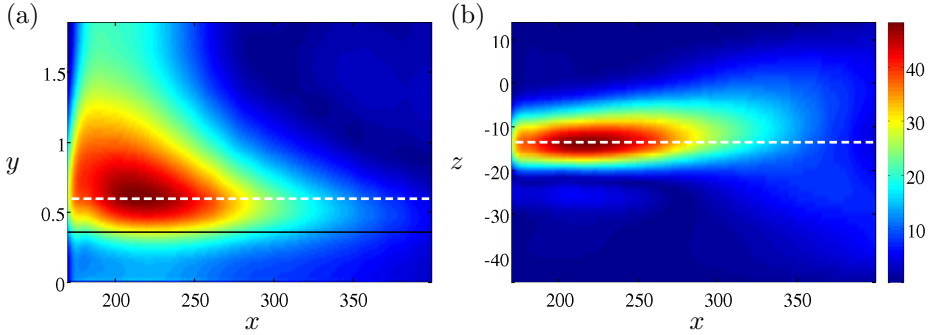


Figure 9: Percentage reduction in streamwise velocity cancellation (case E) at a) plane $z = -13.5$ and (b) plane $y = 0.6$. White lines at $y = 0.6$ and $z = -13.5$ resemble the cross section of the two planes and solid black line at $y = 0.36$ is used by (Li & Gaster 2006) to extract the results.

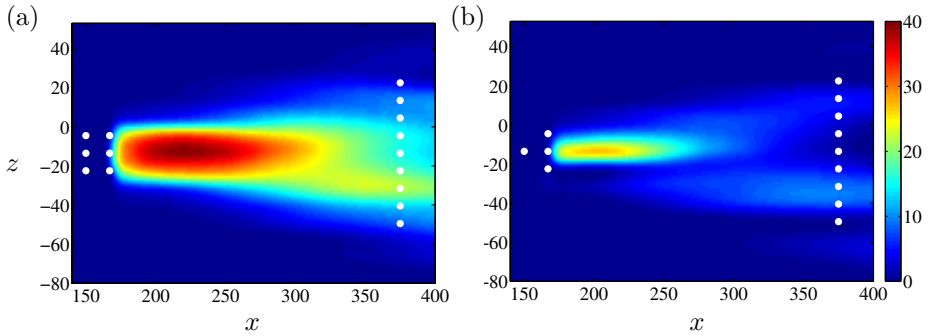


Figure 10: Percentage reduction in streamwise velocity cancellation averaged along wall normal direction for case D (a) and E (b) is shown. The white dots indicate the location of sensors C_1 , C_2 and actuators B_2 .

Consider now the control unit, Case F , from the previous section (3 estimation sensors and 3 actuators). The energy of the signals received by 3 estimation sensors from different numbers of disturbance sources B_1 is shown in Figure 11a. As one can observe, around 70% of the total energy of the signals originate from 3 disturbance sources directly upstream of the estimation sensors. In order to capture 90% of the total energy of the signals, 5 disturbance sources are required in which, the additional 20% of the energy belongs to the two lateral disturbance sources.

To investigate the effect of the crosstalk in the performance of the control unit, we compare two cases. The only difference between them is the number of disturbance sources B_1 considered in the design process. Just as before we

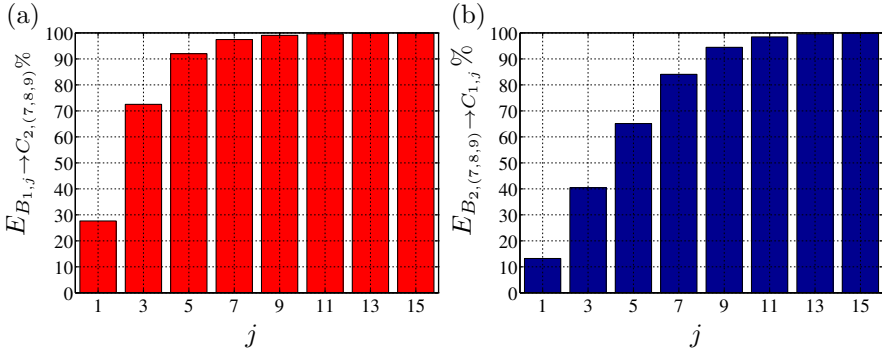


Figure 11: Energy captured by 3 estimation sensors $C_{2,(7,8,9)}$ originates from impulse response of different number of disturbances (a) and energy harvested by using different number of outputs C_1 from the impulse response of 3 actuator $B_{2,(7,8,9)}$ (b). The data is normalised by the maximum value when $j = 18$. The number of disturbances or outputs (elements) denotes as j . $j = 1$ corresponds to an element located at $z = -13.5$ ($i=7$). $j = 3$ corresponds to 3 elements $i \in (6, 7, 8)$. The numbering convention continues the same with the central element located at $i = 7$; for instance, $j = 5$ corresponds to 5 elements $i \in (5, 6, 7, 8, 9)$ and so on.

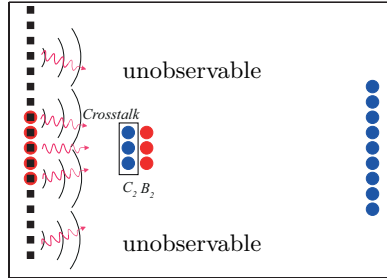


Figure 12: A schematic layout of the control unit. Two kind of perturbations, observed by 3 sensors $C_{2,(7,8,9)}$ are depicted; they include the perturbation coming from sources directly in front of the sensors and the lateral perturbations coming from sides which is referred to as *crosstalk*.

consider 5 disturbance sources B_1 in case with crosstalk (case D) while we reduce the effect of crosstalk and only design the controller for 3 disturbance sources B_1 ($18/3 - 3 - 3 - 9/1$ or case F in Table 3). Table 3 shows the performance of the two systems; the configuration that takes into account 90%

of the total energy can attenuate the energy of the disturbances up to 10.9% while the configuration taking into account only 70% of the total energy can reduce the energy up to 8.7%. This indicates the number of disturbance sources in the control design process depends on the nature of the disturbance (e.g. how fast it spreads in the spanwise direction). Capturing only part of the spreading of a disturbance has a sizable effect on the control performance.

Next, we investigate the performance of the controllers when the control units are replicated along the spanwise direction. First, we consider 6 control units based on the configurations with high level crosstalk and with reduced-level of crosstalk. Table 4 reports the reduction in the energy of the system using these controllers. The performance of 6 control units considering the crosstalk effect (case H) is only 11% less than the centralised controller (case C in Table 2) where all the interconnections between the sensors and the actuators are taken into account. On the other hand, if we only capture part of the crosstalk effect (case J) we loose an additional 9% of performance.

3.2.3. Capturing the spread of the disturbances

Since the wavepackets spread along the spanwise direction while propagating downstream, we need to distribute a minimum number of objective sensors $C_{1,j}$ along the span to correctly capture the energy of the disturbances. On the other hand, we have to be able to control the disturbances detected by outputs C_1 using the actuators B_2 . In fact, the further away the outputs are from the centreline of an actuator, the less we can control the structures detected by that outputs. More specifically, we consider again control units which have 3 actuators ($B_{2,(7,8,9)}$). Figure 11b reports the energy of the signals captured by different number of outputs C_1 , which originate from the impulse responses of the 3 actuators. We can observe that over 90% of the total energy that originated from an impulse in the 3 actuators is captured by 9 outputs. According to this observation, we compare two controllers, whose differentiate only in the number of employed outputs in the control design. In the first configuration (case D in Table 3) we consider 9 outputs ($C_{1,i}$, $i = 4, \dots, 12$) while in the second configuration (case G in Table 3) we implement 3 outputs only ($C_{1,i}$, $i = 7, 8, 9$). As one can observe in Table 3, the reduction in the energy of the system \bar{E}_k in the case with 9 outputs is 10.9% while in the case with 3 outputs is 8.3%.

It is important to note that in both configurations, we take into account the crosstalk effect. If we compare the performance of the controller with 3 outputs (case G) to the controller that only partially accounts for the crosstalk from the previous study in sec 3.2.2 (case F), we can observe that the energy reduction in the second case is larger, 8.3% vs 8.7%. Finally, we compare on the performance of the 6 control units with 9 and 3 outputs in Table 4 (cases H and K). In the former, the energy is attenuated up to 69% while in the latter, it is reduced up to 48%.

Case	Description	Norm Reduction	Energy Reduction
k	—	$1 - \frac{\ G_k\ _2^2}{\ G_n\ _2^2}$	\bar{E}_k
H	18/5 – 3 – 3 – 9/6	88.0%	0.69
J	18/3 – 3 – 3 – 9/6	85.5%	0.60
K	18/5 – 3 – 3 – 3/6	64.7%	0.48

Table 4: In each case 6 control unit are used. The control units distributed equidistantly along the span and does not have any overlap. The noise autocovariance for all the cases are assumed as $\alpha^2 = 10^{-6}$. In addition, the norms are computed for time $t > 2000$.

4. Conclusion

We have investigated and compared two different control strategies, namely a centralised and a decentralised. In the former approach where all the sensors and actuators are connected together, the complexity of the system (due to the number of interconnections) may be too high for implementation in experiments, in particular, as we aim to control over a wider span of the domain. We have presented an alternative decentralised strategy, where several small control units consisting of 3 pairs of actuators-sensors are assembled to cover the full spanwise length of the flat plate. The choice 3 actuators-sensors as well as the number of source disturbances and objective sensors included in the design of a single control unit needs to be chosen with a physical insight on the spatial and temporal scales of the perturbation inside the boundary layer. We have focused on TS wavepackets, streaky structures observed under different conditions inside the boundary layer, may need control units of different order.

As explained in Sec.3.2.3 our results reveal that the best performance is obtained for a control unit which (i) has “sufficient” number of output measurements and (ii) is designed to account for the perturbations which are coming from the lateral sides (crosstalk) of the estimation sensors. We may also conclude that the influence of crosstalk is not as essential as the spreading effect.

The authors wish to thank Ardeshir Hanifi and Onofrio Semeraro for fruitful discussions. Computer time was provided by the Center for Parallel Computers (PDC) at the Royal Institute of Technology (KTH) and the National Supercomputer Center (NSC) at Linköping University in Sweden.

REFERENCES

- BAGHERI, S., AKERVIK, E., BRANDT, L. & HENNINGSON, D. S. 2009*a* Matrix-Free Methods for the Stability and Control of Boundary Layers. *AIAA J.* **47**, 1057–1068.
- BAGHERI, S., BRANDT, L. & HENNINGSON, D. S. 2009*b* Input–output analysis, model reduction and control of the flat-plate boundary layer. *J. Fluid Mech.* **620** (1), 263–298.
- BAGHERI, S. & HENNINGSON, D. S. 2011 Transition delay using control theory. *Philos. Trans. R. Soc.* **369**, 1365–1381.
- BAGHERI, S., HÖPFFNER, J., SCHMID, P. J. & HENNINGSON, D. S. 2009*c* Input-Output Analysis and Control Design Applied to a Linear Model of Spatially Developing Flows. *Appl. Mech. Rev.* **62**.
- BARBAGALLO, A., SIPP, D. & SCHMID, P. J. 2009 Closed-loop control of an open cavity flow using reduced order models. *J. Fluid Mech.* **641**, 1–50.
- BEWLEY, T. R. 2001 Flow Control: New Challenges for a New Renaissance. *Progr. Aerospace Sci.* **37**, 21–58.
- CHEVALIER, M., SCHLATTER, P., LUNDBLADH, A. & HENNINGSON, D. S. 2007 A pseudo-spectral solver for incompressible boundary layer flows. *Tech. Rep. TRITA-MEK 2007:07*. KTH Mechanics, Stockholm, Sweden.
- CORTELEZZI, L., SPEYER, J. L., LEE, K. H. & KIM, J. 1998 Robust Reduced-Order Control of Turbulent Channel Flows via Distributed Sensors and Actuators. *IEEE 37th Conf. on Decision and Control* pp. 1906–1911.
- DADFAR, R., SEMERARO, O., HANIFI, A. & HENNINGSON, D. S. 2013 Output Feedback Control of Blasius Flow with Leading Edge Using Plasma Actuator. *AIAA J.* **51** (9), 2192–2207.
- DOYLE, J. C., GLOVER, K., KHARGONEKAR, P. P. & FRANCIS, B. A. 1989 State-Space Solutions to Standard H_2 and H_∞ Control Problems. *IEEE Trans. Autom. Control* **34**, 831–847.
- GLAD, T. & LJUNG, L. 2000 *Control Theory*. London: Taylor & Francis.
- HAMMOND, E. P., BEWLEY, T. R. & MOIN, P. 1998 Observed Mechanisms for Turbulence Attenuation and Enhancement in Opposition-Controlled Wall-Bounded Flows. *Phys. Fluids* **10** (9), 2421–2423.
- HÖGBERG, M., BEWLEY, T. R. & HENNINGSON, D. S. 2003 Relaminarization of $Re_\tau = 100$ Turbulence Using Gain Scheduling and Linear State-feedback Control Flow. *Phys. Fluids* **15**, 3572–3575.
- JOSHI, S. S., SPEYER, J. L. & KIM, J. 1997 A Systems Theory Approach to the Feedback Stabilization of Infinitesimal and Finite-amplitude Disturbances in Plane Poiseuille Flow. *J. Fluid Mech.* **332**, 157–184.
- JUANG, J.-N. & PAPPAS, R. S. 1985 An eigensystem realization algorithm for modal parameter identification and model reduction. *J. Guid., Con. Dyn.* **8** (5), 620–627.
- KIM, J. & BEWLEY, T. R. 2007 A Linear Systems Approach to Flow Control. *Ann. Rev. Fluid Mech.* **39**, 39–383.
- LEWIS, F. L. & SYRMOUS, L. V. 1995 *Optimal Control*. John Wiley & Sons, New York.
- LI, Y. & GASTER, M. 2006 Active Control of Boundary-Layer Instabilities. *J. Fluid Mech.* **550**, 185–205.
- MA, Z., AHUJA, S. & ROWLEY, C. W. 2011 Reduced-order models for control of

- fluids using the eigensystem realization algorithm. *Theoretical and Computational Fluid Dynamics* **25** (1-4), 233–247.
- MOORE, B. 1981 Principal Component Analysis in Linear Systems: Controllability, Observability, and Model reduction. *IEEE Trans. Autom. Control* **26** (1), 17–32.
- NORDSTRÖM, J., NORDIN, N. & HENNINGSON, D. S. 1999 The fringe region technique and the Fourier method used in the direct numerical simulation of spatially evolving viscous flows. *SIAM J. Sci. Comp.* **20** (4), 1365–1393.
- ROWLEY, C. W. 2005 Model reduction for fluids, using balanced proper orthogonal decomposition. *Intl J. of Bifurcation and Chaos* **15** (03), 997–1013.
- SEMERARO, O., BAGHERI, S., BRANDT, L. & HENNINGSON, D. S. 2010 Linear Control of 3D Disturbances on a Flat-Plate. In *7th IUTAM Symposium on Laminar-Turbulent Transition* (ed. P. Schlatter & D. S. Henningson), , vol. 18. Springer.
- SEMERARO, O., BAGHERI, S., BRANDT, L. & HENNINGSON, D. S. 2011 Feedback control of three-dimensional optimal disturbances using reduced-order models. *J. Fluid Mech.* **677**, 63–102.
- SEMERARO, O., BAGHERI, S., BRANDT, L. & HENNINGSON, D. S. 2013 Transition delay in a boundary layer flow using active control. *J. Fluid Mech.* **731** (9), 288–311.
- STURZEBECKER, D. & NITSCHKE, W. 2003 Active cancellation of Tollmien–Schlichting instabilities on a wing using multi-channel sensor actuator systems . *Intl J. Heat and Fluid Flow* **24**, 572–583.
- THOMAS, A. S. W. 1984 Aircraft Drag Reduction Technology. *Tech. Rep.*. Lockheed-Georgia co Marietta Flight Sciences Division.
- WILLCOX, K. & PERAIRE, J. 2002 Balanced model reduction via the proper orthogonal decomposition. *AIAA J.* **40** (11), 2323–2330.
- ZHOU, K., DOYLE, J. C. & GLOVER, K. 2002 *Robust and Optimal Control*. Prentice Hall, New Jersey.

Paper 5

Energy efficiency and performance limitations of linear adaptive control for transition delay

Nicolò Fabbiane, Shervin Bagheri and Dan S. Henningson

Linné FLOW Centre, KTH Mechanics, S-100 44 Stockholm, Sweden

Submitted to Journal of Fluid Mechanics

Reactive-control techniques have been longly investigated to control local flow instabilities in boundary-layer flows – Tollmien-Schlichting waves – that would eventually cause laminar-to-turbulence transition. Several studies have been published about the control of two-dimensional (2D) disturbances supposing a transition delay. In this study, a three-dimensional (3D) disturbance environment is considered in a 2D zero-pressure-gradient boundary-layer flow. A control-law based on a multi-input-multi-output (MIMO) filtered-x least-mean-squares (fxLMS) adaptive algorithm is introduced and its performances are analysed for increasing disturbance amplitude. Transition delay is achieved by the investigated control set-up; moreover, an energy budget is conducted in order to asses the net energy saving capabilities of the investigated control approach. Ideal as well as real actuators models are considered, focusing in particular on dielectric-barrier-discharge (DBD) plasma actuators. To our knowledge, this is the first time that drag-reduction and energy-saving capabilities are studied for reactive transition-delay techniques.

Key words: fxLMS, plasma actuator, drag reduction

1. Introduction

In low free-stream turbulence conditions, the transition to turbulence in a flat-plate boundary-layer is dominated by Tollmien-Schlichting (TS) instabilities. These disturbances have the form of travelling waves that grow exponentially while propagating downstream. When they reach a critical amplitude, around 1% of the free-stream velocity, they non-linearly interact with each other and eventually lead to turbulent state. This scenario is known as the classical route to transition, as described in the review work by Kachanov (1994). Since a turbulent boundary layer leads to higher friction force, it is of engineering interest to develop control techniques that allow the flow to stay laminar as long as possible.

The general aim is to control the TS-waves instabilities when their amplitude is still small such as they reach the critical amplitude farther downstream. In

this way, the non-linear breakdown is used to our advantage; the disturbances are cancelled when their amplitude is low and the force requirement is small, where one can expect that the energy-saving because of the drag-reduction induced by the transition-delay is very large. These considerations lead to an inherent – but not verified – high energy-gain by this control strategy. Because of its potential, reactive flow control has been subjected to several studies in the past decades; the two-dimensional (2D) control of flow instabilities has been widely investigated both from a numerical (e.g. Bagheri *et al.* 2009; Dadfar *et al.* 2013) and experimental (e.g. Kurz *et al.* 2013; Juillet *et al.* 2014; Kotsonis *et al.* 2015) point of view. Successful attempts to control complex three-dimensional (3D) environments can be found in the literature (Li & Gaster 2006; Semeraro *et al.* 2013; Dadfar *et al.* 2014) but, to our knowledge, no systematic study on transition delay and energy saving has been conducted yet.

The present work aims to understand the transition-delay capabilities of reactive flow control and assess the potential net-energy-saving. In particular, the present work focuses on an adaptive control technique, which is based on an on-line computation of the control law. This is in contrast to static control techniques (Semeraro *et al.* 2013; Juillet *et al.* 2014), where the control law is precomputed, usually based on a model of the flow.

A multi-input multi-output (MIMO) filtered-x least-mean-squares (fxLMS) algorithm is used. This adaptive control technique has been studied by the experimental community and shown to be effective in 2D TS-wave control (Sturzebecher & Nitsche 2003; Kurz *et al.* 2013). A recent study by Fabbiane *et al.* (2015*b*) highlighted its robustness to varying external conditions when compared to static control. In particular, the algorithm was able to change the control law when the free-stream velocity was slightly varying from the nominal condition. The weak non-linearities that TS-waves encounter in the first stages of the transition to turbulence can also be regarded as uncertainties; therefore, the algorithm should be able to adapt to the weak non-linearities and extend the transition-delay capabilities of the investigated control set-up.

The manuscript is organised as follows: after a brief introduction to the numerical set-up (§2) and the implemented adaptive algorithm (§3), the control performances are investigated in linear (§4.1) and non-linear (§4.2) regimes and transition-delay capabilities are analysed (§4.3). Finally, the energy efficiency of reactive transition-delay is evaluated (§5) by using both ideal actuators and plasma-actuator models.

2. DNS/LES simulations

The incompressible Navier-Stokes equations govern the flow:

$$\frac{\partial \mathbf{u}}{\partial t} + (\mathbf{u} \cdot \nabla) \mathbf{u} = -\frac{\nabla p}{\rho} + \frac{1}{Re} \nabla^2 \mathbf{u} + \lambda(\mathbf{x}) \mathbf{u} + \mathbf{f}, \quad (1)$$

$$\nabla \cdot \mathbf{u} = 0, \quad (2)$$

where ρ is the density, $\mathbf{u}(\mathbf{x}, t)$ the velocity, $p(\mathbf{x}, t)$ the pressure at each time t and position $\mathbf{x} = (X, Y, Z) \in \Omega$. The axis X is aligned with the free-stream velocity U , Y is normal to the surface and Z defines a right-hand triad with the others, see Figure 1. Using a pseudo-spectral code (Chevalier *et al.* 2007), DNS and LES simulations are performed in order to analyse the control strategy. Periodicity is assumed in the spanwise and streamwise directions; the fringe forcing $\lambda(\mathbf{x})$ enforces periodicity in the streamwise direction in the last 20% of the streamwise domain length (Nordström *et al.* 1999). The spatial coordinates are non-dimensionalised by the displacement thickness in the beginning of the domain δ_0 . The resulting Reynolds number is defined as $Re = U\delta_0/\nu = 1000$, where ν is the kinematic viscosity. For the time-integration a fourth-order Crank-Nicolson/Runge-Kutta method is used with a constant time-step $\Delta t = 0.4$.

Two different computational domains are used in this work. A shorter domain Ω_S is used for the parametric study over the perturbation amplitude in §4.2. It extends for $[0, 1000] \times [0, 30] \times [-75, 75]$ in the X , Y and Z directions and the flow is expanded over 1536×384 Fourier modes in the XZ -plane and 101 Chebyshev's polynomials in the wall-normal direction. A second and longer domain Ω_L is used to assess the transition delay and energy saving capabilities of the control technique in §4.3. It extends for $[0, 2000] \times [0, 45] \times [-125, 125]$ and it uses $1536 \times 151 \times 384$ Fourier-Chebyshev-Fourier basis. De-aliasing is performed along the Fourier-discretised direction with a $3/2$ rule.

Depending on the disturbance magnitude, turbulence may appear at the end of the longer domain. Since we are interested in the onset of turbulence and not in turbulence itself, a relaxation-term model (ADM-RT) is used as sub-grid model in order to avoid to increase the spatial resolution (Stolz *et al.* 2001). This model has shown to be accurate and robust in predicting transitional flows (Schlatter *et al.* 2004).

2.1. Inputs and outputs

The input/output (I/O) set-up is composed of four rows of equispaced and independent objects (Figure 1). Two rows of sensors are placed at $X = 300$ and $X = 500$, a row of actuators is placed at $X = 400$. The disturbances are introduced farther upstream at $X = 65$ by a row of synthetic vortices. These objects are positioned with a constant spanwise separation to cover the domain span. Semeraro *et al.* (2013) showed that a span-wise spacing $\Delta Z = 10$ is necessary to effectively control a TS wave-packet for the current setup; this results in 15 objects per row in the smaller domain Ω_S and 25 in the larger domain Ω_L . Disturbance sources and actuators are modelled by the forcing term $\mathbf{f}(X, Y, Z, t)$ in (1):

$$\mathbf{f} = \mathbf{f}_d + \mathbf{f}_u = \sum_l \mathbf{b}_{d,l} d_l(t) + \sum_l \mathbf{b}_{u,l} u_l(t). \quad (3)$$

The constant spatial functions $\mathbf{b}_{d,l}(X, Y, Z)$ and $\mathbf{b}_{u,l}(X, Y, Z)$ are modulated by the disturbance and control signals $d_l(t)$ and $u_l(t)$, respectively.

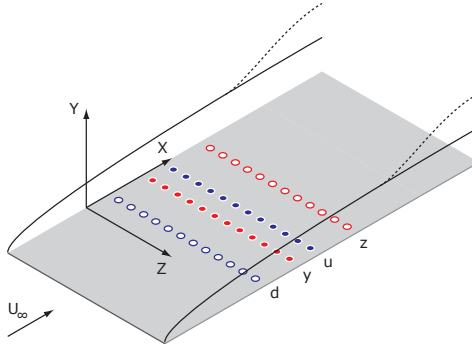


Figure 1: Control set-up. Random 3D disturbances are generated by a row of localised independent forcings d . The measurements from the sensors y and z are used by an adaptive FXLMS algorithm to compute the actuation signal for the actuators u in order to reduce the amplitude of the detected disturbances.

Disturbance sources are modelled by localised synthetic vortices (Semeraro *et al.* 2013),

$$\mathbf{b}_{d,l} = \begin{bmatrix} \chi \tilde{Y} \\ -\gamma \tilde{X} \\ 0 \end{bmatrix} \exp\left(-\tilde{X}^2 - \tilde{Y}^2 - \tilde{Z}^2\right), \quad (4)$$

where:

$$\tilde{X} = \frac{X - X_{d,l}}{\chi}, \quad \tilde{Y} = \frac{Y}{\gamma} \quad \text{and} \quad \tilde{Z} = \frac{Z - Z_{d,l}}{\zeta}.$$

The l -th disturbance source is centred at $(X_{d,l}, 0, Z_{d,l})$ and its spatial support is given by $\chi = 2$, $\gamma = 1.5$ and $\zeta = 4$.

The control actuators are modelled as plasma actuators based on the experimental data by Kriegseis *et al.* (2013). This type of actuators has been adopted by Kurz *et al.* (2013); Fabbiane *et al.* (2015b); Kotsonis *et al.* (2015).

Following the work by Fabbiane *et al.* (2015b), localised measurement of the streamwise skin friction are used as sensors in order to model surface hot-wires (Li & Gaster 2006; Sturzebecher & Nitsche 2003; Kurz *et al.* 2013). Each signal is subtracted by its time-average over 750 time units in order to remove the mean-flow contribution to the wall stress.

2.2. Flow configurations

Each disturbance source d_l is independently fed with unitary uniform white-noise $w_l(t)$,

$$d_l(t) = a_d w_l(t), \quad (5)$$

where the gain a_d defines the amplitude. A uniformly distributed noise provides a better control of the maximum forcing amplitude that is fed to the flow, since the disturbance signal ranges between $\pm a_d$. Since the disturbance forcing in (4)

a_d	$A(100)$	$A(400)$	Short box (Ω_S)	Long box (Ω_L)
Linear behaviour				
1.0×10^{-4}	0.006%	0.01%	S-LIN0	–
1.0×10^{-3}	0.056%	0.09%	S-LIN1	L-LIN1
2.0×10^{-3}	0.113%	0.19%	S-LIN2	L-LIN2
Weakly non-linear behaviour				
3.0×10^{-3}	0.170%	0.33%	S-WNL1	L-WNL1
4.0×10^{-3}	0.226%	0.55%	S-WNL2	L-WNL2
Non-linear behaviour				
5.0×10^{-3}	0.283%	0.86%	S-NL1	L-NL1
6.0×10^{-3}	0.340%	1.33%	S-NL2	L-NL2
7.0×10^{-3}	0.398%	2.03%	S-NL3	L-NL3
Transitional behaviour				
8.0×10^{-3}	0.456%	2.97%	S-TR1	L-TR1
9.0×10^{-3}	0.511%	4.00%	–	L-TR2
1.0×10^{-2}	0.568%	5.21%	–	L-TR3

Table 1: Flow configurations. The simulations are classified by the perturbation behaviour in the actuation region. The disturbance signals $d_l(t)$ are uniform white noises that ranges between $\pm a_d$. The amplitude $A(X)$ of the resulting perturbation field is reported close downstream the disturbance source ($X = 100$) and at the actuators position ($X = 400$).

in aligned with the streamwise direction and its spanwise component is zero, the resulting perturbation is dominated by TS-wave.

Table 1 reports the flow configurations that are used in this work. The amplitude of the perturbation field is defined as:

$$A^2(X) = \max_Y \left\langle \left(\frac{u'}{U} \right)^2 \right\rangle_{Z,t}, \quad (6)$$

where u' is the streamwise component of the velocity with respect to the mean-flow. The angled brackets $\langle \cdot \rangle$ indicate the average operator and the subscripts the averaging variables. In Table 1, the perturbation amplitude is reported at $X = 100$, closely downstream to the disturbance-source location; a linear relation holds between the measured perturbation amplitude and the disturbance signal range a_d for all the investigated flow cases. Hence, $A(100)$ is used to identify the introduced disturbance in the following.

The cases are grouped according to the perturbation behaviour at the actuators location ($X = 400$). In this study, three levels of non-linear behaviour are identified. The flow is *weakly non-linear* when the perturbation amplification deviate from the linear prediction but the control algorithm performance is not effected by the non-linearity. Increasing the amplitude further, however, the adaptive algorithm is able to compensate only partially for the non-linear behaviour of the flow; this scenario is thus identified as *non-linear*. By increasing even further the disturbance amplitude, the laminar-to-turbulence transition reaches the actuation location and the control does not effectively control the perturbation field. The latter flow cases are *transitional*.

3. Control strategy

The control action is performed by a row of localized, equispaced actuators forcing the flow in the proximity of the wall. Their action $u_l(t)$ is computed based on the measurements $y_m(t)$ by a row of sensors upstream of the actuators: for this set-up, the number of sensors is equal to the number of actuators and they are aligned with the flow direction (Figure 2).

We assume a linear control law and an equal number ($M + 1$) of sensors and actuators. As a consequence, the number of transfer functions between the $M + 1$ sensors y_m and the actuators u_l is $(M + 1)^2$. This imposes a computation constraint when $M + 1$ is large, which is the case when covering a large spanwise width with the controller. However, since the flow is spanwise homogeneous, the same transfer K_m function from all the sensors y_l to one actuator can be replicated for each actuator u_m (Figure 2). This assumption reduces the number of transfer functions to be designed from $(M + 1)^2$ to $M + 1$. The finite impulse response (FIR) filter representation of the control law reads,

$$u_l(n) = \sum_{m=-M/2}^{M/2} \sum_{j=0}^N K_m(j) y_{m+l}(n-j) \quad (7)$$

where $u_l(n)$ and $y_l(n)$ are the time-discrete control and measurement signals respectively, $K_m(j) \in \mathbb{R}^{(M+1) \times (N+1)}$ is the convolution kernel of the compensator and $N\Delta t$ is the time horizon of the FIR filter (Aström & Wittenmark 1995; Fabbiane *et al.* 2014).

The design of the compensator consists in computing the time-discrete convolution kernel $K_m(j)$. In this work, a MIMO version of the FXLMS algorithm is used to dynamically design the compensator. The algorithm aims to minimise the sum of the squared measurement signals $z_l(n)$, i.e. the downstream row of sensors in Figure 1,

$$\min_{K_m} \left(\sum_{l=-M/2}^{M/2} z_l^2(n) \right). \quad (8)$$

The kernel is updated via a steepest descend algorithm at each time step,

$$K_m(i|n+1) = K_m(i|n) - \mu \lambda_m(i|n), \quad (9)$$

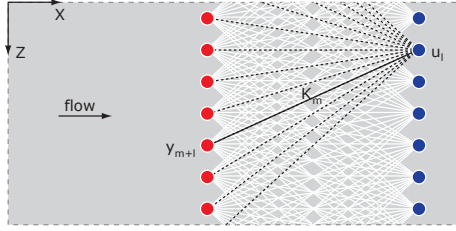


Figure 2: Compensator structure. The action of each actuator u_m is computed by filtering the signals from all the sensor y_l via a linear filter K_m . An adaptive FXLMS filter is responsible of computing the K_m response in order to maximize in real time the control performances measured by the error sensors z_l .

where the descend direction $\lambda_m(j|n)$ is given by

$$\lambda_m(i|n) = \frac{\partial (\sum_l z_l^2(n))}{\partial K_m(i)} = 2 \sum_{l=-M/2}^{M/2} z_l(n) \frac{\partial z_l(n)}{\partial K_m(i)}. \quad (10)$$

In order to compute the derivative in the previous equation, it is necessary to carry out the $z(n)$ dependencies by the control kernel $K_m(i)$. The error sensor signal is given by the superposition of the disturbance sources d_l and actuators u_l ,

$$z_l(n) = z_{l,d}(n) + z_{l,u}(n). \quad (11)$$

Only the term $z_{l,u}$ depends on the control law $K_m(i)$,

$$\begin{aligned} z_{l,u}(n) &= \sum_r \sum_j P_{zu,r}(j) u_{r+l}(n-j) = \\ &= \sum_r \sum_j P_{zu,r}(j) \sum_m \sum_i K_m(i) y_{m+r+l}(n-j-i) = \\ &= \sum_m \sum_i K_m(i) \sum_r \sum_j P_{zu,r}(j) y_{r+m+l}(n-j-i) = \\ &= \sum_m \sum_i K_m(i) f_{m+l}(n-i), \end{aligned} \quad (12)$$

where $f_l(n) = \sum_r \sum_j P_{zu,r}(j) y_{r+l}(n-j)$ are the *filtered* signals. For sake of simplicity, the limit of the sums are omitted in (12): indices r, l step from $-M/2$ to $M/2$ and i, j from 0 to N . The same spanwise homogeneity assumption has been made for the plant kernel $P_{zu,r}(j)$, which represents the transfer functions $u_r \rightarrow z_l$. Hence the descend direction reads

$$\lambda_m(i|n) = 2 \sum_{l=-M/2}^{M/2} z_l(n) \frac{\partial z_l(n)}{\partial K_m(i)} = 2 \sum_{l=-M/2}^{M/2} z_l(n) f_{m+l}(n-i). \quad (13)$$

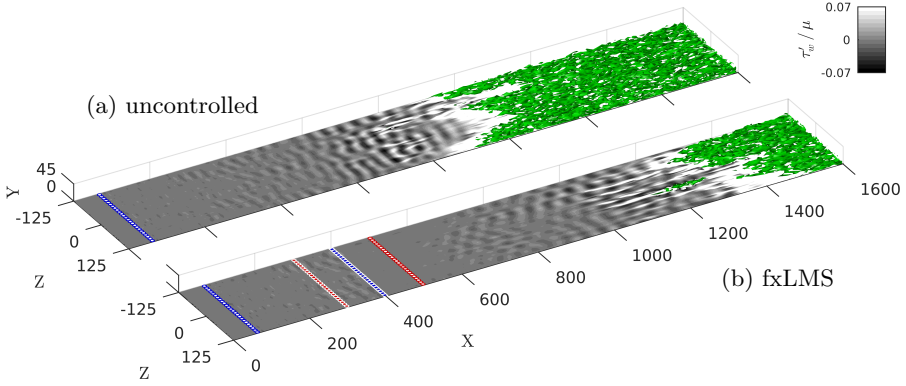


Figure 3: Disturbance attenuation and transition delay. The shaded gray area report the skin friction fluctuations τ'_w (eq. (14)). The green surfaces indicate the λ_2 -criterion with a threshold of -2×10^{-3} . The disturbance sources result in a perturbation field with amplitude $A(100) = 0.11\%$ (case L-LIN2). The fringe region is not shown.

Note that this method is not completely model free as $P_{zu,l+m}(i)$ is needed to compute $f_l(n)$. In this paper, this transfer function is computed via a linear impulse response of the actuator u_l . This transfer function is commonly addressed as the *secondary path* (Sturzebecher & Nitsche 2003).

3.1. The compensator in action

The fxLMS algorithm is used to control randomly generated perturbations. Figure 3a shows the transition to turbulence in the uncontrolled case. The flow is perturbed with 25 disturbance sources; each one of these inputs is fed with an independent uniform white-noise signal that ranges between $\pm 2 \times 10^{-3}$, (L-LIN2 in Table 1). In Figure 3, turbulent eddies are visualised by the λ_2 -criterion in green (Jeong & Hussain 1995); the disturbances grow and trigger transition in the second half of the domain. The gray shaded area shows the friction fluctuation $\tau'(X, Z, t)$ at the wall with respect to the laminar solution:

$$\tau'_w = \tau_w - \tau_{w,lam}. \quad (14)$$

From the friction footprint, it can be seen that the disturbance sources create a random pattern of TS-wave-packets that grow while being convected downstream by the flow. When they reach a critical amplitude, they non linearly interact and trigger turbulence. The controlled configuration is shown in Figure 3b; it is asked to delay the transition process, within the same disturbance environment. The disturbance amplitude drops downstream of the actuators (in blue) and the transition is significantly delayed with respect to the uncontrolled case.

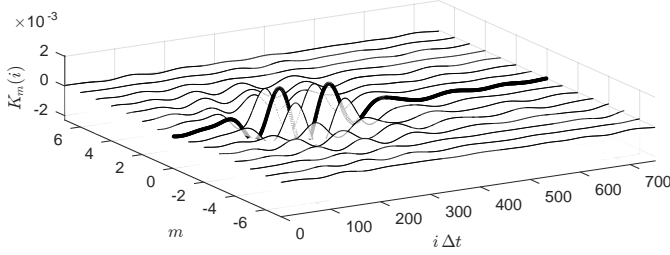


Figure 4: Control kernel. The thick line indicates $K_0(t)$, i.e. the connection between sensors and actuators at the same spanwise location.

The algorithm builds the control kernel $K_m(i)$ on-line based on the measurement upstream and downstream of the actuation region. In a low disturbance environment, the kernel will eventually converge to a steady solution; Figure 4 shows the control kernel $K_m(i)$ for the presented simulation. The subscript m is the spanwise shift between actuator u_l and reference sensor y_{m+l} , hence it is directly related to the spanwise support of the control law. Its compact support in the spanwise direction indicates that the information given by the sensor is relevant only to compute the control signal for a limited number of actuators. This fact is related to the spanwise spreading of a wave-packet and shows how the control kernel is related to the structure of the disturbance that is meant to control. The spanwise support of the control kernel is independent of the streamwise distance between sensors and actuators rows, as reported by Fabbiane *et al.* (2015a).

4. Control performance and limitations

In this section, the performance of the control is analysed for small (§4.1) and increasing magnitude of the perturbation field (§4.2), up to the point where no transition delay and drag reduction is observed (§4.3).

4.1. Linear control of linear perturbations

In order to better understand how the compensator acts on the flow, the performance of the controller is studied when the perturbation field is small enough for its behaviour to be considered linear. For the flow case S-LIN0, the smaller computational domain Ω_S is used and the flow is perturbed by 15 disturbance source fed by 15 independent uniform-white-noise signals with amplitude $a_d = 1.0 \times 10^{-4}$.

A Fourier transform is computed in time and in the spanwise direction. Hence a general flow quantity, e.g. the streamwise wall stress τ_w , is transformed as:

$$\hat{\tau}_w(X, \beta, \omega) = (\mathcal{F}_z \circ \mathcal{F}_t) (\tau_w(X, Z, t)), \quad (15)$$

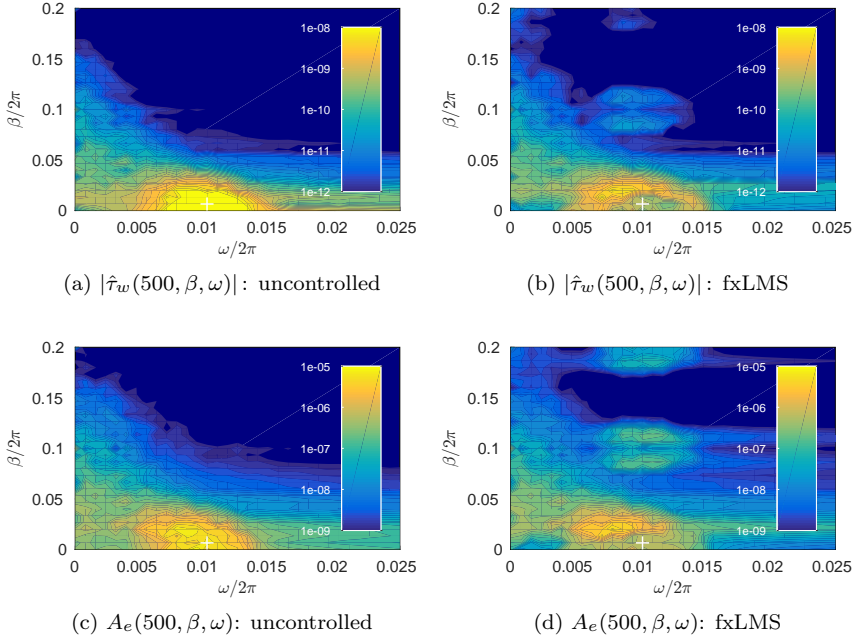


Figure 5: Control performance in low-disturbance environment. (a-b) depict the skin-friction spectra $\hat{\tau}$ for controlled and uncontrolled simulations at z_l -sensors location $X = 500$, while (c-d) report the energy-based amplitude A_e at the same streamwise location. The spectra refer to the flow case S-LIN0, see Table 1. The dark-blue areas indicate values below the lower bound of the colorbar. The white cross indicates the Fourier-mode reported in Figure 6.

where β and ω are the spanwise wave-number and angular frequency, respectively. The temporal transform is based on 512 flow fields, 10 time-units apart from each other; they are sampled after simulations reach statistical uniformity.

Figure 5a-b shows uncontrolled and controlled spectra for the skin friction $\hat{\tau}$ at the error sensor location, $X = 500$. In the uncontrolled case, the disturbance field is present in a limited region of the spatio-temporal frequency space. The effect of the control is to damp the peak near to $(\omega, \beta)/2\pi = (0.01, 0)$, as it can be observed in Figure 5b.

Figure 6a shows a mode in the region of maximum amplification for the uncontrolled simulation. The mode has the appearance of a TS-wave triggered at the disturbance location and spatially growing throughout the domain. The effect of the control on the mode is clearly visible in Figure 6b; the perturbation grows until the actuator location ($X = 400$), after which it is cancelled almost completely within 100 spatial units. This confirms that the cancellation is not

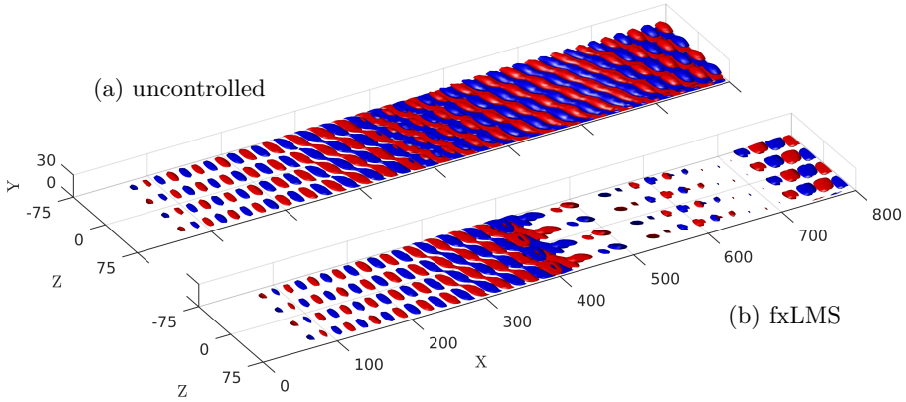


Figure 6: Fourier mode $\hat{\mathbf{u}}(X, Y, \beta, \omega)$ in physical space for $\omega/2\pi \approx 0.01$ and $\beta/2\pi = 2/L_Z$. Positive (red) and negative (blue) isosurfaces depict the real part of the streamwise velocity. The data refers to the same flow case as shown in Figure 5 (S-LIN0).

occurring suddenly at the actuator location. The actuator generates a counter-phase wave-packet that – once fully developed – cancels the original disturbance. Farther downstream, towards the end of the domain, the perturbation reappears and is convected out of the domain. A similar behaviour is common to all the Fourier-modes in the damped region of the spectrum.

The control introduces some disturbances that are not present in the uncontrolled case, such as the double-peak at $\beta/2\pi = 0.1$ in Figure 5b. This perturbation is introduced by the actuators’ spatial shape and spanwise distribution. These peaks are present for the super-harmonics of the fundamental spanwise wave-number of the actuator spacing $2\pi/\Delta Z$. The actuator spacing is chosen according to Semeraro *et al.* (2013) in order to avoid these disturbances having support in TS-wave region and, hence, interacting with the control action. Because of the limited amplitude and their short spanwise wave-length, they do not appear to compromise the control effect, also for higher disturbance levels.

The streamwise wall-stress τ_w is a measurement of the disturbance at the surface. An integral measurement along the wall-normal direction is introduced to assess whether an overall reduction of the disturbance is correlated to a reduction of τ_w :

$$A_e^2(X, \beta, \omega) = \int_0^{L_Y} |\hat{\mathbf{u}}(X, Y, \beta, \omega)|^2 dY, \quad (16)$$

where $\hat{\mathbf{u}}(X, Y, \beta, \omega)$ is the Fourier transform of the velocity $\mathbf{u}(X, Y, Z, t)$. Figure 5c-d report A_e for the controlled and uncontrolled case; both present the same features as the wall-stress spectra in Figure 5a-b. This shows that a

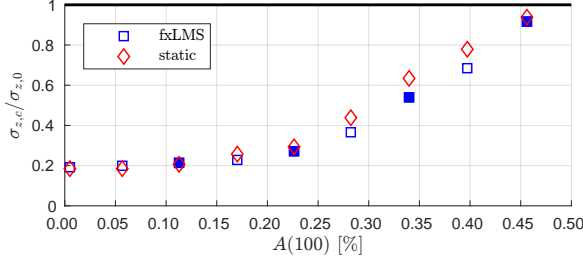


Figure 7: Performance indicator $\sigma_{z,c}/\sigma_{z,0}$ as a function of the seeded perturbation amplitude $A(100)$. The filled markers indicate the flow cases reported in Figures 9-10.

reduction of the disturbance stress corresponds to a reduction of the disturbance energy; moreover, it confirms that the choice of measuring the disturbance amplitude by measuring its friction footprint is prudent.

4.2. The non-linear challenge

In this section, it is shown (i) how the linear-control limits the performance of the investigated control strategy when non-linearity is present and (ii) how adaptivity can reduce this performance loss. A parametric study over the perturbation amplitude is performed, where the 15 disturbance sources in Ω_S are fed with independent white-noise signals of increasing amplitude.

Once the coupled compensator-flow system has reached the statistical steady state, the performance of the control action is tracked as a function of the disturbance level upstream the actuation point. As introduced in §2.1, the sensors y_l and z_l measure wall-stress fluctuations, hence they are related to the amplitude of the perturbations at the sensing location. The amplitude measured by the error sensors is given by the measurement-signals variance,

$$\sigma_z^2 = \frac{1}{M+1} \sum_{l=-M/2}^{M/2} \langle z_l(t)^2 \rangle_t, \quad (17)$$

where each signal $z_l(t)$ has a zero temporal mean. The performance of the control action is assessed by the ratio between the controlled ($\sigma_{z,c}$) and uncontrolled ($\sigma_{z,0}$) standard deviation of the error signals.

Figure 7 reports the performance indicator as a function of the perturbation amplitude $A(100)$. For perturbation amplitudes up to 0.11%, the control performance does not appear to be influenced by the disturbance amplitude. For higher amplitudes the control performance gradually departs from the linear behaviour, as the non-linearities start to become relevant at the actuator position. Figure 8 reports $A(X)$ at the actuator location $X = 400$ for the uncontrolled case; the perturbation behaves nonlinearly when $A(100)$ is greater

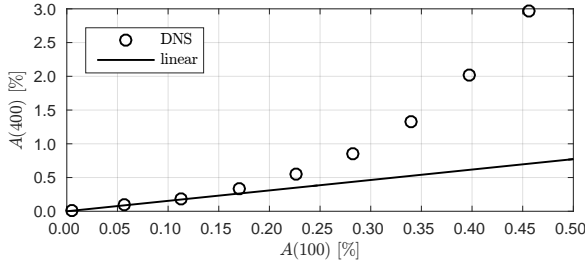


Figure 8: Perturbation amplitude $A(400)$ at the location of the actuators as a function of the perturbation amplitude $A(100)$.

than $\sim 0.17\%$. Comparing with Figure 7, it is clear that the performance loss of the control strategy is related to the rise of non-linearities in the flow.

The gradual loss of performance by the compensator can be analysed by studying at the wall-friction spectra at the location of error-sensors; Figure 9 shows the uncontrolled and controlled spectra for increasing disturbance amplitudes, while Figure 10 reports instantaneous flow fields for the same simulation parameters. For the lowest reported amplitude, the flow has a linear behaviour. TS-waves start to non-linearly interact with themselves and generate the structures close to the β -axis; this is visible both for the uncontrolled and control cases.

As the amplitude increases (Figure 9a-b and Figure 10a) obliques waves appear for the uncontrolled case at $(\omega, \beta)/2\pi \approx (0.005, 0.075)$, while in the controlled case they are present only in a limited region of the spectrum and with a lower amplitude. By cancelling the the perturbation in the TS-wave region, the control is able to delay the growth of the secondary disturbances that will eventually lead to turbulence.

Figure 9c-d and Figure 10b show the limit amplitude for which the control has an effect on the perturbation field. The peak related to the TS-wave is still damped but the modes due to non-linear interactions of the perturbation field are clearly visible in both cases; the perturbation behaviour is already non-linear at the actuation location (see Figure 8). Finally, in Figure 9e-f and Figure 10c the uncontrolled and controlled simulations are almost undistinguishable; for this amplitude, transition to turbulence will take place just downstream the error sensor location and no transition delay is noticeable, see §4.3.

In all the presented scenarios the control is able to directly damp only disturbances in the TS-wave region. The algorithm shapes the control law based on a linear model of secondary path P_m , i.e. the transfer function between the actuators u_l and the error-sensor z_{l+m} ; in other words, the secondary path provides the algorithm the information of how it can effect the flow.

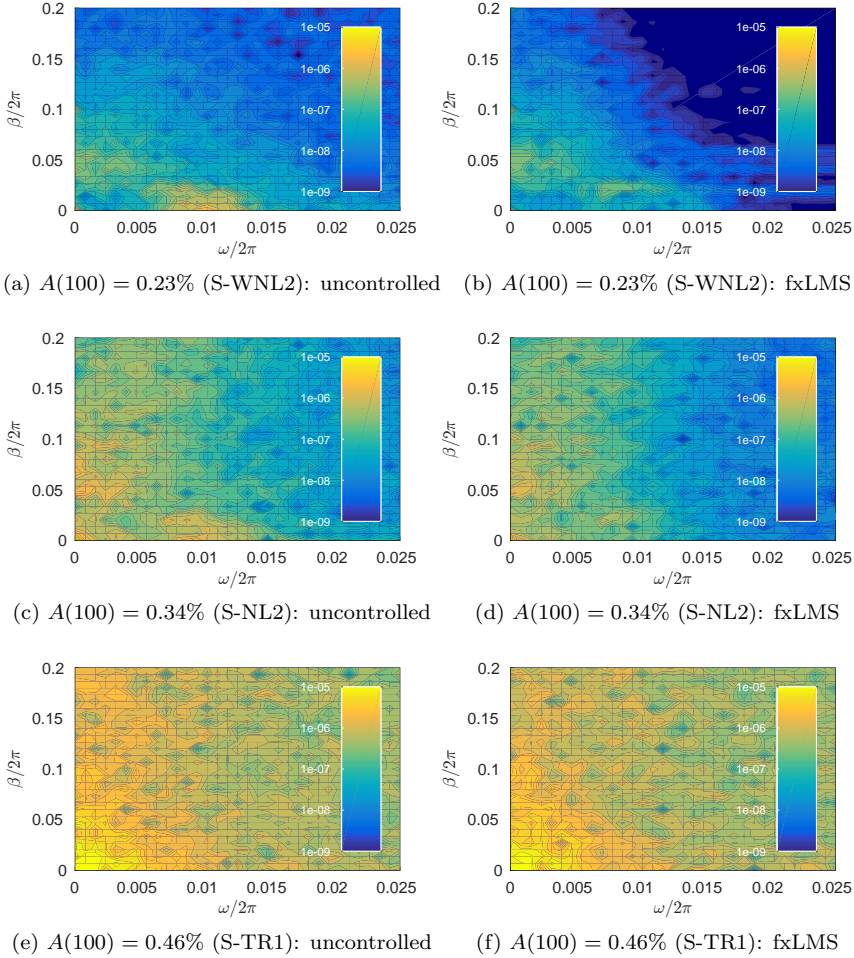


Figure 9: Skin-friction spectra for uncontrolled and controlled simulations at z_l -sensors location $X = 500$. The disturbance sources produce a perturbation field with amplitude $A(100)$ as in the subcaption of the figures. The dark-blue areas indicate values below the lower bound of the colorbar.

The adaptivity properties of the fxLMS algorithm are favourable when it comes to slowly varying conditions in the flow (Fabbiane *et al.* 2015b). However, when it comes to non-linearities, they are only capable of a marginal improvement of the control performance. As introduced in §3, the fxLMS algorithm acts on the control law by changing the control kernel $K_m(i)$ according to the measurement from the error sensors. The role of the adaptivity in controlling non-linear flows is highlighted by comparing the adaptive fxLMS algorithm

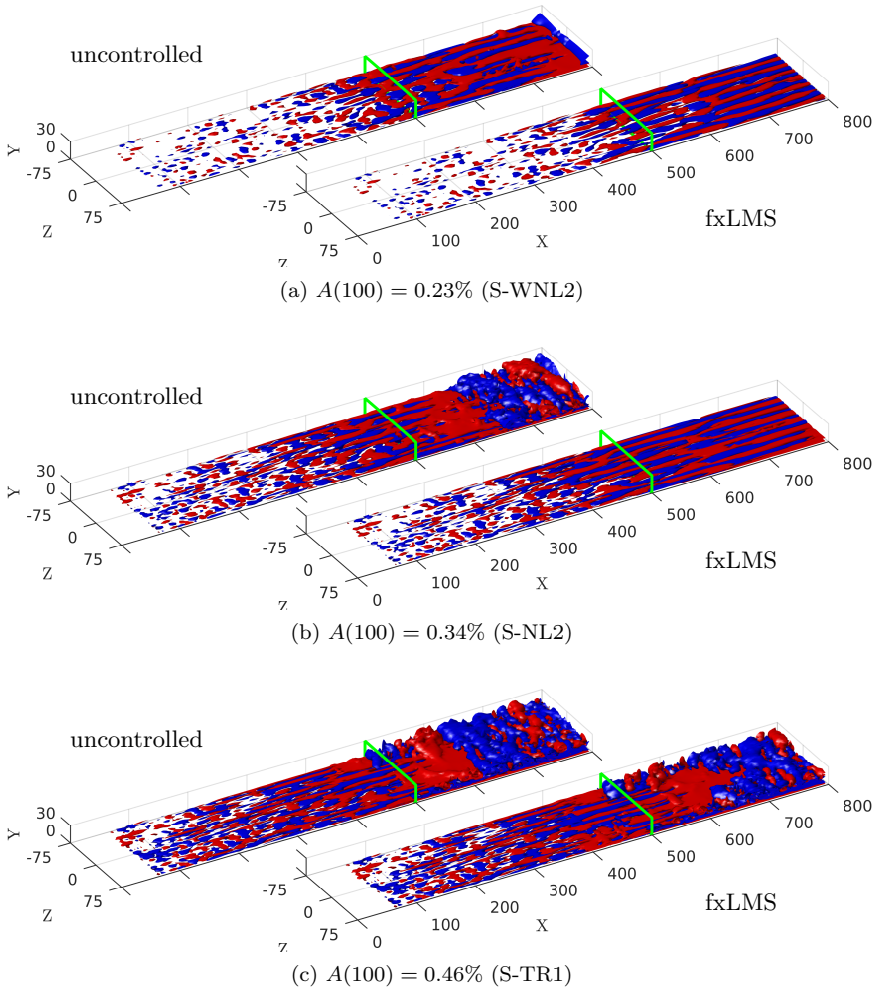


Figure 10: Velocity fluctuations isosurfaces u' with respect to the laminar solution for increasing disturbance amplitude. Red and blue isosurfaces are obtained for $u'/U = \pm 0.25\%$. The green plane indicates the streamwise position ($X = 500$) where the spectra in Figure 9 are computed.

to a static control law, where the adaptive fxLMS algorithm is switched off. The red diamond symbols in Figure 7 report the control performance when the static control law is considered. Figure 11 shows the converged control kernel connection $K_0(i)$ between sensors and actuators with the same spanwise location, for three different disturbance amplitudes.

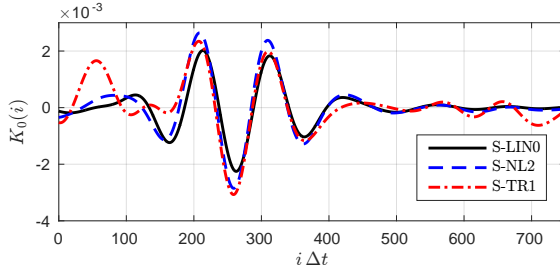


Figure 11: Comparison of the control kernels $K_0(i)$ for three different disturbance levels. The kernel for the case S-LIN0 is also the static control law in Figure 7.

Adaptive effects appear when the non-linearities arise in the flow. In this range of amplitudes, the fxLMS solution show slightly better performances with respect to the static controller. At this point the non-linearities are weak and their effect is limited to a change in the amplification and phase shift of the travelling waves. The algorithm modifies the control kernel by increasing the gain and reducing the time-shift between sensors and control signals (dashed line in Figure 11). However, the adaptive capabilities of the algorithm have a limit. Since the non-linear flow modification also has an effect on the input/output behaviour of the system, the secondary-path model used by the algorithm is no more consistent with the real secondary-path in the flow. The algorithm is able to compensate this error, if the phase difference between real and modelled secondary path is lower than $\pi/2$ in absolute value (Snyder & Hansen 1994; Simon *et al.* 2015). Hence, the control will continue to reduce the amplitude of the disturbances modelled by the secondary path, up to the point where the phase error caused by the non-linearities in the flow is large enough to destabilize the fxLMS algorithm.

At this point, the performance margin given by the adaptivity with respect to the static control tends to zero. This occurs when the transition is incipient in the region of the flow where the control action takes place, as seen in Figure 9g-h. The dot-dashed line in Figure 11 shows the control kernel in this scenario; the flow is already transitional at the actuator location and the adaptive algorithm introduces non-physical solutions of the control kernel.

4.3. Transition delay

It has been shown in the previous section that the control is able to reduce the perturbation amplitude downstream of the actuators. This section analyses how this disturbance reduction translates into a transition delay. The long box Ω_L is used to assess where the transition to turbulence occurs both in uncontrolled and controlled cases.

Delaying the laminar-turbulent transition means extending the portion of the flow that is laminar, which results in a lower total skin friction. Figure 12a

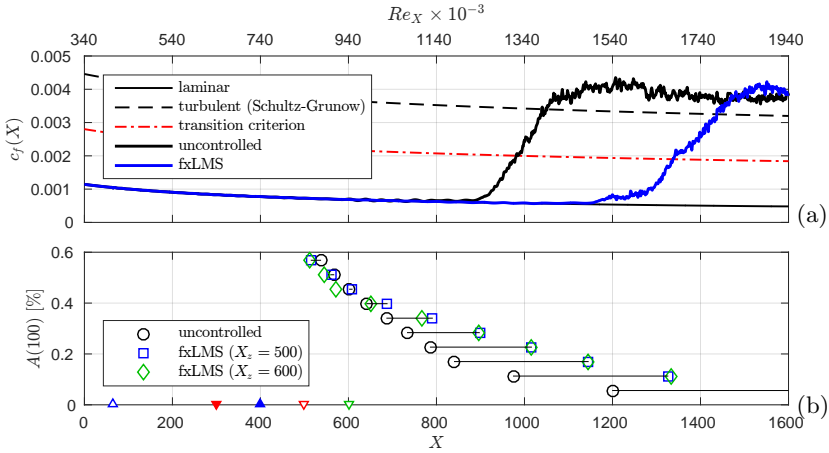


Figure 12: Transition delay. (a) reports the spanwise averaged friction coefficient for the flow case in Figure 3, L-LIN2. (b) reports the transition location for increasing perturbation amplitude $A(100)$; the reported positions are computed based on a time-averaged flow over 1200 time units. The top axis reports $Re_X = (X - X_{le})U/\nu$, where X_{le} is the extrapolated leading-edge position according to Blasius boundary-layer solution.

shows the spanwise-averaged friction coefficient, defined as

$$c_f(X) = \frac{\langle \tau_w \rangle_Z}{\frac{1}{2}\rho U^2}, \quad (18)$$

corresponding to the flow shown in Figure 3. The friction rise related to the onset of the turbulent regime is clearly delayed and the laminar friction region is extended in the controlled case.

The transition location is identified as the point where the average friction in the flow crosses the average between the laminar solution and the turbulent value as predicted by the Schultz-Grunow formula (Schultz-Grunow 1940). The transition location moves upstream as the disturbance level increases (Figure 12b). The perturbation-amplitude reduction, which the control is capable of, leads to a transition-delay for all investigated disturbance levels. However, the delay reduces as the amplitude increases and the disturbance reduction becomes less effective.

The green diamond symbols in Figure 12b report the transition location when the error sensor is displaced downstream by 100 spatial units. A performance loss is observed for lower amplitude than the original set-up; this shows that the performance limit is given by the disturbance amplitude at the error sensor location and not at the actuator location. This is in contrast with the linear analysis by Fabbiane *et al.* (2015a), where they show that better performances are obtained when the error sensors are far from the actuators.

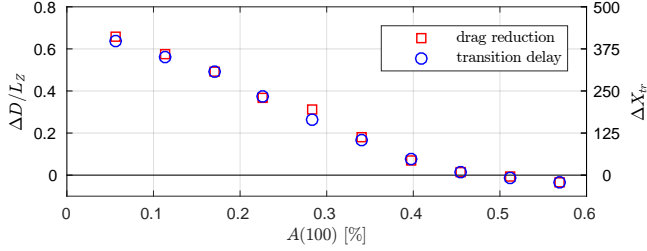


Figure 13: Drag save and transition-delay as a function of the perturbation level $A(100)$. The reported quantities are based on a time-averaged flow over 1200 time units.

The transition delay results in a drag reduction. The amount of saved drag is given by the area between the controlled and uncontrolled curves in Figure 12a:

$$\frac{\Delta D}{L_Z} = \int_0^{L_x} \langle \tau_{w,0} - \tau_{w,c} \rangle_Z dX, \quad (19)$$

where $\tau_{w,0}$ is the wall shear-stress in the uncontrolled case and $\tau_{w,c}$ in the controlled one. By repeating the same procedure for the different disturbance amplitudes in Figure 12b, the drag reduction as a function of the perturbation level is shown in Figure 13.

For the higher amplitudes the transition location approaches the region where the actuation takes place; as shown in the previous section, the non-linearities that eventually lead to transition start to develop at the error sensors location, which reduces the control capabilities of the algorithm. Hence, the investigated control technique is effective in delaying the laminar-to-turbulence transition when the perturbation amplitude at the actuation location is lower than 2% of the free-stream velocity, according to the amplitude definition in (6). For higher amplitudes, the control is not able to delay the already incipient transition; the strong non-linear behaviour of the flow inhibits the adaptive algorithm to converge to an effective control-law. This introduces eventually disturbances that shorten the transition region and, as a consequence, leads to the drag-increase as shown in Figure 13.

5. Energy efficiency

In the previous section it was shown that the investigated control strategy is able to delay the transition to turbulence and consequently reduce the friction drag. In this section, ideal and real actuator models are introduced in order to assess the energy efficiency of this control technique. To the best of our knowledge, this is the first time that the energy gain given by reactive laminar-flow control techniques is assessed in a systematic manner.

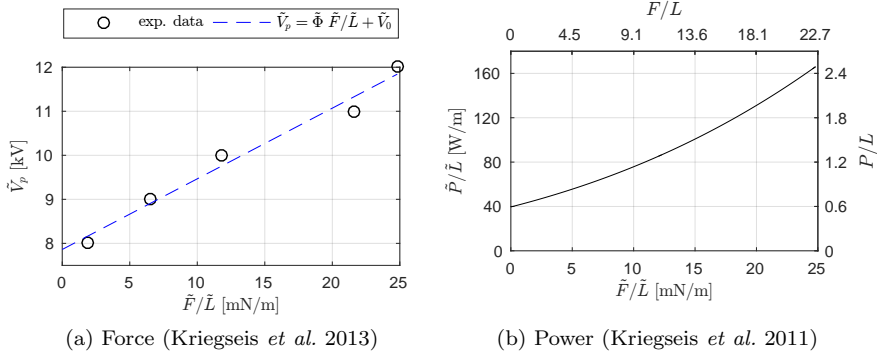


Figure 14: Plasma-actuator constitutive laws. The tilde indicates dimensional quantities.

5.1. Actuator models

Actuator models are introduced in order to compute the consumed power by the actuators in order to perform the control action. An ideal actuator is introduced in order to assess the theoretical energy gain and then compared with a more realistic experimental model of plasma actuators.

The ideal actuator is based on the volume integral across the domain of the local power ($\mathbf{u} \cdot \rho \mathbf{f}_u$) exchanged between the flow and the volume forcing:

$$P_{c,i} = \left\langle \left| \int_{\Omega} \mathbf{u} \cdot \rho \mathbf{f}_u d\Omega \right|_t \right\rangle. \quad (20)$$

The actuator use power both if it is on average pulling (negative integral) or pushing (positive integral) the flow. A similar approach is used when it comes to blowing/suction actuators (e.g. Stroh *et al.* 2015), where the time average of the absolute value of the instantaneous power needed to enforce the the mass flux is used to compute the used power by the control technique.

As introduced in §2.1, a dielectric-barrier-discharge (DBD) plasma actuator is considered as a model for the actuator volume forcing. In particular, the work by Kriegseis *et al.* (2013) is used, where the plasma actuator force field is reconstructed starting from PIV flow measurements. Based on their measurement it is possible to correlate the AC voltage supply V_p and the provided force F/L . As reported in Figure 14a, the voltage-force relation can be well represented by the linear regression:

$$V_p = \Phi \frac{F}{L} + V_0, \quad (21)$$

where L is the spanwise length of the actuator and Φ and V_0 are *ad-hoc* coefficients. In particular, the latter indicates the voltage for which the plasma actuator is giving zero force and can be considered as a lower limit for the

supplied voltage. In fact, the plasma actuator is not capable to supply a negative force; in order to overcome this issue, two different operation modes are typically considered:

1. Dual mode: two plasma actuator facing each-other are considered for each actuation station u_l . One is responsible for the positive part of the actuation signal and one is responsible for the negative one.
2. Hybrid mode: a single plasma actuator is considered. An offset is applied to the voltage in order not to cross the zero-forcing voltage V_0 ; the offset depends on the minimum amplitude of the control signal $u_l(t)$ in the averaging window. The constant forcing that results from the offset has a stabilizing effect on the boundary layer (Kurz *et al.* 2013); in the present study this effect is not taken into account.

Once the operation mode is defined, the power used by the actuator is estimated via the relation proposed by Kriegseis *et al.* (2011):

$$\frac{P}{L} = \Theta \sqrt{V_p^7 f_p^3} = \Theta \sqrt{\left(\Phi \frac{F}{L} + V_0\right)^7 f_p^3}, \quad (22)$$

where f_p is the plasma-actuator AC-supply frequency. The coefficient Θ is found to be an almost-universal coefficient equal to $5 \times 10^{-4} \text{ W/m(kHz)}^{-\frac{3}{2}} (\text{kV})^{-\frac{7}{2}}$ (Kriegseis *et al.* 2011). For the current case a dimensional supply frequency $\tilde{f}_p = 15 \text{ kHz}$ is considered. All the quantities in (22) are non-dimensionalised by considering kinematic viscosity $\tilde{\nu} = 1.5 \times 10^{-5} \text{ m}^2/\text{s}$, free-stream velocity $\tilde{U} = 60 \text{ m/s}$, density $\tilde{\rho} = 1.225 \text{ kg/m}^3$ and Reynolds number $Re = \tilde{U}L/\tilde{\nu} = 1000$ as in the simulations, see §2.

The force $(F/L)_l$ required by each actuator can be computed by knowing the control signal $u_l(t)$ and its forcing shape $\mathbf{b}_{u,l}$ from (3). Since the control forcing is time-dependent, the time-averaged power is considered to evaluate the power consumption of the actuator. Hence, the individual power consumption $(P/L)_l$ is computed and the total power consumption $P_{c,p}$ is estimated by summing the time-averaged contribution of each actuator:

$$P_{c,p} = \sum_{l=-M/2}^{M/2} \left\langle \left(\frac{P}{L}(t) \right)_l \Delta Z \right\rangle_t. \quad (23)$$

where ΔZ is the spanwise support of the actuator.

5.2. Power gain

The saved power is quantified by the product of the drag reduction ΔD and the free-stream velocity U (Stroh *et al.* 2015):

$$P_s = U \Delta D. \quad (24)$$

In Figure 15a P_s is compared with the power used by the actuators computed via the different actuator models. Ideal and plasma actuator show similar trends with increasing disturbance level; they consumes more power as the

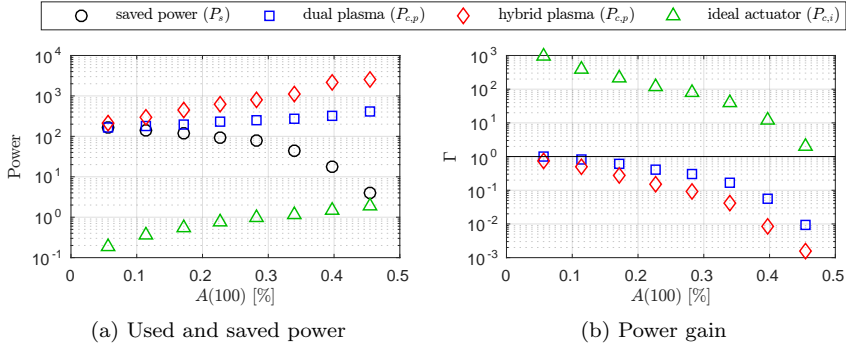


Figure 15: Energy budget. The reported quantities are computed based on a time-averaged flow over 1200 time units. The solid black line in (b) indicates $\Gamma = 1$, i.e. the break-even point for the control strategy.

disturbance amplitude becomes larger. On the other hand, the saved power reduces because of the control performance loss due to the non-linearities at the actuation location.

The power-gain coefficient is defined as:

$$\Gamma = \frac{P_s}{P_c}. \quad (25)$$

This coefficient gives the saved power because of the transition delay as fraction of power P_c invested in the control. The break-even point is given by $\Gamma = 1$, when the energy that is spent for the control is equal to the saved energy P_s .

For the ideal actuator, a theoretical gain between 10^3 and 10^2 is possible for perturbation amplitude on the order of few percent (Figure 15b). For larger disturbance amplitudes, the gain gradually decays and eventually crosses the break-even point.

The energy gain based on the plasma-actuator power-consumption estimation is lower than the break-even value for all the investigated cases. In order to better compare it to the ideal actuator model, let us introduce a measurement of the actuator efficiency:

$$\eta_p = \frac{P_{c,i}}{P_{c,p}} = \frac{\Gamma_p}{\Gamma_i}. \quad (26)$$

According to this definition, the plasma actuator has an efficiency on the order of 0.1% (Figure 16). This result is in agreement with the experimental investigation by Jolibois & Moreau (2009) who showed a similar efficiency for a steady forcing. Hence, the present estimation, based on the work by Kriegseis *et al.* (2011, 2013), indicates that the low efficiency by the plasma actuators erodes the potential gain by the presented control technique. A technical challenge in designing more efficient plasma-actuators is to increase the efficiency from 0.1% to 1% in order to push Γ over the break-even point. A critical aspect is identified in

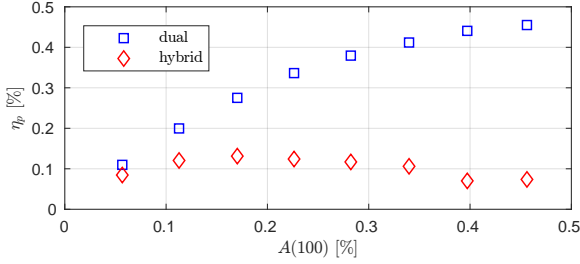


Figure 16: Plasma actuator efficiency η with respect to the ideal actuator.

the zero-forcing voltage V_0 in (21); this offset represents the energy that the plasma actuator needs to create the plasma stream that will cause the force on the flow. This energy is not directly used to control the disturbance in the flow and, hence, it does not contribute to the transition delay.

However, the presented control technique can be generalised to other types of actuators that are able to produce a TS-wave-like disturbance. Examples of this type of actuators can be found in the review by Cattafesta & Sheplak (2010).

6. Conclusions

Reactive laminar-flow control can efficiently delay the laminar to turbulence transition in a realistic low-amplitude disturbance environment. Moreover, it is shown that the drag reduction that results from the transition delay leads to a net power saving up to the order of 10^3 , when an ideal-actuator model is considered.

The proposed control scheme is able to delay the laminar-to-turbulence transition up to an incipient transition occurs at the actuation position. The performance degrades gradually as the amplitude of the perturbation increases. Adaptivity is able to marginally improve the control performances with respect to the non-linear behaviour of the flow, at least for the investigated set-up.

Large net energy saving is shown in an ideal framework, highlighting the potential performances of reactive transition-delay control. However, in a more realistic scenario where a plasma actuator model is considered (Kriegseis *et al.* 2011), the energy gain is estimated to drop below the break-even point for almost all the investigated cases. The reason for this is to be found in the poor efficiency of plasma actuators; an improved actuator design is solicited in order to take advantage of the potential of the investigated control technique.

The authors acknowledge support by the Swedish Research Council (VR-2012-4246, VR-2010-3910) and the Linné Flow Centre. Simulations have been performed at National Supercomputer Centre (NSC) and High Performance

Computing Center North (HPC2N) with computer time provided by the Swedish National Infrastructure for Computing (SNIC).

REFERENCES

- ASTRÖM, K. J. & WITTENMARK, B. 1995 *Adaptive Control*, 2nd edn. Addison Wesley.
- BAGHERI, S., BRANDT, L. & HENNINGSON, D. S. 2009 Input–output analysis, model reduction and control of the flat-plate boundary layer. *J. Fluid Mech.* **620** (1), 263–298.
- CATTAFESTA, L. N. & SHEPLAK, M. 2010 Actuators for Active Flow Control. *Ann. Rev. Fluid Mech.* **43**, 247–272.
- CHEVALIER, M., SCHLATTER, P., LUNDBLADH, A. & HENNINGSON, D. S. 2007 A pseudo-spectral solver for incompressible boundary layer flows. *Tech. Rep. TRITA-MEK 2007:07*. KTH Mechanics, Stockholm, Sweden.
- DADFAR, R., FABBIANE, N., BAGHERI, S. & HENNINGSON, D. S. 2014 Centralised versus decentralised active control of boundary layer instabilities. *Flow, Turb. and Comb.* **93** (4), 537–553.
- DADFAR, R., SEMERARO, O., HANIFI, A. & HENNINGSON, D. S. 2013 Output Feedback Control of Blasius Flow with Leading Edge Using Plasma Actuator. *AIAA J.* **51** (9), 2192–2207.
- FABBIANE, N., BAGHERI, S. & HENNINGSON, D. S. 2015a Adaptive control of finite-amplitude 3D disturbances in 2D boundary-layer flows. In *Proceedings of TSFP-9*. Melbourne.
- FABBIANE, N., SEMERARO, O., BAGHERI, S. & HENNINGSON, D. S. 2014 Adaptive and Model-Based Control Theory Applied to Convectively Unstable Flows. *Appl. Mech. Rev.* **66** (6), 060801.
- FABBIANE, N., SIMON, B., FISCHER, F., GRUNDMANN, S., BAGHERI, S. & HENNINGSON, D. S. 2015b On the Role of Adaptivity for Robust Laminar-Flow Control. *J. Fluid Mech.* **767**, R1.
- JEONG, J. & HUSSAIN, F. 1995 On the identification of a vortex. *Journal of Fluid Mechanics* **285**, 69–94.
- JOLIBOIS, J. & MOREAU, E. 2009 Enhancement of the Electromechanical Performances of a Single Dielectric Barrier Discharge Actuator. *IEEE Transactions on Dielectrics and Electrical Insulation* **16** (3), 758–767.
- JUILLET, F., MCKEON, B. J. & SCHMID, P. J. 2014 Experimental Control of Natural Perturbations in Channel Flow. *J. Fluid Mech.* **752**, 296–309.
- KACHANOV, Y. S. 1994 Physical mechanisms of laminar-boundary-layer transition. *Annual review of fluid mechanics* **26** (1), 411–482.
- KOTSONIS, M., SHUKLA, R. K. & PRÖBSTING, S. 2015 Control of Natural Tollmien-Schlichting Waves using Dielectric Barrier Discharge Plasma Actuators. *Intl J. of Flow Control* **7** (1-2), 37–54.
- KRIEGSEIS, J., MÖLLER, B., GRUNDMANN, S. & TROPEA, C. 2011 Capacitance and power consumption quantification of dielectric barrier discharge (DBD) plasma actuators. *Journal of Electrostatics* **69** (4), 302–312.
- KRIEGSEIS, J., SCHWARZ, C., TROPEA, C. & GRUNDMANN, S. 2013 Velocity-Information-Based Force-Term Estimation of Dielectric-Barrier Discharge Plasma Actuators. *J. Phys. D* **46** (5), 055202.

- KURZ, A., GOLDIN, N., KING, R., TROPEA, C. D. & GRUNDMANN, S. 2013 Hybrid Transition Control Approach for Plasma Actuators. *Exp. Fluids* **54** (11), 1–4.
- LI, Y. & GASTER, M. 2006 Active Control of Boundary-Layer Instabilities. *J. Fluid Mech.* **550**, 185–205.
- NORDSTRÖM, J., NORDIN, N. & HENNINGSON, D. S. 1999 The fringe region technique and the Fourier method used in the direct numerical simulation of spatially evolving viscous flows. *SIAM J. Sci. Comp.* **20** (4), 1365–1393.
- SCHLATTER, P., STOLZ, S. & KLEISER, L. 2004 LES of transitional flows using the approximate deconvolution model. *Intl J. Heat and Fluid Flow* **25** (3), 549–558.
- SCHULTZ-GRUNOW, F. 1940 Neues Widerstandgesetz für glatte Flatten. *Luftfahrtforsch* **17**, 8.
- SEMERARO, O., BAGHERI, S., BRANDT, L. & HENNINGSON, D. S. 2013 Transition delay in a boundary layer flow using active control. *J. Fluid Mech.* **731** (9), 288–311.
- SIMON, B., NEMITZ, T., ROHLFING, J., FISCHER, F., MAYER, D. & GRUNDMANN, S. 2015 Active flow control of laminar boundary layers for variable flow conditions. *Intl J. Heat and Fluid Flow* **56**, 344–354.
- SNYDER, S. D. & HANSEN, C. H. 1994 The effect of transfer function estimation errors on the filtered-x LMS algorithm. *IEEE Transactions on Signal Processing* **42** (4), 950–953.
- STOLZ, S., ADAMS, N. A. & KLEISER, L. 2001 The approximate deconvolution model for large-eddy simulations of compressible flows and its application to shock-turbulent-boundary-layer interaction. *Phys. Fluids* **13**, 2985.
- STROH, A., FROHNAPFEL, B. & SCHLATTER, P. 2015 A comparison of opposition control in turbulent boundary layer and turbulent channel flow. *Phys. Fluids* **27**, 075101.
- STURZEBECKER, D. & NITSCHKE, W. 2003 Active cancellation of Tollmien–Schlichting instabilities on a wing using multi-channel sensor actuator systems. *Intl J. Heat and Fluid Flow* **24**, 572–583.